Study on Upper Atmosphere by Using Remote Sensing with Radio and Infrasonic Waves: An Application of KUT Dense Infrasound Sensor Network in Japan

by

MARIO BATUBARA
Student ID Number: 1216008

A dissertation submitted to the
Engineering Course,
Department of Engineering,
Graduate School of Engineering,
Kochi University of Technology,
Kochi, Japan

Assessment Committee:

Supervisor	: Professor Masa-yuki Yamamoto
Co-Supervisor	: Professor Katsushi Iwashita
Co-Supervisor	: Professor Masataka Takagi
Co-Reviewer	: Associate Professor Hirokazu Kobayashi
Co-Reviewer	: Associate Professor Shuji Taue

March 2020

ABSTRACT

***

This dissertation is about the data analysis and processing based on the active-passive radar and infrasound observations. Obviously, the terms between two of them are absolutely different set of instruments, however the combination of two of them may give a possibility to study a wide range of atmospheric phenomena. In this dissertation, three different observations, such as the allSKy interferometric METeor (SKiYMET) radar as an active remote sensing technique and the Kochi Forward Scatter Meteor Radar (KFSMR), as well as the Infrasound network observation systems as a passive remote sensing technique for the upper atmosphere. The SKiYMET radar and the KFSMR radar systems were used to investigate the changes in meteor peak height according to solar activity, represented by the solar radio index F10.7, and the number of solar sunspots, R, compared with the empirical results of the Mass Spectrometer Incoherent Scatter Extending (MSISE) and Committee on Space Research International Reference Atmosphere models as well as the orbital parameters of the meteor. The infrasound observation from the infrasound sensor network of KUT was used to infer the source signal detection, e.g., the arrival direction and the apparent speed based on the implementation of the method of Doppler Radar Beam Swinging. Therefore we have chosen to split up the scenario of the study in two parts. One is in the field of radar system as the radio remote sensing, and the second part is in the field of infrasound system as the sound wave remote sensing. While the primary targets of this dissertation are the audience working with ground based observations to study the atmosphere, and also aimed to make it accessible and useful to a wider user.

It was found that (i) the daily meteor count rates at above the meteor radar sites in the period from 2003 to 2016 could be used to determine the dynamics in the upper atmosphere, where peak conditions occurred in the middle of the year; (ii) through a statistical approach using the normal distribution function, the variation in meteor peak height showed a positive correlation with the trend in solar activity; and (iii) comparison between the two empirical models and our observations showed two points where annual air density seemed to have a clear relationship

with peak meteor height. In addition, the annual neutral density pattern of the model was related to the daily meteor count every year, although it showed a pattern opposite to the solar activity trends. From the meteor observation with the three-receiver interferometer system, the average speed of the Geminid meteor shower observations shows a peak speed of around 35 km/s which confirms the results of similar observations previously.

In different part of this dissertation, low frequency signals from the Mt. Shinmoedake in Japan are used to estimate the horizontal atmospheric wind velocity at certain altitude. Depending on the background atmospheric condition at low-mid altitude, the arrival signals are observed during sequence of explosive volcanic activities. It was also found that the comparison of the atmospheric wind speed between the infrasound observation and the radiosonde observation are relatively in good agreement, whereas the wind at above the radiosonde altitude still remain works for validations and comparisons.

Additionally, the implementation of the Doppler Radar Beam Swinging into the infrasound sensor array system gives a possibile way to detect the source waves for further atmospheric wind estimation, even though it still meets several limitation during the processing. However, these results suggest the utilities of both radio and infrasound techniques could be used for atmospheric study.

DEDICATION

***

In the name of Allah, the Most Gracious and the Most Merciful.

All praises to Allah and His blessing for the completion of this dissertation. I thank God for all the opportunities, trials and strength that have been showhered on me to finish writing the dissertation. I experienced so much during this process, not only from the holy Prophet Muhammad (Peace be upon him) whose way of life has been a continuous guidance for me.

The journey that led to the publication of this work started back in 2008. I can vividly remember my first introduction to ground based remote sensing by Juergen Rotger, during a private workshop in radar observation. I was totally amazed by the explanation that we can use how the radiowave can sense the wind in the atmosphere, I was well pleased I could continue in the field after this internship.

The real journey of this work started at the month of March 2017 at the Kochi University of Technology (KUT), with the kickoff studying of the ground based remote sensing in recent Yamamoto-lab's project, Kochi, Japan. The project is a collaborative infrastructure design study, gathering various atmospheric observation techniques (Infrasound, Forward Scatter (FS) radar, camera, Very Low Frequency receiver and rocket sounder) to study atmospheric disturbances of interest. For the project, I would be involved in the utilization of infrasound and FS-data for the development and analysis: a challenging but interesting work package, that formed the basis of this dissertation. Although it was not planned initially, our work in the project evolved into a doctoral plan and eventually this dissertation. The work continued in the 2^{nd} year of my study, now focusing on the road towards data assimilation of infrasound-data. What followed after my first coming in 2017 is an unforgettable list of meetings, conferences, and discussions: Japan, India, Thailand and Greece. It has been a long journey from the beginning of this experience to where I am now. Nevertheless, this doctoral dissertation would not have realize possibly without the project in Yamamoto's lab of KUT, all the meetings, and with-

out all the people involved in the project. The importance of speaking how to read and interpret the data from the instrument is the thing I will not easily forget. I became aware of the fact that it is not just knowledge that is important, but the analysis design as well as the scientific language. The past years, data assimilation through processing development has been the word I tried to fight out the most and it is simply not that easy to completely setup. Assimilation of new observation system requires a long way, something I did not realize when joining in the project. We aim to use the two observation datasets, FS radar and infrasound, towards the implementation of combination ground based observation data for atmospheric study in the next 10 to 20 years, significant progress of the project has been made during the past five years. This doctoral dissertation primarily focuses on short-term goals for study the upper atmosphere by using remote sensing with radio and infrasonic waves: to develop new methods, applications, for the utilization of infrasound data and analysis the radar data as well. However, hopefully it does contribute to the long-term impacts as well.

In my mind, the content of this doctoral dissertation is much more than its scientific value. Hopefully, it might convey some useful knowledge for certain experts in some fields of researches. This doctoral dissertation, for me, represents a magnificent journey in science and in life.

Dear Prof. Masa-yuki Yamamoto, thanks a million for this journey, starting from accepting me in the project and be your student, giving the accessible in the Lab's facility especially in infrasound and FS radar to everything that followed along: a research position and even this doctoral opportunity. Notwithstanding, I got something way more important in return. I enjoyed how you insist on simplicity to explain complex things and to approach new challenges. This is an expertise you seek to carry on to all of your students, which I appreciated a lot when guiding all together.

Many thanks to Prof. Katsushi Iwashita, Prof. Masataka Takagi, Assoc. Prof. Hirokazu Kobayashi, and Assoc. Prof. Shuji Taue, for the warm welcome during discussion in your office. Although my research topic is kind of odd compared with the ideal world of remote sensing usage for atmospheric studies, I never had felt like an outsider. Thank you for carefully reviewing this material.

I would like to thanks to all my colleagues in the lab. Thank you all for the tremendous support, discussion, and free talks. Special thanks to Dr. Saito for the discussion. Thank you Otsuka-san, for all of your helps as a tutor during my first come until now.

I am grateful to the IRC of Kochi University of Technology for the Special Scholarship Program to make this research possible. Thank you prof. Sakikawa for your kindly helps, and many thanks to all IRC staff of KUT for all informations and guidance.

I am grateful to the Indonesian National Institute of Aeronautics and Space (LAPAN), Indonesia and Research Institute for Sustainable Humanosphere (RISH), Kyoto University, Japan, for providing the meteor radar data. I acknowledge use of NASA/GSFC's Space Physics Data Facility's OMNIWeb (or CDAWeb or ftp) service and OMNI data.

My belove family, Weri, Eira, and my little boy, Zaidan, I could not have achieved this dissertation without your support. Thanks for always being my side. A big hug and kiss.

Thank you dad and mum for the everlasting support and your endless encouragement, even though I was not available.

Mario Batubara,
Kami City - Kochi, Japan,
March 2020

CONTRIBUTORS AND FUNDING SOURCES

***

Contributors

This work was supported by a dissertation committee consisting of Professor Masa-yuki Yamamoto (advisor), Professor Katsushi Iwashita (co-advisor), Professor Masataka Takagi (co-advisor), Associate Professor Hirokazu Kobayashi (co-reviewer), and Associate Professor Shuji Taue (co-reviewer).

The infrasound data analyzed in this work was retrieved from the FTP server of Yamamoto's lab, managed by its IT team. The meteor radar data were obtained from the IUGONET-RISH Kyoto University and LAPAN database center. The solar sunspot and solar radiation index F10.7 were obtained from the World Data Center Sunspot Index and the NASA OMNIWeb Space Physics data facility, provided by NASA. The atmospheric model-derived data were obtained from the Community Coordinated Modeling Center, provided by NASA.

Funding Sources

Graduate study was supported by a fellowship from Kochi University of Technology and a dissertation research fellowship from Yamamoto's lab Foundation.

NOMENCLATURE

***

Abbreviations

PBL	the Planetary Boundary Layer
UV	the Ultraviolet
LIDAR	the Light Detection and Ranging
RADAR	the Radio Detection and Ranging
HMW	the Horizontal Wind Model
MSIS	the Mass Spectrometer and Incoherent-Scatter radar
NRLMSISE-00	the Naval Research Laboratory Mass Spectrometer and Incoherent-Scatter radar Exosphere
EUV	the Extreme Ultraviolet
NRL	the Naval Research Laboratory
WDC-SILSO	the World Data Center-Sunspot Index and Long-term Solar Observations
MERRA-2	the Modern-Era Retrospective Analysis for Research and Application, version 2
GMAO	the GLobal Modeling and Assimilation Office
NASA	the National Aeronautics and Space Administration
US	the United States
GEOS-1	the Goddard Earth Observing System, version 1
EUV	the Extreme Ultraviolet
DBS	the Doppler Beam Swinging
VAD	the Velocity-Azimuth Display
VED	the Velocity-Elevation Display
SOUSY	the SOUnding SYstem
MU	the Middle and Upper atmosphere

CLOVAR	the Canadian London, Ontario VHF Atmospheric Radar
PANSY	the Program of the Antarctic Syowa
MAARSY	the Middle Atmosphere Alomar Radar SYstem
EAR	the Equatorial Atmosphere Radar
EMU	the Equatorial Middle and Upper atmosphere
SAR	the Synthetic Aperture Radar
SDI	the Spatial Domain Interferometry
MST	the Mesosphere–Stratosphere–Troposphere
FDI	the Frequency Domain Interferometry
LO	the Local Oscillator
IF	the Intermediate Frequency
RMS	the Root Mean Square
DFT	the Discrete Fourier Transform
FFT	the Fast Fourier Transform
DC	the Direct Current
AC	the Alternating Current
SNR	the Signal-to-Noise Ratio
ACF	the Autocovariance Function
IMS	the International Monitoring System
CTBT	the Comprehensive Nuclear-Test-Ban Treaty
AoA	the Angle of Arrival
PMCC	the Progressive Multi-Channel Correlation
MEMS	the Micro-Electro-Mechanic System
KISONS	the Kochi University of Technology Infrasound Observation Data Network System
CSV	the Comma Separated Value
KUT	the Kochi University of Technology
SKiYMET	allSKy interferomteric METeor

MWR	the Meteor Wind Radar
MLT	the Mesosphere and Lower Thermosphere
JWH	John, Webser, and Hocking
RDAS	the Radar Data Acquisition
CEV	the Confirmed Event
MPD	the Meteor Position Data
ASCII	the American Standard Code for Information Interchange
RISH	the research Institute for Sustainable Humanosphere
LAPAN	the Lembaga Penerbangan dan Antariksa Nasional
PC	the Personal Computer
FS	the Forward Scatter
KFSMR	the Kochi Forward Scatter Meteor Radar
HRO	the Ham-band Radio meteor Observation
MT	the Meteor Trajectory
VHF	the Very High Frequency
IDL	the Interactive data Language
ESESL	the Earth Space and Exploration System Laboratory
PWs	the Planetary Waves
UTC	the Universal Time Coordinated
DSP	the Digital Signal Processing
CIRA	the COSPAR International Reference Atmosphere
COSPAR	the Committee on Space Research
DoY	the Day of Year
JANET	the Joint Army-Navy Network
JMA	the Japan Meteorological Agency
MODIS	the Moderate Resolution Imaging Spectroradiometer
MIROVA	the Middle InfraRed Observation of Volcanic Activity

LANCE-MODIS	the Land Atmosphere Near real-time Capability for EOS-MODIS
VRP	the Volcanic Radiative Power
JST	the Japan Standard Time
PSD	the Power Spectral Density
GES-DISC	the Goddard Earth Sciences Data and Information Services Center
CCMC	the Community Coordinated Modeling Center
NOAA	the National Oceanic and Atmospheric Administration
PRF	the Pulse Repetition Frequency

Symbols

λ	the wavelength
u	the zonal wind velocity
v	the meridional wind velocity
w	the vertical wind velocity
v_{rad}	the radial component of the velocity
φ	the radar signal phase
v_H	the horizontal component of wind speed
δ	the tilt of radar beam from vertical
d	the the distance between two antennas
θ	the arrival angle
c_n	the consistency in the number of Net
C_{ij}	the correlation function for sensor *i* and *j*
ε	the threshold in the consistency evaluation
Δt_{ij}	the time delay between sensor *i* and sensor *j*
v_{app}	the apparent velocity
h_m	the measured meteor height
h_T	the height of a meteor echo
σ_P	the standard deviation of h_m

σ_T	the uncertainty in meteor height
h_P	the meteor peak height
F10.7	the solar radio flux at 10.7 sm
R	the sunspot number
r_i	the echo range at each candidate
r_e	the Earth's radius
c	the signal speed, which for radar is the speed of light
ϕ_{ij}	the phase measurement between antenna i and j
β	the angle of arrival

PUBLICATIONS AND DISSEMINATIONS

***

Papers

Batubara, M., Yamamoto, M.-Y., Madkour, W., & Manik, T. (2018). *Long-term distribution of meteors in a solar cycle period observed by VHF meteor radars at near-equatorial latitudes*. Journal of Geophysical Research: Space Physics, 123, 10,403– 10,415. https://doi.org/10.1029/2018JA025906.

Mizumoto, S., Yamamoto, M.-Y., & Batubara, M. (2019). *Construction of a meteor orbit calculation system for comprehensive meteor observation at Kochi University of Technology*. Planetary and Space Science, 173,35-41. https://doi.org/10.1016/j.pss.2019.03.004.

Batubara, M., and Yamamoto, M.-Y. (2020). *Infrasound Observations of Atmospheric Disturbances Due to a Sequence of Explosive Eruptions at Mt. Shinmoedake in Japan on March 2018*. Journal of MDPI: Remote Sens. 2020, 12(4), 728; https://doi.org/10.3390/rs12040728.

Batubara, M., Yamamoto, M.-Y., & Saito, H. (2020). *Results from infrasound monitoring using integrated sensors data by means of a network along multisite point over Japan*. Proceedings of the 14th International Conference on Vibration Problems (ICOVP 2019).

Conferences

Batubara. M., Yamamoto, M.-Y., Madkour, W., & Manik, T. (2018). *A study of the effect of solar activity on the meteor height distribution in the equatorial region of Indonesia*. The Japan Geoscience Union (JpGU) Meeting 2018. 20-24 May 2018, Chiba, Japan.

Batubara, M., Yamamoto, M.-Y., & Saito, H. (2019). *Results from infrasound monitoring using integrated sensors data by means of a network along multisite point over Japan*. 14th International Conference on Vibration Problems (ICOVP2019). 1-4 September 2019, Crete, Greece.

Batubara, M., Yamamoto, M.-Y., & Saito, H. (2018). *The Infrasound observation network in Kochi prefecture, Japan: system description and initial results*. The 15th International Symposium on Equatorial Aeronomy (ISEA-15). 22-26 October 2018, the PRL, Ahmedabad, India.

Batubara, M., Yamamoto, M.-Y., & Saito, H. (2019). *Utilization of seismic activity infrasound signals to estimate wind in the atmosphere*. The 7th International Symposium on Frontier Technology (ISFT2019). 24-25 August 2019, Pattaya, Thailand.

Batubara. M., Yamamoto. M.-Y., & Saito, H. (2019). *Infrasound observations of atmospheric disturbances due to a sequence of 2018 explosive volcano eruptions in Japan*. The Japan Geoscience Union (JpGU) Meeting 2019. 26-30 May 2019, Chiba, Japan.

TABLE OF CONTENTS

Page

LIST OF FIGURES

FIGURE Page

LIST OF TABLES

TABLE Page

Chapter 1

INTRODUCTION

***

1.1 The Atmospheric Dynamics and Structure

The Earth's atmosphere is the gaseous covering and protecting the earth. Because it is a fluid system, the atmosphere is capable to centrally transfer energy between the sun and the Earth's surface and from one region to another in order to control the equilibrium of the thermal and the earth's climate. Like any fluid system, the atmosphere can be described by the laws of continuum mechanics. According to the laws of mechanics and thermodynamics, the atmospheric behaviour can be described in terms of the properties of their positions, temperatures, motion and constituent densities. The system of their mobility governs the complexity of their dynamics, which are different in each of atmospheric structure.

Based on three of properties above, one can distinguish the neutral atmosphere as the troposphere, stratosphere, mesosphere, thermosphere, and exosphere from the ground to space, depending on the solar activities (Figure 1.1). The troposphere, extending from the Earth's surface to $\sim$10-15 km, that is, the interface between the lithosphere and the middle atmosphere, which contains about 80% of the mass of the atmosphere, nearly all water vapor and clouds. In between this region, the tropopause is existed by the altitude where the inversion begin and vary with height. The region of the troposphere closest to the Earth's surface is commonly termed to as the planetary boundary layer (PBL), mostly weather change takes place. During the day, the temperature drops with height in the lower troposphere due to earth's surface heated by the sun, leading to wave generation and upward wave refraction, until a temperature minimum is reached at the tropopause. Meanwhile, at night the condition becomes stably stratified where a clear night generates a temperature inversion and a strong wind jet, allowing the sound refracted back to the ground. At middle latitudes, the troposphere is specified by regional of horizontal wind jets, just at a few km above it, the stratosphere is a stratified layer, which is separated

from the troposphere by the tropopause, at altitude about 10-15 km up to 50 km. The temperature increases rapidly with height as a result of the increased absorption of UV radiation by the ozone molecules with altitude. The ozone is formed in the stratosphere as a product of the reaction of the sun with the oxygen molecules with heat. During the summer, the stratospheric temperatures are warmest in the higher latitudes, while they are becoming colder during the winter. Moreover, during the winter period in the Northern hemisphere, the stratosphere also characterized to the existence of a stratospheric jet stream, similar to the tropospheric jet stream but of larger scale and magnitude. The jet is essentially strong enough to overcoming a stratospheric duct that permits the wave refracted back to the ground. In addition, the stratospheric jet stream reverses seasonally: on northern hemisphere, it flows westward during the hot seasons and oppositely during the winter. Above the stratosphere, the mesosphere exists just between the stratosphere and thermosphere, which temperature decreases with altitude, compared to the stratosphere. Meteors burn up in this layer due to meteor particle collides with atmospheric molecules and produce a trail of the ionized particle, producing straight light in the night. Above the mesosphere, the upper most region of the atmosphere, depending dominantly on the solar activity. The temperature increases dramatically with height, caused by the absorption of the solar radiation. Contrastly different, the density in this region is much smaller than that is found in the lower atmosphere, affecting the severe absorption on the long wave propagation.

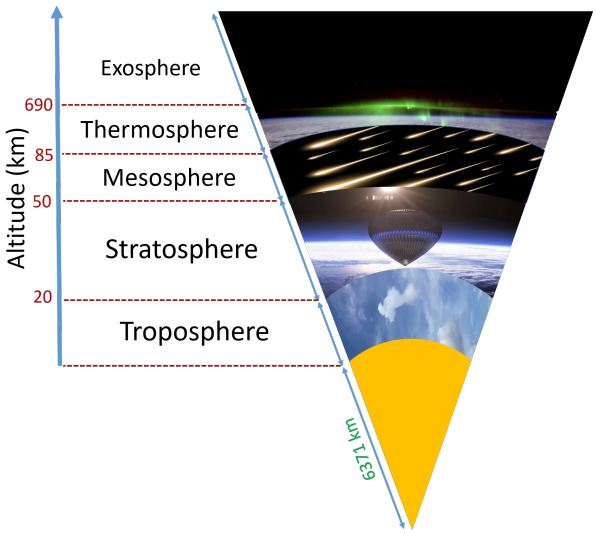

Figure 1.1: Vertical layer of the Earth's atmosphere.

1.2 Atmospheric Observation

To properly understanding the upper atmospheric properties, a viable meteorological observation system must integrate with the fully operational numerical weather prediction system. Recently, the lower atmosphere is the most well resolved and understood region. The various observation techniques and global analysis has provided the global information. However, and presently, understanding and dynamical characteristics of higher atmospheres, with global spatial and temporal coverage, are constrained by difficulties in making routine direct measurements of the middle and upper atmosphere. Now, this is an active scope in scientific research to develop methods for measuring the properties of the atmosphere in this region. Apart from technological developments and improvements made over the past few decades in studies towards achieving the research objectives with ground-based remote sensing, such as Light Detection and Ranging (LIDAR) (Gardner et al. [1995]), and / or Radio Detection and Ranging (RADAR) (Yi et al. [2016], Stober et al. [2014], John et al. [2011]), and global databases of weather prediction with actual atmospheric measurements over the stratosphere are still relatively sparse. Nevertheless, wind information from these altitudes is important for the assessment of middle atmospheric dynamics in general and as a basis for planetary waves (PWs) or infrasound propagation estimates. The current state-of-the-art profiles on wind, temperature, and composition in the mesosphere and lower thermosphere are given by semi-empirical models such as the Horizontal Wind Model (HWM) (Hedin et al. [1988, 1991], Emmert et al. [2008], Drob et al. [2008, 2015]), and the Mass Spectrometer and Incoherent-Scatter Model (MSIS) developed by the Naval research Lab (NRL). More recently, the Modern-Era Retrospective Analysis for Research and Applications, version 2 (MERRA-2) developed by the NASA's Global Modeling and Assimilation Office (GMAO) and they began an effort to reanalysis development with the production of the Goddard Earth Observing System, version 1 (GEOS-1) and with more advanced significantly production of the previous MERRA to produce specifications up to 0.01 hPa altitude within 72 hybrid-eta levels (Bosilovich and Suarez [2016], Gelaro et al. [2017]). These tools will contribute to an improved understanding of higher atmospheric characteristics and processes.

1.2.1 Radar Remote Sensing

The fundamental describing of the atmospheric specification and their characteristics that various radar studies have been invented earlier, in the period following World War II. Two mainly goals were (i) studies of probability in radar detection for civil applications and (ii) ionospheric studies for long-range communication. The first goal of the idea aims to investigate the tropospheric intensively, and the second aim to more elaborate studies of the upper atmosphere and ionosphere. Fundamentally, the radar principle for range-detection basically comes from a short pulse of an electromagnetic wave within typically several microseconds of periods is transmitted from the radar transmitter through the antenna, whereupon it finally may hit the target to observe the effects that the atmosphere has on the scattered wave. Once upon the signals strike the target, which then causes interaction in the form of bending of the radio wave path, or reflection and scattering back to the radar antenna from the target as the received signal, it is called echo. If there are multiple targets, many echoes can be detected. Echo samples are examined at consecutive time steps and taken at a series of successive delays, called range gates. In more advanced analysis, these echoes are recorded and stored as a time series of complex data samples to be then transformed into Doppler frequency spectra or covariance functions. The output of this function contains information about the target, such as the scatter cross-section, the Doppler frequency shift as a function of range or height. This chapter will begin by looking briefly at the introduction of Doppler methods that step forward ensued in the 1960s and 1970s.

a. Doppler Methods in Radar Application

Recognizing and investigating atmospheric structures is a useful exercise, in which the ability to determine the associated wind patterns and dynamic movements of the scatter, provides a new field of expertise for radar engineering. One of the measurement of the atmospheric winds with radar was generally made using the Doppler method, in which one or more high-gain narrow beams is pointed to different off-vertical directions of the sky, then Doppler shifts of the scatter echoes are measured from various beams in order to produce an estimate of the horizontal wind speeds associated with the scatter over the radar (Gage and Balsley [1978]).

The Doppler shift of the backscattered signal is utilized for wind determination, and typically used techniques are called "Doppler Beam Swinging (DBS)" techniques (Figure 1.2a. The method is simplified version of the well-known VAD (Velocity-Azimuth Display) and VED (Velocity-Elevation Display),as well as information about VAD and VED can found in the articles by Browning and Wexler [1968], Koscielny et al. [1984]. Since the late 1990s, several radars demonstrated their developments, and their evolution. Recently, previous radars use DBS technique for atmospheric wind measurements, such as the SOUSY (SOUnding SYstem) radar was operated firstly in 1970s at the Harz mountains, Germany. More detail description of the SOUSY radar can be found in the article by Czechowsky et al. [1976]. The second era of atmospheric radar, the Middle and Upper atmosphere (MU) radar was completely constructed in 1984 in Japan. The detail of the MU radar is discussed in the article by Fukao et al. [1985a,b]. The third is the pioneer of atmospheric radar, the CLOVAR (Canadian [London, Ontario] VHF Atmospheric Radar in Canada, (Hocking [1997]). More recently, newer radar located in the Antartic region at Syowa station, named the PANSY radar, which was first successfully conducted observations in March 2011, (Sato et al. [2014]). The MAARSY (Middle Atmosphere Alomar Radar SYstem) radar is located on the island of Andoya in Northern Norway. The overview of this radar is described by Latteck et al. [2012]. Presently, as continuing the road map of the MU radar and the Equatorial Atmosphere Radar (EAR), the Equatorial Middle and Upper (EMU) atmosphere radar will be operated under close long-term collaboration between Japan and Indonesia, and will constitute a global observation of compact radio network. The full description of this project can be found in Tsuda et al. [2016].

Fundamentally, the VAD method uses, at least three fixed beam positions, one at a zenith angle equals zero as well as two or more other beam directions at a zenith angle different from zero and at different azimuth angle. Preferably, the azimuths for the off-vertical beams should be orthogonal if only two off-vertical beams are used. The three component of the velocity (u, v, and w) can be obtained directly from the measurements of radial velocity along the three fixed beam directions. However, the simplest method uses only two pointed beams at different azimuths and assumes that the vertical velocity, w, is negligible. In order to determine the vertical velocity, w, a VED can be used within the azimuth is kept constant and the elevation

angle is tilted constantly.

Basically, the standard Doppler theory explains that if the scatterer moves relatively to the radar, and the path length between the radar systems and the scatterer changes. This may change the phase of the scattered radio waves in a certain time period, which is equal to the v_{rad} (the subscript refers to the 'radial' component). In the application of monostatic radar, the mean rate of phase change is a value of the mean radial velocity of the received signals, which is expressed as follows, $\langle v_{rad} \rangle = \frac{\lambda}{4\pi} \left\langle \frac{d\varphi}{dt} \right\rangle$, where $\langle\rangle$, v_{rad}, λ, φ, $\frac{d\varphi}{dt}$ are respectively represent the average value, the radial component of the velocity, the radar wave length, the phase, and the rate of phase change.

In more realistic situation, there will be multiple back-scattered signals on the radar beam that make complexity features of the spectrum when using this method to determine wind speeds. And there exist many complicating features when using the Doppler method to determine the wind. It is sometimes assumed that the vertical wind, *w* is negligible, so that the horizontal wind in the azimuthal direction can be inferred from the available off-vertical beams. The illustration of this condition is drawn in Figure 1.2. Their horizontal component can then be determined by the following expression, $v_H = v_{rad}/sin(\delta)$, where v_H, δ, and v_{rad} are respectively refers to the horizontal component of wind speed in the vertical plane, the tilt of radar beam from vertical, and the radial velocity. As shown in the figure 1.2, v_H consists of *u* and *v* for the eastward and the northward components. In a such condition, the radar beam, one, pointed out to Northward and another pointed out to Eastward, allows to determine the mean horizontal wind. However, each beam recorded the scatter from different region of the sky (Figure 1.2c), and it is known that the desirable wind vector is described at a single point in the sky. Provided that the wind does not vary too much above the radar, it is possible to assume that both components of the wind, vertical (w) and horizontal (v_H) applied immediately above the radar. Sometimes, the divergence of the wind field can be substantial. If its divergence is relatively small, then it is possible to determine the vertical wind speed, *w*, over the radar by using a vertical beam. Then $v_{rad} = v_H \sin\delta + w\cos\delta$ and so, $v_H = \frac{v_{rad} - w\cos\delta}{\sin\delta}$.

b. Multiple Receiver and Multiple Frequency in Radar Applications

This subsection will discuss about how the multiple receivers and multiple frequency techniques can be used in atmospheric remote sensing. Before going further, the term multiple receiver will be used along this subsection to describe a radar system that is capable of receiving and recording atmospheric signals on two or more spatially separated single antennas or

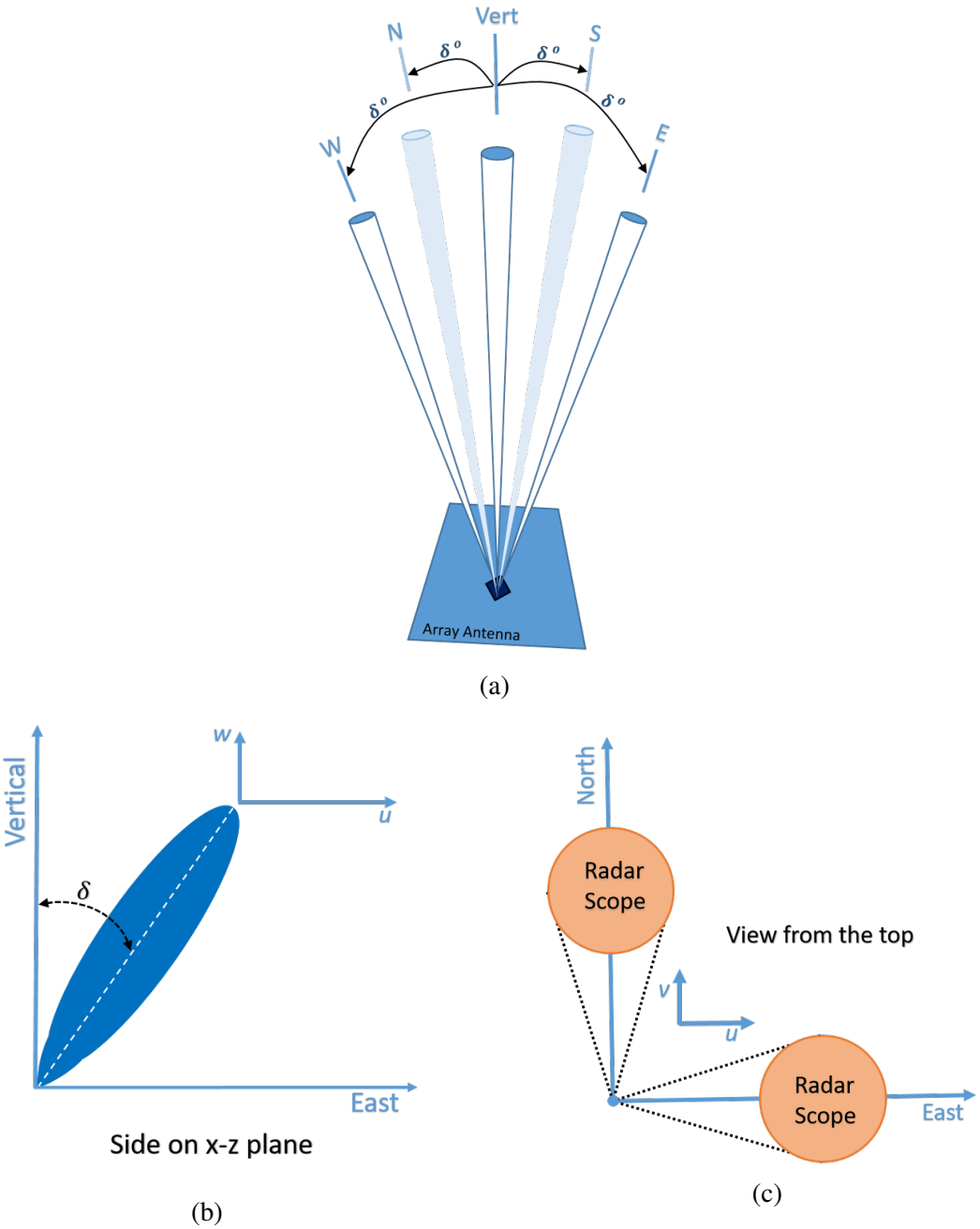

Figure 1.2: The multi-beam DBS method antenna direction. (b) Radar beam from side on x-z plane view. (c) Two perpendicular radar beam from above the horizontal plane.

groups of antennas. Moreover, multiple frequency describes to a radar system that is capable of transmitting and receiving atmospheric signals from two or more frequencies.

Many multiple receivers and multiple frequency techniques had been used to estimate wind profiles in the atmospheric applications in the lower and upper atmosphere. For the following descriptions, this part will make a detail discussion between the terms spaced antenna or correlation techniques, radar interferometry, and radar imaging. These approach ideas are closely related and they have distinct and important differences between each other. The correlation technique are principally used to observe the wind speeds, however the techniques does not concern on the scattering structure in the sky in too much detail. The term radar interferometry refers to the signal processing works to catch the motions of a particular scatterer or a group of scatterer from their location. In contrast, the term radar imaging is relatively new used currently to produce a reconstruction of atmospheric reflectivity fields of the probing radar through inversion algorithms. However, each technique takes advantages of radar signals received using multiple receivers and/or frequencies.

1) Radar Interferometry Methods

The interferometry using radio waves had been widely used in source detection and positioning, radio astronomy, and atmospheric research. This method had been applied in addition to particular for remote sensing of the topography of the Earth's structures, moon, and planets. A Synthetic Aperture Radar (SAR) was the pioneer invention of this technique as planetary radar. The radar interferometry, or as Spatial Domain Interferometry (SDI) detect and analyses echoes, which result from targets illuminated by the transmitter, to extract the information about the scatterers through computation of correlation and/or covarian function. The application of the interferometer method can also replace electronic beam swinging by digital off-line processing.

The interfermetry as one important method was introduced in the 1980s, where multiple receivers on the ground can be used for ionospheric incoherent scatter radar studies by simply comparing phases between antennas - typically three or four larger numbers of antennas were only used (Farley et al. [1981]). On of the early study, Röttger and Ierkic [1985] introduced a simpler forms of interferometry to firstly applicable in the MST radar studies, i.e. the

atmospheric/ionospheric structure in the case of MST radar imaging.

Figure 1.3 illustrates the above underlying concept, the left panel shows the simplest case of radar interferometry. The two antennas are separated by a distance d, detected the simple scatter from a single point. The phase difference between the two received signals at the antenna will simply be as a function of θ, which can directly track the motion of the scatterer. The treatment of the problem was primarily intended to illustrate the concepts of calculating the angle of arrival. The radar interferometry applies the measurement of phases of radar echoes on one wave-length at two or more antennas displaced in horizontal space. This improves the resolution in the direction perpendicular to the beam direction. Phases differences measured by this technique at two antennas are mainly related to the zenith or swing angle θ. Both information about the horizontal persistence (correlation distance) and horizontal displacements of scattering structures are done in the spectrum analysis.

2) Frequency Domain Interferometer Method

An equivalent to the radar interferometry is the Frequency Domain Interferometry (FDI), where the spatial coordinates d in the radar interferometry are replaced by wavelength. The framework of this technique was firstly formulated in 1980 (Kudeki and Stitt [1987]). The FDI applies the measurement of phases of radar echoes on two or more wavelengths at one antenna. This improves the resolution in the vertical direction. Likewise, phase differences measured by FDI on two frequencies extract the information about the range of a scattering structure and the vertical displacement as well as the vertical structure persistence, i.e. structure thickness. The right panel of Figure 1.3 shows the case of scatter from a surface or layer at height z that is parallel to the ground. A monostatic radar is used to examine two distinct frequencies, then the phase difference between the received signal can be obtained, if the waves for both frequencies have the same initial phase. In some cases, only portion of the phase difference is known in the time modulo(2π).

c. Processing of Doppler Radar Signals

The reception of radar signals requires a receiver, which principally performs several signal processing. The low-level from the antenna is fed to the low-noise preamplifier through a

band-pass. Frequently also a calibrated noise injection, which is turned on and off by the radar controller, is directly fed into the receiver front end. This is important to consider not only the noise due to the receiver itself, but also the noise due to the ambient temperature, noise from antenna and feed lines, and also the amplification of noise as it progresses through the receiver. Thus, it allow a well calibrated estimate of the receiver amplification factor. In the first mixer, the receiver signal is mixed with the signal from the first Local Oscillator (LO1) to the Intermediate Frequency (IF). Then, a pass-band filter separates the wanted IF from the unwanted mixing products. Before further amplification usually a variable attenuator is implemented to adjust the total amplification of the receiver and thus the output levels for the final baseband mixer and the analog-digital converters. Following the mixing to baseband with the LO2 signal, i.e. the quadrature detection (Re and Im), a lowpass filter is applied which usually should match the signal bandwidth to obtain two orthogonal baseband signals: in-phase (I) and quadrature (Q) components which together constitute a complex time series. Hence the received signal can be writen as $s(t) = I(t) + iQ(t)$, where $i = \sqrt{-1}$. The in-phase component is sometimes referred to as "real" component, and the quadrature component as the "imaginary" component. The values in "real" component are the amplitudes of the cosine waves, while the values in the "imaginary" component are the amplitudes of the sine waves. This actually represents all the information in the complex number, which allow us to determine the parameter with both an

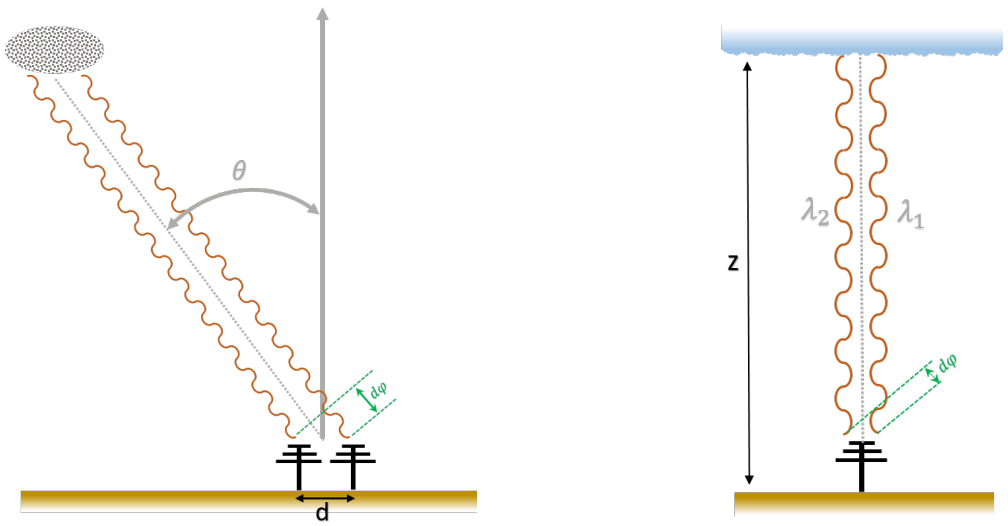

Figure 1.3: The principle of multiple-receiver and multiple frequency interferometry.

magnitude and a *phase*.

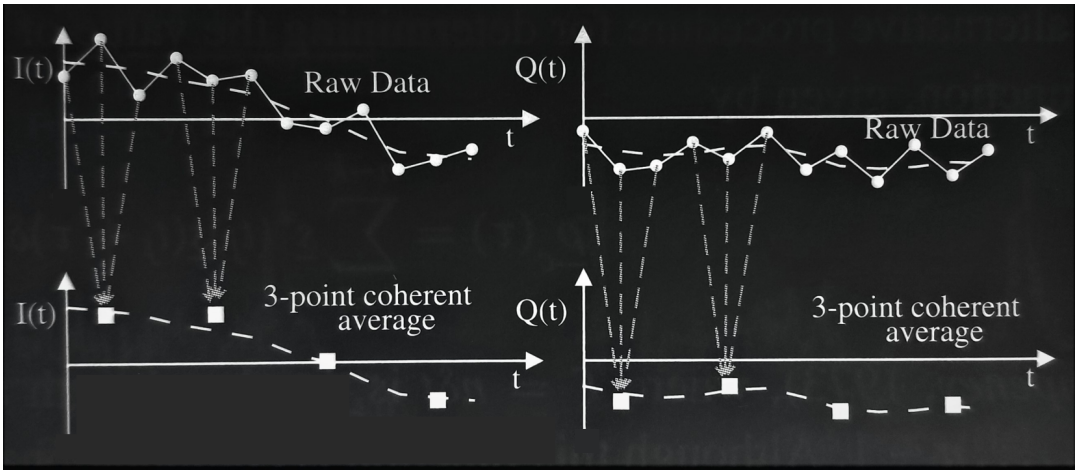

(a)

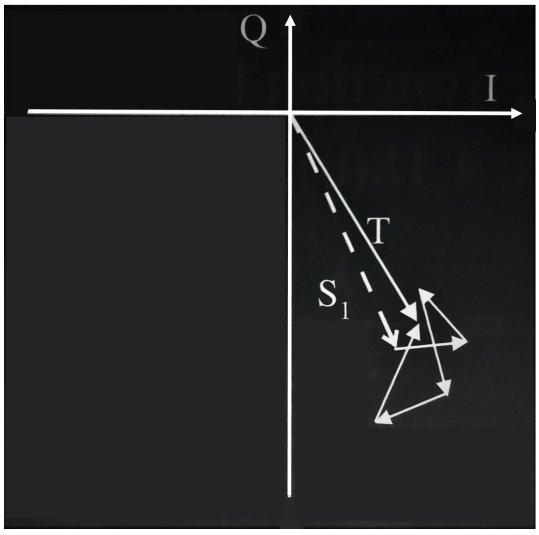

(b)

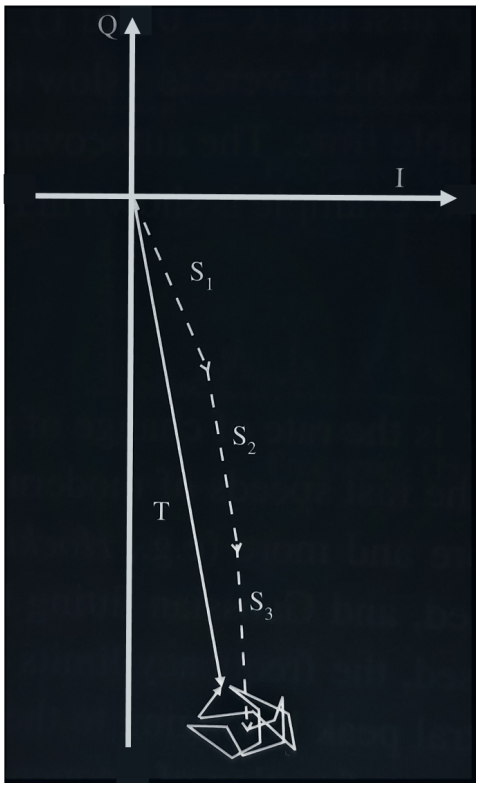

(c)

Figure 1.4: The process scheme of coherent integration. Figure adopted from Hocking et al. [2016].

Radar signal processing can be conducted in both the time and/or frequency domains, which is the alternative ways of representing signals. The Fourier transform is the scheme relationship

between these two representations. The Discrete Fourier Transform (DFT) is one of the most important tools in Digital Signal Processing (DSP), because it capable to calculate a signal's *frequency spectrum*, allowing systems to be analyzed in the *frequency domain* and able to extract the signal's information, i.e. the *frequency*, *phase*, and *magnitude*. The DFT, when one can be conducted, called the Fast Fourier Transform (FFT), is an ingenious calculation that is typically faster than the previous one. As noted previously, the names *real part* and *imaginary part* originate from the complex DFT, where they are used to differentiate between those components. Other important technique in DSP, called digital filters that are used for two general purposes: first, signals restoration which have been distorted in some ways, and second, separation signals that have been combined. In typical process, sometime, a "windowing" as the way of convolution usually used in signal processing for optimization results. More description about DSP and its implementation in programming can be read in Smith [1997].

Since the noise and the signal are independent of each other, their quadrature components include the noises come from DC-bias, and radar clutter, adding to the initial quadrature component, and they are additive. The instrumental DC-bias can be eliminated by averaging, called instrumental DC-elimination. In practical way, the radar system oversample the signals. which yields an extremely high raw data rate. Oversampling is very useful in processing weak signals, such as from turbulent scatter, and a high data rate must be obtained. Since the radar is coherent radars and the received signal is phase coherent over many interpulse period, this permits the integration of several samples over 2N interpulse periods with goal of increasing the SNR by reducing the data rate. The process is termed *coherent integration* (Farley [1985]). The idea behind this integration is shown in Figure 1.4. This procedure must be preformed before any spectra or auto correlation functions are formed. Figure 1.4a shows the complex components of the signal for a short time interval. The black dot-line represents the raw data, which consist of both noise and signal. The 'true' signal that would have not been included the noise, plotted by the dash line. Thus, the raw data obviously fluctuate higher and lower than the true signal. In order to improve the signal quality, a group of three data of the raw data have been averaged to produce the new data, plotted as the black squares in the lower plots of Figure 1.4a. Figure 1.4b and 1.4c show a different scheme to the above process. Figure 1.4c shows the effect of

a coherent integration that it has rotated slightly with time rather than the process shown in Figure 1.4b.

As noted, the long-term "DC components" deduced in the elimination procedure in each range gate from the quadrature components of the short-term signal time series and will be used to compute covariance function in the time domain and spectrum analysis in the frequency domain after the data preprocessing procedure described previously is performed. Since the power spectrum and the covariance function are Fourier transforms of each other, both properties has the same related purposes, i.e. detectability and the radial velocity estimation. This time-domain method is often referred to as autocovariance function (ACF) in order to achieve the necessary frequency resolution as detectability and further the radial velocity estimation.

1.2.2 Atmospheric Study by Infrasonic Observation

In the previous chapter, it was clear that radar was able to be used to study the dynamics of the Earth's atmosphere. By measuring the Doppler frequency shift of the echo signal from a multi-directional beam, the combination of vertical and horizontal wind speed components can be immediately concluded. Obviously, the wind factor in the atmosphere plays a very important role in the stability of the earth's atmosphere dynamics. Therefore, information about the wind character profile in each layer of the earth's atmosphere is important to know, especially the wind speed in the upper atmosphere. Up to now, it can be assert that at least a little ground-based observation systems that can provide wind profile information in the upper atmosphere. This situation did not rule out the possibility for scientists to collaborate with engineers to invent techniques or innovation of ground-based observation to study the Earth's atmosphere. One of them is the detection of very low frequency waves (i.e. infrasound) which can potentially be used to calculate the wind speed of the Earth atmosphere up to the height of the upper atmosphere, as described in the following chapter.

a. Infrasound waves

Living creatures, especially humans, are born with the hearing senses, i.e. ear to be able to understand the information in the form of sound around us. The sound we hear is a wave phenomenon that originates from the movement of the oscillating particles of the propagating

medium in the same direction as propagation, otherwise known as longitudinal waves. During its propagation, this oscillation disturbance is manifested as a form of coupled deviation in the pressure and density from the equilibrium state, as well as the consequences of compression and refinement, which triggers the movement of a number of medium material packages at the typical speed of sound. Therefore, the characteristics of the intermediary medium play an important role during their propagation. Sound waves in the atmosphere can be heard by humans, named audible sound if the frequency is in the range from 20 to 20000 Hz. Ultrasonic sound is inaudible sound by humans and has a frequency higher than 20000 Hz. At another end of the spectrum, sound also becomes inaudible when its frequency is lower than about 20 Hz, which is then called infrasound, equivalent to low-frequency light called invisible or infrared light. Infrasound are generated by a large variety of artificial and natural sources and has their frequency range is in the range of 0.003 to 20 Hz. A detailed inventory list of both typical observed infrasonic waves, including their typical frequency range and maximum amplitude can be found in Campus and Christie [2009]. A list of infrasound sources that are of interest to current researchers are earthquakes (Arrowsmith et al. [2012]) and volcanic eruptions (Evers and Haak [2005], Fee et al. [2010]). Probably the early history of infrasound studies comes from the most phenomenal of volcanic eruption is the eruption of Krakatoa, Indonesia on August 27^{th}, 1883, producing in powerfull explosions, huge tsunamis, heavy-gigantic ash plumes. One of the investigations on barograph shows that the pressure disturbances had been measured all over the world (Symons [1888]).

Because of its low frequency characteristics, infrasound has only experienced a little attenuation, therefore they can travel more than thousands of kilometers (Sutherland and Bass [2004], Evers and Haak [2009]) due to the strengthening by atmospheric waveguides and dynamics in the lower regions, between the lower land and atmosphere (Drob et al. [2003]). The earth atmosphere, as the inhomogeneous medium, i.e. the earth atmosphere, is a highly dynamical medium and varies strongly with geographical location, which leads infrasound propagation characteristics varies around the world and causes multi-variety of the recorded infrasonic waveforms. This takes a beneficial advantage to be used to monitor and study the atmospheric variability, especially to monitor the atmospheric winds in the stratopause and lower thermo-

sphere.

b. Infrasound Observations and Its Importance

As noted, infrasound is a typical sound wave that is capable of carrying a package of source information to a very distant location. The information package is described by various fluctuations in its intermediate media that can be measured, such as the temperature, density, particle velocity or pressure. Typically, the sound is measured from the pressure measurement which is the most common as the quantity is most easily measured by the specific instrument, e.g. pressure sensor. Every pressure sensor works based on a transducer that converts an absolute or differential pressure into a voltage.

Infrasound measurements are carried out thanks to a special set of equipment which is commonly called an "infrasound sensor". The infrasound sensor measures changes in atmospheric pressure over a very large dynamic range and may be used to measure the variation of absolute pressure around the ambient pressure. Therefore, mechanical assemblies that are sensitive to pressure and associated transducers is the main point in the infrasound sensor part. Many principles of transduction and mechanics have been developed over decades for infrasound observation. Various types of infrasound sensors with their reviews can be read in Ponceau and Bosca [2009].

Currently, infrasound sensors are installed and operated all over the world. As an example, there are at least 60 infrasound observation stations but 48 of 60 planned ones are currently operated recording continuous infrasound waves in the International Monitoring System (IMS) network that is used for verification of compliance with the Comprehensive nuclear-Test-Ban Treaty (CTBT). In the context of the CTBT, the IMS has given many supports to various studies on the long-waves propagation for understanding the atmospheric dynamics. The earth atmosphere, as the inhomogeneous medium, e.q. the earth atmosphere is a highly dynamical medium and varies strongly with geographical location, which leads infrasound propagation characteristics varies around the world and causes multi-variety of the recorded infrasonic waveforms. This takes a beneficial advantage of infrasound applications to be used to monitor and study the atmospheric variability, especially to monitor the atmospheric winds in the stratopause and lower thermosphere. The detection of the explosion is of particular interest.

c. Infrasound Data Processing

In general, the purpose of processing and analyzing infrasound signals is to estimate and detect the direction of the angle of arrival (AoA) from which the source of the low-frequency wave originated. While processing is done, at least, it requires the installation of a typical infrasonic array composed of three or more infrasound microphones that are distributed on the ground surface. The traditional two-step method for estimating and detecting the direction of the source waves are the followings. First, wave-frequency frequency analysis is used in each data interval (Olson and Szuberla [2005, 2008]). Then, the confidence level of wave detection in each data interval is performs using algorithms such as Fisher's F-statistics (Smart and Flinn [1971], Olson and Szuberla [2008]). Highest correlation in each window of data can be used to evaluate a signal detection.

One technique called the Progressive Multi-Channel Correlation (PMCC) originally developed and designed by Cansi [1995] as well as Cansi and Klinger [1997] for seismic data and proven to be efficient for extracting low-amplitude coherent signals among non-coherent noise at successive element triplets within array using band-pass filters, cross-correlation functions, and time delays between sensors. The signal detection algorithm of Cansi [1995] assumes the fact that infrasound waves can be represented by a set of propagation plane waves. At first, the correlation function is used to calculate the time difference between signal arrival Δ_{ij} at two sensors i and j in each triangular sub-array. In the case of a wave propagating without distortion, the sum of the time delays satisfies the closure relation $\Delta t_{ij} + \Delta t_{jk} + \Delta t_{ki} = 0$ at successive element triples within an array (i, j, and k). However, the background noise presents in the signal receptions, the delays measured in this case were fluctuated due to unstable of the phase signals. Hence, the closure relation given above is no longer valid. Then, a progressive procedure is performed in the second implementation of the PMCC method. The computation of the procedure uses a triangular sub-array R_n consists of n closely two sensors in order to examine the consistency C of the set of delays of all the sensors of R_n. Once the consistency is lower than an initialized threshold, a detection is declared and recorded as a pixel attributed with a frequency, time, angle of arrival direction, and apparent velocity (v_{app}). In general, the progressive procedure and correlation computation for each frequency band and time window

are the key point in the PMCC algorithm. The PMCC algorithm has just described, visually as shown in flow chart of Figure 1.5.

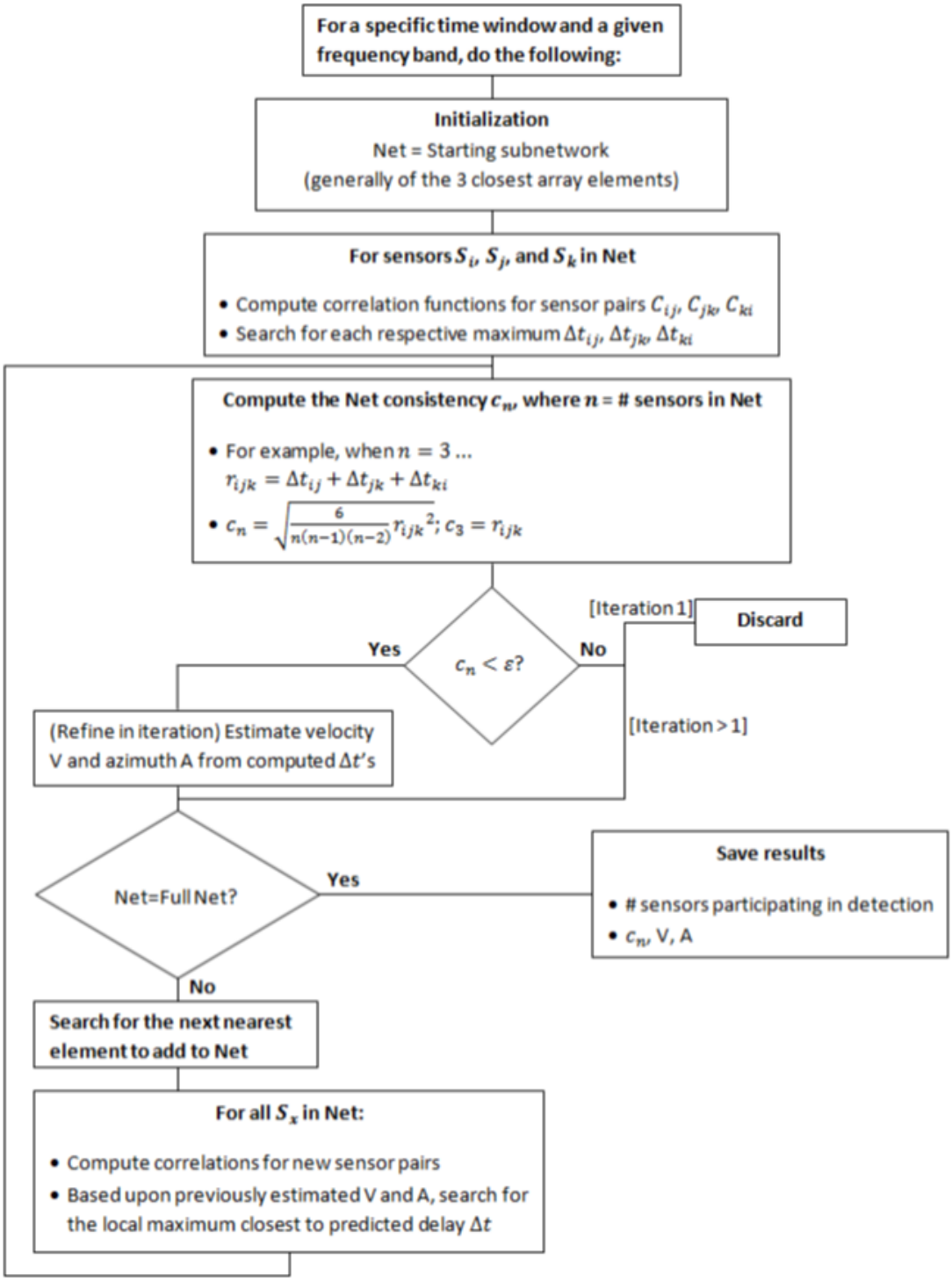

Figure 1.5: The PMCC flow chart describing the procedure to produce a source detection (Runco [2013]).

1.3 Instrumentations Used in this Work

1.3.1 Infrasound Network Systems of KUT

Since 2005, KUT has collaborated with several local institutions in an initiative to build an infrasound sensor that is integrated with several micro-electro-mechanic system (MEMS) sensors to measure 3-axis acceleration in seismic waves, atmospheric temperature, atmospheric pressure, and the RMS level of audible noise. Providing an information about natural disaster such especially as earthquake and tsunami over the Shikoku region, the network likewise uses 2 different types compact sensors to ensure the detection of infrasound waves generated by both natural and man-made activities. The sensor system is also equipped with a signal processing unit for continuous real-time processing and network-connecting ports for data acquisition (Yamamoto and Yokota [2015]). A full description of the specifications of the infrasound instrument is given in Table B.2 in the appendix B.

At almost all stations, the four parameters are continuously digitized at 4 Hz by each individual sensor. The instrument was specially designed to be windproof and easy to install. The sensor can be used to monitor infrasound sources from geophysical activities, such as volcanic eruptions, snow slides, landslides, thunderstorms, and tornadoes, as well as human-made activity (e.g. explosions, spaceship re-entry, etc.). The infrasound system, consisting of four types of high sensitivity sensors with additional of a dynamic data logger and a high speed digitizer in which able to monitor the ambient condition of the environment (e.g. ground acceleration, local temperature, audible noise level, atmospheric pressure and sound pressure level) and is therefore flexible to control through the internet connection. In 2016, the first five infrasound sensors as a model ADXII-INF01 (Fig. 1.6) had been installed in the Kuroshio Town and continue in 2017 expanded to a total of 15 locations over Kochi Prefecture.

Finally, the year 2018, the 30 of total amount of infrasound sensors were successfully distributed uniformly over the Japanese Islands and are in continuous operation. The expansion could be spread to the zonal-meridional landside of the world (e.g. Philippine and Indonesia as one of candidates of the lower latitude expansion area in the future). This development, however, will focus on the infrasound monitoring component to study infrasound characteristic especially on mechanism of wave propagation in order to provide the information about natu-

ral disaster mitigation. The whole infrasound stations in Japan are shown in Figure 1.7, with their geographic coordinates listed in Table B.1 in the appendix B. The network is denser on Shikoku Island, where it is used for the detection of natural disasters, such as tsunamis and volcanic eruptions.

Description of the Infrasound Data Set

The collection of observational data from our infrasound sensor network can be monitored through the KISONS-Kochi University of Technology Infrasound Observation Data Network System (Kochi University of Technology (KUT) [2015]). This data set includes the 3-D acceleration of earthquakes (Gal), audible sound (dB), atmospheric pressure (kPa), infrasound pressure (mPa), and sensor temperature (^{o}C). They are provided for each time period of data

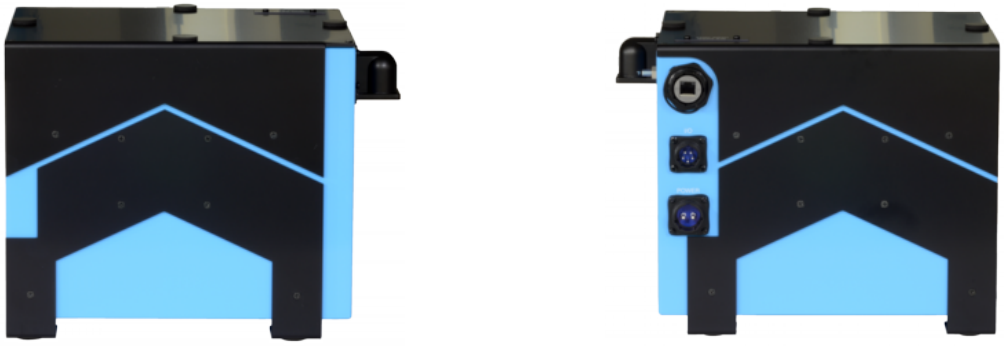

Figure 1.6: Infrasound sensor ADXII-INF01 (image taken from wwww.saya-net.com)

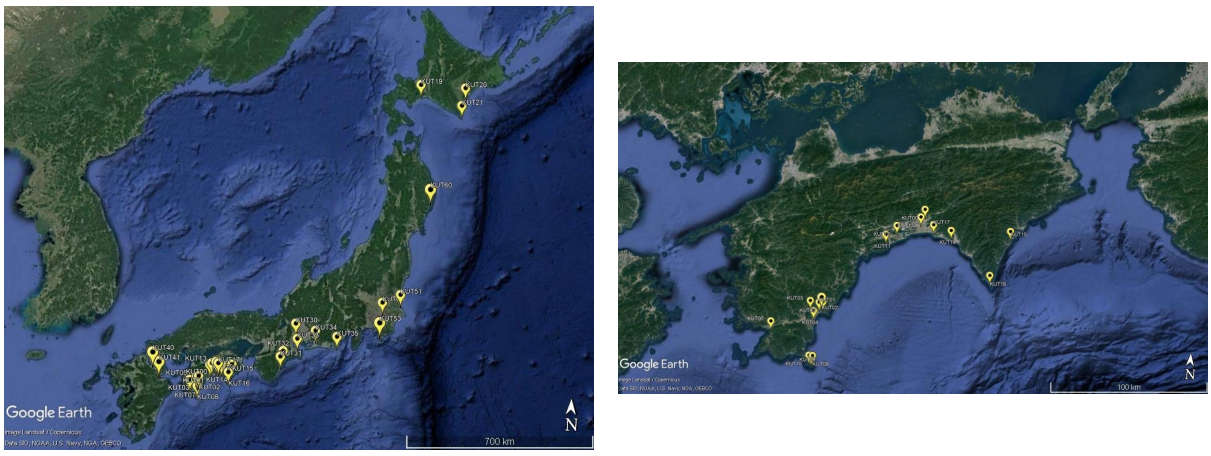

Figure 1.7: The location of infrasound sensor (type ADXII-INF01) over Japan (left) and focused over the Shikoku Island (right).

needed by the user in the form of a comma separated value (CSV) file format, with file naming formats such as

`SS_Y1Y1Y1Y1M1M1D1D1h1h1m1m1s1s1_Y2Y2Y2Y2M2M2D2D2h2h2m2m2s2s2s2.csv`,

and the information in Table 1.1.

Table 1.1: List of information on filename code.

filename Code	information
SS	Station code
$Y_nY_nY_nY_n$	Year
M_nM_n	Month
D_nD_n	Day
h_nh_n	Hour
m_nm_n	Minnute
s_ns_n	Second

Index "n" describes the beginning (numbered 1) and end (numbered 2) of the time period over which data were selected. For the purposes of infrasound analysis, we recommend using the infrasound AC signal parameter (column 10 in the CSV file). It should be noted that the data displayed on the webpage could change at any time due to maintenance and internal investigations of the system. Therefore, the availability and demand for data can vary and should be determined before use of the system. The observation data set used in this study can also be accessed in repository stores, such as Figshare (Space Laboratory of KUT [2019]).

1.3.2 Meteor Wind Radar Systems at Equatorial Latitude

There are two meteor radar systems installed in the Indonesian Archipelago. These radar systems are located in the western part of Indonesia, at Kototabang (0.20^o S, 100.32^o E), and in the eastern part, at Biak (1.17^o S, 136.10^o E) (Fukao et al. [2003]). The two instruments are both allSKy interferometric METeor (SKiYMET) radar systems, which are optimized for upper atmospheric measurements. The meteor radar in Kototabang has been operating since November 15, 2002, 1 year after the establishment of the Equatorial Atmosphere Radar (EAR) system (Fukao et al. [2003]). A decade later, a meteor radar system was installed in eastern Indonesia, on the island of Biak, which has been operational since May 31, 2011. The two

radar systems are separated by approximately 4000 km. The specifications of both meteor radar systems are listed in Table 1.2.

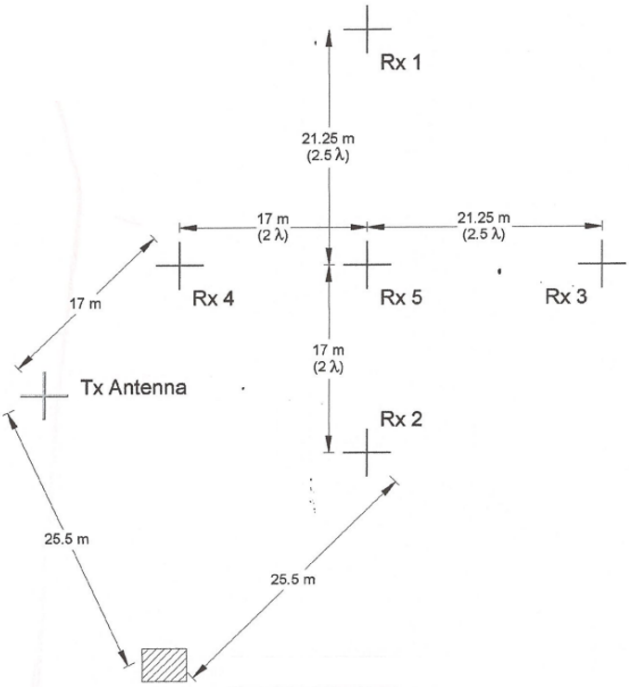

(a)

(b)

(c)

Figure 1.8: The antenna of Meteor Wind Radar (MWR). (a) Antenna configuration (credit: Genesis Pty. Ltd.). (b) Three-element cross Yagi antenna for transmission. Photographed by the author in 2009.(c) Two-element cross Yagi antenna for reception. Photographed by the author in 2009.

Recently, state-of-the-art SKiYMET radars were installed at the above locations for continuous monitoring of the atmospheric dynamics within the MLT region. Detailed descriptions of this radar and the meteor detection algorithms can be found in Hocking et al. [2001]. The receiving antenna uses the configuration initiated by Jones et al. [1998] named the JWH configuration, and is arranged into two perpendicular arms with spacing of 2 and 2.5 λ to yield unambiguous angles of meteor arrival. As shown in Figure 1.8, the antenna system is typically composed of a single 3 element Yagi antenna is used for transmission (Figure 1.8b), and five 2-element Yagi antennas are used for reception (Figure 1.8c). These radars utilize the interferometric technique to determine the position of meteor trails in the sky without ambiguity in the angle of arrival.

The radar data acquisition system (RDAS) represents another type of radar system, operated by a single PC using a unix system to control and analyze selected observation parameters; the RDAS also has multi-tasking capabilities. The data obtained from RDAS are written to a new type of file, called a Confirmed Event (CEV) file. The contents of this CEV file are used to determine the locations of meteors in the sky and other physical parameters of meteors. The parameters are then written into an ASCII text file, the Meteor Position Data (MPD), file for further study. The fields of the MPD file are described in Table 1.3. Data from both meteor radars can be accessed via the Repository Data Sains Antariksa data base server in Indonesia and the Research Institute for Sustainable Humanosphere (RISH) databases (Kyoto University [2015], Lembaga Penerbangan dan Antariksa Nasional (LAPAN) [2015]).

1.3.3 Kochi FSMR: Systems overview

The Kochi Forward Scatter Meteor Radar (KFSMR) is a type of radar that received a scattered continuous of radio waves from the radar target, i.e. ionozed meteor trail. Since 2005, the system had been installed at the Kochi University of Technology (KUT) in Japan with the operating frequency of 53.750 MHz (Mizumoto [2015]). The idea behind KFSMR is to understand the dynamic mechanism in the upper atmosphere based on the measurement of the characteristic of meteor echoes in such way that the parameters of the incident meteoroid can be determined for many echoes seen above the radar site. The design of the system takes a common approach: in addition to the time delays, interferometry is used to determine the di-

Table 1.2: Specifications of Meteor Radar Systems in Kototabang and Biak

Parameter	MWR Kototabang	MWR Biak
Frequency (MHz)	37.7	33.32
Bandwidth (kHz)	200	200
Pulse width (us)	13.3	13.3
Output power (kW)	12	12
Duty cycle (%)	5(max)	5(max)
Pulse repetition Frequency (Hz)	2144	2144
TX antenna	Single circular polarized three-element cross Yagi	Single circular polarized three element cross Yagi
RX antenna	Five circular polarized two-element cross Yagi	Five circular polarized two-element cross Yagi

Table 1.3: Description of the MPD file

Data field	**Description**
Date	Detection data relative to UTC
Time	Time of detection in UTC
File	File name extension used to store the raw data for a given detection
Rge	Range of the detection in km
Ht	Corrected height above ground of the detection in km
Vrad	Radial drift velocity of the trail in m/s
DelVr	Standard deviation of the radial velocity measurement obtained from the five antenna pairs in the interferometer
Theta	Zenith angle of the detection in degrees
Phi0	Azimuth angle of the detection in degree

rections of the echoes which are known to be orthogonal to the meteoroid trajectories (Brown et al. [2008]). Here, our system to observe the ionized trail of the meteor is based on the the method of Ham-band Radio meteor Observation (HRO), which has been established in Japan decades ago Maegawa [1999]. The receiver is located at the main site consists of 5 spaced antennas arranged as two of 3-element interferometer arrays along orthogonal axes with the center antenna common to both (Figure 1.9). The key point of this configuration is that the range distance between the center antenna and the two other sides antennas in each array differ by one half-wavelength ($\lambda/2$). This promises to estimate an unambiguous of the angle-of-arrival relative to the array. As used in the HRO method, meteors can be observed by receiving the VHF beacon wave used in the amateur radio band. Our system is designed to received the VHF wave of 53.750 MHz, transmitted from the National Institute of Technology, Fukui College

at Sabae, Fukui prefecture (Figure 1.10). At present, the software routines in the main system employed by the KUT to compute several computation, such as automated meteor echo counter described in Noguchi's work in 2009, based on the previous spectral analysis software resulted from his work in 2007 using the IDL (The Interactive Data Languange) language platform for radio observation software. The observation status of the system in the period from 2014 to 2016 i shown in Table 1.4.

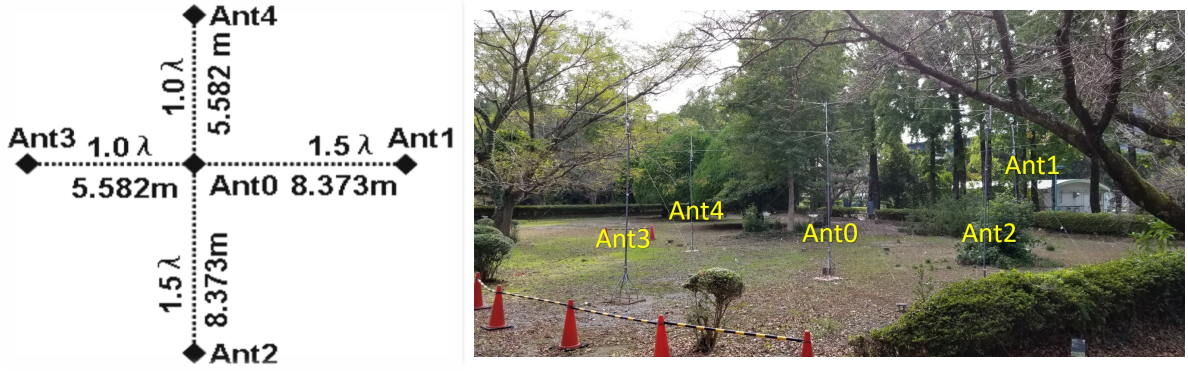

(a) (b)

Figure 1.9: Antenna Configuration of KFSMR (left) and the picture of the antenna, Photographed by the author on 28 October 2019 (right).

Table 1.4: Observation status of Forward Scatter Radar at KUT. Translated from Mizumoto [2015]

Year	**2014**											
Month	April	May	June	July	Aug	Sept	Oct	Nov	Dec	Jan	Feb	March
Status	1 point observation & equipment restoration						3-point radio observation preparation & trial					
Year	**2015**											
Month	April	May	June	July	Aug	Sept	Oct	Nov	Dec	Jan	Feb	March
Status	Single point observation & selection of observation method & server construction				2-point radio observation & server construction				3-point radio observation probability			
Year	**2016**											
Month	April	May	June	July	Aug	Sept	Oct	Nov	Dec	Jan	Feb	March
Status	Construction of meteor integrated observation system (meteor radio wave, optics, infra sound observation and remote monitoring system construction)											

1.4 Problem Statement of the Research

The understanding of the atmosphere up to at higher altitude, with a particular coverage area over period of time, is still have a question by the challenges of obtaining data analysis from

direct measurements in the middle and upper atmosphere. Obtaining an observation to measure the properties of the atmosphere above the stratopause is the main field of research area. In spite of the progressive instrument development over the past decades in studies to measure the properties of the upper atmosphere with combination ground-based probes, such as radar and high sensitive atmospheric sensors remain sparse. The current state-of-the-art specification of basic atmospheric parameters, such as density and horizontal wind are available given by global atmospheric models. More recently, the Modern-Era Retrospective Analysis for Research and Applications, version 2 (MERRA-2) developed by the NASA's Global Modeling and Assimilation Office (GMAO) and they began an effort to reanalysis development with the production of the Goddard Earth Observing System, version 1 (GEOS-1) and with more advanced significantly production of the previous MERRA to produce specifications up to 0.01 hPa altitude within 72 hybrid-eta levels (Gelaro et al. [2017]). The US Naval Research Laboratory (NRL) developed a global reference model of the Earth from ground to space. It models the temperature and densities of the atmosphere's component (Picone et al. [2002]).

It has been reviewed in the past that various phenomena around us are suitable for providing

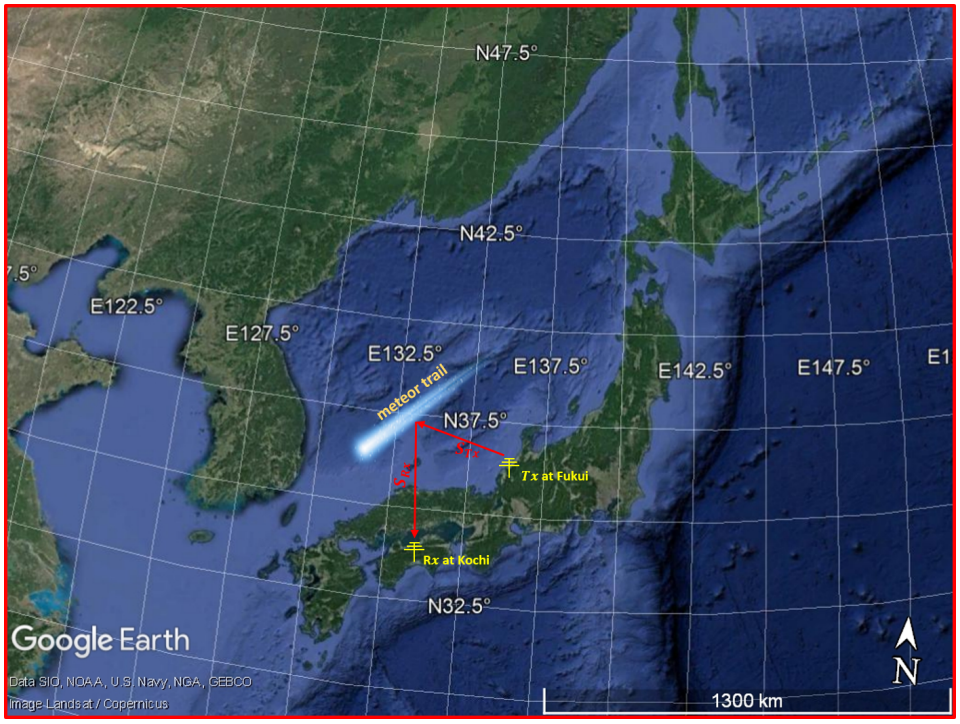

Figure 1.10: illustration of a meteor reflecting/ scattering a transmitting signal from Fukui (35^{o}56'14.4"N;136^{o}10'18.9"E).

full facilitation to explore and study the atmosphere by sensing and probing their parameters, mostly the ground-based observations permit the measurements. Since the ablation and explosion of the meteor as well as shock wave in the Earth's atmosphere are sensitive to air particle and wind in the atmosphere, this suggests that meteor radar and infrasound may be used to probe for understanding the dynamic properties and horizontal wind specifications in the upper atmosphere. This is supported by the availability of continuous meteor radar and infrasound observations (i.e. Meteor Wind radar and the Kochi infrasound network).

New integrated sensors had been distributed and continuously operated in several stations over Japan coastal line since 2015. Previously, all of these data have been treated automatically with assuming a constant data sampling rate to detect the event that indicates a source of infrasound wave. This research has found that the sampling rate of the recorded data was instable, due to its polling style data acquisition, and this problem is suspected because there are indications of lack of time in data transfer between local PCs and PC servers and bring an effect to the spatial data calculation. The Earth Space and Exploration System Laboratory (ESESL) of Kochi University of Technology (KUT), Japan is working to process a portion of infrasound data to detect the location of infrasound wave sources. However, regardless of the type of program used, the existing processing still needs to be developed especially in the characteristics of the infrasound signal detected for further analysis, such as the clarification point at which the direction of the arrival signals and the characteristics of the detected signals.

All the installed sensors at different places are composed to be an irregular array system. Augmenting an array with signal processing techniques not only enhances directivity but also allows us to aim the directivity pattern without physical changes. Furthermore, by using signal processing techniques, we can aim it in different direction simultaneously. As used and introduced in radar application, radar beam swinging as one of the possibilities and has been used in a wide variety of array processing algorithms. This method permits to focus the array's signal pointing in a particular direction. Moreover, radar beam swinging has capable to identify the source direction by steering the beam towards the source. The problem is, how to apply the algorithm into the irregular array on infrasound sensor. This research plan to implement and modify the algorithm to allow the development of the beam steering design due to its

performance and suitability for implementation.

The specific goals of this dissertation research are to:

- Investigate the period of meteor activity that passes through the Earth's atmosphere as well as variations in meteor height trends due to the potential effects of solar activity.
- Estimate the wave characteristics of the infrasonic source through the implementation of radar beam swinging algorithm.
- Positively identify infrasound waves produced from sources of natural activity phenomena and reveal the influence of atmospheric conditions and the topography of Earth's land surface on the characteristics of detected infrasound waves.
- Understand the design concept of instrument technology to observe the natural infrasound waves.

1.5 Motivation of the Research

The main motivation of this dissertation is to better understand the physical properties of the Earth's atmosphere and their dynamical processes, by using radio and infrasonic wave observation datasets. To accomplish this, the observations data were retrieved from monostatic meteor radar operated in the equatorial region, forward scatter meteor radar developed by the Kochi University of Technology, Japan as well as the the infrasound sensor network over Shikoku Island in Japan.

An important question come in this work are: What air parameters play an important role in the Earth's atmosphere? What is the causal effect between the Earth's atmosphere and solar activity? How well solar activity affects the change of meteor height? What makes it cause to happen? To answer these questions, sets of observation data are needed; however, these require multiple observation datasets. As known in general, the meteor radar technique has been used since years ago, and collected a long period data. This places chance on how well the air density in the meteor height is affected by the solar activity. Another way to answer the question is the utilization of the infrasound observation is quite new for the possibility to study the Earth's atmosphere. The detection of air pressure change within low frequency is of particular interest, in the context of high explosion and strong friction monitoring.

1.6 Novelty of the Research

The key contribution of this research is the concept of acoustical measurement and instrumentation. It includes the introduction concerning new measurement instruments and also a proposal concerning new measurement concepts to investigate the phenomena of low frequency vibration. In addition to introducing concept measurement and instrumentation, the concept also includes a useful signal processing technique for measuring wave characteristics and source localization in the face of the infrasonic detection systems. This addresses a very real issue faced by researchers and practitioners in the remote sensing system area. Beyond the application of the concept, the instrument is also relevant for researchers designing new implementations of measurements. Ultimately these research evaluate the observation data of such instruments is subject to the infrasonic detection covered by the signal processing technique introduced in this dissertation. This research have encountered several research projects where the strong wind noise in the infrasonic detection during the application of a performance instrument caused significant problems. The work presented in this dissertation helps to prevent such problems in the future.

1.7 Dissertation Overview

This dissertation discusses the upper atmospheric study by using meteor head echo observations conducted with the meteor radar systems of the allSKy interferometric METeor (SKiYMET) as well as forward scatter meteor radar developed by KUT and infrasound observations conducted with the infrasound observation network of KUT over Japan. The dissertation outline is as follows.

Chapters 2-4 explain the analysis of meteor observation data by using meteor radar to study each of the dynamics, characteristics of the upper atmosphere. In addition, the implementation of the phased array radar signal processing method into the infrasound sensor array system at KUT is described.

Finally, in Chapter 5, conclusions and a discussion on possibilities and outstanding issues for the future work/research options are presented.

Chapter 2

THE APPLICATION OF METEOR RADAR TO STUDY THE EFFECT OF SOLAR ACTIVITY ON THE DISTRIBUTION OF METEOR HEIGHTS IN THE EQUATORIAL ATMOSPHERE

***

Abstract In this chapter, diurnal and annual variations in the peak height of meteor and the total number of meteor echoes during the complete phase of the solar cycle for upper atmosphere characterization and specifications are discussed. The information of meteor observation when a meteor penetrates the Earth's atmosphere can be used to study the possible relationship between solar activity and variations in meteor height distribution during the period of full solar cycle. The relevance to the dissertation topic is in understanding the dynamical features of the Earth's atmosphere, especially in layers at altitude where meteor interact with Earth's atmosphere, i.e. 90-120 km. Considering the region on the low latitude (e.q. equatorial region) is closest to the sun, the turmoil of the atmospheric variability at this region is strongly influenced by the solar activity from the external side and the internal side of the Earth as well. From the external factors, in addition to the solar activity index data, air density and fundamental parameter of the atmospheric profiles from the calculation of global atmospheric models such as NRLMSISE-00 and CIRA86 are used for further analysis. In short, the observation results of meteor at equatorial region show a positive relation between solar activity index and variations in meteor peak height. In addition, the average atmospheric temperature and total atmospheric density at the equatorial region calculated by the global atmospheric model reinforce this relation.

2.1 Meteor-Earth's atmosphere Interaction

The Earth's atmosphere is actually a perfect layer recording the solid particle of the solar system impacts upon the Earth other than protecting live being on the Earth. Although the estimated amount varies, around more than 100 tons of solar system dust, and particles enter and collide against Earth's atmosphere as a meteoroid, meteors, and micro meteors per day which can usually be seen as a fast line of light in the night sky. They can be investigated in different sections from different viewpoints: observational and theoretical. Figure 2.1 shows a diagram describing the importance of the entire meteoroid complex that can be demonstrated by their myriad, by their variety sizes, and also by the large diversity in their composition and structure. The penetration of a meteoroid into the Earth's atmosphere at very high speed may then give different phenomenon, depending mostly on their sizes and partly on velocities. A survey that inventorying the basic terminology used for the solid particle of the solar system interacting with the Earth is demonstrated as a sketch in Figure 2.2. The most complete case of a meteoroid interaction with the Earth's atmosphere was originated from their orbital motion which is dominated by the gravity of the Sun and travel in the designated orbital line. When the line approaches the Earth's atmosphere, the individual constituents of the meteoroid particles start to preheating within a seconds until the next stage of atmospheric penetration on the meteoroid called the ablation including fragmentation and evaporation. During their interaction in the atmosphere, ions and free electrons are produced as forming ionized column that has high plasma density which can reflect radio waves when hitting on it. This provides a possibility to understand and study meteor phenomena by radio remote sensing.

2.2 Meteor Observations

In the 1930s, Skellet together with his collaborators at the Bell Telephone Laboratories successfully observed the existence of the Leonid meteors ionized trail using a pulsed transmitter (Skellett [1935, 1931]). Pioneer implementation of radio techniques in meteor studies can be found in the article (Millman and McKinley [1963]). It is known commonly that radar observations are not limited by weather conditions and by the daily sunlit. This creates some ideas to develop the meteor radio-astronomy technologies more rapidly. A variety instruments have

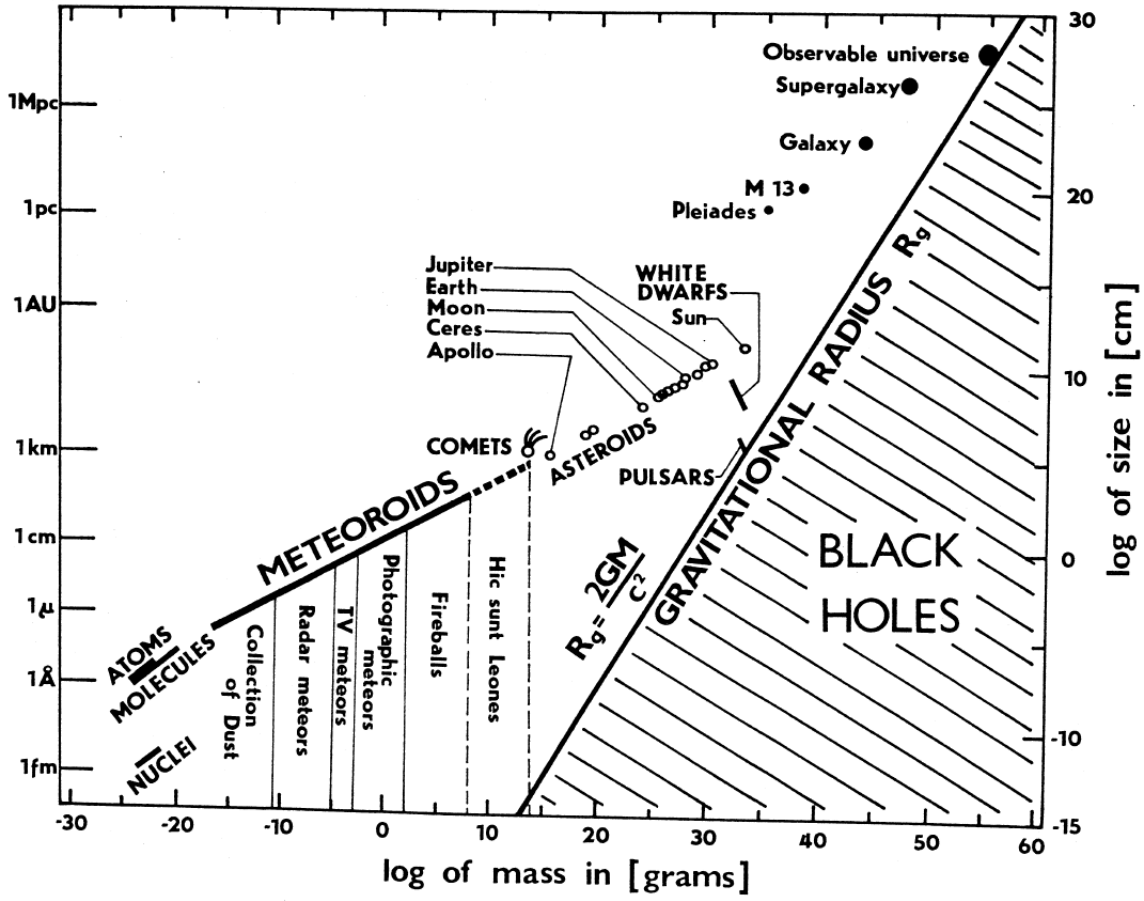

Figure 2.1: Diagram of meteoroid complexity in size versus mass range of several objects known and observed from the universe. (Figure adopted from Ceplecha et al. [1998])

been used for understanding the meteor phenomena, from large-space radar with power full transmission like EAR to small systems employing low cost development. Interestingly, the meteor radar can measure the location of the trail, and determine the radial velocity due to the wind from phase and Doppler shift measurements, and these information will then be used to produce the winds velocity (Franke et al. [2005], Jones et al. [2003]) and temperatures estimation in the 80-100 km altitude region (Hocking [1999]). More elaborated documentation of the development and advancement of meteor radars are discussed in Hocking [1999, 2004a,b] as well as Singer et al. [2004].

Since the main focus of the meteor radar utilities is the atmospheric understandings using meteor trails, and mostly and primarily instruments used for such goals are based on the interferometric radars. Herewith, such radar like SKiYMET radars developed by Mardoc Inc. and Genesis Software Pty Ltd (Hocking [2001]), and/or their duplications as a reference point

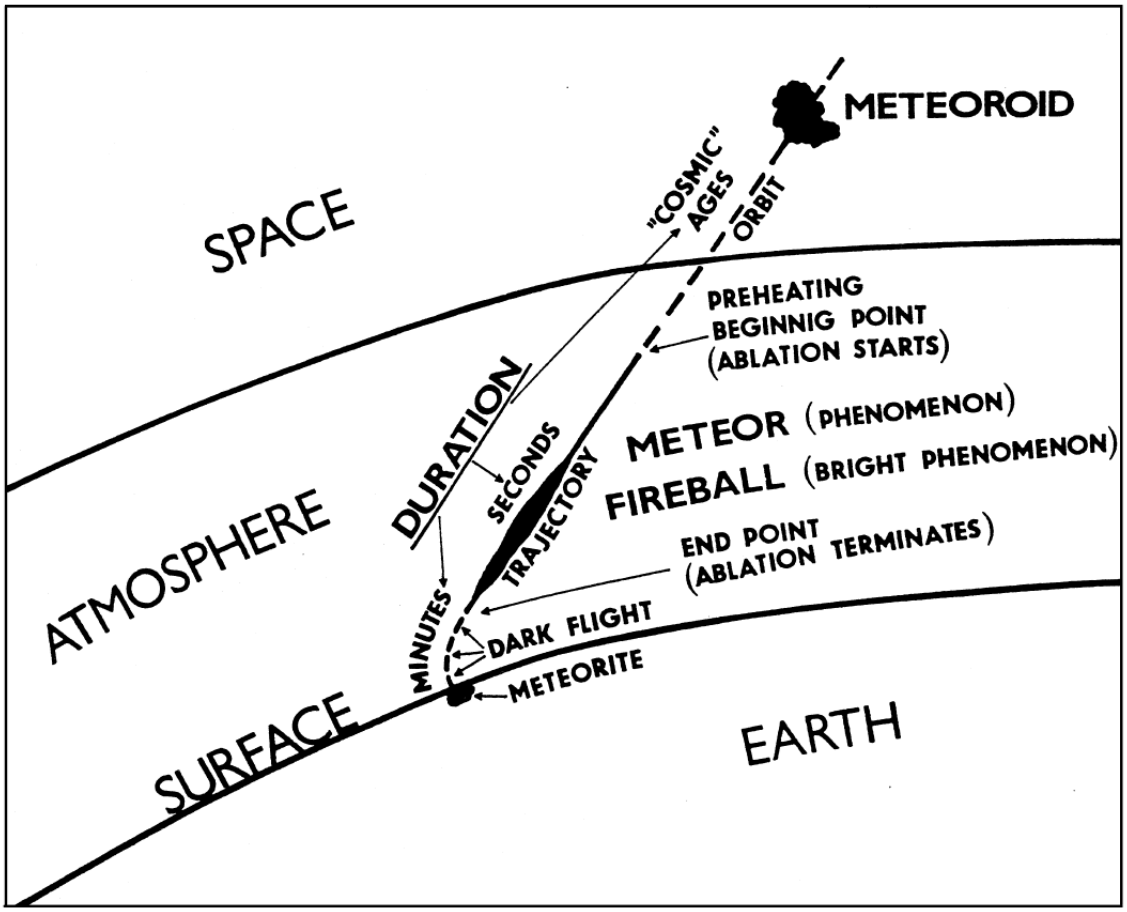

Figure 2.2: A skecth of basic meteor terminology. (Figure adopted from Ceplecha et al. [1998])

will be used for the basic design and principle of meteor radar in this chapter. The antenna configuration of the interferometer as one of the main brand concept of meteor method which helped make the observation more effective. Specifically, the system use five-receiver spaced antenna layout (Hocking [1997], Jones et al. [1998]) is illustrated in Figure 2.3 for the general configuration.

Using Figure 2.3, there are several antenna configurations that can be made, such as (1) an antenna configuration can be built with five-receiver antennas, thereby producing T-shape (Figure 2.3a), at which the distance between two antennas needs to be less than a half-wavelength of operating radar frequency apart in order to reduce the ambiguities in the detection of angular direction. This configuration allows the interferometer technique to function properly and removes angular ambiguities. Although the five-receiver system effectively reduces angular ambiguities, the antennas need to keep far enough apart at the same time to avoid the mutual

impedance-coupling problems. (2) Other pairings of receiver antenna configuration as shown in Figure 2.3b can be applied, such as 3.5 and 3.0 wavelength-pairs, however the phase difference of this layout need a larger antenna spacings to determine a higher precision (i.e., avoid 2π ambiguities), which can improve the signal-to-noise ratio. Many other interferometer configurations have been used. For example, the configuration of four-receiver antennas produce a good angular discrimination (Hocking and Thayaparan [1997], Hocking [1997], Poole [2004]). In general, and however, the five-receiver antennas configuration seems to give optimum cost-to benefit ratio.

2.3 Background and Arising Problem of the Research

There is considerable complexity in the Earth's atmospheric conditions, especially pertaining to neutral atmospheric density and temperatures in the mesosphere and lower thermosphere (MLT) region. Temporally and spatially, the trends of these two parameters are affected by the external energy of the MLT system, its internal dynamics, and coupling of the thermosphere and ionosphere (Qian and Solomon [2011]). To date, information on the meteor backscatter signal has allowed us to determine variations in atmospheric neutral density (Clemesha and Batista [2006], Lima et al. [2015], Stober et al. [2014], Takahashi et al. [2002], Yi et al. [2018]) and atmospheric neutral temperature in the region of meteoroid ablation (Hocking et al. [1997],

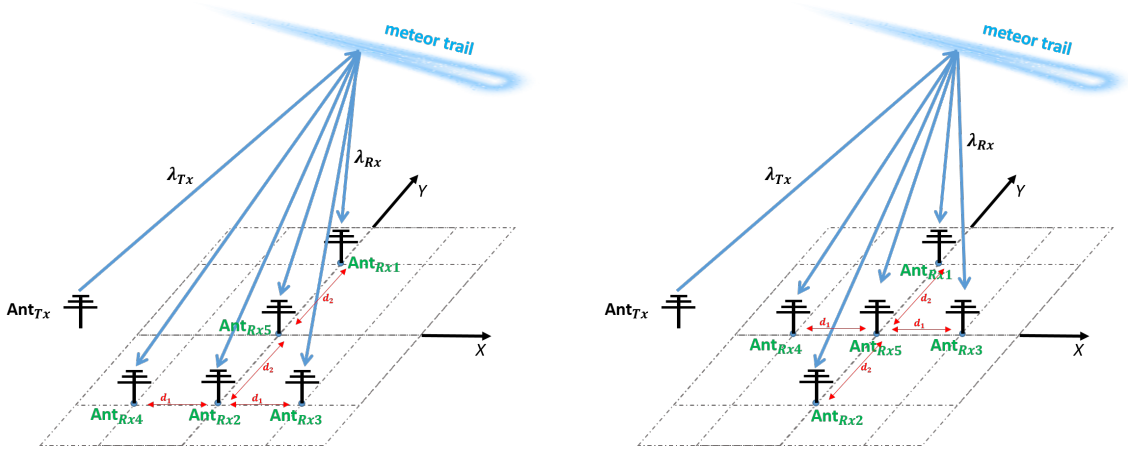

(a) (b)

Figure 2.3: Five-receiver interferometer array antenna configuration used in meteor radar. A wide beam of transmitted radar signal λ_{Tx} hit the ionized meteor trail and then five-receiver antennas $Ant_{Rx1-Rx5}$ receive the signals λ_{Rx} reflected from the trail.

Holdsworth et al. [2006], Kozlovsky et al. [2016], Yi et al. [2018]). However, neutral atmospheric conditions in the MLT region are generally determined via empirical models. Recently, the atmosphere model NRLMSISE-00 explicitly added the "oxygen anomaly" component to describe the contribution of non thermospheric species at high altitudes and allow the user to calculate the total neutral mass density of the thermosphere, thus revealing the thermospheric mass density and anomalous oxygen contribution in the thermosphere (Picone et al. [2002]). The model database contains relevant observation data (e.g., satellite and ground-based data) and produces a temperature and density structures similar to an equatorial mesosphere layer. Qian and Solomon [2011] comprehensively reviewed variation in neutral atmospheric conditions at thermosphere altitudes using the model. Meanwhile, Stober et al. [2012] used the NRLMSISE-00 prediction model to analyze neutral atmospheric variation in terms of solar activity effects in the middle region. The neutral density variations seem dependent on the solar cycle effects over spanning one solar cycle. The Committee on Space Research (COSPAR) devised an empirical atmosphere model, called the COSPAR International Reference Atmosphere (CIRA), of atmospheric temperatures and densities. The model accurately reproduces most of the characteristic features of the atmosphere and the general structure of the tropopause, stratopause, and mesopause with almost global coverage ($80^oN - 80^oS$). For example, Clemesha and Batista [2006] evaluated atmospheric temperature trends in the MLT region with a simulation tool of the CIRA86 model for analysis of meteor height variation.

The role of solar activity in meteor height and meteor rate has been reported and discussed. Several researchers have observed variation in the intensity of meteor echoes and meteor rates due to the influence of solar activity (Hajduk et al. [1980], Lindblad [1967], Liu et al. [2017], McIntosh and Hajduk [1977], Prikryl [1983], Šimek and Pecina [2000], Szasz et al. [2004], Yi et al. [2018], Younger et al. [2009], Zigo et al. [2009]). Additionally, other researchers have been used from radar at low latitude on southern hemisphere (Lima et al. [2015]) and on the northern hemisphere, Jacobi [2014], Pecina and Simek [1999], Pellinen-Wannberg et al. [2009], Porubcan and Cevolani [1983] investigate the effects of solar activity, described by solar radio flux, F10.7, and the number of solar sunspot (R), on meteor height distribution. It is well known that the effects of the condition of the upper atmosphere and solar activity on

meteor altitude have been relatively seldom reported for the equatorial region. Investigating the phenomenon of meteoroid entry into the Earth's atmosphere could be important because of effects of solar activity, the influence of Earth's atmosphere as the penetration medium, and other aspects. In this study, we investigated the phenomenon of meteoroid penetration into the Earth's atmosphere in a context of the variation in meteor heights observed by meteor radar around the equator. Specifically, we addressed three aspects. First, we checked that the period of data collection was appropriate for further processing. Second, we compared our findings with the results of empirical atmosphere models. Third, we evaluated the results in terms of the insights gained. The characteristics of our radar system and the radar data format are described herein.

2.4 Data for Analysis

This work used data from both meteor radars to cover the total solar cycle (January 2003 to December 2016). The possibility of detecting a meteor in the upper atmosphere depends on its speed, range, zenith angle, height, and position. We began by checking the signal-to-noise ratio (SNR) and the amplitude of the radio signals emanating from the meteor trails. The zenith angle is very important because it is used to calculate the heights for the corresponding positions of each meteor detection. Thus, the zenith was chosen as the main metric for selecting the desired radio signals. In this study, we limited the zenith angle to less than 50^o to allow selection of strong meteor echoes and avoid the range uncertainty associated with detections closer to the horizon, when evaluating the trends in meteor rate and height. The all-sky radar can detect large populations of meteor echoes, which are normally distributed within the altitude range of 70–100 km with a peak value of around 90 km (Hocking et al. [1997]). Each detected meteor echo is also likely to include the effects of instrument errors, such as bias errors, that could cause more diversity in the measured heights. Thus, we cited the above proposed method to perform bias correction by inverting the equation of measured meteor height (h_m), to extract the corrected meteor height. A Gaussian distribution function was used for our data fitting to obtain statistical information on the meteors. Then we applied the meteor height correction

equation proposed by Hocking et al. [1997]:

$$h_T = \frac{\sigma_T^2 + \sigma_P^2}{\sigma_P^2} h_m - \frac{\sigma_T^2}{\sigma_P^2} h_P. \tag{2.1}$$

where h_T is the height of a meteor echo, h_m is the measured height of the echo, σ_P is the standard deviation of h_m, σ_T is the uncertainty in meteor height, and h_P is the height at the peak meteor count rate. Currently, the meteor observation data in Indonesia already cover almost the entire 11-year solar cycle, represented by F10.7 and R. The number of solar sunspots has long been known to vary with a period of repetition of about 11 years, that is, the solar cycle. The peak sunspot population is known as the solar maximum, which is separated from the next maximum by a gap known as the solar minimum. We attempted to evaluate the trends in these parameters over the complete period of the solar cycle and compared them to our meteor radar data results. The monthly R values, provided by the World Data Center Sunspot Index and the Long-term Solar Observations (Royal Observatory of Belgium (ROB) [2013]), were applied to evaluate the variation in solar cycle activity. Because there is a close connection between shortwave solar radiation and radio microwaves, F10.7 was taken as an indicator of the shortwave radiation from the Sun. Daily values of F10.7, as recorded at the NASA OMNIWeb Data Facility (The National Aeronautics and Space Administration (NASA) [2005]), were used in the present analysis. Finally, we investigated the atmospheric conditions in the MLT region, especially the variations in neutral atmospheric density and temperature and compared these with our analysis results. All of these parameters were obtained from the NRLMSISE-00 Atmosphere Model (Community Coordinated Modeling Center-NASA [2002]) and the CIRA86 of the Community Coordination Model Center (COSPAR International Reference Atmosphere (CIRA) [1990]).

2.5 Results and Discussion

At the beginning of our investigation, we evaluated the Kototabang and Biak meteor radar data within the range of SNR values considered appropriate for further processing. The zenith angle was selected to limit the range of the desired SNR values to the criterion values above the median value, which is more concentrated in the zenith angle less than 1 radian, or equal to 57^o

(Figure 2.4a). Figure 2.4b shows the trend in height distribution and the total number of meteor echoes detected by the Kototabang meteor radar on 14 December 2005, based on the previously selected zenith angle. The left panel shows the meteor height distribution plot calculated based on the total detection rate (1-km height resolution; horizontal pink bars) and the scatter plot of the meteor height distribution based on continuous detection (black dots, center). The bottom panel shows the daily trend in the total number of meteor echoes detected per hour. In general, in 1 day, the peak number of meteor echoes can reach about 600 counts at a height of about 90 km, at the time of sunrise (red arrow). This clearly shows that the largest meteor counts appear globally between midnight and dawn, and usually, the peak counts occur near sunrise, as explained by several studies on daily cycles (Hajduk et al. [1980], Lindblad [2003], McIntosh and Hajduk [1977]); continuous changes in the intensity of solar radiation could cause changes in the level of ionization in the atmosphere at the height of meteor passage and thus affect the total quantization of meteor echo detection. In addition, the Earth's orbit motion and the direction of Earth's rotation affect the number of meteoroids that hit the Earth's atmosphere. The results that we obtained were similar to the meteor distribution patterns measured at other equatorial latitudes, for example, on the island of Ascension at 8^{o}S latitude (Szasz et al. [2004]). Meanwhile, changes in altitude could not be detected in the daily data, so there was a need to investigate data with a longer period, that is, annual data.

The annual variation in meteor rate detected by the Kototabang and Biak meteor radars since their establishments are shown in Figure 2.5. The meteor radars at Kototabang and Biak typically had about 4,000-18,000 and 8,000-32,000 underdense type meteor echo detections per day, respectively. The detection algorithm for both radar systems, explained by Hocking et al. [2001], has proven very effective at removing non meteor signals such as aircraft and lightning signals, as well as sporadic E-region reflections such as ionospheric echoes. In the case of radio waves reflected by meteor trails, how a radio frequency wave reacts with such ionized trails depends on their ionization level due to changes in total electron density within the trail line, as the reflected energy of the incident signals depends on the plasma frequency of the trails. As shown in Figure 2.5, the peak amount of meteor echo received daily by the Biak system is larger than that of Kototabang due to the chosen operating frequency of the system (Table 1.2).

The meteor detections in this study were restricted to meteors detected at the zenith angle range mentioned above, and these ranged in number from 2,000-14,000 to 5,000-30,000 underdense type meteor echo detections per day, respectively. In general, both detection profiles show oscillating patterns, with a peak around midyear. The data for Biak continuously show more than 4,000 detections per day during 2011-2016. However, the detection data for Kototabang were continuous only during the first 9 years of operation. Therefore, we used 9 years' worth of Kototabang meteor radar data (2003-2011) and 6 years of Biak radar meteor data (2011–2016)

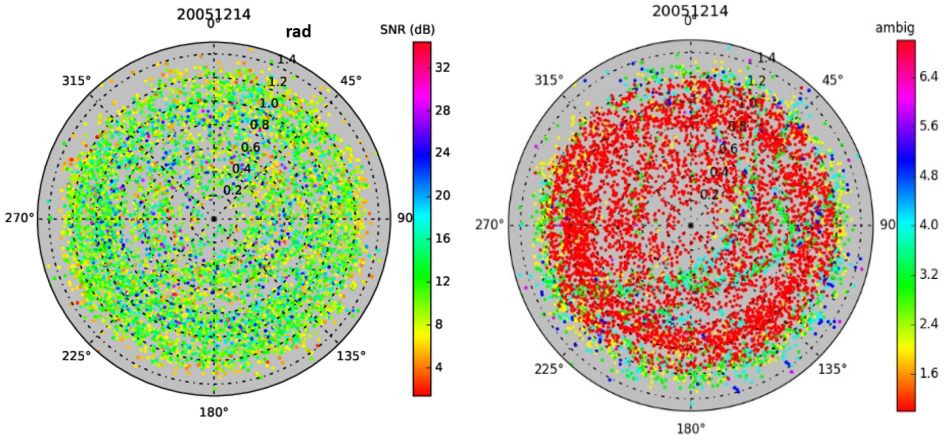

(a)

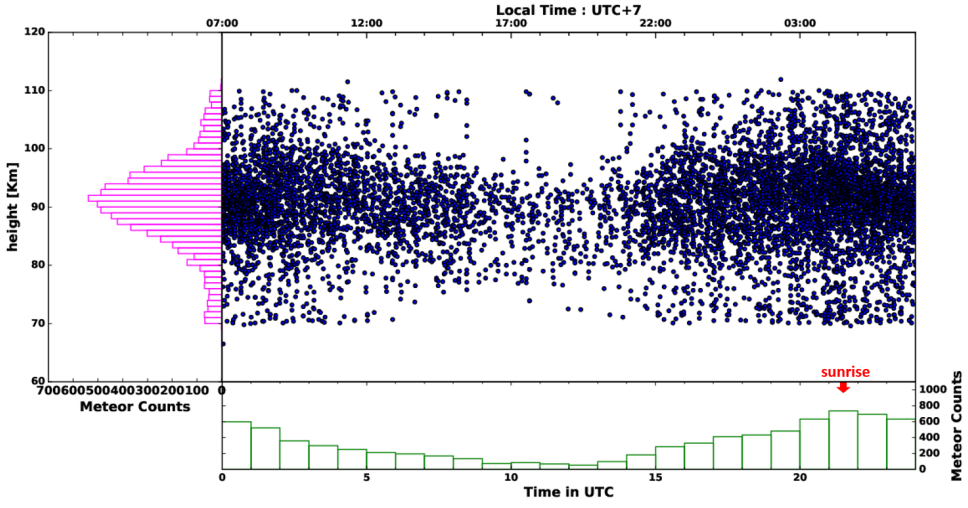

(b)

Figure 2.4: The observation data for 14 December 2005, obtained at Kototabang. (a) The contour of angular distribution of the detected echo signal-to-noise ratio value (left) and detection ambiguity (right). (b) Meteor count as a function of meteor height (horizontal pink bars; left), a scatter plot of detected meteors as a function of meteor height (shown as black dots; center), and diurnal meteor counts (vertical green bars; bottom).

to investigate variation in meteor height. To clarify the variation in annual meteor rate, data were plotted as shown in Figures 2.5c and 2.5d. The annual variation in meteor rate showed a clear periodicity, with two peaks appearing in December–January and June-July, and two valleys occurring around March-April and October–November. The total number of detected meteor echoes depends on the number of radar signal reflected back by ionized particles. In accordance with McKinley [1961], the meteor count depends on the Earth's orbital position with respect to the Sun, and the direction of the radar beam with respect to the meteor trail zone, possible additional factors including the seasonal variation in meteor echoes, and a background ionospheric ionization in the atmosphere formed separately from interactions with meteors. However, interestingly, we observed a trend toward a change in the seasonal meteor rate. It can also be observed that the detection rates increased from the beginning of 2003 to 2006 and showed a decreasing trend thereafter. Therefore, a more in-depth discussion of these results is necessary. We found that the diurnal variation in meteor rates was affected by periodic solar radiation as given by Hajduk et al. [1980], Lindblad [2003], and McIntosh and Hajduk [1977], the variation in meteor count rate reach their peaks once per year (Liu et al. [2017], Szasz et al. [2004], Yi et al. [2018], Younger et al. [2009]), and the annual variation in meteor rates appears to have an inverse relationship with the 11-year solar cycle (Lindblad [1967], Prikryl [1983]).

Range aliasing often occurs in radar implementations that depend on separation between transmitted pulses at a specific pulse repetition frequency. Dealiasing in the echo range is performed by producing various range ensembles for each candidate r_i. The height of a meteor radar candidate, at range r_i and angle θ from the zenith, is then determined using the formula:

$$h_i = \sqrt{r_e^2 + r_i^2 + 2r_e r_i \cos\theta} - r_e. \tag{2.2}$$

where θ is the zenith angle, r_e is the Earth's radius, and $r_i = r + ir_{amb}$; $i = 0, 1, 2, ..., N$; $N = \frac{r_{max}}{r_{amb}}$; $r_{amb} = \frac{c}{2PRF}$. For our radars, the maximum echo range r_{max} is assumed to be about 520 km based on the maximum expected zenith angle of 80^o and a height of 110 km. As shown in Figure 2.4b, the rates of meteor echoes are counted at each altitude and the Gaussian distribution function was used to obtain the meteor heights at the maximum detection rate. The distributions of the meteor peak heights obtained from the Kototabang and Biak meteor radars

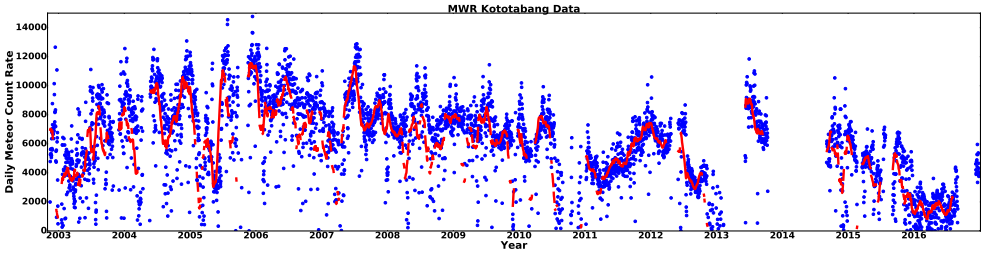

(a)

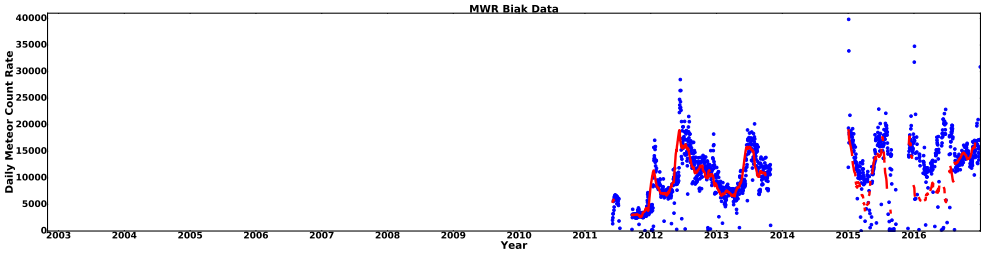

(b)

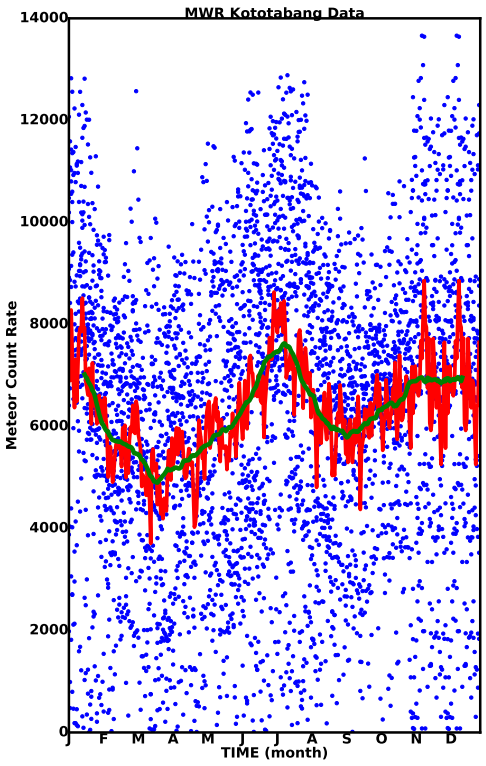

(c)

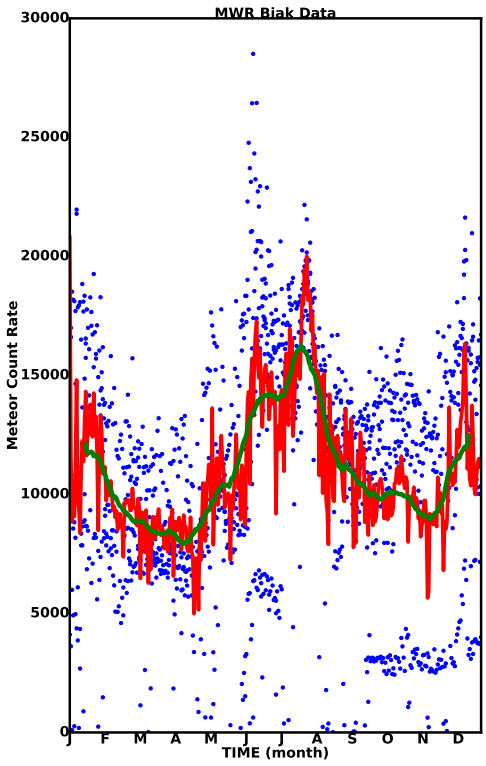

(d)

Figure 2.5: Daily meteor count rate (blue dots) at Biak for the period of 2011-2016 (first row) and at Kototabang for the period of 2003-2016 (second row), together with the 30-day running averages (red lines). Annual variation in meteor count rates at Biak (bottom-left) and Kototabang (bottom-right). The red line is the daily mean count rate and the green line is the 30-day running average. MWR = meteor wind radar.

are shown in Figure 2.6a. The meteor heights show annual and semiannual components that reach a peak at the end of the year, at altitudes of approximately 91.0 km, with minimums occurring mid-year at a height of approximately 89.5 km. Additionally, overall, the meteor height profile shows a parabolic-like curve over the 11-year solar cycle. Therefore, quadratic functions were used to ascertain the change in the meteor count rate trend. The green line shows the parabolic curve, in which the minimum and maximum peaks occur during 2007-2008 and 2012-2013, respectively. On the other hand, there seems to be a connection between the variation in meteor count rate (Figure 2.5) and that in meteor peak (Figure 2.6a). Many factors can influence the meteor count rate (e.g. the background population of ionized particles in the atmosphere and accumulated traces of meteor trails). The connection between solar activity and meteor count rate has been studied and discussed in temporal and spatial terms (Hajduk et al. [1980], Lindblad [2003], McIntosh and Hajduk [1977], Prikryl [1983], Šimek and Pecina [2000]). These studies provided a possible explanation of the changes observed in meteor rate according to variations in solar activity. On a time-scale of many years, variations in shortwave solar radiation during the solar cycle may influence the meteor rates observed by a radar system.

Figure 2.6b shows the R (top panel) and F10.7 (bottom panel) values for the period 2003-2016; the changes in both have been the main targets of study to date, especially in terms of their effects on the atmospheric environment. The correlation between peak meteor height and solar activity is explained by F10.7 and R, as discussed previously in Porubcan and Cevolani [1983], Porubcan [1992], Buček et al. [2012], Porubcan et al. [2012]. The other researchers (Jacobi [2014], Lima et al. [2015], Lindblad [1967]) have conducted similar investigations using a meteor radar operating at a non-equatorial latitude and found good concordance between meteor height and solar activity parameters. Some parameters have provided long-term information about the variation in atmospheric conditions in the MLT region and their relation to solar activity. As mentioned previously, the meteor phenomenon depends on the incoming velocity and mass of the meteoroid. Air density also plays an important role in meteor ablation, wherein the height of the meteor echo peak becomes lower as density decreases (Clemesha and Batista [2006], Stober et al. [2012]). Therefore, the height of the meteor echo peak observed

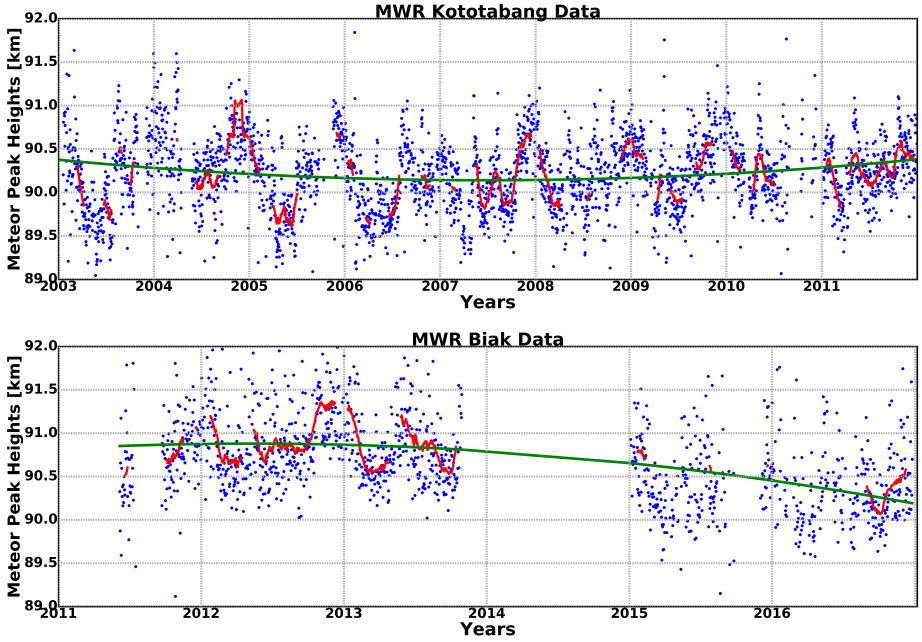

(a)

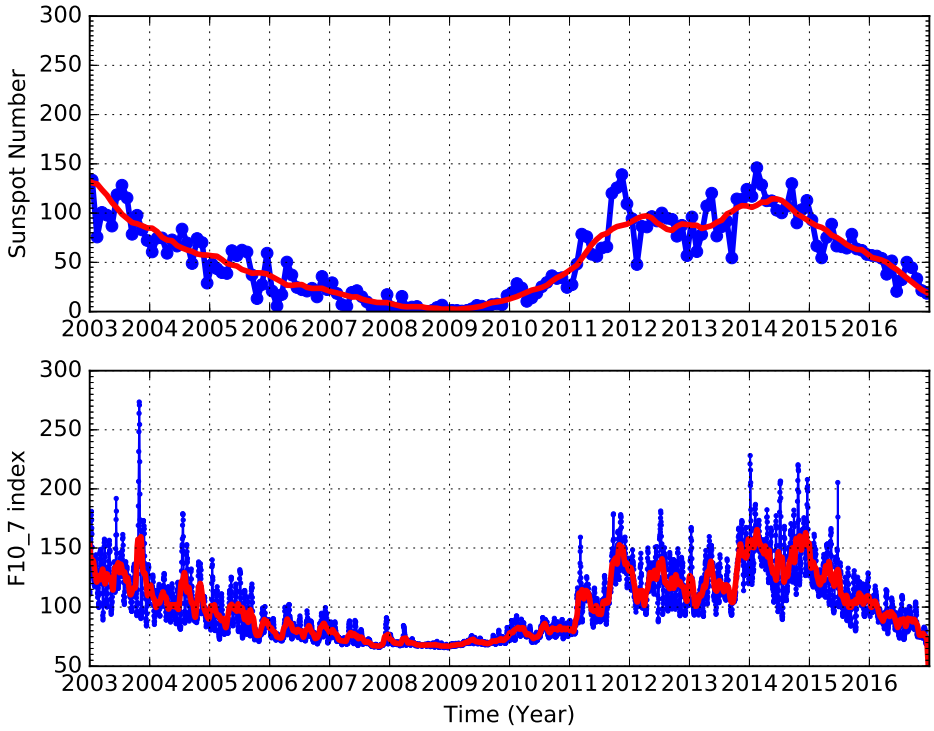

(b)

Figure 2.6: (a) Scatter plots of meteor peak heights at Kototabang for the period 2003-2011 (top) and Biak for the period 2011-2016 (bottom). The red curves show the 31-day running average and the green line is the fitting curve of the data. (b) Time series of the daily solar sunspot number, R (top) (Royal Observatory of Belgium (ROB) [2013]), and the solar radio flux, F10.7 index (bottom) (The National Aeronautics and Space Administration (NASA) [2005]). MWR = meteor wind radar.

during the solar cycle can be interpreted as a consequence of the change in air density in the upper atmosphere caused by solar activity. In the following, an investigation of the relationship between solar activity and meteor peak height in the equatorial latitudes of Indonesia is discussed.

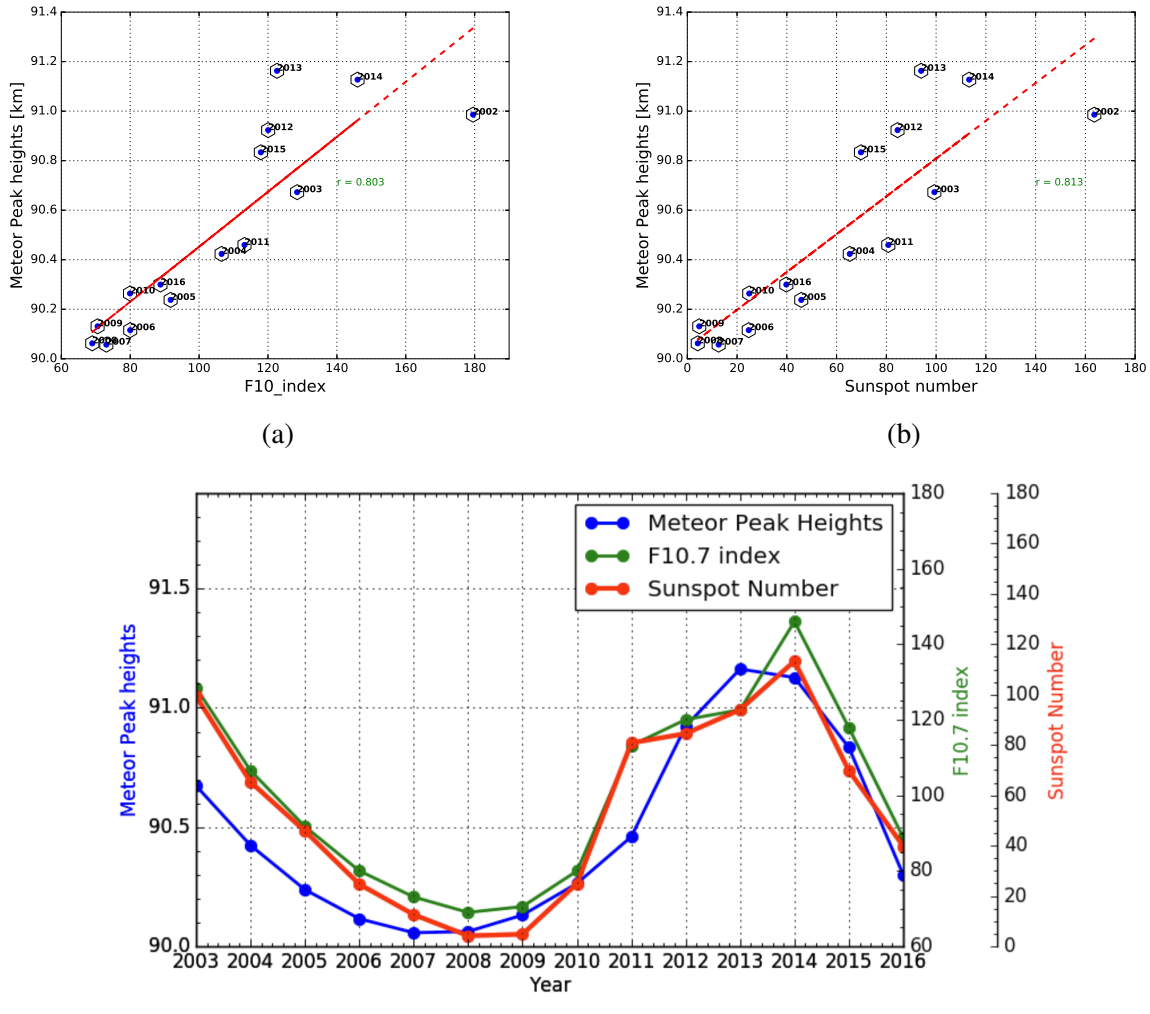

Figure 2.7: Annual mean meteor peak height as a function of annual F10.7 index (a) and R (b), and (c) annual plot of mean meteor peak height (blue), mean R (red), and mean F10.7 (green).

Our observation data include almost a full 11-year solar cycle, which is represented by the daily F10.7 and monthly R values and also by their 30-day running averages (red lines in Figure 2.6b). As shown in Figure 2.6a, there is a similar trend between the fitting curve of meteor peak height and the two solar activity parameters, although there are slight differences in time

between them and an absence of data in 2014 due to system improvements being carried out at that time. To evaluate the correlations between average F10.7 and R values on an annual basis, the average meteor peak heights were used. Figure 2.7 shows three panels. The top-left and top-right panels present mean annual meteor peak height as a function of F10.7 and R values, respectively. The bottom panel shows the annual mean values of meteor peak height (blue line), and F10.7 (green line) and R values (red line). As shown in the Figures 2.7, the annual mean meteor peak height, from the meteor radar observations at the Indonesian equator for 14 years (2003-2016), shows an adequate correlation (in the scale of ∼0.8) with solar radio flux index F10.7 (Figure 2.7a) and solar sunspots R (Figure 2.7b). In addition, Figure 2.7c shows the annual plot of mean meteor peak height as a function of both solar parameters above, in which the trends show its uniformity in phase. Despite the slight changes in the fitting

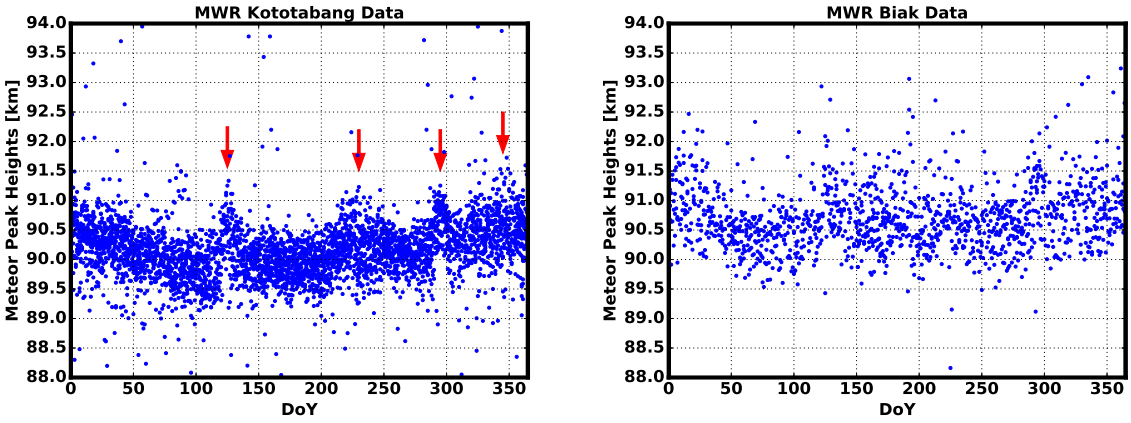

(a) (b)

Figure 2.8: Annual cycle of meteor peak height based on 13 and 5 years' worth of data collected at Kototabang (left) and Biak (right), respectively. MWR = meteor wind radar.

curves seen in the top and bottom panels of Figure 2.6a, it is estimated that the minimum value occurred in 2007-2008, and the peak was in 2012-2013. This indicates a change in the average meteor height of ∼0.1 km over a long period of solar activity, and the residual value is well represented statistically. From this perspective, the correlation between F10.7 and R seems attractive for investigating neutral temperature and density in the region of meteor ablation around the equator based on global empirical model calculations.

The annual height profiles over the altitude range of 88 to 94 km were also derived. These profiles are shown for both Kototabang and Biak in Figure 2.8. In Figure 2.8a (data from Kototabang), a clear cycle is apparent in the data. During the interval from December to February, the peak meteor count rate occurred at heights of ∼90.5 km. However, between June and July, the peak meteor count rate was observed at lower heights (∼90 km). Annual variation in the height of the peak meteor count rate was also observed at Biak (Figure 2.8b). During the period December to February, peak count rates occurred at heights of ∼91 km, but during December to April, the peak count rates were observed at heights of ∼90.5 km. Both profiles showed anomalous meteor peak heights around April, July, October, and December (DoY 120, 220, 290, and 345). These anomalies are thought to have occurred simultaneously with the peak meteor shower period. The peaks of the Lyrid, Perseids, Orionid, and Geminid meteor showers occurred in the four periods (DoY 112, 225, 294, and 348; (International Meteor Organization (IMO) [2007])).

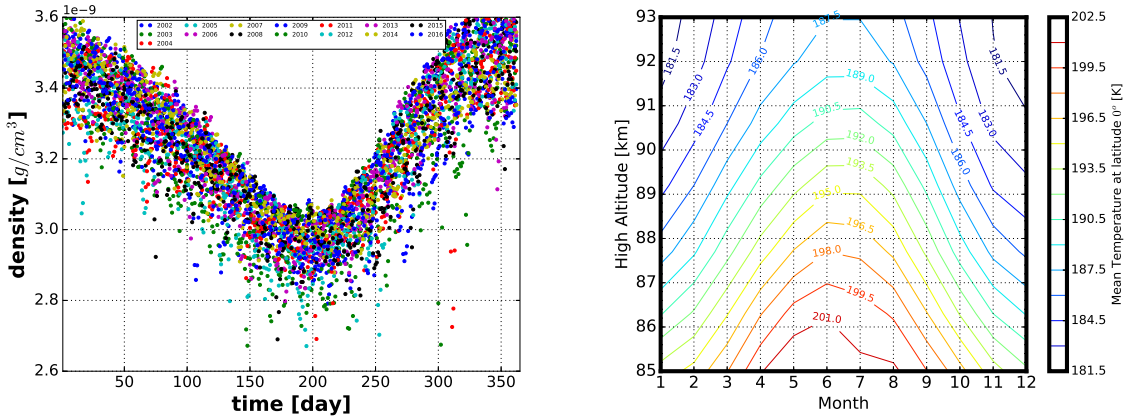

(a) (b)

Figure 2.9: Annual pattern in predicted meteor density based on the NRLMSISE-00 model, as a function of day of the year for a 15-year period (left), and contour plot of mean temperature at equatorial latitudes predicted by the COSPAR International Reference Atmosphere (CIRA) model (right). The density profile is calculated at 90 km altitude.

The temperature profile over the equatorial region calculated by NRLMSISE-00 could not seem to explain the variation of meteor peak height, while the temperature profile of the CIRA calculation shows its representation. To compare the annual trends in meteor peak height and

mass density, as predicted by the empirical models, we used the NRLMSISE-00 model to calculate the predicted density, and the CIRA model to predict the temperature at around 90 km height. As mentioned earlier, the NRLMSISE-00 with solar cycle effects and oxygen anomaly contributions can provide information about the conditions at high atmospheric altitudes. According to Picone et al. [2002], below 73 km, this model uses coefficients from the MSISE90 model, but at the height of the MLT region, the coefficients are constrained to maintain consistency of the total mass density at the ground. According to Stober et al. [2014], in high-altitude cases, the NRLMSISE-00 indicates no agreement between the mass density at MLT altitude and the effects of solar activity shown by the F10.7 and Ap indexes. An illustration of the annual variation in air density at meteor peak heights, during the period of 2002-2016 for the equatorial region derived from the NRLMSISE-00 model, is shown in Figure 2.9a. Similarly, information from the CIRA model on atmospheric temperatures in the MLT region over equatorial latitudes is shown in Figure 2.9b. Overall, Figure 2.9 shows that the minimum density, followed by the maximum temperature at the meteor peak height, occurs midyear (around June-July). On the other hand, the density value per day in 2002–2016 (Figure 2.10a) shows a different phase pattern to that of the solar activity cycle given by F10.7 and R (Figure 2.6a). Underscoring this relationship, the average yearly trend in mass density is shown in Figure 2.10b. These results accord with Stober's study in 2014 regarding the relationship of variations in solar activity with atmospheric density, where the NRLMSISE-00 model shows no obvious effect of the solar cycle at the MLT region according to the F10.7. In fact, they expected that there is no agreement between NRLMSIS and the air density, because NRLMSIS does not account for greenhouse gas effects in the lower and middle atmosphere.

We observed a variety of techniques to determine meteor peak heights in the literature. For example, the techniques of Liu et al. [2017] and Stober et al. [2014] use harmonic functions with a periodicity reflecting that of the solar activity cycle. Three other techniques, that is, those of Jacobi [2014], Lima et al. [2015], and Porubcan and Cevolani [1983], used a linear regression approach to obtain the meteor peak heights. These techniques are all assumed to rely on a combination of the annual mean heights at high latitudes and other periodic components. As described in Hocking et al. [1997], a normal distribution function can be fitted into meteor radar

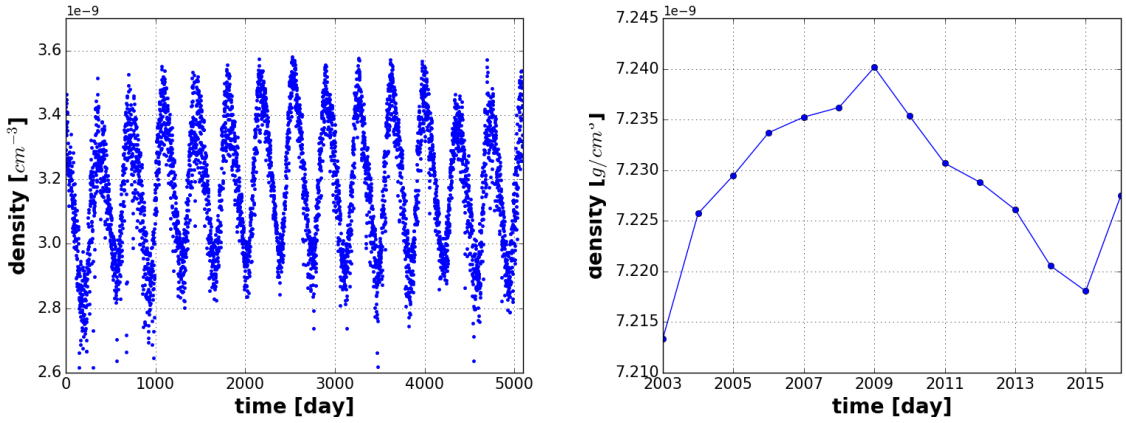

(a) (b)

Figure 2.10: Scatter plot of atmospheric density as a function of time [day 01 = 1 Jan 2003], as predicted by the NRLMSISE-00 model at 90 km altitude (left), and annual mean atmospheric density at 90 km altitude as a function of time (right).

data to obtain meteor peak heights. Note that the present results on meteor height are calculated based on the technique proposed by Hocking et al. [1997], but for the equatorial case, the peak value was taken from the maximum value of height distribution, assumed to be normally distributed. As shown in Figures 2.8 and 2.9, the relationship between density and meteor height seems clear, whereby the air density in the atmosphere each year affects the meteor height. This is in contrast to the results in Figure 2.10 and 2.6a, in which these parameters do not show a clear relationship. As shown in Figure 2.5, in particular for the meteor rate measured at Kototabang, the annual change in the number of detected meteor echoes generally shows an association with the change in atmospheric air density shown in Figure 2.10. The illustration above shows that the effect of solar activity on atmospheric density in the MLT region involves multiple processes, including atmospheric heating, particle drifting, and coupling processes, and remains among the issues that need to be further explored using large data sets at different locations.

Chapter 3

CONSTRUCTION OF A METEOR ORBIT CALCULATION SYSTEM FOR COMPREHENSIVE METEOR OBSERVATION AT KOCHI UNIVERSITY OF TECHNOLOGY

***

Abstract Continuing research works related to radio technology was discussed previously. The utilization of the atmospheric observation from meteor phenomena using techniques which are slightly different from the active radar mode will be discussed in this chapter. As noted, not only radar of back-scatter systems with an active mode that can emit radio waves signal toward the ionized trail of meteor, but also a forward-scatter method in bi-static radar system in which the receiver detect the reflected radio wave energy from a distant transmitter. In 2003, KUT began construction of a radar system for the forward-scatter applications using the interferometry calculation. The system is composed of 5-receiver interferometer antenna channels that are used to receive the reflected radio waves from the signal with frequency of 53.750 MHz emitted from the radio transmitting station at Sabae city, Fukui, Japan. In addition, this chapter discusses the result of an alternative meteor observation based on the forward scatter technique to determine the parameters of the meteor trajectory during the observation campaign period of Geminid meteor shower in 2015. As a result, 20 examples of Geminid meteor shower events with 3 levels of noise signal classification recorded in our observations. The predicted Geminid meteor shower speed is about 34 ± 8.86 km/s based on the average value of 12 meteor shower data groups in the minimum noise signal category.

3.1 Background and Arising Problem of the Research

As noted, the collisions between ablated atoms of the meteoroid and molecules or atoms of the upper atmosphere allows to produce the energy which is sufficient to form the ionized particles. The electrons are the important parts in which the scattering mechanism may suitably occurred, depending on the specification of the meteor trail, i.e. the *underdense* and the *overdense* meteor trail. Developing an oblique scattering from meteor trails by arranging both important instrument, transmitter and receiver, several hundred kilometer apart from, is an attracting scientific aspect. Off course, more comprehensive methods are required to take full advantage of the observation to catch a desirable raising of the best trail. The ellipsoid geometry of the forward-scatter introduces ambiguity in the measurement of several meteor parameters, which can be overcome only by developing additional observation equipment on the country side. Although the methods able to give the estimation of spatial position, trail orientation, and meteor velocity, the methods still remain complexities and imply challenges to the meteor explorer's ingenuity. Fortunately, these particular difficulties were not reduced enthusiasm to the practical implementation of forward-scatter to radio communications. And, thanks to early scientists and engineers who invented the forward scatter method through the first implementation of the principle successfully applied in the JANET system for communication testing (Forsyth et al. [1957]).

In the year of 2003, Kochi University of Technology (KUT), Japan developed a forward-scatter meteor radar, whose concept is similar to a Ham-band Radio meteor Observation (HRO) Interferometer. The configuration of KUT radar system can be found in Mizumoto [2015],and Mizumoto et al. [2019]. Since the initial operation of the KUT forward-scatter meteor radar system, various research achievements have been introduced, such as the automation of meteor echo counting (Noguchi and Yamamoto [2008]) as well as the system improvement reported by Omonori [2011]. In this chapter, the construction of a comprehensive meteor observation as one of the system configuration improvement is discussed. The algorithm for meteor orbit calculation is also described along with sample campaign observational results in a period of Geminid meteor shower 2015 in order to estimate the geometry parameters of the meteor.

3.2 Meteor Orbital Parameter of Three-receiver Station System

KUT is currently operating and observing meteor activity using 5-channel interferometry with application of the forward scattering method. As was shown in Figure 1.9a, the arrangement of interferometric antenna used for our observation. Our arrangement has made follows the concept proposed by Jones et al. [1998] as a new interferometer arrangement which has better directional detection capabilities, lower angular ambiguities and reducing the coupling problems as well. With three antennas arranged to be spaced by distances apart by 0.5λ; for example and refer to Figure1.9a, the phase measurement ϕ_{10} and ϕ_{40} relative to the center antenna then allow unambiguous determination of the angle of arrival since

$$\phi_{10} = \frac{2\pi d_1}{\lambda} \sin\beta, \tag{3.1}$$

$$\phi_{40} = \frac{2\pi d_4}{\lambda} \sin\beta. \tag{3.2}$$

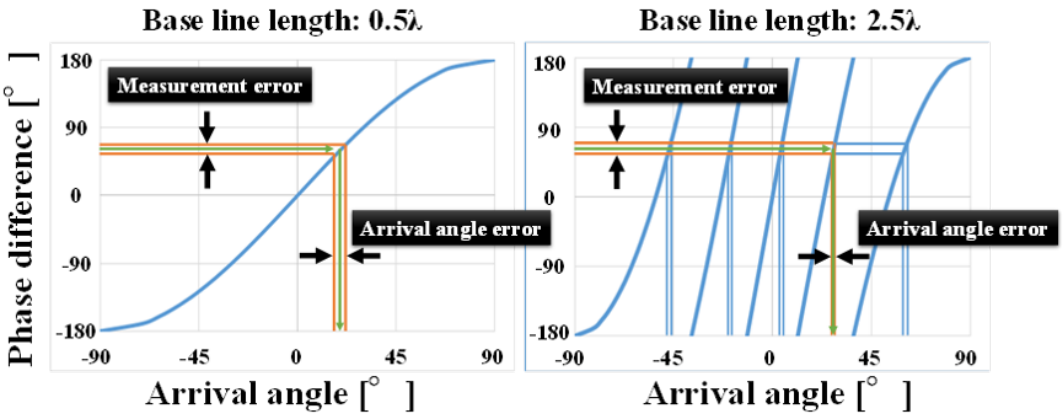

Figure 3.1: The relationship between the measured phase angles and derived angle of arrival. The shaded bands show the degrees of uncertainties effect in the total phases.

where d_1, d_4, and β are respectively refer to the distance between antennas 1 and 4 relative to the antenna 0, and the angle of arrival. Then two estimation of the arrival angle β essentially as follows

$$\sin\beta = \frac{\lambda}{2\pi}\frac{\phi_{10}-\phi_{40}}{d_1+d_4}, \tag{3.3}$$

$$\sin\beta = \frac{\lambda}{2\pi}\frac{\phi_{10}+\phi_{40}}{d_1-d_4}. \tag{3.4}$$

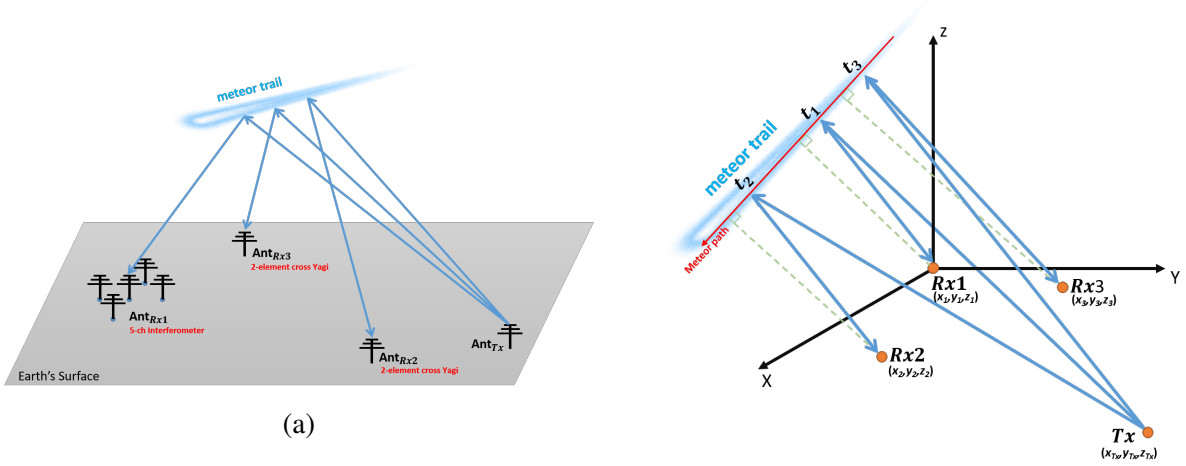

Figure 3.2: Illustration of the three-station system for determining orbital meteor parameters.

The first equation 3.3 provides an accurate result rather than the second equation 3.4 but answer the ambiguity since $(d_1 - d_4)$ is equal to 0.5λ and eliminate the numerator. For example, as our case, with $d_1 = 1.5\lambda$ and $d_4 = 1.0\lambda$ and with $\beta = 40^o$, the quantities of $(\phi_{10} - \phi_{40})$ lower than $(\phi_{10} + \phi_{40})$. This is illustrated in Figure 3.1, where the measured phase of $(\phi_{10} + \phi_{40})$ gives more accurate possibilities from which the selected value of β is determined by the result of $(d_1 - d_4)$.

Using the concept of interferometer described above, the KUT radar system composed of 5-receiver interferometer antenna channels that are used to receive the reflected radio waves from the signal with frequency of 53.750 MHz emitted from the radio transmitting station at the National Institute of Technology, Fukui College at Sabae, Fukui prefecture (Figure 1.10).

In order to determine the orbital parameter of the individual meteor, we applied the radio echo system using three receivers spaced on the ground by a certain km apart (See Figure 3.2).

The geometrical parameters of meteor path from observations at three-spaced stations is shown in Figure 3.2b. The location of all receivers used in this work is shown in Figure 3.3a. Using the geometry system in Figure 3.2b, the 5-channel receiver at KUT, Rx_1 is located at the origin of Cartesian coordinate system. The second and the third receivers Rx_2 and Rx_3 are located at the point (x_2, y_2, z_2) and (x_3, y_3, z_3). The distance of Rx_2 and Rx_3 to Rx_1 are about 10-20 km apart, so that specularly reflected echoes are likely to be received at all three stations from the same meteor trail, assuming that the path length of the trail may have been about 20 km or so. From the amplitude-time records, it could determine the real time t_1 at the master station. It could also find the time from the transmitter Tx to the meteor path and back to Rx_2 and Rx_3 for t_2 and t_3, respectively. Then, the meteor velocity can be measured from any of the

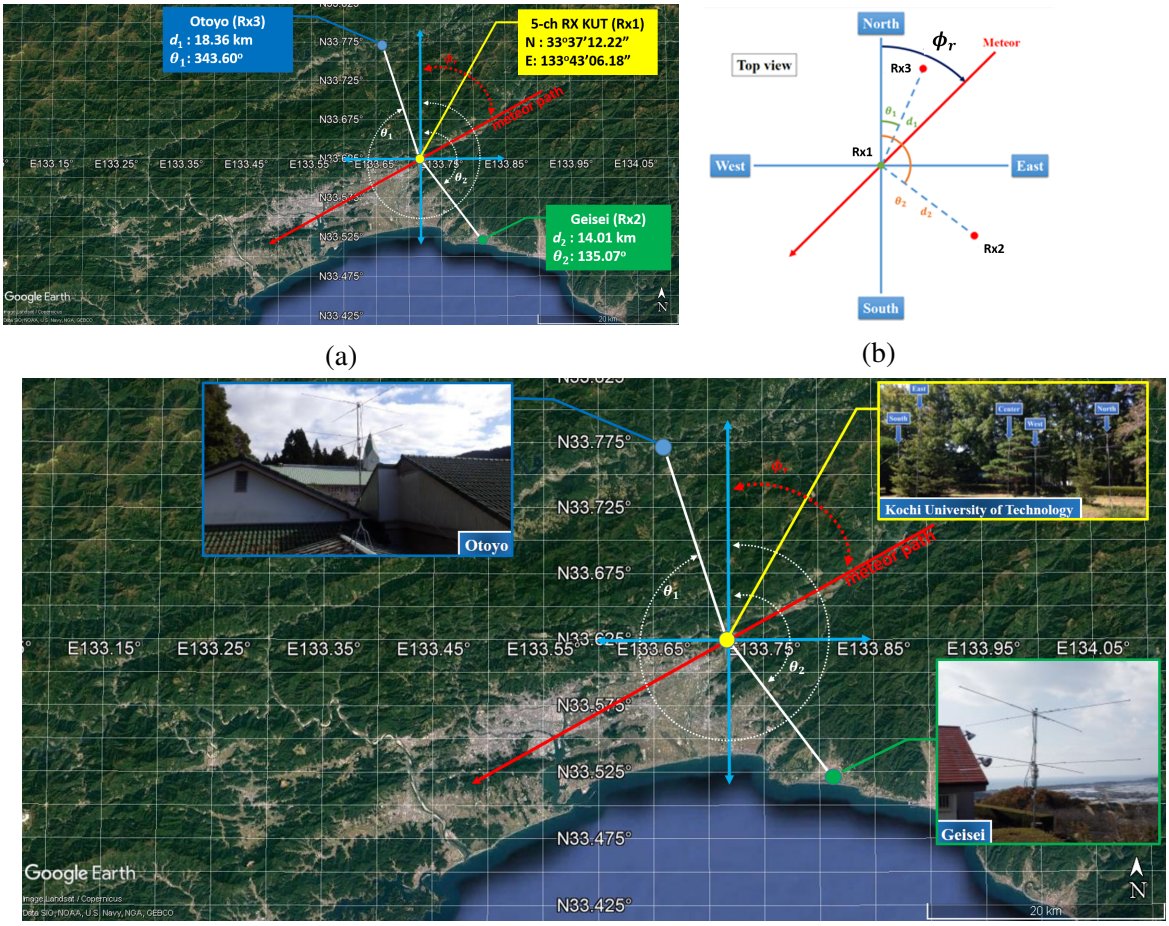

Figure 3.3: Location of each station in the three-station system. (a) Geographical location of individual station. (b) The layout point of each station as seen from the top. (c) The antenna photograph of each station.

records. Hence, to a good approximation, the orbital parameter of individual meteor, e.q. the azimuth angle and velocity can be estimated by the procedures based on the schematics shown in Figure 3.3b.

The equation to derive each parameter of the orbital meteor referred to Figure 3.3b could be approximately as follow:

$$d_1 \cos(\theta_1 - \phi_r) = V_H \Delta t_1, \tag{3.5}$$

$$d_2 \cos(\theta_2 - \phi_r) = V_H \Delta t_2. \tag{3.6}$$

From the equations 3.5 and 3.6,

$$V_H = \frac{d_1}{\Delta t_1} \cos(\theta_1 - \phi_r) = \frac{d_2}{\Delta t_2} \cos(\theta_2 - \phi_r). \tag{3.7}$$

By using the trigonometry rule and the relationship between time and distance for the velocity $v_1 = d_1/\Delta t_1$ and $v_2 = d_2/\Delta t_2$, the equation 3.7 then becomes

$$v_1(\cos\theta_1 \cos\phi_r + \sin\theta_1 \sin\phi_r) = v_2(\cos\theta_2 \cos\phi_r + \sin\theta_2 \sin\phi_r). \tag{3.8}$$

Simplify modification of mathematical formations, the equation 3.8 becomes

$$(v_2 \cos\theta_2 - v_1 \cos\theta_1) \cos\phi_r = (v_1 \sin\theta_1 - v_2 \sin\theta_2) \sin\phi_r, \tag{3.9}$$

and the azimuth angle ϕ_r is given by

$$\phi_r = \tan^{-1}\left(\frac{v_2 \cos\theta_2 - v_1 \cos\theta_1}{v_1 \sin\theta_1 - v_2 \sin\theta_2}\right). \tag{3.10}$$

Further, in order to interpret the entrance speed of meteor, it is necessary to consider the direction where the meteoroid comes from its origin traditionally called the *radiant*, a terminology from the observation when the apparent trails of meteors are then seemingly radiating from one point of the sky. The Earth's rotation, together with its tilt and motion about relatively to the sun, causes the meteor rate variation due to their apparent radiant to vary hour to hour and from season to season. The theoretical meteor echo rate for a point source radiant can be determined

for all positions of the radiant in elevation and azimuth. The geometry for a simple sky observation system is shown in Figure 3.4, where the radiant is at elevation θ_r and azimuth angle ϕ_r, as seen from the observer site. The reflection point **M** with the height **ML** on the meteor trail in the plane **PQRS**, named *echo plane*, is at elevation angle Θ and azimuth of echo plane Φ. Meteors of a given velocity have beginning and end heights h_2 and h_1, respectively. The

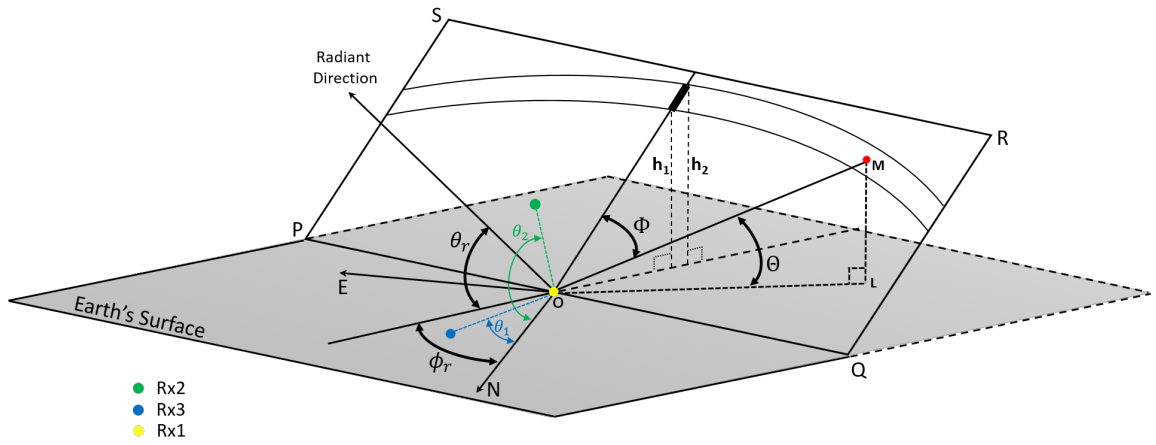

Figure 3.4: Geometry of the echo radiant. The radiant direction is expressed by the elevation angle θ_r and azimuth angle ϕ_r relative to the observer site at **O**.

distances along the meteor trajectory projected on the horizontal plane between (Rx_1-Rx_2) and (Rx_1-Rx_3) are introduced in terms of D_{T1} and D_{T2}. The equations 3.5 and 3.6 then become

$$D_{T1} = d_1 \cos(\theta_1 - \phi_r), \tag{3.11}$$

$$D_{T2} = d_2 \cos(\theta_2 - \phi_r), \tag{3.12}$$

it follows that, using the trajectory distance on the horizontal plane obtained from equations 3.11 and 3.12, the velocity V_H ($V_{H1} = \frac{D_{T1}}{\Delta t_1}$ and $V_{H2} = \frac{D_{T2}}{\Delta t_2}$) of the meteor moving on the horizontal plane is obtained by using the time difference of each point. The horizontal V_H is

$$V_H = \frac{\frac{D_{T1}}{\Delta t_1} + \frac{D_{T2}}{\Delta t_2}}{2}, \tag{3.13}$$

in average.

Referring back to Figure 3.4, the velocity on horizontal plane can be written as

$$V = \frac{V_H}{\cos\theta_r}. \tag{3.14}$$

3.3 Observational Data and Discussion

It was known that from visual observation a shower meteor can be defined by using the position of the shower radiant fixed in the sky and the velocity of the meteor. For the major showers, e.g., the Geminids, the Perseids, or Quadrantids with the maximum hourly count of meteor, at least a little difficulty is found in identifying the meteor shower. In order to examine the configuration of the three-receiver station system described in the previous section, an observation campaign during one week of December 2015 was conducted with hopefully catch Geminid's reflections. Fortunately, around 20 events of Geminid meteors are recorded with various classification of noise level among 56 simultaneous meteor echoes received by all three stations. One typical signal example showing the diffraction patterns observed at three receivers can be found in Figure 3.5. The diffraction fluctuations recorded only after the meteor passed the points corresponding to t_1, t_2, and t_3 in Figure 3.2b. Using the time differences from each two-successive station's records, orbital parameters of the meteor, e.q., meteor velocity, trajectory angle data for 20 meteor echo datasets, and their geographical coordinates were estimated by using the only 20 datasets. The remaining 36 meteor echo datasets could not be used for calculation of actual meteor velocities due to the extensive environmental noise level, suppressing the signal-to-noise ratio level of the received signals. The observation results of the 2015 Geminid meteor shower are shown in Table 3.1.

As for the evaluation of the data shown in table 3.1, the Geminid meteor shower had an average velocity of 34.02$\pm$8.86 km/s based on 12 recorded data of meteors with the A classification of clear signal-to-noise level. This average velocity was relatively close to what the average speed of meteor observed by Ceplecha et al. [1998], Stober et al. [2013], and Jenniskens [1994], which is about 35 km/s. After removing the uncategorized of Geminid meteor shower that has the velocity larger than 50 km/s, it was found that in the distribution of the average velocity from the observation has double peak occurrences at around 35 km/s which

corresponded to that of Geminid observed previously (Stober et al. [2013]) and another peak at the speed range of 50 to 70 km/s, corresponding to sporadic meteor within the peak at around

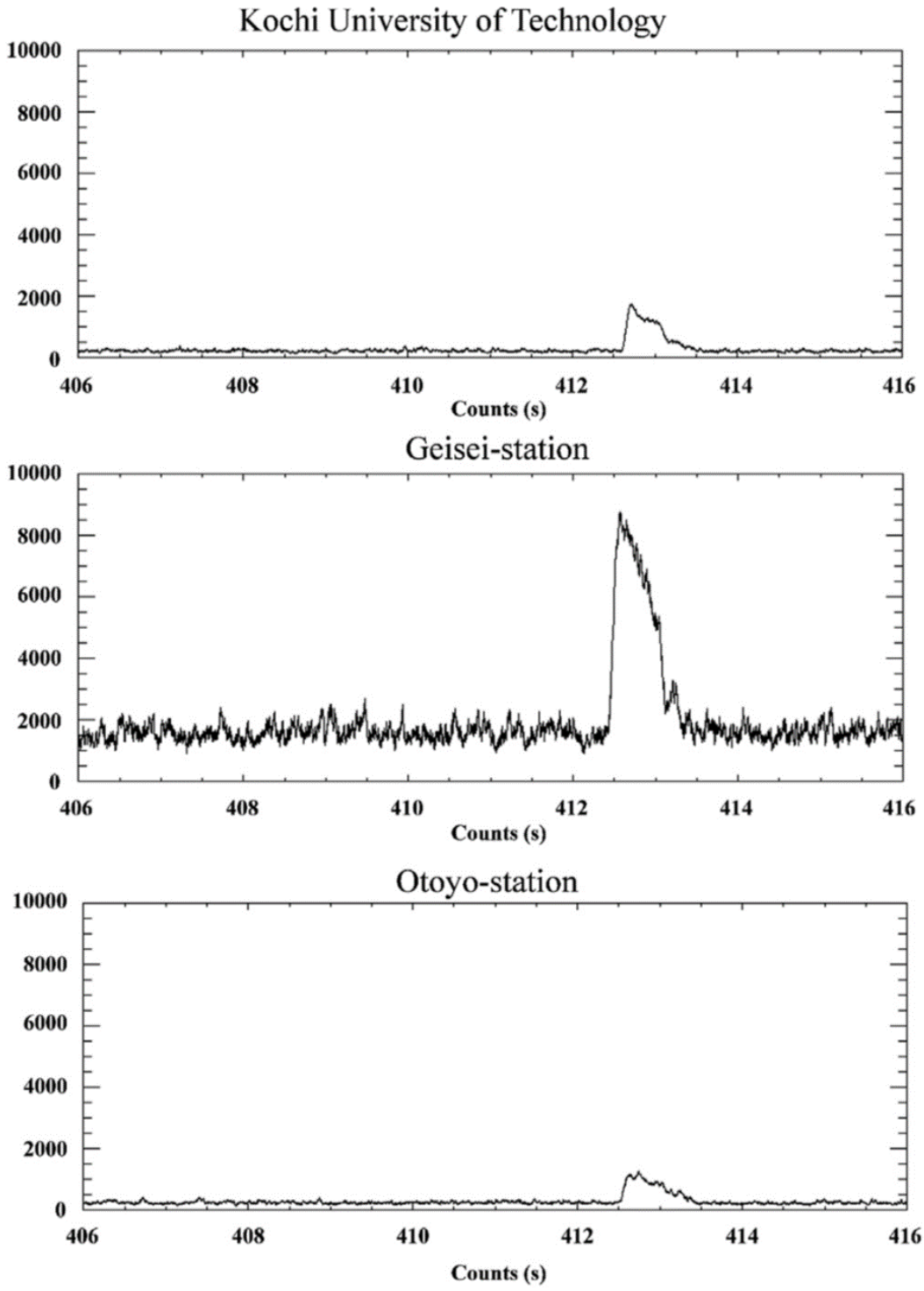

Figure 3.5: 10-seconds of amplitude-time radar records of the meteor echo observed simultaneously at three-stations (KUT, Geisei, and Otoyo) conducted on December 13, 2015. The plots start from 19:26:46. Reprinted from Mizumoto et al. [2019].

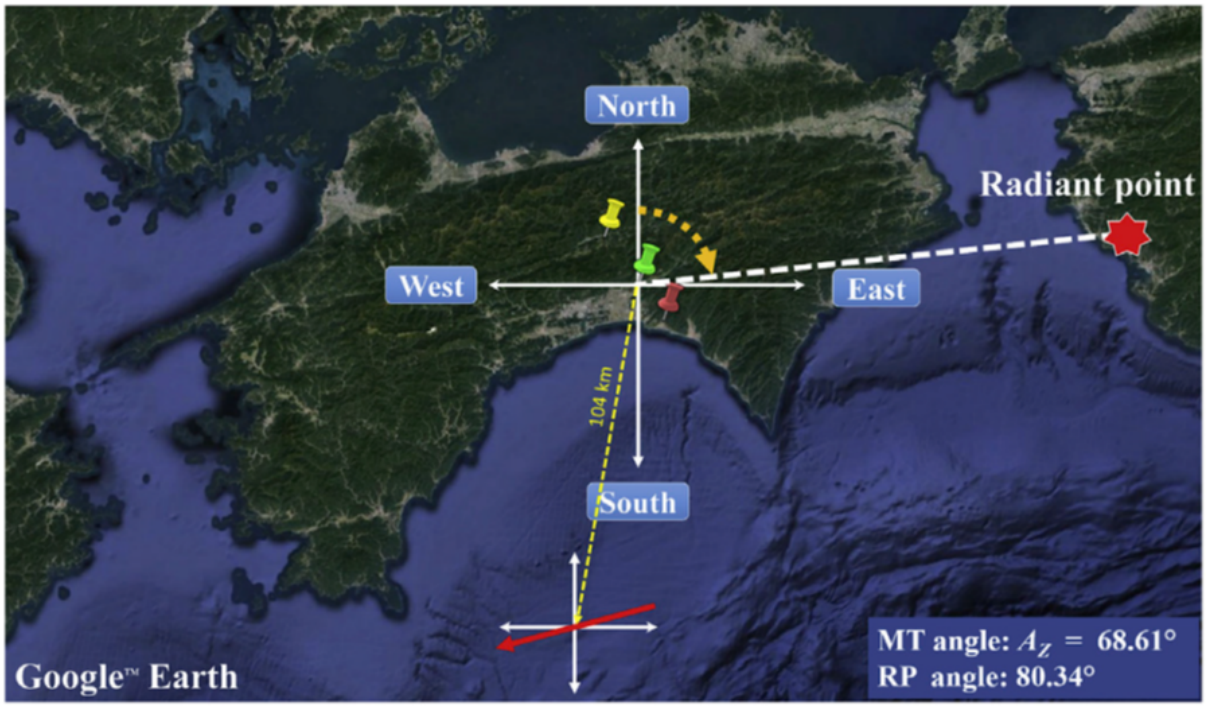

Figure 3.6: The radiant point and meteor trajectory angle of the meteor appearance at 23:13:09 JST on December 13, 2015. Reprinted from Mizumoto et al. [2019].

.

60 km/s and the radiant source may have originated from the north apex (Kero et al. [2012]).

As shown in the Figure 3.6, the radiant point of the Geminid was appeared at the East-North-East, travelling the South-South-West at about 104 km far from the KUT, however, the meteor trajectory was directed to the West-South-West. Therefore, the difference in angle between the meteor trajectory angle (MT) and the radiant point was about 168.27^o, which was almost close to a stright line (i.e., 180^o). This difference may have been assumed due to the effect of the Earth's behavior (e.q. the rotation and the revolution) as well as the error in observation accuracy in the forward scattering meteor radio observation method. Thanks to Noguchi's work in 2009 for the system callibration improvement to increase the accuracy measurement (Noguchi and Yamamoto [2008]), the improvement gives the good result of the 2015 Geminid observation in which the meteor trajectory angle and the radiant point of the meteor indicated a small discrepancy lower than 25^o.

Table 3.1: Observation results of the Geminid meteor shower conducted by Mizumoto in 2015 (Mizumoto et al. [2019]).

Appearance time		Time differences		Appearance location		MT angle	RP direction		Threshold	Meteor entry angle	Horizontal component			Velocity	Distinction	Classified
Date	Time [JST]	t1 [s]	t2 [s]	Latitude	Longitude	Az[°]	RP azimuth [°]	H [°]	Th [°] $\leq \pm 25°$	Z [°]	VH1 [km/s]	VH2 [km/s]	VH [km/s]	V [km/s]	Gem./Spo.	Class
Dec. 11, 2015	16:31:59	-0.090	0.436	-	-	78.59	29.87	-17.00	48.72	107.00	17.78	17.75	17.77	-	Spo.	B
	20:40:29	0.034	0.140	-	-	69.25	65.28	21.92	3.97	68.09	40.88	41.00	40.94	44.13	Gem.	B
Dec. 12, 2015	1:11:57	0.370	0.230	-	-	57.85	92.98	76.89	-35.13	13.11	13.46	13.48	13.47	-	Spo.	A
	5:43:22	0.908	0.417	-	-	55.72	282.98	46.30	-227.26	43.70	6.21	6.21	6.21	-	Spo.	A
	7:11:26	0.292	-1.212	-	-	259.58	291.14	28.75	-31.56	61.26	6.54	6.55	6.55	-	Spo.	C
	7:24:53	1.596	1.336	-	-	60.00	292.47	26.14	-232.46	63.86	2.71	2.70	2.71	-	Spo.	C
	9:24:45	0.310	-0.270	-	-	314.77	306.02	4.44	8.76	85.56	51.87	51.89	51.88	-	Spo.	A
	19:18:55	-0.020	0.210	-	-	75.72	56.53	7.28	19.20	82.72	34.00	34.00	34.00	34.28	Gem.	A
	22:11:47	-0.104	0.278	-	-	83.92	74.46	40.55	9.46	49.45	31.63	31.62	31.63	41.63	Gem.	C
Dec. 13, 2015	6:59:03	0.180	-0.049	-	-	31.13	290.32	30.39	-259.19	59.61	68.89	68.78	68.84	-	Spo.	A
	6:59:15	0.877	-0.173	-	-	35.99	290.34	30.35	-254.35	59.65	12.77	12.77	12.77	-	Spo.	A
	7:37:06	-0.700	0.515	34°20'20.4"N	132°47'42.0"E	153.42	294.10	23.05	-140.68	66.95	25.81	25.83	25.82	-	Spo.	A
	8:44:57	0.152	-0.102	-	-	343.50	301.57	10.57	41.93	79.43	120.79	120.78	120.79	-	Spo.	A
	18:32:05	-0.050	0.185	-	-	80.46	50.94	0.88	29.52	89.12	43.80	43.84	43.82	-	Spo.	A
	18:48:07	0.155	0.088	-	-	57.20	53.10	3.34	4.10	86.66	33.42	33.41	33.42	33.48	Gem.	A
	18:49:58	0.244	0.001	-	-	45.22	53.34	3.64	-8.13	86.36	35.78	40.00	37.89	37.97	Gem.	A
	19:26:52	0.070	0.180	-	-	67.19	57.97	9.89	9.22	80.12	29.29	29.28	29.29	29.73	Gem.	A
	19:44:20	-2.821	0.043	-	-	224.51	60.02	12.99	164.50	77.01	3.17	3.26	3.22	-	Spo.	A
	19:54:29	-0.148	0.262	-	-	91.93	61.17	14.83	30.76	75.17	38.99	39.01	39.00	-	Spo.	A
	19:54:34	0.113	0.233	-	-	66.00	61.18	14.84	4.82	75.16	21.50	21.50	21.50	22.24	Gem.	A
	20:25:32	0.040	0.262	-	-	70.71	64.54	20.58	6.17	69.42	23.25	23.13	23.19	24.77	Gem.	A
	20:39:34	0.525	0.412	-	-	59.54	66.00	23.23	-6.46	66.77	8.50	8.50	8.50	9.25	Gem.	C
	20:50:46	-0.205	0.240	-	-	109.67	67.13	25.38	42.53	64.63	52.73	52.75	52.74	-	Spo.	A
	20:50:55	-0.114	0.246	-	-	87.37	67.15	25.40	20.22	64.60	38.33	38.33	38.33	42.43	Gem.	A
	21:14:37	0.104	0.247	-	-	66.78	69.48	30.00	-2.71	60.01	20.96	20.97	20.97	24.21	Gem.	A
	21:19:52	-2.452	0.232	-	-	221.27	69.99	31.02	151.28	58.98	4.00	4.01	4.01	-	Spo.	A
	21:36:29	-0.011	0.283	-	-	74.43	71.56	34.29	2.87	55.71	24.55	24.28	24.42	29.56	Gem.	C
	21:41:24	-0.100	0.239	-	-	85.57	72.02	35.27	13.54	54.73	38.10	38.08	38.09	46.65	Gem.	A
	21:44:01	0.163	0.209	-	-	63.03	72.27	35.79	-9.24	54.21	20.67	20.67	20.67	25.48	Gem.	A
	22:00:03	-0.060	0.255	-	-	79.41	73.74	38.99	5.67	51.02	31.00	30.98	30.99	39.87	Gem.	A
	22:08:43	0.030	0.120	-	-	69.14	74.54	40.72	-5.40	49.28	47.67	47.58	47.63	-	Spo.	A
	22:36:32	-0.004	0.218	-	-	73.99	77.04	46.35	-3.06	43.65	30.00	31.06	30.53	44.23	Gem.	B
	22:36:56	0.089	0.144	-	-	64.55	77.08	46.43	-12.53	43.57	32.47	32.43	32.45	47.08	Gem.	A
	22:57:48	-0.019	0.200	-	-	75.72	78.95	50.69	-3.24	39.31	35.79	35.70	35.75	-	Spo.	C
	23:13:09	0.200	0.700	32°41'24.7"N	133°34'44.4"E	68.61	80.34	53.84	-11.73	36.16	8.00	7.99	8.00	13.56	Gem.	B
	23:27:58	0.010	4.190	-	-	73.55	81.70	56.89	-8.15	33.11	2.00	1.59	1.80	3.30	Gem.	C
Dec. 14, 2015	0:11:14	-1.510	0.250	-	-	217.77	85.93	65.87	131.84	24.13	7.12	7.12	7.12	-	Spo.	C
	1:35:01	-0.112	0.515	-	-	78.90	102.14	83.29	-23.24	6.71	15.18	15.15	15.17	-	Spo.	B
	5:55:20	0.650	0.440	-	-	58.46	284.77	42.28	-226.30	47.72	7.37	7.39	7.38	-	Spo.	B
	7:48:47	-0.100	0.380	-	-	80.24	295.73	20.10	-215.48	69.90	21.20	21.24	21.22	-	Spo.	C
	9:42:46	0.290	-0.260	-	-	311.77	309.49	0.45	2.29	89.56	53.79	53.81	53.80	-	Spo.	A
Dec. 15, 2015	0:27:49	0.274	0.329	33°50'53.9"N	133°32'24.0"E	62.58	88.24	70.14	-25.66	19.86	12.81	12.80	12.81	-	Spo.	B
	0:33:26	0.025	0.490	-	-	72.57	88.94	71.31	-16.37	18.69	13.20	13.20	13.20	41.20	Gem.	C
	5:38:45	1.455	0.595	34°13'40.4"N	133°26'16.8"E	54.94	283.62	44.84	-228.68	45.16	4.03	4.03	4.03	-	Spo.	C
	6:20:09	0.003	0.170	33°34'10.2"N	133°29'06.0"E	73.24	287.39	36.52	-214.16	53.48	40.00	38.88	39.44	-	Spo.	C
	6:34:56	0.730	1.010	33°59'33.0"N	133°18'00.0"E	63.54	288.78	33.59	-225.24	56.41	4.40	4.40	4.40	-	Spo.	C
	7:05:55	-0.330	0.400	33°43'08.4"N	134°02'09.6"E	107.54	291.76	27.53	-184.22	62.47	31.06	31.05	31.06	-	Spo.	A
	8:43:54	0.250	0.140	34°26'40.6"N	133°04'58.8"E	57.10	302.38	9.37	-245.28	80.63	20.84	20.86	20.85	-	Spo.	A
	10:57:28	-0.455	0.505	34°02'47.4"N	133°15'21.6"E	113.26	321.67	-11.60	-208.40	101.60	25.76	25.76	25.76	-	Spo.	A
Dec. 16, 2015	0:05:32	0.124	0.080	-	-	58.12	86.16	66.32	-28.05	23.68	39.52	39.50	39.51	-	Spo.	A
	8:20:54	-0.200	0.181	34°01'08.4"N	133°27'25.2"E	130.83	300.14	12.75	-169.31	77.25	77.20	77.18	77.19	-	Spo.	B
	11:07:47	0.346	0.271	-	-	59.52	324.17	-13.38	-264.64	103.38	12.92	12.92	12.92	-	Spo.	B
	17:53:56	-0.425	0.387	-	-	130.21	47.18	-3.32	83.03	93.32	36.07	36.07	36.07	-	Spo.	C
Dec. 17, 2015	1:05:06	-0.115	0.151	-	-	103.16	95.73	79.55	7.43	10.45	78.78	78.74	78.76	-	Spo.	A
	2:27:20	-0.049	0.168	33°57'45.0"N	133°18'18.0"E	81.13	259.00	82.81	-177.88	7.19	49.18	49.11	49.15	-	Spo.	C
	2:46:00	-0.245	0.104	-	-	197.61	264.98	78.95	-67.37	11.05	62.12	62.12	62.12	-	Spo.	B

Chapter 4

IMPLEMENTATION OF THE DOPPLER RADAR BEAM SWINGING FOR INFRASONIC SOURCE DETECTION

***

Abstract The radar array system with the doppler beam swinging observation method can be used to study the dynamics in the atmosphere from the vertical profile of the Earth's atmosphere. The method of doppler beam swinging in radar application, in principle, is the swinging of radar signals in a certain vertical direction periodically. As a continuation of this study, this concept will be tried to be applied into the process of infrasound observation data processing, with the hope of being able to obtain the information on the vertical profile of the Earth's atmosphere. As a beginning step, infrasound data related to the sequence of the volcanic eruptions at Mt. Shinmoedake in March 2018, combined with the atmospheric vertical profile based on the suitable global atmospheric model and regional radiosonde launches are used in a comprehensive discussion described in subsections of this chapter. In addition, simple ideas for estimating horizontal wind speeds at certain atmospheric altitudes based on infrasound observation data and their validation and comparison are also explained in this chapter. Hopefully, the explanations written in this chapter can inspire writers in particular and readers in general to be able to take advantage of the benefits of infrasound wave remote-sensing for the study of the Earth's atmospheric dynamics.

4.1 Background and Arising Problem of the Research

In the previous chapter, we have illustrated two examples of direct measurements of all altitudes with a ground-based instrument for understanding the Earth's atmosphere. Other than that the direct measurements above, which are always limited to time and space coverage; Empirical models such as NRLMSISE-00, MERRRA-2, and HWM can provide the average climatology of the upper atmospheric database. Various enhancements to empirical models with data assimilation systems that can account for all the pertinent phenomena are an active field of scientific research at present. Thus, any and all available atmospheric measurements (indirect or otherwise) are useful for further characterization of the Earth's atmosphere. The infrasound measurements can complement all available measurements and provide meaningful information that can be used to improve understanding of current dynamics in the Earth's atmosphere. The advantages of infrasound waves have been exploited by researchers studying the characteristics of sound sources across the globe. Since 2015, in a collaboration between national industries and the Earth Space and Exploration System Laboratory (ESESL) of Kochi University of Technology (KUT), Japan, new instrument designs have been developed to increase land-use efficiency and integrate surface meteorological measurements with seismology components. In addition, the system has been deployed for operation in various locations in Japan, especially in the Shikoku Island region. Since the observation network was established, our sensors have successfully detected and recorded several natural phenomena that produced infrasound waves (e.g., explosive volcanic eruptions and an intense earthquake that occurred in Japan). Three explosive volcanic eruptions were detected by the sensor, at Mt. Aso in 2016, Mt. Sakurajima in 2017, and Mt. Shinmoedake in 2018.

The majority of high-amplitude volcanic infrasound is attributable to the eruptive acceleration of compressed volatiles from vents (Gabrielson [2007], Johnson [2003]). Such infrasound may result from either a long period of acceleration of erupted gas from a compact vent, or from an impulsive source distributed over a large region. In both cases, it is possible to detect infrasound from the eruption. There have been several previous reports of infrasonic observations likely caused by volcanic eruptions. One of these reports was based on the examination of air pressure data from one station, combined with a verification method implemented at an-

other station (i.e., cross-correlation) (Ichihara et al. [2012], and Matoza and Fee [2014]). Other reports were based on the evaluation of air pressure measurements from small-array sensors at locations close to the mountain cauldron (i.e., $<$ 10 km) (Garcés et al. [2003], Johnson et al. [2004, 2006], and Ripepe et al. [2001]), and analyses of the International Monitoring System (IMS) infrasound network (Goerke et al. [1965], Evers and Haak [2001], Le Pichon and Y [2001], Liszka and Garces [2002], Christie et al. [2005], Campus [2005], Evers and Haak [2005], Campus [2006a, 2007], Caudron et al. [2015]) using the progressive multi-channel correlation (PMCC) technique (Cansi [1995], Cansi and Le Pichon [2009]). Similar way in Russia (Lopez et al. [2013]), Italy (Marchetti et al. [2009], Ripepe et al. [2010]), and Ecuador (Johnson et al. [2006]) also detected lower frequency waves associated with volcanic eruptions, in which air pressure disturbances traveled radially and uniformly away from source points. In general, the sensor array system used is relatively close to the observed source point (d $<$10km) with a fairly homogeneous distance between sensors (close and equal distances). These investigations found some clear changes in air pressure originating from volcanic eruptions, with amplitudes of $>$ 20 Pa. However, the propagation speeds inferred from the infrasonic detection (0.02–0.05 Hz) reported in above previous studies varied considerably, with apparent velocities ranging from $\sim$338 to $\sim$420 m/s.

A common objective in infrasound data processing is the estimation of the arrival direction (azimuth) of the incoming signals. Several methods for determining the azimuth of a source have been implemented. Frequency-wavenumber (f-k) analysis in combination with delay and sum beamforming in the time domain of the incoming signals (Olson and Szuberla [2008]), using the PMCC algorithm (Cansi [1995], Cansi and Klinger [1997]), computes time delays, and uses the sum of the delays between unique sensor pairs to establish relationships for estimation of the arrival direction of the source for each window of the data. These methods are conducted using regular arrays of closely spaced sensors. Recently, our lab carried out three-dimensional ray-tracing using the vertical of atmospheric profiles, e.g. horizontal wind and temperature, to figure out the sound propagation profiles.

In this chapter, we report on observations of the infrasound to the lower and upper atmosphere as reflected by sufficient layers. We focus on powerful transient signals that travel

through the atmosphere which provide us with a quantitative basis to estimate infrasound specifications through a Radar Beam Swinging method implementation into our infrasound data processing. We present our findings on far field infrasound returns from Mnt. Shinmoedake in Japan (31.9098^o N, 130.8863^o E), which is observed during sequences of explosive activity. These explosions have estimated results in a strong explosive range. The identified source was then used to determine upper wind speeds and directions from recorded signal properties.

4.2 Activity at Mt. Shinmoedake in March, 2018

Mount Shinmoedake (elevation ∼1,421 m), is a stratovolcano located in southwest Kyushu Island (31^{o}34′46.33”N, 130^{o}39′29.67”E), and is part of a cluster of volcanoes around Mt. Kirishima (red triangle in Figure 4.1).

Figure 4.1: Topographic map of Mt. Shinmoedake and the Mt. Kirishima volcano cluster. The contour image is taken from Japan Meteorological Agency (JMA) website.

Mount Shinmoedake is one of the currently active volcanoes in Japan. According to a report from the Japan Meteorological Agency (JMA) (Japan Meteorological Agency (JMA) [2018]), volcanic activity suddenly recommenced at the beginning of March, 2018, and persisted through to April, 2018. Violent eruptions ejected ballistic projectiles and the resulting ash plume were blown away from the crater. Figure 4.2 shows an automated analysis of Moderate Resolution Imaging Spectroradiometer (MODIS) data distributed by the LANCE-MODIS data system and published on the Middle InfraRed Observation of Volcanic Activity (MIROVA) website (MIROVA [2018]). The figure, showing the thermal anomalies as the volcanic radiative power (VRP) in logarithmic scale, recorded at Mt. Shinmoedake volcano in 2018 clearly shows the sudden intense activity from early March to early April with the category of power intensity in a range between moderate and very high, followed by isolated events in May and June, 2018. The highest peak appeared on March 9 and 10, where the eruptions particularly produced most significant air vibration events. We also evaluated source-region infrasound data recorded by JMA during the major eruptions of the volcano at each start time shown in Table 4.1.

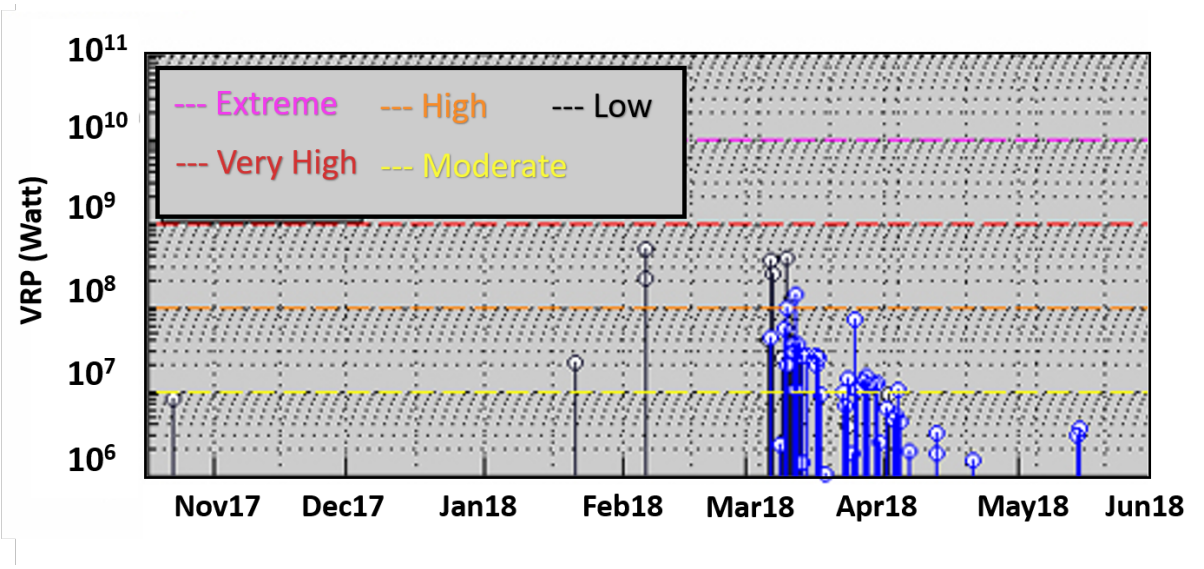

Figure 4.2: Log of the radiative power of Mt. Shinmoedake, Japan, during 2018 (table is taken from the Middle InfraRed Observation of Volcanic Activity (MIROVA) website. (MIROVA [2018]). The color lines respectively describe for extreme level (pink); very high level (red); high level (orange); moderate level (yellow); and low level (black).

Table 4.1: Recorded major eruptions of Mt. Shinmoedake during the period March 10–25, 2018. JST = Japan standard time.

Date of eruption	Time (JST=UTC+9)	Date of eruption	Time (JST=UTC+9)
March 9, 2018	15:58	March 11, 2018	04:05
	01:54		07:46
	04:27	March 12, 2018	12:45
March 10, 2018	10:15		14:13
	13:32		07:35
	18:11		

Our original infrasound data observed in Kochi Prefecture on March 10, 2018, at 01:54, 04:27, 10:15, and 18:11 Japan standard time [JST]) are shown in Figure 4.3. Strong signals and dense vibrations from the individual eruptions were recorded at stations KUT07, KUT08, KUT09, and KUT10. At the closest station to the crater (distance = 204.29 km), KUT07, a pressure change was first observed about 625 s after the eruption, with delays of another few seconds at other stations. Signals at the farthest station, KUT16 (342.90 km), showed relatively long arrival times ($\sim$18 minutes) and similarly dense vibrations to those at stations KUT07, KUT08, KUT09, and KUT10. We also observed other signatures at stations KUT01-KUT05, with small volumes/amplitudes. Figure A.1-A.6 in the appendix A shows similar profiles for other time periods than those in Table 4.1. We found that twelve stations with different locations had their own signatures that were likely to have originated from several sources, such as waves from the seashore, referred to as microbaroms (Garcés et al. [2004]) and mountain-associated waves (Landès et al. [2012]). In this study, an attempt was made to minimize these background signal to obtain infrasound data sourced from volcanic eruptions.

4.3 Basic Methodology

For our analysis, there were two main data processing steps. Firstly, we evaluated the ambient noise at each individual station to estimate the occurrence probability for each frequency bin of the recorded signals. In this step, we parsed the continuous time series for each station into segments (1-h time series) that overlapped by 50% and distributed them continuously throughout the day. This overlapping reduced the variance in power spectral density (PSD) estimates. The PSD processing computed repeating fast-Fourier transforms (FFT) for each of

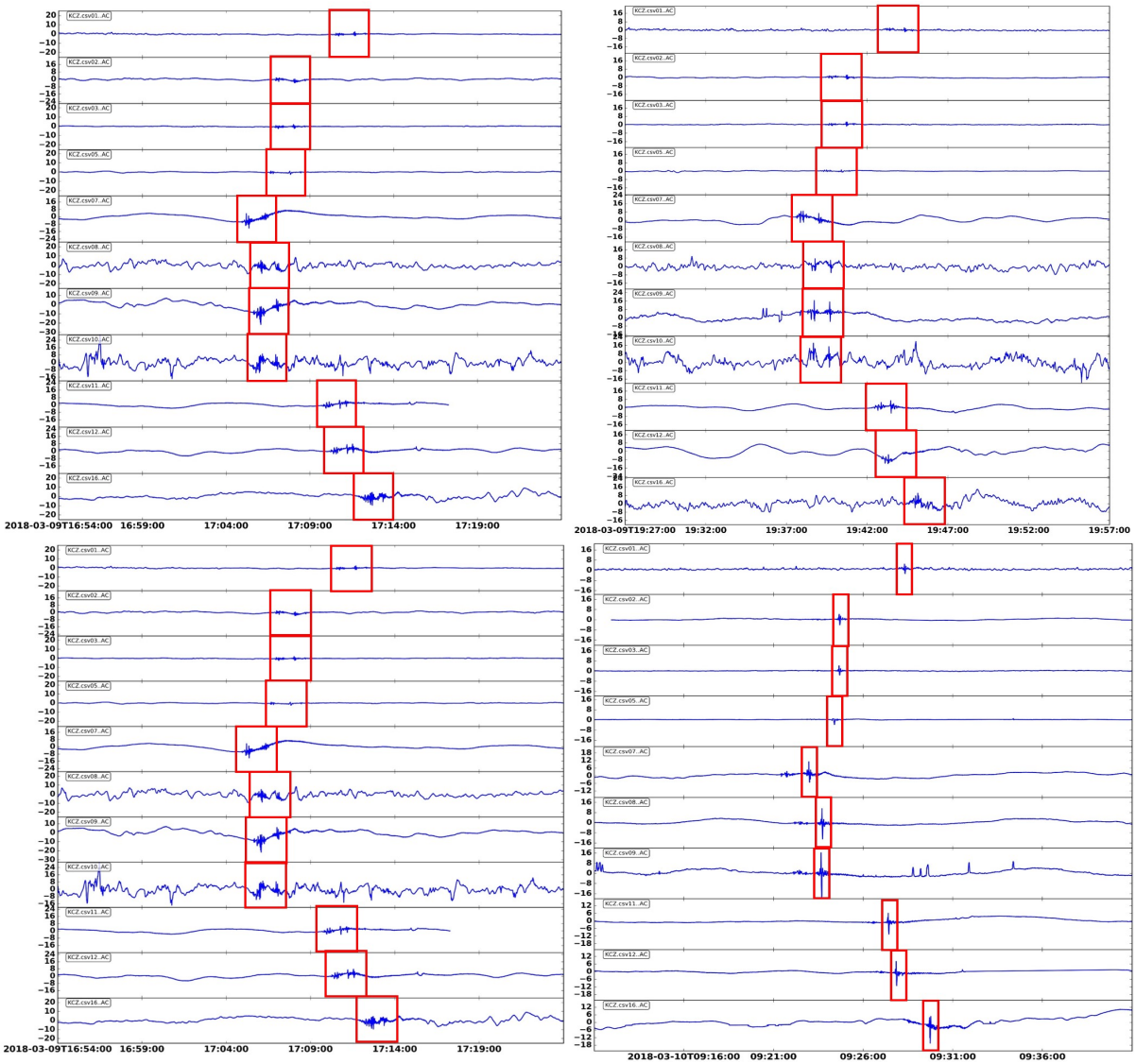

Figure 4.3: Records of infrasonic over-pressure data for March 10, 2018 (at 01:54 Japan standard time [JST; top-left], 04:27 JST [top-right], 10:15 JST [bottom-left], and 18:11 JST [bottom-right]), showing the arrival times of air pressure disturbances for stations on Shikoku Island following the Mt. Shinmoedake eruptions on March 10, 2018. The suspected arrival signals are located in the red square. The x-axis is the observation time in UTC, and the y-axis is the infrasonic over-pressure in Pa.

the separate overlapping time bins of the 1-h time series. The final PSD estimates for the 1-h data were then calculated as the 5^{th} and 95^{th} percentiles of the distribution of individual PSD curves. Plots of the PSDs for our entire period of interest were generated from all individual stations and used for analysis and data quality control.

Secondly, we determined output parameters from array signal processing, such as angle of arrival (azimuth), signal power, the apparent speed and correlation index. In this part, we tried

to implement an array radar observation technique called beam steering. The basic idea of our approach was to use the set of delays between signals to steer the array to different directions in a scanning region. When the steering direction coincided with a source, the maximum output power was observed. Figure 4.4 shows schematics that illustrate the processes undertaken in this step. In more detail , at the beginning, several constants and parameters are initialized beside the recorded files. Then, it comes into the main process that split in three sub processes as follows: (1) The 1^{st} sub-process is called "xyzgeomWINs" where four actions are executed firstly; (2) The process moves to the 2^{nd} part, named "xyzSTEERs" that generates a steering array based on the delays between observed signals; (3) The level of signal coherency between sensors was evaluated for all windowed data at every time shift increment. During this process, rotation scanning to a specific point, based on the calculated time lag between the multiple sensors and a cosine-tapered window function of a certain period length, with the time overlap as a data discontinuity reducer, was applied in the source detection scheme. The window length was chosen to be proportional to the envelope width of the recorded signals. This process continued until the end of the observation data time was reached and parameters such as the azimuth angle, signal strength, apparent velocity, and correlation index were obtained.

The processing schemes is designed for our infrasound sensor array system which is an irregular shape. The detection criteria of the source was evaluated by the coherence level which is larger than 0.8 as the detection threshold. In addition, at the beginning of the process, all raw recorded signals has the DC-component noise been removed by a DC-component elimination process explained in the chapter 1.2.1.

To estimate the atmospheric layer where the signal was deflected or refracted down toward the sensor on the Earth, infrasound wave propagation modeling was applied. The propagation modeling used in this study was an approximation of the planar parabolic equation (PE) method (Waxler et al. [2017]) with a ray tracing model as an addition of the method to draw propagation paths and estimate the arrival time in a three-dimensional inhomogeneous moving medium and the atmospheric background (Gossard and Hooke [1975]). This method is used to estimate the power loss of a wave transmission as a function of range and altitude. The simulation was run to examine a frequency of 1.25 Hz out to 500 km for the sequence of eruptions listed in Table 4.1.

The frequency range is chosen in order to eliminate the frequency of the interference signals such as microbarom signals at around 0.2 Hz and the other mountain-wave signals at around 0.7 Hz. The frequency of 1.25 Hz is the center of our band pass filter (1.0–1.5 Hz). This 1.25 Hz frequency is chosen to avoid the remaining harmonic of those interference signals. For the atmospheric absorption of sound, the method used the parameters from Sutherland and Bass [2004], which works well even in the upper atmosphere up to 160 km. The simulation also assumed a ground boundary condition as a perfect reflector (rigid plane and no topography).

For a typical source, as listed in Table 4.1, the sound level at the receiver position depends on the ground conditions, barriers, and meteorological conditions between the source and re-

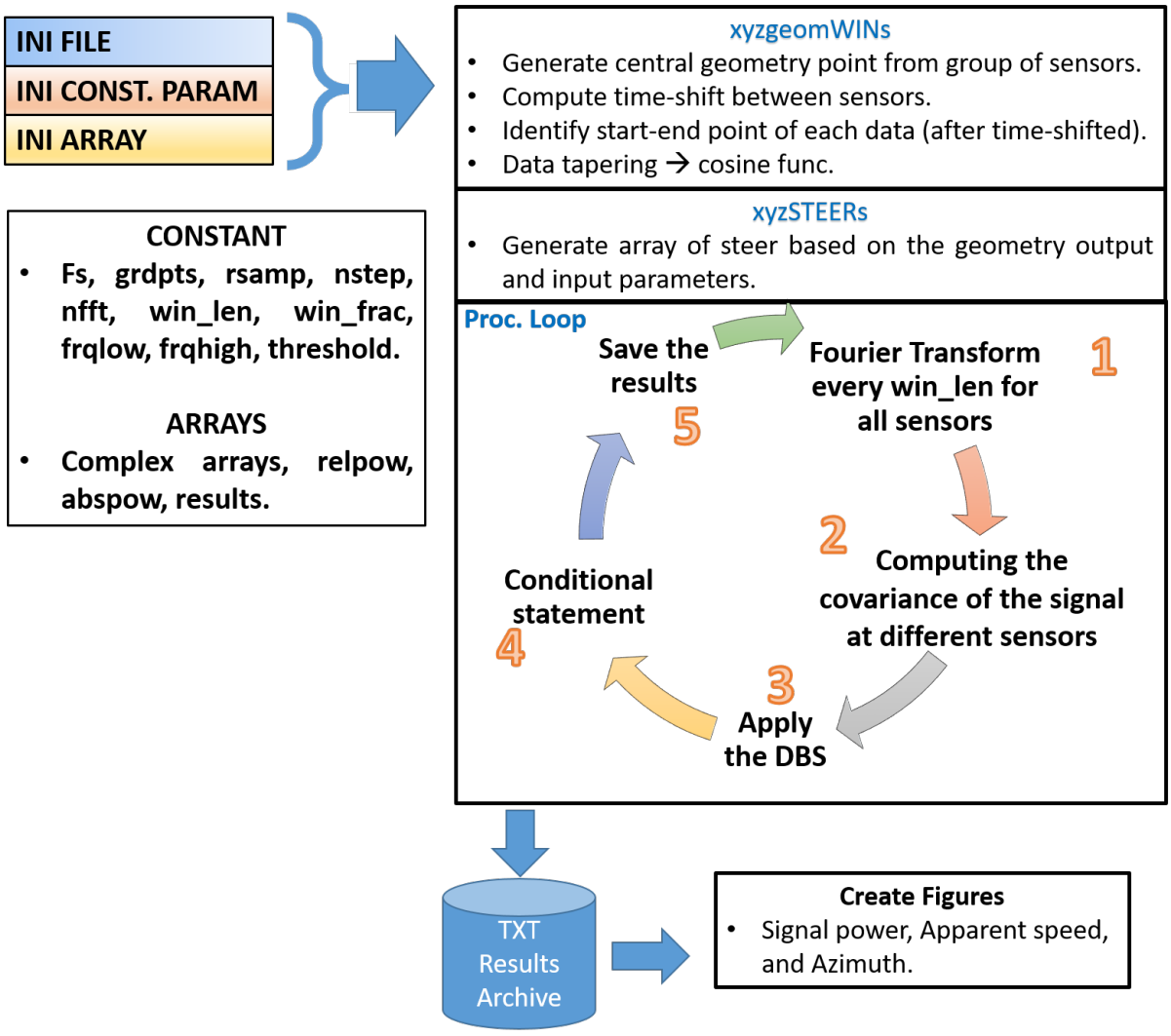

Figure 4.4: Schematic illustrating of the steps in our approach to determine the arrival direction and propagation speed of the incoming signal and the signal's source.

ceiver. In this study, we concentrated on wind effects for sound propagation and ray tracing simulations, assuming the ground surface is perfect reflector without any topography. Therefore, the deviations between the different calculations were caused by parameter variations in the atmospheric profiles. The most important atmospheric effect considered in the study was

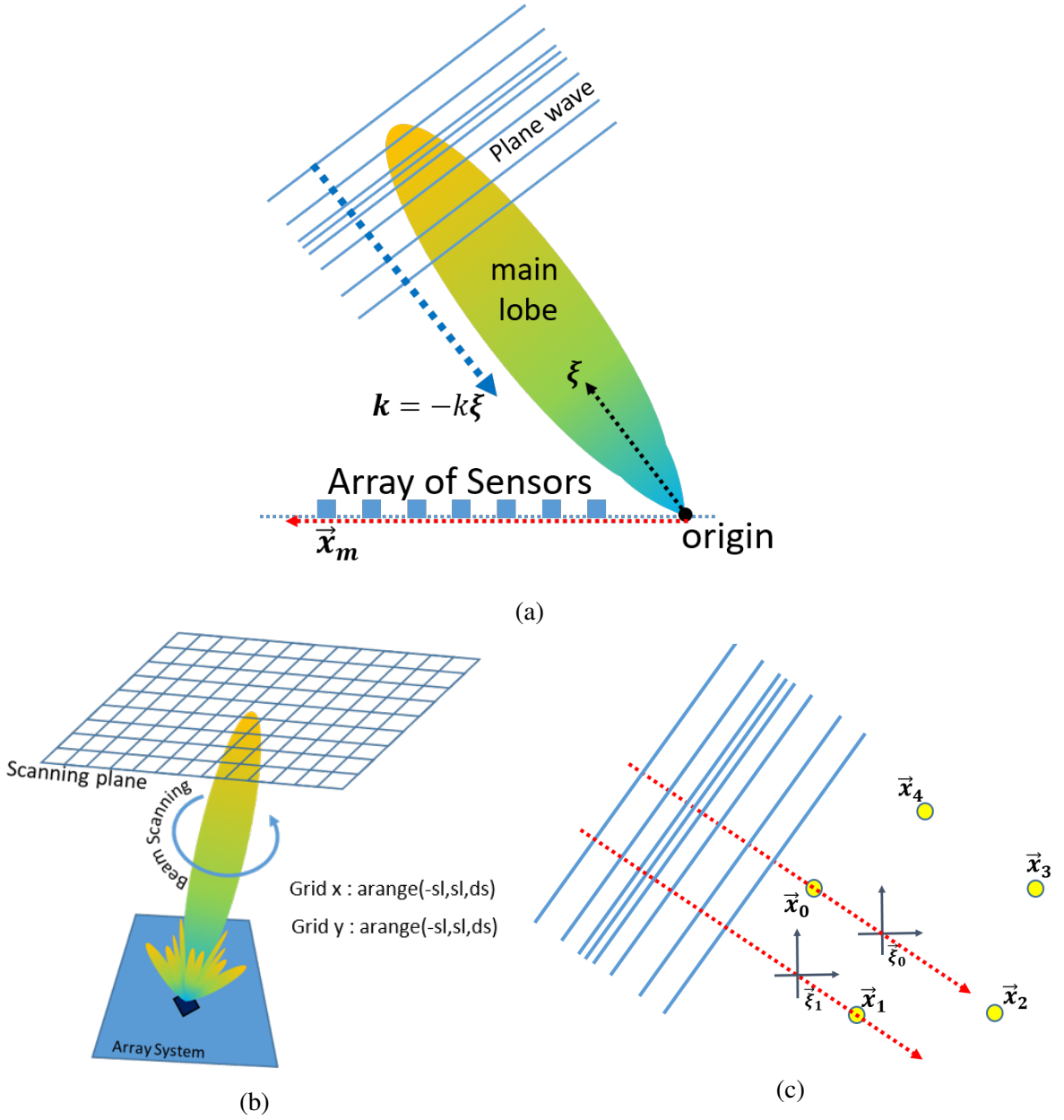

Figure 4.5: The illustration of the idea that is used in the study. (a) A plane wave incident from direction of the mainlobe. (b) The illustration for beam-steering, the radar beam rotate with a constant angle of steering. The beam direction is pointed to a certain direction and projected into a scanning plane. (c) The illustration for far-field propagation, the apparent direction of propagation does not vary with sensor location.

the refraction caused by wind and vertical atmospheric parameters obtained by the Modern-Era Retrospective analysis for Research and Applications, Version 2 (MERRA-2) and Naval Research Laboratory Mass Spectrometer and Incoherent Scatter Radar, Exosphere (NRLMSISE-00) global atmospheric models. For this study, the 3-h time-averaged horizontal wind, pressure, and temperature fields were accessed via the GMAO web service (Goddard Earth Sciences Data and Information Services Center) (Goddard Earth Sciences Data and Information Services Center (GES DISC) [2015]). The neutral atmospheric density is retrieved from the model provided by the Community Coordinated Modeling Center (Community Coordinated Modeling Center-NASA [2002]) in order to complement the atmospheric background conditions in the simulation.

Figure 4.5a show an illustration of beam steering technique in radar application. In this work, the pointing of beam directions are projected into a scanning plane (Figure 4.5b). As illustrated in Figure 4.5c, assuming a planar of m-th sensors at locations $\vec{x}_m$ in the *xy*-plane of our coordinates. The suspected signals which are received by m-th sensors arrived at different time (see Figure 4.3). The idea of our beam-scanning calculations is quite simple: if a propagating signal is present in an array's aperture, the sensor outputs are individually weighted and adjusted by each sensor's delay, and then all signals are added together, reinforcing the signal with respect to noise or waves propagating in different directions. The delays that reinforce the signal are directly related to the length of time it takes for the signal to propagate between sensors. The incident signals , traveling from the source point and an array of all m-th sensors located at $\{\vec{x}_m, m = 0, \cdots, M-1\}$. The array's phase center can be defined as the vector quantity $\sum \vec{x}_m$. For simplify, we choose the origin of our coordinate system to coincide with the phase center, $\sum_{m=0}^{M-1} \vec{x}_m = 0$. The waveform measured by the *m*-th sensor is

$$y_m(t) = f(\vec{x}_m, t)$$

The output of our beam-scanning is

$$z(t) \equiv \sum_{m=0}^{M-1} w_m y_m(t - \Delta_m)$$

where w_m and Δ_m are the amplitude weight and the sensor delay, applying to the output of each sensor. We use the cosine taper function as the amplitude weight to reduce discontinuity between signals. The delays are adjusted to focus the array's beam on signals propagating in a particular direction $\vec{\xi}_0 = -\vec{x}_0/|\vec{x}_0|$. Similarly, at the m-th sensor, the direction of propagation vector $\vec{\xi}_0$ equals $\vec{\xi}_{0,m} = (\vec{x}_m - \vec{x}_0)/r_{0,m}$, where $r_{0,m}$ is the distance between m-th sensor location and $\vec{x}_0$. In the applications, the origin of the source is undetermined whether the source is located in the near or far field. Thus, for far-field (plane wave) propagation, the vector $\vec{\xi}_0$ does not vary with sensor location, however, for near-field sources, the apparent direction of propagation varies across the array and is thus defined relative to the m-th sensor, $\vec{\xi}_{0,m}$. Our case assumes that a far-field source radiates a plane wave having signal s(t) propagates across our array of all m-th sensors in the direction $\vec{\xi}_0$ (Figure 4.5c). The waveform within the array's aperture is given by

$$f(\vec{x}, t) = s(t - \vec{\alpha}_0 \cdot \vec{x})$$

where $\vec{\alpha}_0 = \vec{\xi}_0/c$ is the slowness vector. At a particular sensor, the waveform is expressed by:

$$y_m(t) = s(t - \vec{\alpha}_0 \cdot \vec{x}_m)$$

the signal output of our beam-scanning becomes

$$z(t) = \sum_{m=0}^{M-1} w_m s(t - \Delta_m - \vec{\alpha}_0 \cdot \vec{x}_m)$$

The set of sensor delay is given by:

$$\Delta_m = -\vec{\alpha} \cdot \vec{x}_m = \frac{-\vec{\xi} \cdot \vec{x}_m}{c},$$

thus the output of beam-scanning signal $z(t)$ becomes

$$z(t) = \sum_{m=0}^{M-1} w_m s(t + (\vec{\alpha} - \vec{\alpha_0}) \cdot \vec{x}_m)$$

The output of the velocity vector can then be used to calculate the arrival angle of the target,

defined by:

$$tan^{-1}\left(\frac{\alpha_{0,Y}}{\alpha_{0,X}}\right)$$

as well as the apparent speed proportional to $\frac{1}{\vec{\alpha}_0}$, where $\alpha_{0,X}$ and $\alpha_{0,Y}$ are the slowness in the x and y axes, respectively.

For the purposes of computation, first we consider the input to a single sensor at the location $\vec{x}_m$ in terms of a phase shift rather than time delay as

$$y_m\left(t-\Delta_m\right) = y_m\left(t\right)\cdot e^{-i\omega\Delta_m}$$

where $y_m\left(t\right) = e^{-i\left(\omega t-\vec{k}\cdot\vec{x}_m\right)}$ and the term of $e^{-i\omega\Delta_m}$ represents the phase delay associated with the signal at the m-th sensor, called steering vector $\boldsymbol{e}$. The wavenumber vector $\vec{k} = [k_x, k_y]$ for 2D case is the propagation vector giving both the magnitude and is related to the Cartesian coordinates by:

$$k_x = k\sin\theta\cos\phi$$

$$k_y = k\sin\theta\sin\phi$$

where k denote the wavenumber equal to $2\pi/\lambda$ or $2\pi c/f$, and x-component of the wave vector, k_x, determines the rate of the phase change of the wave propagating in the x-direction. The beam-scanning output may again be expressed as

$$z\left(t\right) = \sum_{m=0}^{M-1} w_m\cdot y_m\left(t\right)\cdot e^{-i\omega\Delta_m}$$

Then, if the phase delay is included in the received signal vector $\mathbf{Y} = y_m\left(t\right)\cdot e^{-i\omega\Delta_m}$, the term $z(t)$ in vector notation becomes $\mathbf{z} = \boldsymbol{w}^H\mathbf{Y}$, where $\boldsymbol{w}$ is the weighting vector and H denotes the complex conjugate transpose. Assuming that the array has not been steered in a particular direction, the power of the output signal could be estimated by:

$$P\left(\mathbf{z}\right) = \sigma^2 = \mathbb{E}\left\{\left|\mathbf{z}\right|^2\right\} = \boldsymbol{w}^H\mathbb{R}\boldsymbol{w}$$

where $\mathbb{R} = \mathbb{E}\left\{\mathbf{Y}\mathbf{Y}^H\right\}$ is the correlation matrix of the incoming signal, $\mathbb{E}\left\{\right\}$ is the expectation operator, and σ is the variance of the received signal. However, we want to measure the output

power as a function of scanning angle or more precisely as a function of the steering vector. Therefore, $\mathbb{R}$ must also be a function of the steering vector, $\boldsymbol{e}$, that is

$$\mathbb{R}(\boldsymbol{e}) = \boldsymbol{e}^H \mathbb{R} \boldsymbol{e}$$

where $\boldsymbol{e}$ is the $M \times 1$ vector of phase delay associated with each individual sensor and it can be written as

$$\boldsymbol{e} = e^{j\vec{k}\cdot\vec{x}_m} = \begin{bmatrix} e^{j\vec{k}\cdot\vec{x}_0} \\ e^{j\vec{k}\cdot\vec{x}_1} \\ \vdots \\ e^{j\vec{k}\cdot\vec{x}_{M-1}} \end{bmatrix} = \begin{bmatrix} e^{j\frac{2\pi}{\lambda}(\sin\theta\cos\phi\cdot x_0 + \sin\theta\sin\phi\cdot y_0)} \\ e^{j\frac{2\pi}{\lambda}(\sin\theta\cos\phi\cdot x_1 + \sin\theta\sin\phi\cdot y_1)} \\ \vdots \\ e^{j\frac{2\pi}{\lambda}(\sin\theta\cos\phi\cdot x_{M-1} + \sin\theta\sin\phi\cdot y_{M-1})} \end{bmatrix}$$

where θ and ϕ are the elevation and the azimuth angles. Using the term of steering vector $\boldsymbol{e}$, the power of the array output may then be given by using the correlation matrix $\mathbb{R}$ and the steering vector $\boldsymbol{e}$ as

$$P(\boldsymbol{e}) = \boldsymbol{w}^H \mathbb{R}(\boldsymbol{e}) \boldsymbol{w} = \boldsymbol{w}^H (\boldsymbol{e}^H \mathbb{R} \boldsymbol{e}) \boldsymbol{w}$$

This term, for a homogeneous array sensor system where each sensor has equal weighting factor, the expression of the output power is simplified to $P(\boldsymbol{e}) = \boldsymbol{e}^H \mathbb{R} \boldsymbol{e}$. According to distortionless and minimize the noise power constraints (Ferguson [1998]), in order to minimize the contribution of the interference to the output $z(t)$ and to have the beam of our array been unity gain in the output, the weight vector $\boldsymbol{w}$ is the solution to the following optimization problem:

$$\begin{cases} \arg\min \boldsymbol{w}^H \mathbb{R} \boldsymbol{w} \\ w^H \boldsymbol{e} = 1 \end{cases}$$

The solution for the weight vector based on the above restriction is given by:

$$\mathbf{w} = \frac{\mathbb{R}^{-1}\boldsymbol{e}}{\boldsymbol{e}^H \mathbb{R}^{-1} \boldsymbol{e}}$$

and the output becomes

$$\mathbf{z} = \boldsymbol{w}^H \mathbf{Y} = \left(\frac{\mathbb{R}^{-1}\boldsymbol{e}}{\boldsymbol{e}^H \mathbb{R}^{-1}\boldsymbol{e}} \right)^H \mathbf{Y},$$

where

$$\mathbf{Y} = \begin{bmatrix} y_0(t) \cdot e^{j\vec{k}\cdot\vec{x}_0} \\ y_1(t) \cdot e^{j\vec{k}\cdot\vec{x}_1} \\ \vdots \\ y_{M-1}(t) \cdot e^{j\vec{k}\cdot\vec{x}_{M-1}}. \end{bmatrix}$$

Finally, we determine the upper wind speed from our infrasound records. In general, Sound propagation involves acoustic waves undergoing almost all physical processes, such as reflection from boundaries, reflection caused by temperature-and wind-gradients, diffraction resulting from boundary property changes, scattering caused by turbulence- and temperature-fluctuations as well as by particle of water droplet and snow, absorption, and etc. Certainly, all these processes actually make complexity and complication in analyzing sound propagation. However, in order to facilitate our study, these processes have to be dealt with separately and limited into a limited scope, which now mainly involves the problem of refraction and reflection in stratified layered of the atmosphere via the viewpoint of the ray simulation. In this study, we consider a global atmospheric model where each layer shows its own characteristics and therefore the sound rays are curved and undergo refraction by the use of a multi-layered atmosphere. In addition, according to the acoustics, sound waves do not usually experience an abrupt change in medium properties. Instead the speed of the wave varies gradually over a vertical distance. The speed of a sound wave in air depends on the local temperature. In an atmosphere without wind, sound waves travel with the adiabatic sound speed, which is a function of the temperature of the atmosphere. Our atmosphere, the Earth's atmosphere as an atmosphere with wind is commonly called a moving atmosphere. Therefore, the computation of sound wave propagation in a moving atmosphere is more complex than the computation of sound propagation in an atmosphere without wind. For simplification, a moving atmosphere can be approximated by an atmosphere without wind with an *effective sound speed* $c_{eff}(z) = c(z) + u(z)$, where $c(z)$ is the adiabatic sound speed and $u(z)$ is the horizontal component of the wind velocity in the direction of sound propagation, which are function of altitude. Spatial variations of the temper-

ature and the wind velocity in the atmosphere correspond to spatial variations of the effective sound speed. These variations cause atmospheric refraction. Often the change in the sound wave speed, and the resulting refraction, is due to a change in the local temperature of the air. In this study, we utilize the speed of the sound that varies continuously in the atmosphere to approach the wind speed at an upper refraction layer. As the ray becomes more horizontal at its apex, the trace velocity on surface approximately equals the effective sound speed along its propagation path at altitude there, $c_{eff}(z_{tr}) = \nu c(z_o)$, where $c_{eff}(z_{tr})$, $c(z_o)$, and ν are referred to as the effective sound speed at an upper altitude of the refraction, the trace velocity, and the constant factor, i.e. the initial launch angle and atmospheric properties. The trace velocity is the apparent horizontal velocity and is what is actually observed on the surface. Our sensor measures the trace velocity just at the ground surface, then the sound speed at the upper refraction level, named as turning height can be obtained. The sound speed at the turning height was the sum of the sound speeds as a function of the vertical temperature and the horizontal wind components in the direction of propagation. The calculated sound speed at the turning height was therefore $c_{eff}(z_{tr}) = c(z_{tr}) + w(z_{tr})$, where z_{tr} represents the turning height. The upper altitude of refraction was estimated by the procedure described in Donn and Rind [1971] and implemented in the acoustic ray tracing model (Waxler et al. [2017]), including the possibility of atmospheric wind, and three fundamental atmospheric profiles, retrieved from MERRA-2 and NRLMSISE-00 models for corresponding time periods above the source location. We employ a direct wind measurement from a regional radiosonde observation to be compared with the result of wind estimation.

4.4 Results and Discussion

4.4.1 Coherent ambient infrasonic noise across stations on Shikoku Island, Japan

Before proceeding to the next analyzing steps, which includes filtering process of the signals to reduce background noise and contributions from signals originating from sources that were not of current interests, we first applied our method to evaluate the amount of coherent ambient noise for an infrasonic source, using 6–12 hours of data at the same times of the eruption events described in section 4.2.

It should be noted that all installed sensors are surrounded by mountainous areas and some

of them are close to the ocean. Previous studies investigated mountain-associated infrasound waves by using small arrays of infrasound sensors (Wilson and Olson [2003], Wilson et al. [2009]). It was found that the orographically generated infrasonic waves were continuous,

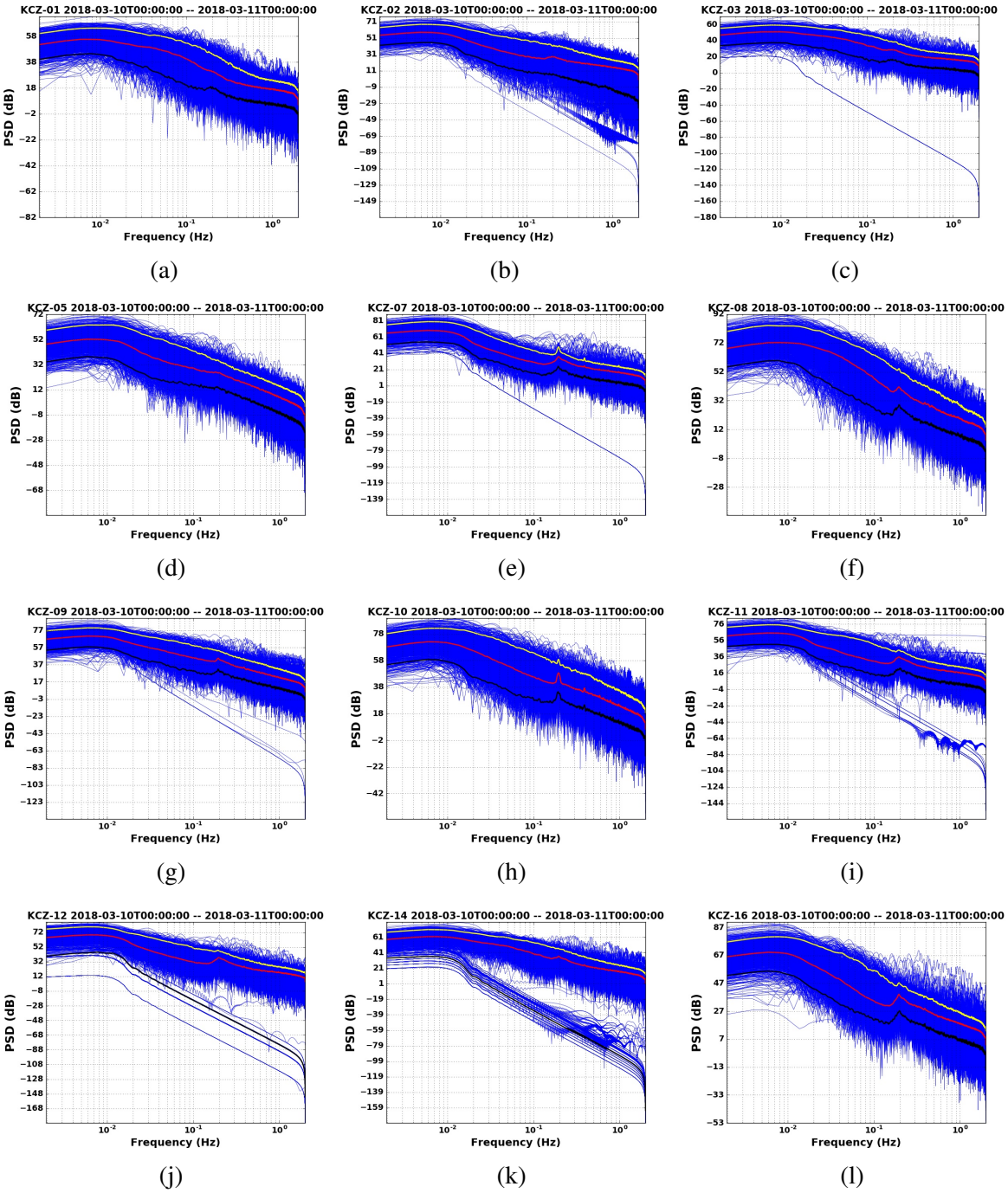

Figure 4.6: A set of power spectral density (PSD) plots for stations on Shikoku Island during a one-day period on March 10, 2018 (blue). The 5^{th} and 95^{th} percentiles (black and red), the median (white) for each plot. Each figure shows a PSD for individual station.

with a frequency range of 0.007–0.1 Hz and their amplitudes were usually fairly small, but occasionally exceeded 1 Pa. The airflow over mountain ranges can generate low-frequency infrasonic waves that can propagate over distances up to 10–20 km. There is strong evidence that a significant proportion of the events observed in this study were related to wave oscillations at the surface of the ocean (e.g., microbaroms and surf). These ubiquitous waves have a frequency range of 0.12–0.35 Hz for microbarom sources (Garcés et al. [2004]), and that of 1–20 Hz for sea surf (Garcés et al. [2003]). The microbaroms are also usually characterized by an energy peak between 0.2 and 0.3 Hz in the background infrasound noise and are known to interfere with the detection of explosive events (Evers and Haak [2001]) and long-range volcanic eruption signals (Matoza et al. [2011]). As is shown in Figure 4.6 as well as in Figures A.7-A.9 in the appendix A, the observations at all locations were dominated by these typical airflow signals. More comprehensively, Figure 4.6 shows an example set of PSD-noise plots for 12 stations on Shikoku Island during one-day period on March 10, 2018, from consecutive 3-minute data segments. PSD for selected stations draw in blue, the 5^{th} and 95^{th} percentiles are plotted in red and black, and the median in white. Three-minute windows and cosine-tapper are used to minimize smoothing of the amplitude distribution in the outer of each data window.

All plots of PSD were generated for all stations and used for data quality control and interpretation. Figures A.10-A.12 in the appendix A show a set of PSD plots for stations on Shikoku Island for three time periods (e.g., September, November, and December) when the volcano was not in the active phase. Based on all PSDs, the interpretations were as follows. (1) A bit slope spectrum appeared in the data during the time period of the volcanic eruption. This patterns are thought due to the existence of time gaps in the data (Figure 4.6b, 4.6c, 4.6e, 4.6g, 4.6i, 4.6j, and 4.6k). (2) At stations located on a small mountain slope, such as stations KUT05 (Figure 4.6d), KUT 01 (Figure 4.6a), and KUT02 (Figure 4.6b), mountainious winds mostly affected the characteristics of the recorded data as infrasonic pressure anomalies. This resulted in the spectral distribution, in the frequency range between 0.01 and 0.1 Hz, undergoing a wide expansion, which depressed the microbarom signals. We noted that the mountain-associated waves were predominantly recorded at the stations in mountainous regions. (3) Signals with a high intensity in the frequency of about 0.2 Hz, commonly called microbaroms, appeared

to dominate the recorded data from the stations located close to the ocean (e.g., KUT07 (Figure 4.6e), KUT08 (Figure 4.6f), KUT09 (Figure 4.6g), KUT10 (Figure 4.6h), KUT14 (Figure 4.6k), and KUT16 (Figure 4.6l)). (4) There were monthly seasonal changes in the cumulative signals recorded by each sensor. The total signal recorded during the winter period was more intense than in the opposite season (Donn and Rind [1971, 1972]). Through global atmosphere circulation, especially in the mid-latitude region, jet stream flows stronger during winter period than the opposite one. (5) Finally, as an addition to the PSD results described above, a comparison was made of the daily background noise among all individual stations. Their variations at infrasound stations were highly variable by season, time of day, and station. Station KUT07 was selected as a sample for the examination of daily PSD variations because it was more responsive to the changes in spectral variations of the received signals. As a result, similar to Bowman's study (Bowman et al. [2005]), we found no significant peak anomalies in the infrasonic noise spectra during noontime (Figure 4.7). Other similar profiles for other stations during the same time period are shown in Figures A.13-A.14 in the appendix A. The dominant frequency found in the PSD profile was then used as the basis for selecting filtered frequencies in our array processing scheme, described in section 4.3.

4.4.2 Infrasound propagation during the March, 2018, eruptions at Mt. Shinmoedake, Japan

Infrasound generated by explosive eruptions of the volcano was recorded by typical microphones at various distances from the crater. In general, the observed signals traveled across the infrasound stations at near-acoustic wave speeds, indicating that the infrasonic wave fronts propagated a great distance along the Earth's surface.

In combination with automated processing, the infrasound data provides a basis for more detailed propagation studies assessing wave characteristics. When the location of the source can be associated with a known infrasound source, confidence in estimations of the source localization and propagation speed from the events is high. To illustrate these properties, we focused on data from events described in section 4.2., where the origin time determined for each event is shown in Table 4.1. Each event generates multiple arrival times at different stations, where the times increase as a function of propagation distance (Figure 4.8). These

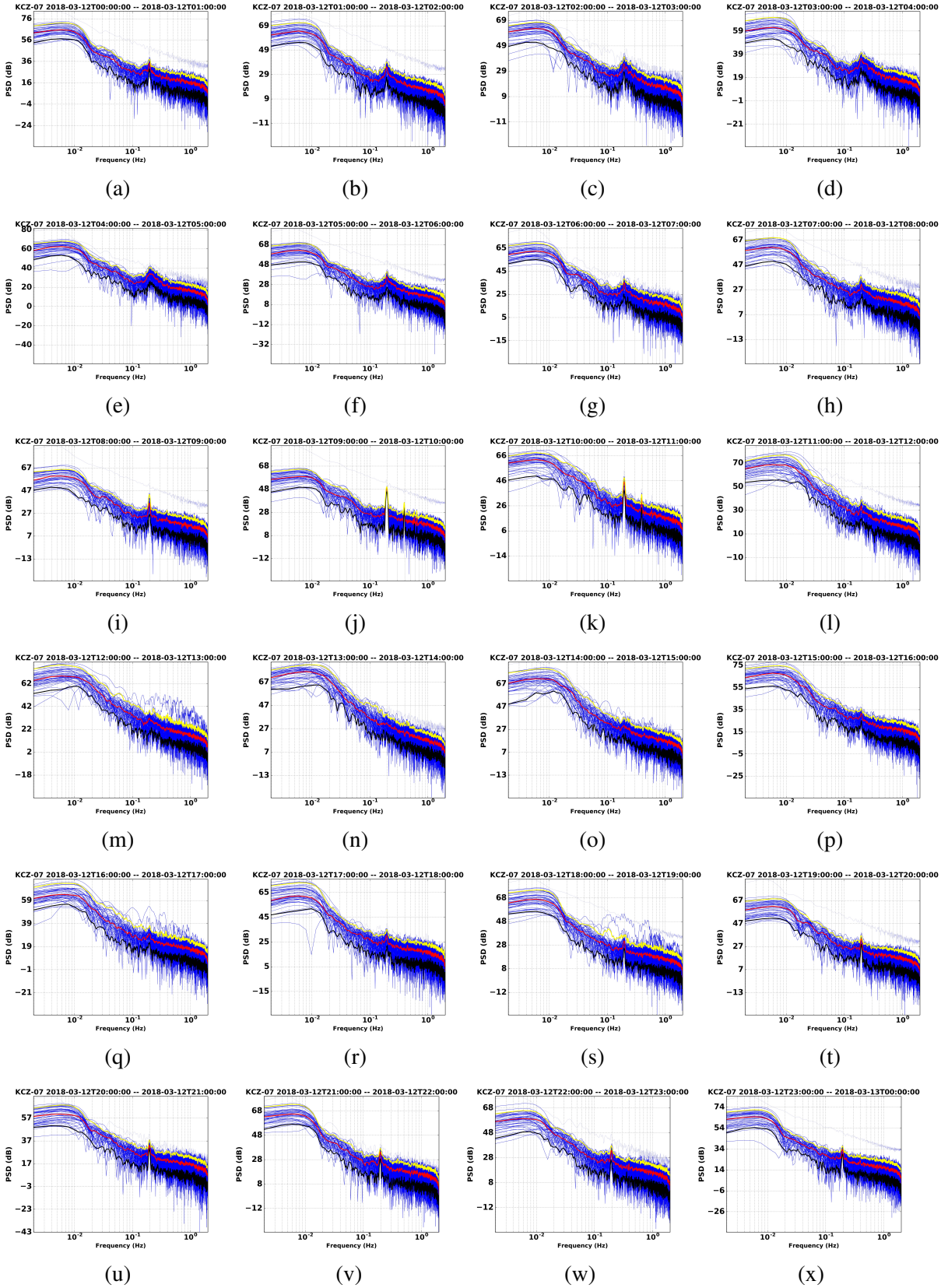

Figure 4.7: Power spectral density (PSD) for station KUT07 on 12 March 2018 (00:00 UTC-23:00 UTC) for all 1-hour time intervals (blue), the 5^{th} and 95^{th} percentiles (yellow and black), and the median (red) value for each time interval.

Table 4.2: Overall summary of the calculated propagation speeds of the detected signals. $t_{detection}$ is the starting time of the source signals at the closer station from the volcano. Δ t is the travel time of the wave between $t_{detection}$ at the closer and the farthest station.

No.	Event time (JST)	$t_{detection}$ (after event time, s)	Δt (s)	Estimated speed (m/s)
1	01:54 on March 10, 2018	657	413	334.18
2	04:27 on March 10, 2018	637	398	346.78
3	10:15 on March 10, 2018	683	419	329.40
4	11:18 on March 10, 2018	625	409	337.45
5	04:05 on March 11, 2018	659	406	339.95
6	12:45 on March 10, 2018	652	416	331.77

figures show typical records for the Mt. Shinmoedake eruptions during March, 2018, from stations across Shikoku Island, after bandpass filtering between 1.0 and 1.5 Hz, avoiding the interference signals from the sources described in Section 4.4.1 (based on Figure 4.3). Similar

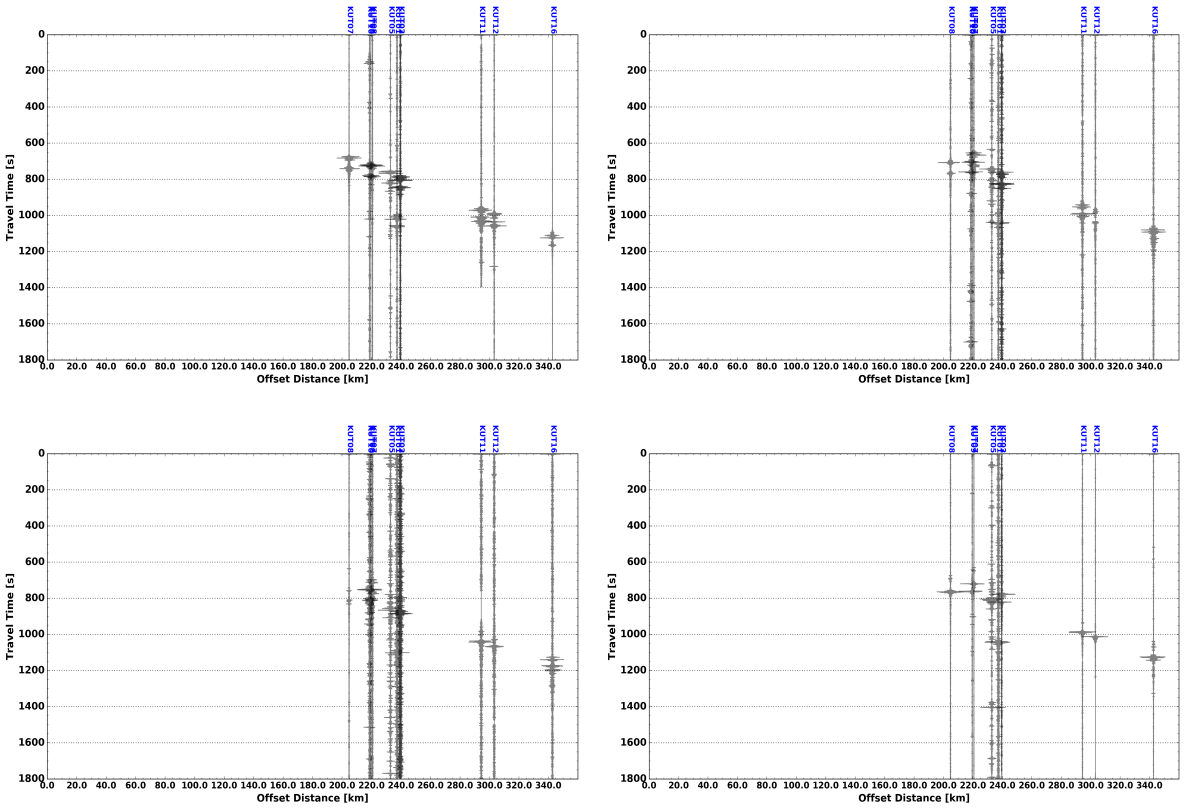

Figure 4.8: Records of the Mt. Shinmoedake eruptions on March 10, 2018 (at 01:54 JST [top-left], 04:27 JST [top-right], 10:15 JST [bottom-left], and 18:11 JST [bottom-right]) from the stations on Shikoku Island. The results are filtered in the frequency range 1.0–1.5 Hz based on the PDF plot shown in Figure 4.3.

plots for the events on 11 and 12 March, 2018, are shown in Figures A.15 and A.16 in the appendix A. Each figure clearly shows the propagation of the disturbance signature at ∼625 s after the explosion. To estimate the propagation speed of the incoming waves, an envelope of source waves was calculated based on the absolute amplitude of the infrasonic waves recorded at the infrasound stations. In general, four terms could be used to characterize such signals: the beginning, transition, middle, and end periods of the sound wave. The envelope of the signals has their own pattern. Thus the starting point of each suspected detection was chosen based on the pattern of the envelope slope and phase. Each estimated point corresponds to the position and time of a suspected detection. The gradient of the data for six samples, obtained using numerical linear regression, was used to estimate the propagation speed (see Table 4.2). The propagation speed of the detected signals from the sequence of explosive eruptions of Mt. Shinmoedake on March 2018 was estimated to be 336.6 $\pm$ 6.3 m/s.

Notably, this propagation speed (∼336 m/s) is the speed that the wave travel on the surface from the closest station, sensor number KUT07, to the farthest one, sensor number KUT16. In this case, the sound velocity is about 333 m/s. In a report of Campus (2006), they estimated a similarly low propagation speed (∼324 m/s) for the 2005 eruption of Lascar volcano in northern Chile, which was recorded by an IMS station is about 800 km from the crater (Campus [2006a]). For another event, the 2002 eruption of the Hekla Volcano in the Iceland, Liszka and Garces (2002) found that the infrasound propagation speed varied between 315 and 324 m/s. Meanwhile, a higher speed was also detected by an IMS station. The 2005 eruption of Mt. St. Helens generated low-frequency waves traveling at about 352 m/s (Campus [2006a]). The discrepancy between the two eruptions is understandable since the two types of disturbance occurred at different locations.

However, in general, infrasound in the atmosphere propagates at the sound speed of around 340 m/s near the surface of ground. It is also generally accepted that infrasound propagates at a velocity that typically varies with temperature and the fundamental properties of the propagation medium, as well as the wind velocity (Evers and Haak [2009]). From the above, the speed inferred from our analysis (∼336 m/s) is in the range of typical propagation speeds of infrasonic pressure disturbances from both natural and artificial explosion sources (e.g., chemical

and nuclear explosions) (Assink et al. [2018], Ceranna et al. [2009]).

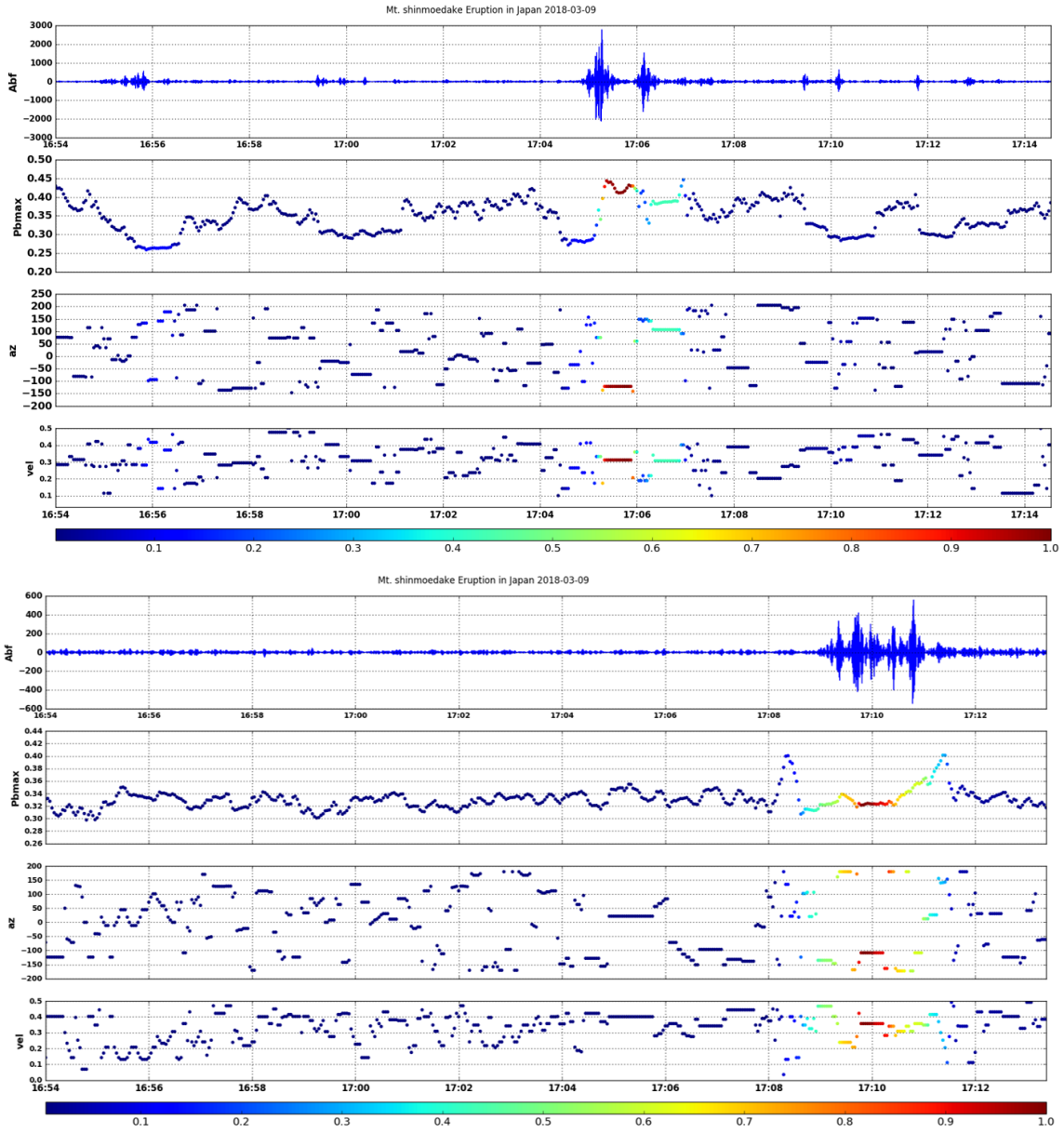

Figure 4.9: (Top panel) Array processing results for the event at 16:54 UTC on March 9, 2018 based on the data of the closest station (stations number: KUT07, KUT08, KUT09, and KUT10) to the source point. Clear arrival with both arrival direction and apparent velocity are presented in stable value. The detection period is colored by the coherent coefficient. (Bottom panel) Similar processing on the same period based on the second group of station data (stations number: KUT11, KUT12, and KUT16).

4.4.3 Infrasound source detection

After applying the spectral analysis technique to all infrasound data recorded several hours after the event, it was found that the dataset indicated a peak high spectral density value of around 0.2 Hz, which was the microbarom signal. To avoid this dominant microbarom signal, the frequency range was band-pass filtered with range of 1.0–1.5 Hz. This frequency range was then applied to the filtered data to detect signals in the second process described in section 4.3. Figure 4.9 shows the typical results of the detection process from our calculation, applied to selected station data in the period following the first Mt. Shinmoedake eruption at 16:54 UTC on March 9, 2018. The figure shows data from four stations located close to the volcano (top panel in Figure 4.9) and three stations located around 290 km from the source point (bottom panel in Figure 4.9). From top to bottom, the figure shows the stacked signals received after bandpass filtering, the maximum power at every processing step, the arrival direction as the azimuth angle, and the velocity along the waveform. The color scale indicates the correlation coefficient for the corresponding time window and is a measure of the statistical significance of the source detection. In the recorded data for the event at 16:54 UTC on March 9, 2018, all of the infrasound data detected by the sensors were propagated at constant speeds, but the estimated azimuths of the incoming signals differed slightly from the actual location of the volcano, which was likely due to the presence of winds and the surface height (i.e., hills), which can cause a signal's path to stray from the arc of a circle that connects the source to the sensors. A second example is shown in the bottom panel of Figure 4.9 where the recorded signals were taken from sensors located around 290 km from the infrasound source. In this figure, the signal amplitude is clearly lower amplitude than the result of the upper panel due to many factors, such as topographic absorption and atmospheric conditions. In addition, there was an indication of signals originating from the lower stratosphere within the stable velocity area seen in the velocity panel. A signal phase higher than the sound speed at the ground will be refracted back to the ground along a path where their effective sound speed is approximately equal to the apparent velocity. The apparent speed is calculated based on the sequence signals that is recorded by the sensors at stations located close to the source (top Figure 4.9), indicating the arrival signal as a refraction from the layer at about the troposphere. Meanwhile, the apparent

speed in the bottom of Figure 4.9, showing higher speed than the speed shown in the top Figure 4.9. Therefore, in Figure 4.9 bottom, the arrival wave is deducted as a result of refraction at the altitude higher than the troposphere (e.g stratosphere) due to the flow strength of jet stream on both layers. Generally, jet stream on the stratosphere has a speed higher than on the troposphere. In identifying signal phases and their propagation paths, the celerities or apparent speeds, and back azimuths can be used as a consistency check. The celerity or apparent speed of the arrival waves are defined as the ratio of the range to travel time for one or multiple bounces.

4.4.4 Infrasound ray-propagation

To make an infrasound source map, a wave propagation simulation was performed for a broad source area using the planar approximation parabolic equation (PE) method. The empirical atmospheric data from MERRA-2 and NRLMSISE-00 models were used to predict the power of transmission depending on elevation and distance. The resulting MERRA-2 atmospheric specifications provided global estimates of the winds, temperature, and pressure up to 76 km altitude at 3-hour intervals and were used in the wave propagation calculations. Taking account for atmospheric density, available lower and middle atmospheric data were typically provided by the NRLMSISE-00 empirical model.

Figure 4.10 shows the atmospheric background state above Mt. Shinmoedake at 16:30 UTC on March 9,2018. The left panel depicts the eastward and northward winds, denoted by blue and red lines, respectively. Fundamental atmospheric components are shown in the right panel. Long-range sound propagation is primarily determined by horizontal wind components and temperature gradients in terms of altitude, time, and geographic location. Sound is refracted downwards by positive temperature gradients ($\frac{dT}{dz} > 0$) as well as the sound speed at the refraction layer is larger than or equal to the sound speed at the ground, $c(z_{tr}) \geq c(0)$ in the windless condition. In the wind case, horizontal wind components such as positive wind shear may play an important role in the refraction process. As shown in Figure 4.10, in the troposphere, temperature decreased up to altitudes below 20 km but, interestingly, a positive temperature gradient occurred twice around altitudes of 10 km which is suitable for the sound refracted back to the ground. The layer above this, the stratosphere, was characterized by a strong positive tempera-

ture gradient that was predominantly due to the absorption of solar energy in the ozone layer. A smaller layer above it, the stratopause, had a local maximum vertical temperature at an altitude of around 40 to 50 km. In the mesosphere, the temperature decreased dramatically to the minimum state. In general, the zonal wind speed was higher than its meridional counterpart in two

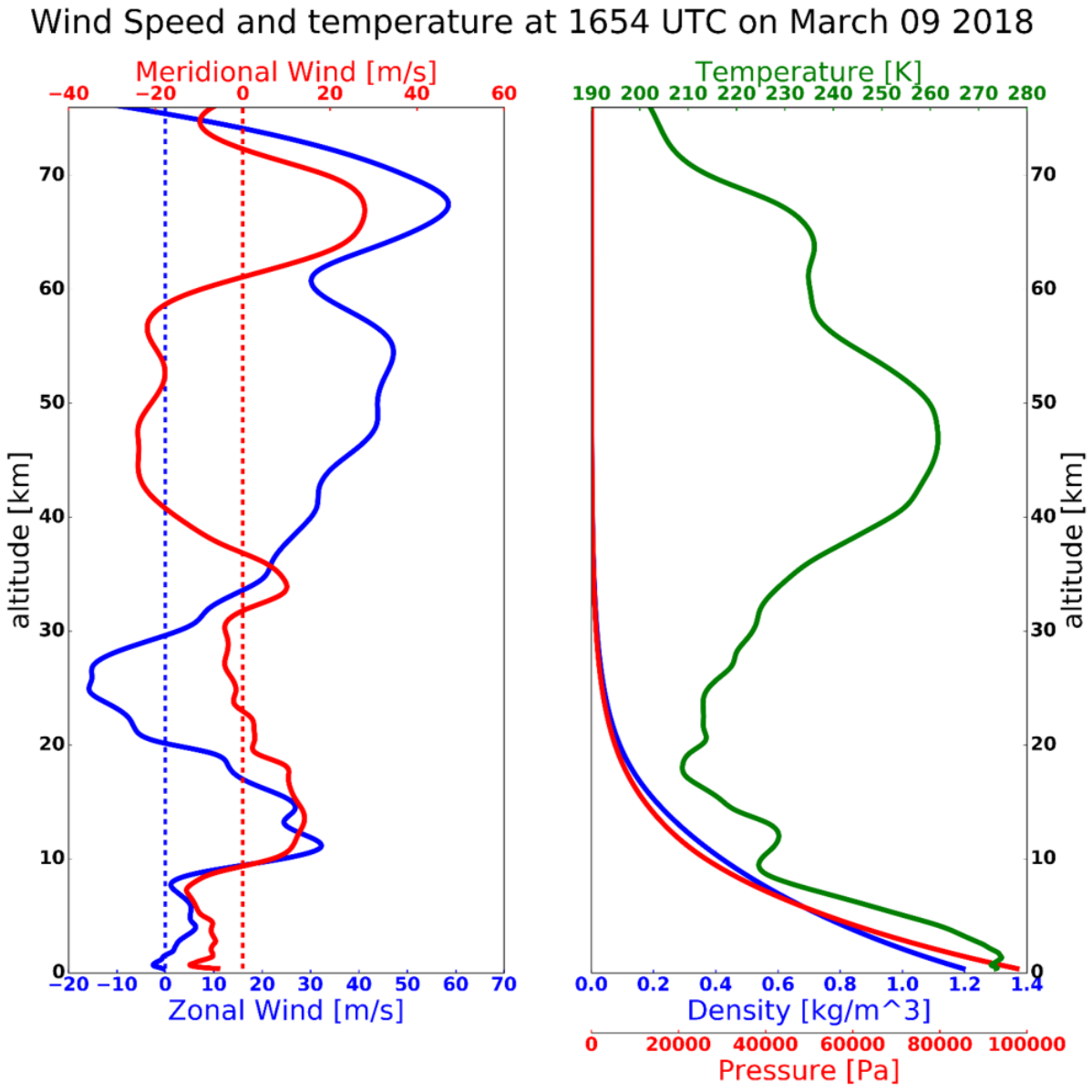

Figure 4.10: Modern-Era Retrospective analysis for Research and Applications, Version 2 (MERRA-2) and Naval Research Laboratory Mass Spectrometer and Incoherent Scatter Radar, Exosphere (NRLMSISE-00) atmospheric profiles at 16:30 UTC on March 9, 2018 above the source for use in the wave propagation calculation. (left panel) Eastward winds is shown as a blue line and northward wind as a red line. (right panel). Fundamental atmospheric parameters, temperature, density, and pressure shown in green, blue, and red lines, respectively.

regions i.e., the altitudes above 10–20 km as well as 30–60 km. The maximum value of these jet streams at altitudes near the stratopause and tropopause may have contributed to a ducting layer that refracted sound propagation in a downward direction. Furthermore, during the event, the winds were characterized by a moderately strong eastward zonal wind jet, peaking at ∼40 and ∼62 m/s at altitudes of 10, and 68 km, respectively. The meridional winds were greatest at an altitude of 10–20 and 65–70 km. Both the zonal and meridional components of the tropospheric winds had a positive direction, triggering a tropospheric jet to the northeast. For propagation to the north, the sound was predicted to be ducted in the stratosphere, beginning at an altitude of ∼60 km. The main features of the wind specification in the period at around 16:30 UTC on March 9, 2018 were a dominance of strong eastward and northward jet streams, peaking at ∼60 and ∼10 km for the stratospheric and tropospheric jets, respectively.

The effective sound speed profiles for propagation to the east predominantly reflected these two wind jets, with great tropospheric and stratospheric ducting predicted for the selected event beginning at altitude ∼10 and ∼60 km. In Figure 4.11, the along-path wind speed is represented by the difference between the adiabatic (blue line) and effective sound speed (red line) in all directions of wave propagation. It is clearly shown that the westerly wind has a significant impact by completing the formation of the tropo-stratopause sound duct. There was no sound ducting predicted for the west and south propagation, but there was significant tropo-stratospheric ducting for the north and east propagation. Additionally, in this case, the jet stream was large enough to have a qualitative impact on the effective sound speed profiles.

By incorporating the calculated horizontal wind components and vertical atmospheric parameters from the models (see Figure 4.10), upper altitude reflections of infrasound sources from the north to the east were obtained, as shown in Figure 4.11. According to the classical ray theory, strong arrivals (totally ducted) were refracted from altitudes for which the effective sound speed was larger than the adiabatic sound speed at the source level (purple shaded color). Figure 4.11 shows that, for northern propagation, the ducting layer was formed at altitudes above 60 km, although the effective speed of sound at the height of 10 km (see Figure 4.11) appeared to be greater than the adiabatic sound speed and was a possible candidate for the ducting process; however, the index of the sound speed ratio was not sufficient to form

a ducting layer due to the weak meridional component at this height. In the east and northeast propagation, shown in Figures 4.11 and 4.12, infrasound waves were refracted back to the ground by two different layers, at 40 and 10 km (for eastward propagation) and above 45 and 10 km (for northeast propagation). The eastward and northeastward propagations had three dominant sound speed ratios, which occurred at altitudes around 10 and 40 km. Both profiles had the same index ratio at an altitude of 10 km, however, at altitudes above 40 km, they began to show different behaviors in each direction of propagation. For the eastward direction shown in Figure 4.12, in addition to being deflected at an altitude of 10 km, the infrasound wave was guided back to the ground at an altitude of 40 km and less of the wave energy propagated to the higher altitude. This was presumably because the index of the two sound speed ratios at

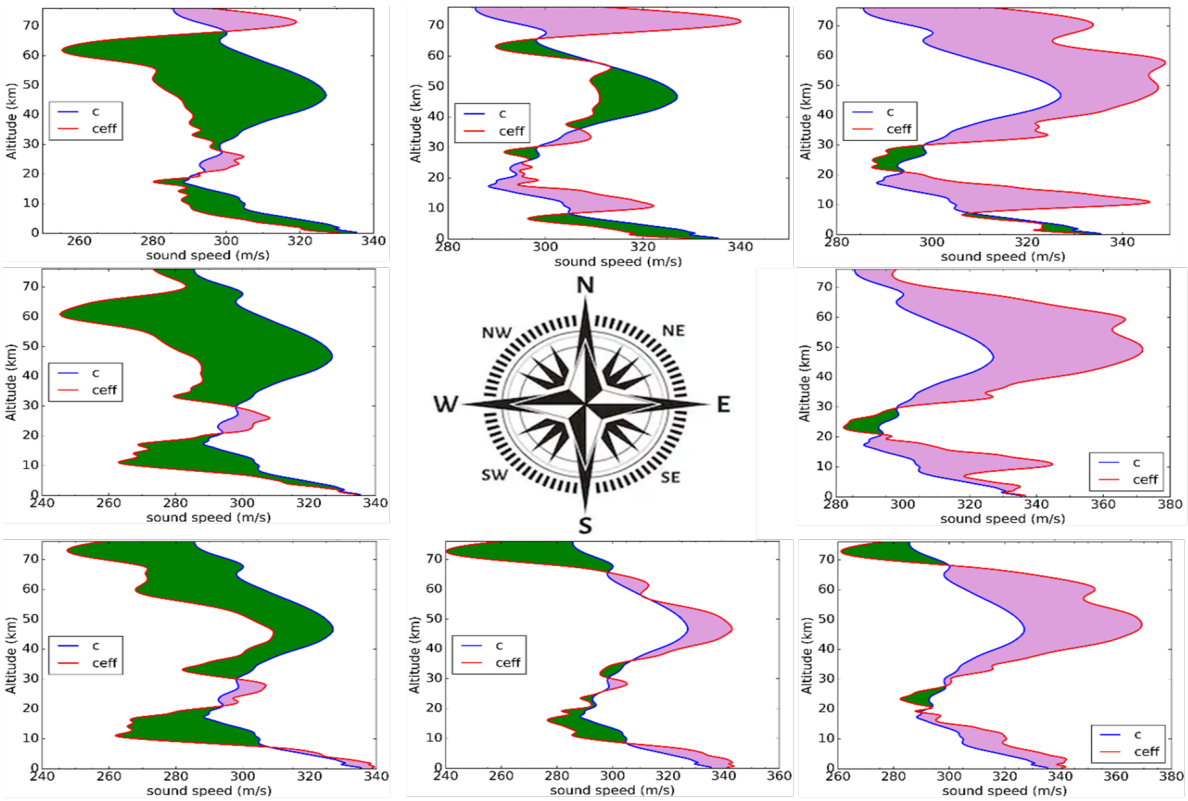

Figure 4.11: Effective sound speed comparisons for Modern-Era Retrospective analysis for Research and Applications, Version 2 (MERRA-2) and Naval Research Laboratory Mass Spectrometer and Incoherent Scatter Radar, Exosphere (NRLMSISE-00) model specifications above Mt. Shinmoedake for the event at 16:30 UTC on March 9, 2018. Purple shading represents the condition when $c_{eff}(z) \geq c(z)$, where $c_{eff}(z)$ denote the effective sound speed as a functions of height z, $c_{eff}(z) = c(z) + u(z)$. The adiabatic sound speed and the horizontal component of the wind velocity are respectively denoted by $c(z)$ and $u(z)$.

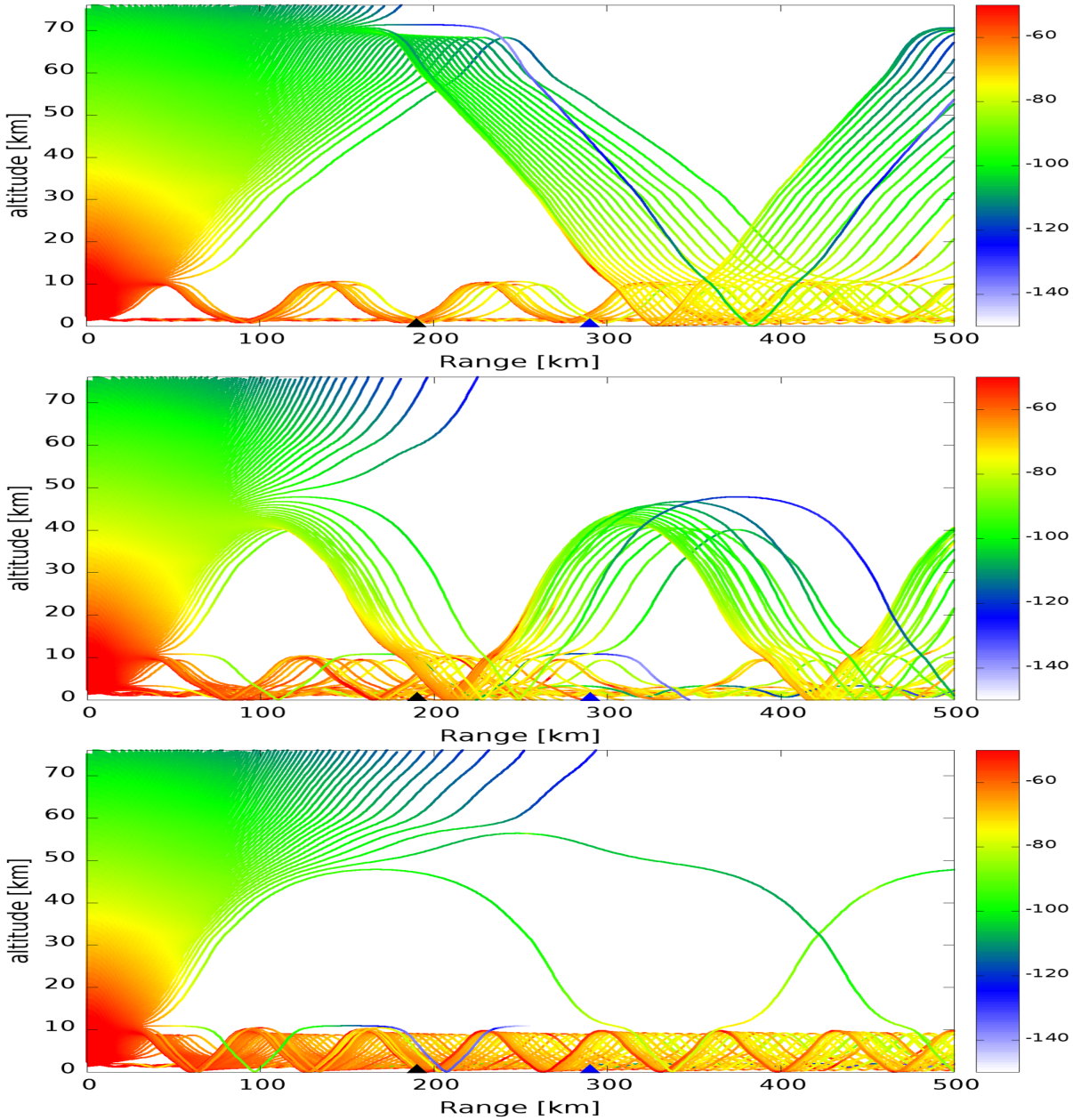

Figure 4.12: Ray tracing plot for the power transmission from Mt. Shinmoedake at 0 km at the left edge of the plot out to 500 km. The plot was constructed using atmospheric data for the event at 16:30 UTC on March 9, 2018. The top, middle, and bottom figures show the results for the northward, eastward, and northeastward propagation directions, respectively. The color plot represents the sound wave power transmission in dB per km of propagation of the infrasonic wave at a frequency of 1.25 Hz.

an altitude of 40 km in the profile of eastward propagation was significant enough to produce a ducting layer that could guide the wave back to the ground. Infrasound wave energy could possibly have a bias for the upper layer when the index of the two sound speed ratios at a lower altitude was not sufficient to trigger the ducting process, as seen in the eastward and north-

eastward propagation profiles and clearly in the relationship shown in Figure 4.11 for similar propagation directions.

The wind jet streams that flowed eastward during the event were significantly larger than those that flowed in the opposite direction. The jet stream produced large tropospheric channels to the east and northeast directions at an altitude of about 10 km, and in the stratosphere at an altitude of 40–60 km. At the stations used in this study, which were almost located northeastward of the source location, some tropospheric and stratospheric arrivals were recorded. Based on Figures 4.8 and A.12-A.13 in the appendix A, two examples of station groups were selected, with the results shown in Figure 4.9. The first and second groups of stations were each about 190 and 290 km from the source location (marked by the black and blue triangles in Figure 4.12). In addition, at our selected stations, which were located at a distance of about 190 km northeast from the source, only the arrival of the tropospheric north-east propagation was estimated throughout the day, mainly due to the strong wind jet flow around the troposphere and a negative inversion in the boundary layer, with a positive temperature gradient. For the second station group (marked by blue triangles), the two northeast propagation arrivals from the troposphere and stratosphere were estimated throughout the day, because of the presence of the two jet streams in those layers.

In the case of the Mt. Shinmoedake explosion on March 10, 2018, the range-dependent power transmission reception of the selected frequency of 1.25 Hz as a function of azimuth and range out to 500 km was also estimated and is shown in Figure 4.13. The rays intersecting an area of radius $\sim$500 km, centered on the source point (marked by the red triangle), were selected to construct a power transmission map. The color code shows the intensity of the power strength at the arrival of the infrasound for each area of the grid. This figure shows the effect of the wind jet corresponding to the background condition of the vertical atmosphere above the source, with the blue colors indicating higher observed amplitudes. As expected, waves propagated over a large area to the northeast of the volcanic region as a potential infrasound source and, thus, a large possible source area was defined. At the time of the eruption, the strong zonal wind blowing toward the northeast would limit the detection of sources west of the volcano. The intensity of the partial strength (blue) repeated itself in concentric bands,

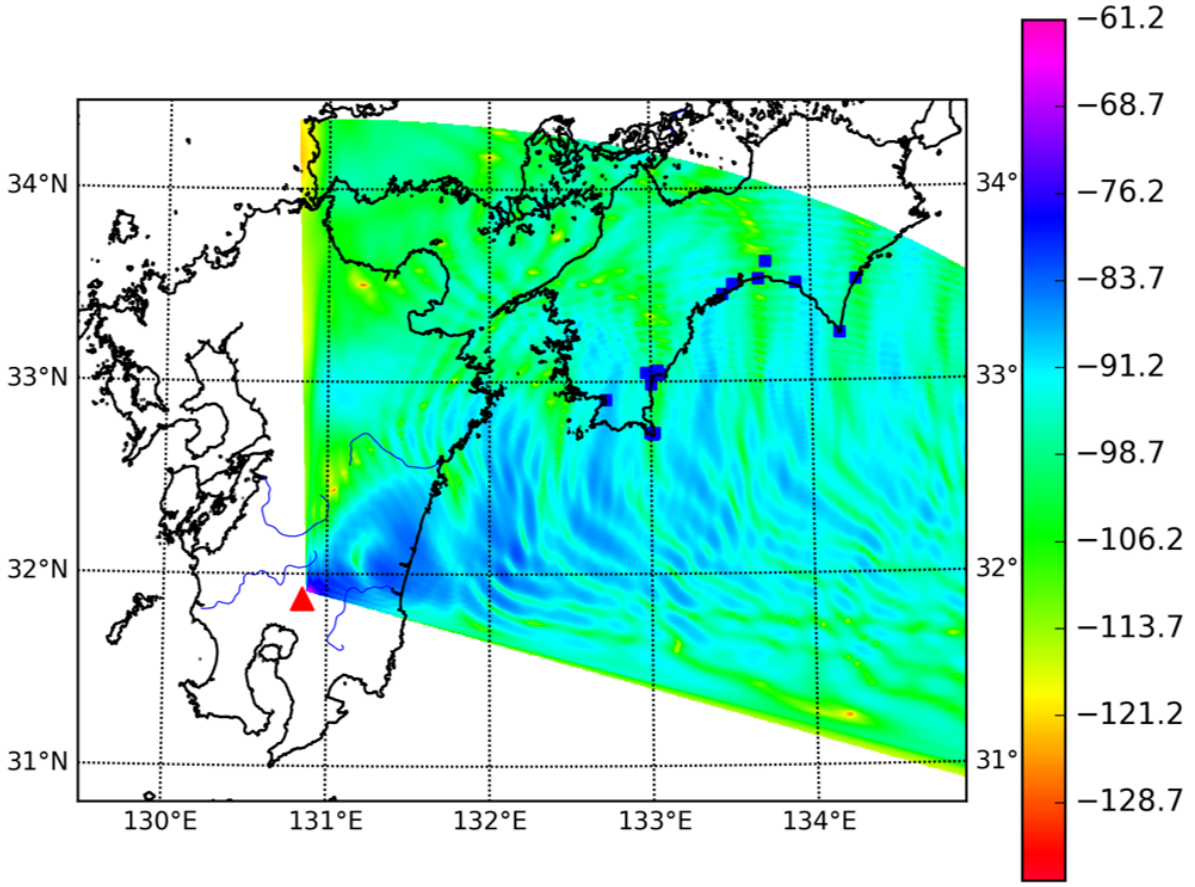

Figure 4.13: Sound wave power maps in dB for the event at 16:30 UTC on March 9, 2018, from the 1.25 Hz propagation modeling. The red triangle is the Mt. Shinmoedake volcano. The color plot represents the sound wave power loss in dB, where the blue is a larger loss than the green.

resulting from some dominant deflection to the ground. Fortunately, several infrasonic stations detected some signatures of signals from volcanic eruptions, with two phases arriving from the stratosphere and troposphere. The arrival of tropospheric infrasonic waves dominated the signal reception in the first station group, while the stratospheric arrivals were received at the second station group. In addition, the attenuation was very high, with a high absorption power estimated to the south and west after ∼300 km from the source point. In other situations, although the northeast propagation generally dominated, a small number of our sensors in the eastern part of Shikoku Island detected the event.

The various phases of an infrasonic arrival observed by sensors on ground can be determined by the type of propagation path. The paths are predominantly through the tropospheric, stratospheric, and thermospheric waveguides, and depend on their travel times. A wave quan-

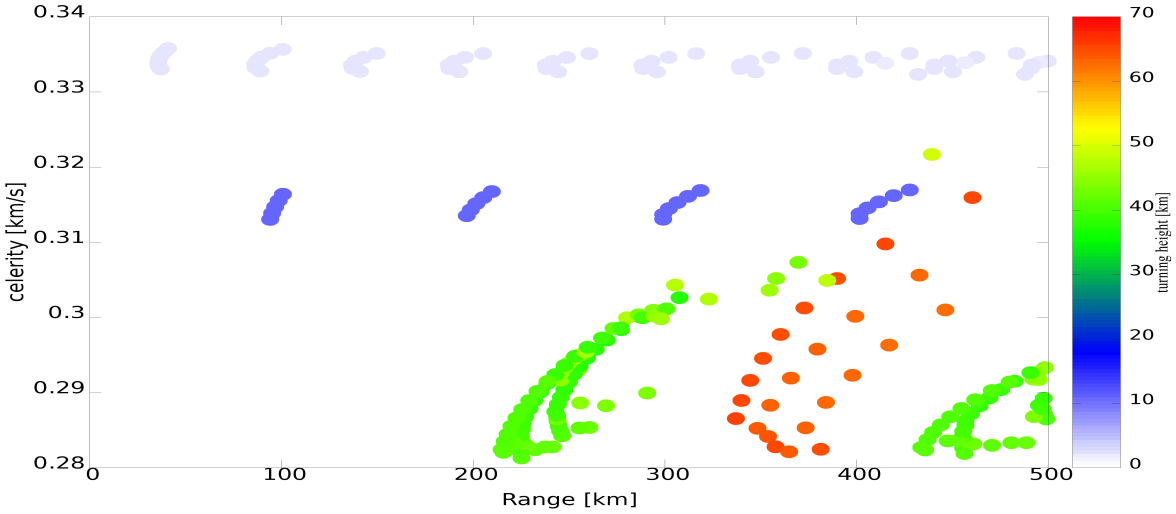

Figure 4.14: Celerity-range diagram for the event at 16:54 UTC on March 9, 2018. The colored dots represent tropospheric and stratospheric ductings according to the turning height. Each dot represents the celerity value on every reflection on the ground surface.

tity called celerity can be used to infer the properties of the signal phase. The celerity or the apparent speed of the arrival waves is defined as the ratio of the range to travel time for one or several multipath bounces and is a measure of the horizontal propagation speed and the path length. Consequently, the closer the propagation path to the horizontal vector, the closer the propagation speed is to the speed of sound on ground. Signals that travel along the troposphere obviously arrive first, with celerities close to the speed of sound at the ground level. Hence, by measuring the trace velocity at the ground surface, we could estimate the sound speed at the altitude of reflection. The predicted reflection altitude as a function of range and celerity was determined to infer the signal phase properties and propagation paths. For this, we presented a typical example of the analysis of data from the Mt. Shinmoedake eruption period at around 16:54 UTC on March 9, 2018, which enabled a detailed study of sound propagation over time. From classical ray theory, we inferred that the waveguide would be fully channeled if the effective sound velocity at a certain height was relatively large against the sound speed at the ground level. The results were shown as the turning height, with the function of celerity and range shown in Figure 4.14. Typically, three types of arrival were estimated. The first type of arrivals, were called boundary arrivals and were turned back at a height around $\sim$2 km, with a

celerity range of between 0.33 and 0.34 km/s. The second type turned back at altitudes around 10–20 km, with an estimated celerity around 0.31 km/s. Along the stratospheric path, there were two turning heights (at the altitude of 30–40 km and 60–70 km). It was clearly shown that the presence of a strong horizontal wind flow at a certain altitude could alter the length of time required to travel through their paths. This effect is shown as a slope pattern in each turning height and the difference in the distance between the bouncing groups at each turning height where the distance between the reflection groups at low altitudes is denser compared to the above altitudes (in Figure 4.14).

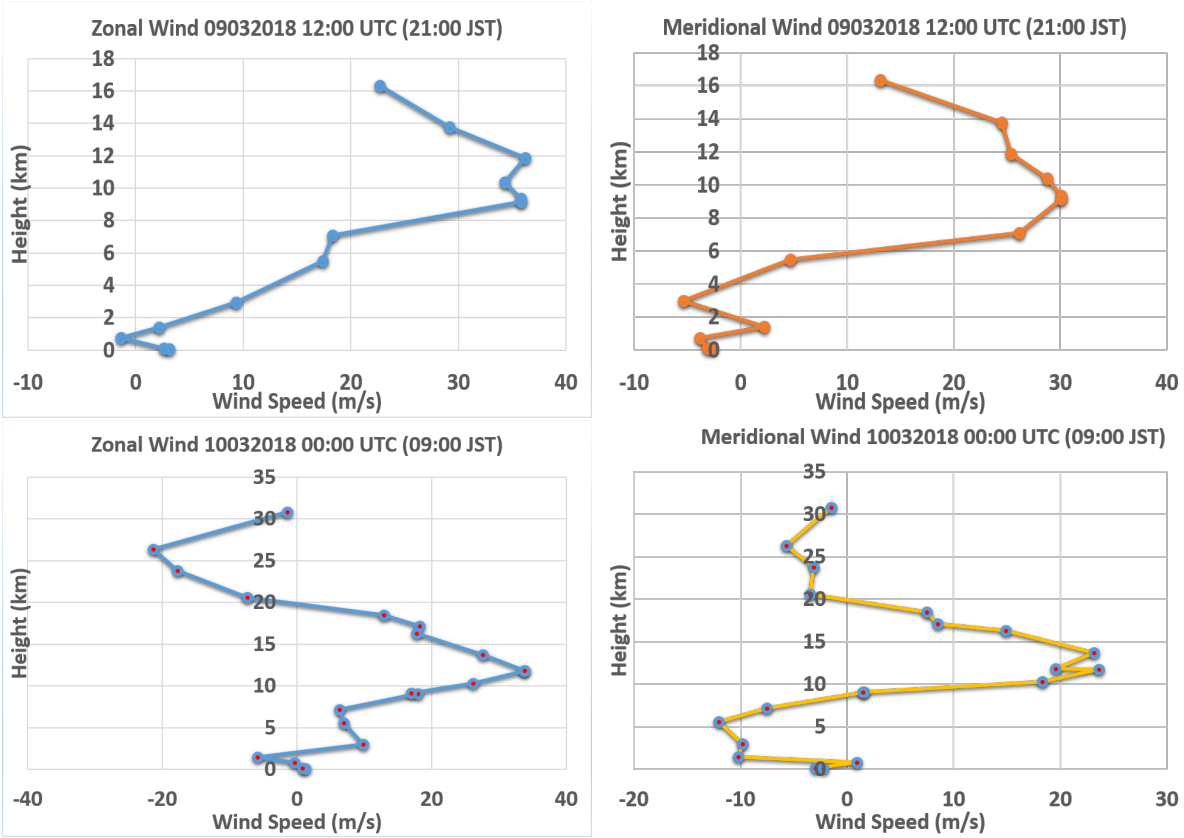

Figure 4.15: A typical result from radiosonde observation above Shionomisaki station, Japan (33.45^o N, 135.77^o E) at 12:00 UTC on March 9, 2018 (the first row panel) and 00:00 UTC on March 10, 2018 (the second row panel). The zonal and the meridional winds are respectively drawn in blue and yellow line.

4.4.5 Comparison of wind speed

As described in the methodology, section 4.3, the atmosphere is a type of stratified-ceaseless motion medium which is not only the parameters that represent their properties (e.g. temper-

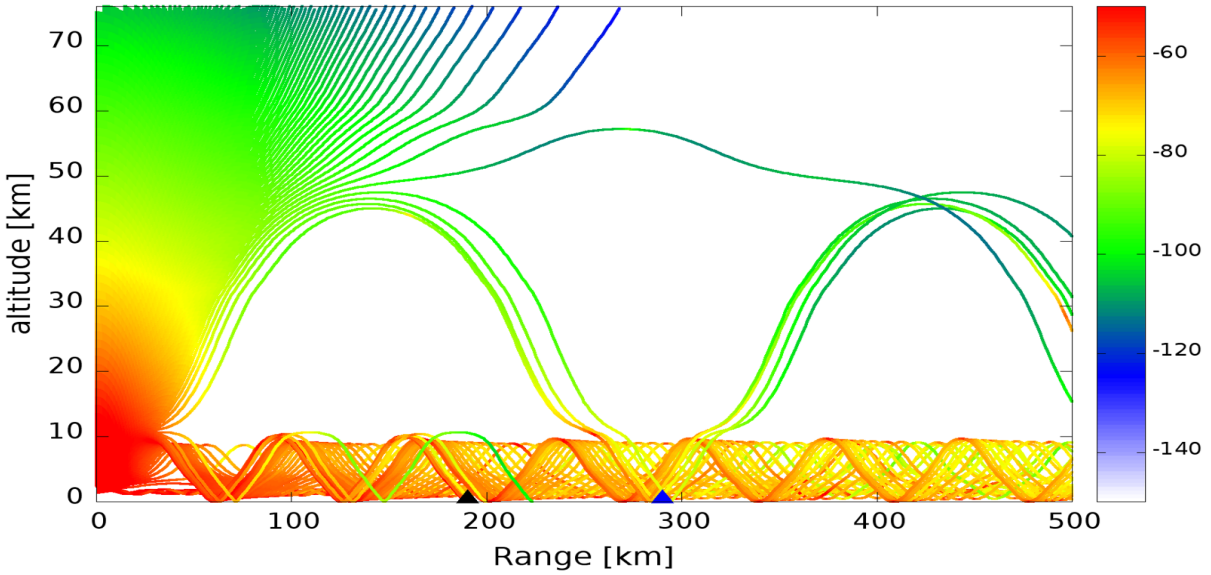

(a)

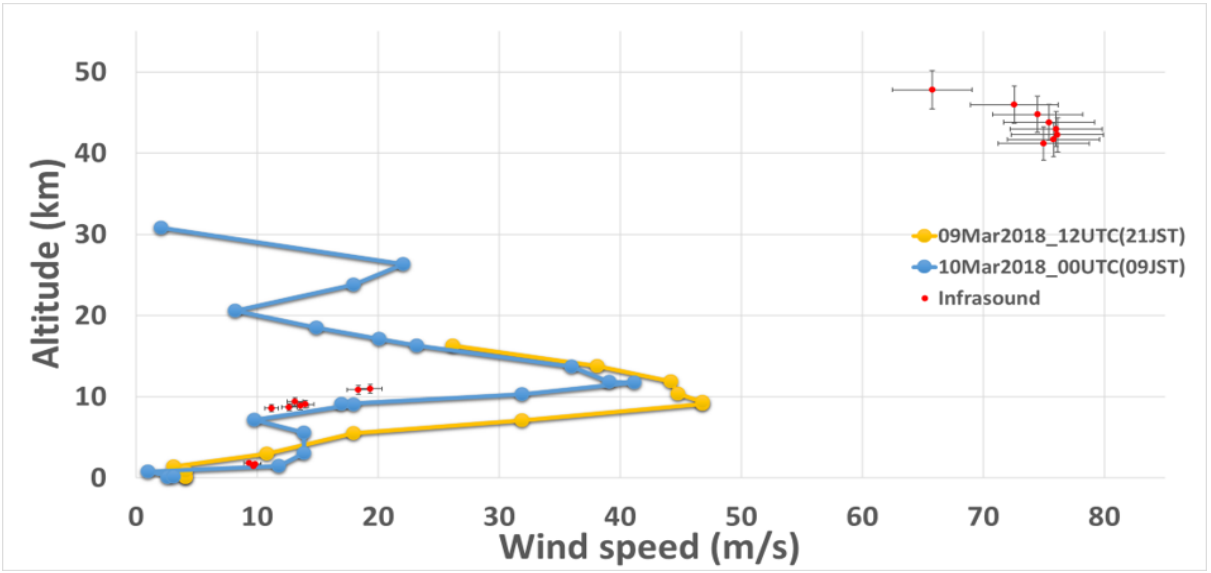

(b)

Figure 4.16: Typical results for the event at 16:54 UTC on March 9, 2018. (a) Typical ray-tracing results for a real azimuth propagation from the source to the sensor array. (b) Wind velocity obtained by calculation (black star) and radiosonde observations (blue, and gold circles for 12:00 UTC on March 9, 2018, and for 00:00 UTC on March 10, 2018). The colored plot represents sound wave power transmission in dB per kilometer of propagation of the infrasonic wave at a frequency of 1.25 Hz.

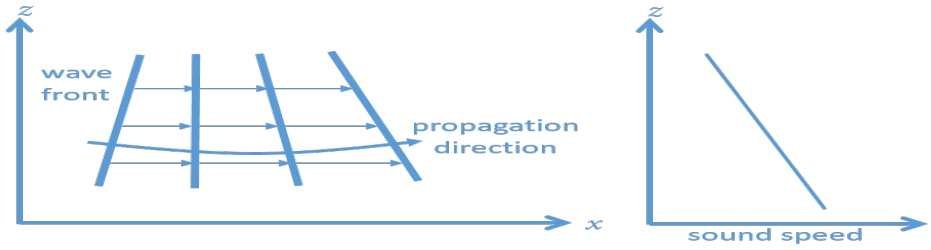

(a)

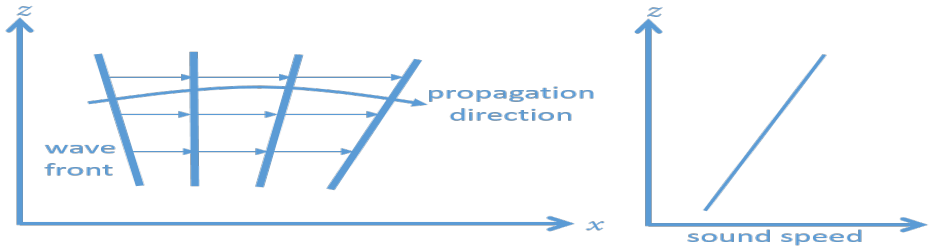

(b)

Figure 4.17: The illustration of atmospheric refraction. (a) Illustration of upward refraction of sound. (b) Illustration of downward refraction of sound. The wavefront moves to the right at four successive times. The bent curve shows the propagation direction, defined as the vector normal direction to the wavefront at each point.

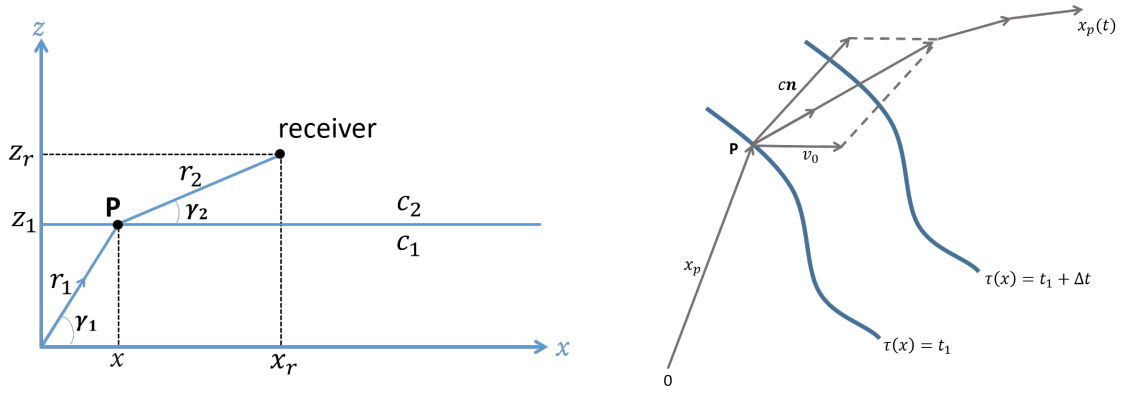

(a) (b)

Figure 4.18: Illustration of sound ray refraction from a point source to a receiver in the atmosphere. The source, point P, and the receiver are respectively at coordinate $(0, 0)$, (x, z_1), and (x_r, z_r).

ature and density), but also the parameters that represent their movement described as wind speed. Therefore, sound waves are refracted and reflected at the interfaces between layers, just at interfaces between different media. The reflection is so small that it can be neglected, whereas, the refraction happens gradually and continuously. This atmospheric refraction when

sound waves are bent toward regions where the sound speed is low. This is illustrated in Figure 4.17, which shows two examples of a moving wave front. Spatial variations of both of sound speed and wind speed gradient in the atmosphere contribute to the change of propagation direction of sound waves. For a sound refraction caused by sound speed gradient, assuming that wind speed is neglected ($v_{wind} = 0$), and a sound speed c that is varies with temperature, the sound rays will bend toward the direction where the sound speed is smaller and deviate away from the propagation direction. This is illustrated in Figure 4.18a, a wavefront moves at speed c at a fixed coordinate system and shows the illustration for an atmosphere where the sound speed c is a function of altitude z:

$$c(z) = \begin{cases} c_1 & \text{for } z \leq z_1 \\ c_2 & \text{for } z > z_1, \end{cases}$$

where z_1 is the height and c_1, c_2 are constants. The sound ray consists of two segments, with a discontinuous slope at $z = z_1$. We have $\gamma_2 > \gamma_1$, corresponding to $c_1 > c_2$, thus downward refraction is formed in this case.

In the case of the propagation medium moves at a speed v, thus sound is refracted by wind speed gradients (Figure 4.18b). The direction of the rays differs slightly from the direction of $\boldsymbol{n}$. The speed of wave $c\boldsymbol{n}$ will be transformed into v+$c\boldsymbol{n}$ where $\boldsymbol{n}$ is the normal unit vector of the wavefront. In homogeneous medium where the coordinate system moves at the same speed as the speed of medium, thus the propagation direction $\boldsymbol{n}$ are the same. The point $\boldsymbol{x}_p(t)$ is moving at every time change with the speed is given by:

$$d_t \boldsymbol{x}_p = v(\boldsymbol{x}_p, t) + \boldsymbol{n}(\boldsymbol{x}_p, t) c(\boldsymbol{x}_p, t) \equiv v_{ray},$$

in which the ray's trajectory $\boldsymbol{x}_p$ variate over time t in space and d_t express the differential equation regarding the rate of change in time. The speed of the wave front in the normal direction is defined by the dot product of $v(\boldsymbol{x}_p, t) + \boldsymbol{n}(\boldsymbol{x}_p, t) c(\boldsymbol{x}_p, t)$ and $\boldsymbol{n}$, which is equal to c+$v \cdot \boldsymbol{n}$. It is difficult to apply the above equation directly in the heterogeneous media, because it needs $\boldsymbol{n}$ along the ray path to be determined at every time. To avoid this, another additional

differential equation that can estimate the rate of change in time of $\boldsymbol{n}$ is applied as well as the wave delay vector $\boldsymbol{s(x)}=\nabla\tau(\boldsymbol{x})$ is adopted. Considering the wave fronts at spaced time interval between t and $t+\Delta t$, the position of ray trajectory $\boldsymbol{x}_p(t)$ at time $t+\Delta t$ can be approximated by $\boldsymbol{x}_p(t)+\dot{x}_p(t)\Delta t$ (Figure 4.18b). Because of $t=\tau(\boldsymbol{x}_p)$, $\nabla\tau=\boldsymbol{s}$, and $\nabla\tau$ is perpendicular to the curved surface t, the slowness vector at any given moment is given by:

$$\boldsymbol{s}=\frac{\boldsymbol{n}}{c+\boldsymbol{v}\cdot\boldsymbol{n}}$$

The detailed of this term originated in reference (Salomons [2001]) with a condition of a constant frequency of plane wave and the direction of $\boldsymbol{s}$ is parallel to $\boldsymbol{n}$.

In addition to the wind case of sound refraction, even in the same medium, both refraction and reflection can also occur at the boundary between two regions having relative movements. In this region, wind speed gradients may cause the refraction of the sound waves. Under certain atmospheric profile (as shown in Figure 4.10), the ray-tracing computation is an important subject in the analysis of atmospheric acoustics. Actually, the atmospheric changes can cause correspondingly acoustic ray distribution more complicated. Sometimes the term called "$unusual$" or "$anomaly$" $propagation$ phenomenon will occur. This term refers to an imagine phenomenon that the sound can be heard in very long distances away, let say 300 km, but it could not be heard within short distances away from the source. This situation is commonly called a silent zone problem. As an assumption for this situation that there should be a temperature inversion layer above the convection layer was formed. To explain this phenomenon, for simplification, horizontal wind effect was involved and the rays starting from the source and bending due to refraction process. The rays with initial angle θ_0 will bend to the ground when they reach the height of turning point, z_{tr} and the rays travel in a direction is nearly horizontal. The turning height, z_{tr} is defined by:

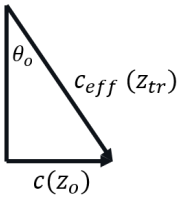

$$c(z_{tr})+w(z_{tr})=\frac{c(z_o)}{\sin\theta_0}$$

where w is the horizontal wind speed, θ_0 is the initial angle, and $c(z_o)$ is the sound speed at the ground surface. The wind speed at the ground is almost small, thus it can be neglected. According to this equation, in such condition if the rays start from the source point and then return back to the ground, it must be satisfied that $c_{eff}(z) = c(z) + w(z)$ at certain height is larger than the ground sound speed $c(z_o)$. In fact, this condition can be explained by the profile shown in Figure 4.10 and the rays-tracing are plotted in Figure 4.16a.

From the measurement of the horizontal propagation velocity of the incident waves, sweeping accross the infrasound sensor and using the expression of calculated sound speed at the upper refraction height, $c_{eff}(z_{tr}) = c(z_{tr}) + w(z_{tr})$, described in Section 4.3, the estimated wind speed $w(z_{tr})$ can be obtained. The measured trace velocity or the sound speed at the ground surface, $c(z_o)$ is obtained from the array processing, the computed of sound speed at top level of reflection height, $c_{eff}(z_{tr})$ and θ_0 are obtained from the ray-tracing program with the atmospheric background condition above the source location obtained from the atmospheric model. All of this condition are based on the many assumption, such as the atmosphere possesses only as a macroscopic structure layer which involve two type of processes, refraction and reflection, while the turbulence structures as microscopic one can be ignored. At the ground surface, the wind speed is approximately zero, due to friction at the ground surface. The ray-tracing simulation calculated of the paths of all sound rays between the source and the receiver, and calculated the received sound pressure by summation of the all contributions of sound rays. For a downward refracting atmosphere, the complex pressure amplitude p_c is given by (see Salomons [1998]):

$$p_c = \sum_{m=1}^{N_{rays}} A_m e^{i\phi_m},$$

where N_{rays} is the sound rays number. The phase ϕ_m of ray m is given by $\phi_m = \int k(z)ds = \omega \int c^{-1}(z)ds$, where the path length along the ray is denoted by s, ω is the angular frequency. The amplitude A_m of ray m can be calculated by $A_m = f_m C_m^{N_m}$, where C_m, f_m, and N_m are respectively for a reflection coefficient, a focusing factor, and ground reflections number. The focusing factor f_m is important for the condition in a curved sound rays which is depend on their concentration in the atmosphere. The amplitude A_m can be written in general expression

as (see Brekhovskikh [2012]):

$$f_m = \left(\frac{r^2 + (z_s - z_r)^2}{r^2}\right)^{1/2} \left(\frac{\cos\gamma_s |\delta\gamma_s|}{\rho_r |\sin\gamma_r|}\right)^{1/2},$$

where r is the horizontal range from the source, the height of the source and the receiver are denoted by z_s and z_r, the elevation angle at the source is denoted as γ_s, and the quantity ρ_r typically 10^{-5}. The ground reflection $C_m^{N_m}$ uses the spherical-wave reflection coefficient, which is a function of the ground impedance. It is not available for a refracting atmosphere.

Typical velocity results for the recorded signals at 12:00 UTC on March 9, 2018 and 00:00 UTC on March 10, 2018 above Shionomisaki station, Japan (33.45^o N, 135.77^o E) from direct measurement technique of radiosonde is shown in Figure 4.15. The observation data can be accessed from the JMA database (Japan Meteorological Agency (JMA) [2019]) and NOAA (National Oceanic and Atmospheric Administration) (National Oceanic and Atmospheric Administration (NOAA) [2019]). The jet stream in the troposphere, at around 10 km of altitude, flows strongly in the northeast direction as similar as the MERRA-2 model shown in Figure 4.10. By incorporating the known wind and temperature at the time of observation into the ray-tracing program, top-level reflection of the infrasound from the source location is obtained as given in the ray diagram of Figure 4.16a. The rays are plotted at 1^o intervals of incidence angle and represent in color code for power transmission loss of the wave along the propagation range. The result of ray tracing implements a normal mode for propagation of a single tone in a stratified atmosphere to compute the power transmission loss TL(r, z) in dB was defined by (see Jensen et al. [2011]):

$$TL(r,z) \simeq -20\log\frac{1}{\rho(z_s)}\sqrt{\frac{2\pi}{r}}\sqrt{\sum_{m=1}^{\infty}\left|\Psi_m(z_s)\Psi_m(z)\frac{e^{i(k_m+i\alpha_m)r}}{\sqrt{k_m}}\right|^2}$$

where Ψ_m denotes the particular eigen function $\Psi(z)$ of the eigenvalue problem in the generalized Helmholtz equation, z denote altitude above the ground surface, r represent the radial horizontal range, α_m is the atmospheric attenuation coefficient, k_m denote real value of wave numbers, and ρ denote the mean density of the atmosphere.

Using the array processing result and the ray propagation model result at 16:54 UTC on

March 9, 2018 (see Figures 4.9 and 4.14), the sound speed at an altitude of about 40 km was rather low (∼298 m/s at ∼41 km, see Table 4.3), indicating the propagation velocity in this layer. Table 4.3 shows about the estimation of the wind at two reflection layer (at height lower than 10 km and around 40 km). Both top level of the refraction height and sound speed at its apex are listed in the second and third column of Table 4.3. The array processing compute the trace velocity from two different group stations (KUT07, KUT08, KUT09, KUT10 for the closest group to the source point and KUT11, KUT12, KUT16 for the farthest one). The first group receives the arrival waves after it was refracted back at the height of ∼10 km (see Figure 4.16b). The estimated wind speeds for this period are shown in the right column of Table 4.3. A comparison of the calculated wind velocities and radiosonde observation up to the altitude of the radiosonde indicated a qualitative agreement. However, there is still a need to obtain the calculated wind velocities above the radiosonde altitude for a comparison with direct measurements (e.g., a stratospheric balloon experiment). The other calculated wind speeds and their comparisons for the eruption times listed in Table 4.1 are shown in Table B.3-B.7 of the appendix B.

Table 4.3: Trace velocity, sound speed and wind speed estimated from two groups station for the eruption event at 16:54 UTC on March 9, 2018.

Trace velocity (km/s)	computed reflection level (km)	speed of sound at reflecting level (km/s)	computed wind at reflecting level (m/s)
0.3350	1.4399	0.3253	9.7222
0.3350	1.5166	0.3253	9.7253
0.3350	1.5961	0.3252	9.8042
0.3350	1.6845	0.3252	9.8399
0.3350	1.8324	0.3256	9.3737
0.3350	9.5787	0.3238	11.2130
0.3350	9.7079	0.3223	12.6592
0.3350	9.8632	0.3214	13.5737
0.3350	10.0666	0.3210	13.9832
0.3350	10.3885	0.3219	13.1369
0.3350	10.8367	0.3166	18.3671
0.3350	10.9657	0.3157	19.3458
0.3732	41.1735	0.2982	74.9928
0.3732	41.6614	0.2974	75.8096
0.3732	42.2479	0.2971	76.1437
0.3732	42.9495	0.2972	76.0207
0.3732	43.7830	0.2978	75.4465
0.3732	44.7582	0.2987	74.4873
0.3732	45.9465	0.3006	72.5645
0.3732	47.7888	0.3074	65.7910

Chapter 5

THE LINKAGE BETWEEN PART OF STUDY

***

The Sun-Earth system displays a typical relationship of a terrestrial planet around its parent star. This connection between Sun and Earth is more clearly represented by the space weather system: Sun, heliosphere, magnetosphere, and atmosphere-ionosphere. Without investigation of these systems and their interactions with each other, the effects of Sun on Earth's atmosphere cannot be fully understood. Overall, Earth is influenced by Sun directly and indirectly via radiative, thermal, dynamic and electro dynamical processes. Earth's atmosphere is stably stratified and consists of different regions of varying chemical and physical properties. In particular, Earth's upper atmosphere system is controlled by solar process from above and by internal waves from below.

About five billion years ago, our Sun was formed, and is the main source energy supplier of life on the Earth. The Sun emits continuous stream of energy radiation that interacts with the neutral atmosphere of the Earth. The associated radiation consists of a broad range of electromagnetic waves, ranging from radio waves to very high-energy. The solar radiation, particularly in the UV- and EUV-range plays the important role of ionization in the Earth's atmosphere. The number of sunspots and F10.7 index are good proxy for solar activity. The sunspots number vary with time and it reaches a maximum every 11 years. The solar radio flux at 10.7 cm, which is often called the F10.7 index, correlates well with the sunspot number as well as a number of Ultraviolet (UV) radiation record. The emissions of Extreme UltraViolet (EUV) which is impact and modify the upper atmosphere indicate well with the F10.7 index.

The Earth's atmosphere, a layer of gas surrounding the Earth's Lithosphere, is composed various regions, forming the neutral atmosphere. The neutral atmosphere extends from ground to 500-900 km, which is characterized by variations in temperature resulting mainly from the solar radiation. At the upper atmosphere, the neutral atmosphere is greatly affected by

the incoming solar EUV/UV radiation. The Sun is the main source of heat, traveling to the Earth through space in the form of radiation. This radiation is absorbed by the Earth's surface and the atmosphere. Some parts of the Earth receive more of this radiation than others due to the curvature of the Earth. In particular, at higher latitudes, the radiation from the Sun is spread over a much larger surface area and the radiation also travels through a greater depth of atmosphere nearer the poles in comparison to the equator, thus more radiation is lost to scattering and absorption by the composition of the atmosphere. The tilt of the Earth means that the polar regions do not see daylight during the winter, the thickness of the clouds, and the Earth's surface are also an important factor in determining how much of the Sun's radiation is used for heating the Earth. The combined effect of all of these processes sets up a thermal gradient between each latitudes and develop a various spatial-temporal scales of atmospheric waves.

The atmospheric waves play an important role in the transport of momentum and energy in the atmosphere, as well as in the generation of turbulence and mixing. Gravity waves and sound waves are commonly waves, propagating in the atmosphere. The gravity waves are important for the transport momentum and energy in the middle atmosphere, as well as the main role in the generation of turbulence and mixing at there. They can be generated at the variety of ways, flow over mountains and the motion of the ocean surface are their common production method. When this waves are generated and grow larger in amplitude and speed as they propagate vertically. This is because the waves deposit or conserve energy and momentum as they dissipate in the atmosphere, and affect the wind and the temperature distribution. In the troposphere, convection, thunderstorms, mass-flow over the orography, among others are possible potential sources of the gravity waves. However, the origin of the waves are still an issue in need to further investigation. In the upper region of the atmosphere, especially the stratosphere and mesosphere are relatively large magnitudes, which are ideal place to study these waves. Naturally, these waves do not always propagate in straight lines. Thus, they can experience reflection, refraction, and break down during their propagation in the atmosphere. The issue of refraction of these waves has been recognized that their refraction could not occur not only as a function of height (it is well known case), but also as a function of latitude. Thus the

distribution of wave motions in the higher latitudes of the middle atmosphere might not properly reflect the distribution at the source region. Refraction as a function of height is probably an important consideration. If the wave approaches a critical level where the frequency of the wave goes to zero, the vertical group velocity becomes zero and there is no propagation occurs. This such situation, the wave usually breaks and the wave will reflect backwards, called turning level. If the vertical temperature and wind structures are suitable, the wave may reflected from the upper level and re-reflected at a slightly lower height, leading to reflection back of "wave duct" between upper and lower level. In such circumstances, the gravity waves may travel for hundreds of kilometers.

The gravity waves can be observed and identified in many ways. In-situ observation techniques, such as balloons, rockets, and aircraft, many types of parameters like pressure, density, and wind velocity can be measured. With regard to remote sensing, the waves can be identified due to chemical reactions that produce optical emissions in the middle-upper atmosphere, or visual effect such as 'wave-like clouds' , or by Lidar, the density and temperature perturbation can be measured directly. The rocket techniques may involve smoke or TMA (Tri-methyl aluminum) trail releases to study the waves. Balloons with temperature sensor and anemometers can measure up to altitude of the stratosphere. With regard to radar experiment, most methods are based on the wind velocities measurement by the spaced antenna method or interferometric methods, or using steered beams and Doppler measurements. The radar method is possible to measure the velocity vector with good resolution and high accuracy to be then used in the wind determination. However, the Doppler method can only measure one component of the wind in any one beam. This method is not always valid for gravity waves studies. It may be satisfactory for waves with periods of many hours, but for short-term fluctuations with period of tens of minutes cannot be conducted, since each beam will look at a different part of the wave and may come and have a significant phase differences. In addition, the method is not valid to avoid the vertical component of the wind. Therefore, the spaced antenna measurement can provide all three components of the wind simultaneously, but a good design of experiment needs to consider the wide radar beam. This study use meteor radar that apply the wide radar beam, thus the system able to measure the momentum flux as one important parameter in waves

studies.

The best known atmospheric waves and the main part of the object studied in this study is infrasound waves. The sound waves are longitudinal waves formed by a series of compressions and expansions of a fluid. In addition to the usual sounds whose frequency spectrum covers the range of human hearing response, the atmosphere also contains a lot of infrasound whose frequency is below the lower hearing limit. The Earth's atmosphere is a fluid that is continually followed up by gravity, therefore its density will definitely decrease with increasing altitude, and thus a gradient is formed. This density gradient may cause the ordinary sound waves, referred to as acoustic gravity waves (AGW) propagate in the stratified fluids under the influence of both the compressibility of the fluids and the restoring force of gravity. When this restoring force has been strengthened further such that it cause the dominant motion in the atmosphere, internal gravity waves are created. Atmospheric tide and wind generated internal gravity waves are ubiquitous in the ocean. This waves is associated with the numerous effects on the atmospheric circulation, the temporal and spatial structure variability of temperature, density, pressure of all atmospheric layers, starting from troposphere and up to the altitude of the middle-upper atmosphere. As mentioned above, numerous observations of variations in temperature, density, and wind velocity of the lower and middle atmosphere using lidar, radar, rocket sounding, optical sounding from space show that the gravity waves significantly contribute to these variations. The variations in temperature and wind velocity, in which their spatial scales are much larger than the wavelengths of the sound waves, cause refraction, leading to the fluctuation time of sound propagation, the effective sound speed, the angle of arrival of incoming signals, and error of source localization. Ray-tracing method can be used to study the effects of gravity wave perturbations on infrasound propagation. Long-term monitoring of both natural and artificial sources of infrasound waves will give us the temporal variations of travel times for upper atmosphere arrivals.

By mentioned above, the key point is the gravity and infrasound waves as one of the atmospheric wave system. These waves are the main role in the global atmosphere circulation, depending on their variation. How large are they variate in spatial and temporal? How to identify these structures? What their source and its origin? Radar techniques with spaced antenna

method and wide range beam capable to measure their fluctuation and direction, except their origin. For example, the meteor radar can be used to study the variation of atmospheric waves by investigating the momentum flux. With dense infrasound observation network, may obtain their source location. And, the sensitivity of infrasound to atmospheric wind and temperature, and the advantage of infrasound to travel over large horizontal distance through the middle-upper atmosphere make infrasound remote sensing a prospective technique for atmospheric studies, especially in the investigation of atmospheric waves structures.

Chapter 6

DISSERTATION SUMMARY AND FUTURE WORKS

***

6.1 Dissertation Summary

This dissertation has provided an overview of alternative methods of ground-based remote sensing which comprises three related works with the motivation to better understand the Earth's atmosphere. To accomplish this, one solar cycle data distribution of meteor activities at equator, one week simultaneous forward scatter radar measurements in Japan, and multi-site infrasound observation in Japan were conducted.

Chapter 2 described the observations data of meteor radar system, and evaluated the variation in the meteor peak height distribution during the full solar cycle activity. We noted the following:

- Annually, variations in meteor height peaks in the equatorial region showed a uniform double peak pattern and varied by neutral atmospheric density in the MLT region at equatorial latitudes.

- In contrast, the average trend in annual neutral density did not vary by solar activity, which reinforces Stober's suggestion Stober et al. [2012] regarding the relationship between solar activity and atmospheric density based on MSISE model calculations.

- The variation in atmospheric density predicted by the MSISE model at 90-km altitude followed the meteor count rate trend observed at the equatorial region for the period of 2003–2016.

Considering these results, the annual change in meteor peak height involves complex mechanistic processes independent of the major influence of solar activity, such as widening and narrowing at the intersection area between trajectories of the circular meteoric belt, according

to the thickness of the Earth's atmosphere, which can in turn shift the region of meteoroid interaction with the Earth's atmosphere in a vertical direction parallel to altitude. Whether there is a causal relationship between the above parameters and meteor interactions with the Earth's atmosphere remains an open question. Nevertheless, the results over the equatorial region obtained in this study may serve as a reference for future studies of global atmospheric dynamics.

In Chapter 3, we described a construction of the three-receiver system according to the interferometer principle. The three-receiver system incorporates a 5-channel interferometer receiver with two individual receivers separated by several km to obtain the orbital parameter of meteor. The constructed system was motivated to encounter this objective. We conduct a simultaneous observation campaign, about one week in the end of 2015 to investigate the meteor velocity of the Gemini as well as the angle of the meteor origin, i.e., radiant point and trajectory. About 56 simultaneous meteor echoes were collected in the order of noise level. Several confirmed objects as meteor from all stations were determined. The time difference of the detected meteor echo between stations can be obtained by computing the correlation function between two separated stations. We estimated the average velocity of the Gemini meteor shower and their arrival angle and confirmed the meteor occurrence with the existing optical measurements. The estimated speed of 34 ± 8.86 m/s for the Geminid meteors coincides with the results of the similar observations previously.

Chapter 4 described the computation for source wave detection, the concept of Doppler Beam Swinging (DBS) applied in the calculation to determine the source wave parameter used to estimate the horizontal atmospheric velocity at certain altitude. The Doppler Beam Swinging was motivated to deal with the source wave detection algorithm with an irregular infrasound sensor array system. Similar way with the DBS, the essence in the infrasound processing is to steer the arrays in a particular directions in a scanning plane. When the steering direction coincides with a source, the maximum output power will be obtained. It applies a delay and an amplitude weight to the output of each sensor. The delays are chosen to maximize the sensitivity of the arrays to the waves propagating from the origin direction. By using the delays, the arrays can be steered towards the source, and the waveforms captured as the detected source. The parameter output of the detected source waves are then used to estimate the horizontal

atmospheric velocity at certain altitude and compared with observation result provided by the regional radiosonde data.

6.2 Future Works

There are many possible future avenues of work that can help to improve the understandings of the Earth's atmosphere. For the future work, we plan to pay our efforts to continue this works for multiple ground based observation for atmospheric studies. Some suggestions to follow up this work are mentioned as follows:

In Chapter 2-4, two different observation systems were introduced with the radar and infrasound applications. For the meteor radar measurement, it is also possible to determine the wind profile of the upper atmosphere from the diffusion time period of the meteor. One possibility to further work is to further develop the velocity estimation algorithm is to utilize the diffusion time period of the meteor. The velocity can be used to validate the velocity estimated from the infrasound measurements.

Regarding the equatorial region has a unique dynamical process on the atmosphere, i.e., equatorial fountain which involved the atmospheric waves energy transfer upward and distribute to the higher latitudes, we would like to implement the infrasound observation to investigate the profiles. In chapter 4, the algorithm to estimate the horizontal wind velocity was developed and checked the impact of the selection of number of the sensor to the output performance. Actually, four sensors were selected based on sensor locations. The algorithm would be more powerful if it can be applied adaptively according to the sensor locations. In addition, the weighting factor for the sensor will be important point to keep the performance of the algorithm and establish adaptive condition of the process. Therefore, for the short-time plan, the algorithm in the infrasound data processing needs some improvements, especially in reducing the limitation factor appeared in the previous calculations.

For the orbital parameter of the meteor estimation, the multi-station receiver can be considered in the forward-scattering technique. By using this technique, it could roughly estimate the directions location of the origin meteor and the speed. The multi-station receiver system could be operated under this technique is an efficient way to avoid the full-scale search through all possible direction angle to determine the orbital meteor parameters. It is preferable in future

to use the concept of this technique to observe the meteor activity in the equatorial region and make a comprehensive measurements with the existing meteor radar systems.

REFERENCES

***

S. Arrowsmith, R. Burlacu, K. Pankow, B. Stump, R. Stead, R. Whitaker, and C. Hayward. Modeling the generation of infrasound from earthquakes. *The Journal of the Acoustical Society of America*, 132(3):2047–2047, 2012. doi: 10.1121/1.4755526. URL https://doi.org/10.1121/1.4755526.

J. Assink, G. Averbuch, S. Shani-Kadmiel, P. Smets, and L. Evers. A Seismo-Acoustic Analysis of the 2017 North Korean Nuclear Test. *Seismological Research Letters*, 89(6):2025–2033, 08 2018. ISSN 0895-0695. doi: 10.1785/0220180137. URL https://doi.org/10.1785/0220180137.

R. L. Bosilovich, M. G. and M. Suarez. MERRA-2: File specification. *GMAO Office Note No. 9 (Version 1.1)*, 9(1.1):73, 2016. URL http://gmao.gsfc.nasa.gov/pubs/office_notes.

J. R. Bowman, G. E. Baker, and M. Bahavar. Ambient infrasound noise. *Geophysical Research Letters*, 32(9), 2005. doi: 10.1029/2005GL022486. URL https://agupubs.onlinelibrary.wiley.com/doi/abs/10.1029/2005GL022486.

L. Brekhovskikh. *Waves in Layered Media*. Applied mathematics and mechanics. Elsevier Science, 2012. ISBN 9780323161626. URL https://books.google.co.jp/books?id=tDuNmVJAPXEC.

P. Brown, R. Weryk, D. Wong, and J. Jones. A meteoroid stream survey using the Canadian Meteor Orbit Radar: I. Methodology and radiant catalogue. *Icarus*, 195(1):317 – 339, 2008. ISSN 0019-1035. doi: https://doi.org/10.1016/j.icarus.2007.12.002. URL http://www.sciencedirect.com/science/article/pii/S0019103507005994.

K. A. Browning and R. Wexler. The determination of kinematic properties of a wind field using doppler radar. *Journal of Applied Meteorology*, 7(1):105–113, 1968. doi:

10.1175/1520-0450(1968)007<0105:TDOKPO>2.0.CO;2. URL https://doi.org/10.1175/1520-0450(1968)007<0105:TDOKPO>2.0.CO;2.

M. Buček, V. Porubčan, and P. Zigo. Solar activity and Perseid meteor heights. *Contributions of the Astronomical Observatory Skalnate Pleso*, 42(1):22–32, Apr 2012. URL https://ui.adsabs.harvard.edu/abs/2012CoSka..42...22B.

P. Campus. Detection of infrasound from the eruption of Manam volcano on January, 2005. In *Proc. 2005 infrasound technology workshop, Tahiti*, Tahiti, 2005.

P. Campus. Monitoring volcanic eruptions with the IMS infrasound network. *Inframatics*, 15:6–12, 2006a. URL https://www.researchgate.net/publication/283592132_Monitoring_volcanic_eruptions_with_the_IMS_infrasound_network.

P. Campus. The IMS infrasound network: Detection of a large variety of events including volcanic eruptions. In *Proc. 2007 infrasound technology workshop*, Tokyo, Japan, 2007.

P. Campus and D. R. Christie. Worldwide observations of infrasonic waves. In Infrasound Monitoring for Atmospheric Studies, editor, *Le Pichon, Alexis and Blanc, Elisabeth and Hauchecorne, Alain*, pages 185–234. Springer Netherlands, Dordrecht, 2009. ISBN 978-1-4020-9508-5. doi: 10.1007/978-1-4020-9508-5_6. URL https://doi.org/10.1007/978-1-4020-9508-5_6.

Y. Cansi. An automatic seismic event processing for detection and location: The P.M.C.C. method. *Geophysical Research Letters*, 22(9):1021–1024, 1995. doi: 10.1029/95GL00468. URL https://agupubs.onlinelibrary.wiley.com/doi/abs/10.1029/95GL00468.

Y. Cansi and Y. Klinger. An automated data processing method for mini-arrays. *News Lett*, 11, 1997. URL https://www.researchgate.net/publication/237698457_An_automated_data_processing_method_for_mini-arrays.

Y. Cansi and A. Le Pichon. Infrasound event detection using the progressive multi-channel correlation algorithm. In Handbook of Signal Processing in Acoustics, editor, *Le Pichon,*

Alexis and Blanc, Elisabeth and Hauchecorne, Alain, pages 1425–1435. Springer Netherlands, Dordrecht, 2009. doi: 10.1007/978-0-387-30441-0_77. URL https://link.springer.com/chapter/10.1007/978-0-387-30441-0_77.

C. Caudron, B. Taisne, M. Garcés, L. P. Alexis, and P. Mialle. On the use of remote infrasound and seismic stations to constrain the eruptive sequence and intensity for the 2014 kelud eruption. *Geophysical Research Letters*, 42(16):6614–6621, 2015. doi: 10.1002/2015GL064885. URL https://agupubs.onlinelibrary.wiley.com/doi/abs/10.1002/2015GL064885.

Z. Ceplecha, J. Borovička, W. G. Elford, D. O. ReVelle, R. L. Hawkes, V. Porubčan, and M. Šimek. Meteor phenomena and bodies. *Space Science Reviews*, 84(3):327–471, 1998. ISSN 1572-9672. doi: 10.1023/A:1005069928850. URL https://doi.org/10.1023/A:1005069928850.

L. Ceranna, A. Le Pichon, D. N. Green, and P. Mialle. The Buncefield explosion: A benchmark for infrasound analysis across central Europe. *Geophysical Journal International*, 177(2):491–508, 2009. doi: 10.1111/j.1365-246X.2008.03998.x. URL https://onlinelibrary.wiley.com/doi/abs/10.1111/j.1365-246X.2008.03998.x.

D. Christie, B. Kennett, and C. Tarlowski. Detection of regional and distant atmospheric explosions at IMS infrasound stations. In *Proc. 27th Seismic Research Review: Ground-Based Nuclear Explosion Monitoring Technologies*, Kailua-Kona, Hawaii, 2005. URL https://www.researchgate.net/publication/267839487_DETECTION_OF_REGIONAL_AND_DISTANT_ATMOSPHERIC_EXPLOSIONS_AT_IMS_INFRASOUND_STATIONS.

B. Clemesha and P. Batista. The quantification of long-term atmospheric change via meteor ablation height measurements. *Journal of Atmospheric and Solar-Terrestrial Physics*, 68(17):1934 – 1939, 2006. ISSN 1364-6826. doi: https://doi.org/10.1016/j.jastp.2005.12.008. URL http://www.sciencedirect.com/science/article/pii/

S1364682606000423. Long-term Trends and Short-term Variability in the Upper, Middle and Lower Atmosphere.

Community Coordinated Modeling Center-NASA. NRLMSISE-00 atmosphere model, 2002. URL https://ccmc.gsfc.nasa.gov/modelweb/models/nrlmsise00.php. Last accessed 12 February, 2018.

COSPAR International Reference Atmosphere (CIRA). Empirical models of atmospheric temperature and densities, 1990. URL https://ccmc.gsfc.nasa.gov/. Last accessed February 12, 2016.

P. Czechowsky, J. Klostermeyer, J. Röttger, R. Rüster, G. Schmidt, W. Pollitt, and R. Francisco. The SOUSY-VHF-radar for tropo-. strato- and mesospheric sounding-1976. In *17th Conference on Radar Meteorology of the American Meteorological Society (AMS, Oct. 26-29)*, Seattle, USA, 1976. URL http://repositorio.igp.gob.pe/handle/IGP/335.

W. L. Donn and D. Rind. Natural Infrasound as an Atmospheric Probe. *Geophysical Journal International*, 26(1-4):111–133, 1971. ISSN 0956-540X. doi: 10.1111/j.1365-246X.1971.tb03386.x. URL https://doi.org/10.1111/j.1365-246X.1971.tb03386.x.

W. L. Donn and D. Rind. Microbaroms and the temperature and wind of the upper atmosphere. *Journal of the Atmospheric Sciences*, 29(1):156–172, 1972. doi: 10.1175/1520-0469(1972)029<0156:MATTAW>2.0.CO;2. URL https://doi.org/10.1175/1520-0469(1972)029<0156:MATTAW>2.0.CO;2.

D. P. Drob, J. M. Picone, and M. Garcés. Global morphology of infrasound propagation. *Journal of Geophysical Research: Atmospheres*, 108(D21), 2003. doi: 10.1029/2002JD003307. URL https://agupubs.onlinelibrary.wiley.com/doi/abs/10.1029/2002JD003307.

D. P. Drob, J. T. Emmert, G. Crowley, J. M. Picone, G. G. Shepherd, W. Skinner, P. Hays, R. J. Niciejewski, M. Larsen, C. Y. She, J. W. Meriwether, G. Hernandez, M. J. Jarvis,

D. P. Sipler, C. A. Tepley, M. S. O'Brien, J. R. Bowman, Q. Wu, Y. Murayama, S. Kawamura, I. M. Reid, and R. A. Vincent. An empirical model of the Earth's horizontal wind fields: HWM07. *Journal of Geophysical Research: Space Physics*, 113(A12), 2008. doi: 10.1029/2008JA013668. URL https://agupubs.onlinelibrary.wiley.com/doi/abs/10.1029/2008JA013668.

D. P. Drob, J. T. Emmert, J. W. Meriwether, J. J. Makela, E. Doornbos, M. Conde, G. Hernandez, J. Noto, K. A. Zawdie, S. E. McDonald, J. D. Huba, and J. H. Klenzing. An update to the Horizontal Wind Model (HWM): The quiet time thermosphere. *Earth and Space Science*, 2(7):301–319, 2015. doi: 10.1002/2014EA000089. URL https://agupubs.onlinelibrary.wiley.com/doi/abs/10.1002/2014EA000089.

J. T. Emmert, D. P. Drob, G. G. Shepherd, G. Hernandez, M. J. Jarvis, J. W. Meriwether, R. J. Niciejewski, D. P. Sipler, and C. A. Tepley. DWM07 global empirical model of upper thermospheric storm-induced disturbance winds. *Journal of Geophysical Research: Space Physics*, 113(A11), 2008. doi: 10.1029/2008JA013541. URL https://agupubs.onlinelibrary.wiley.com/doi/abs/10.1029/2008JA013541.

L. Evers and H. Haak. The detectability of infrasound in the Netherlands from the Italian volcano Mt. Etna. *Journal of Atmospheric and Solar-terrestrial Physics*, 67:259–268, 2005. doi: 10.1016/j.jastp.2004.09.002. URL https://ui.adsabs.harvard.edu/abs/2005JASTP..67..259E.

L. Evers and H. Haak. The characteristics of infrasound, its propagation and some early history. In Infrasound Monitoring for Atmospheric Studies, editor, *Le Pichon, Alexis and Blanc, Elisabeth and Hauchecorne, Alain*, pages 3–27. Springer Netherlands, Dordrecht, 2009. ISBN 978-1-4020-9508-5. doi: 10.1007/978-1-4020-9508-5_1. URL https://doi.org/10.1007/978-1-4020-9508-5_1.

L. G. Evers and H. W. Haak. Listening to sounds from an exploding meteor and oceanic waves. *Geophysical Research Letters*, 28(1):41–44, 2001. doi: 10.1029/2000GL011859. URL https://agupubs.onlinelibrary.wiley.com/doi/abs/10.1029/2000GL011859.

D. T. Farley. On-line data processing techniques for MST radars. *Radio Science*, 20 (6):1177–1184, 1985. doi: 10.1029/RS020i006p01177. URL https://agupubs.onlinelibrary.wiley.com/doi/abs/10.1029/RS020i006p01177.

D. T. Farley, H. M. Ierkic, and B. G. Fejer. Radar interferometry: A new technique for studying plasma turbulence in the ionosphere. *Journal of Geophysical Research: Space Physics*, 86(A3):1467–1472, 1981. doi: 10.1029/JA086iA03p01467. URL https://agupubs.onlinelibrary.wiley.com/doi/abs/10.1029/JA086iA03p01467.

D. Fee, M. Garces, and A. Steffke. Infrasound from Tungurahua volcano 2006–2008: Strombolian to Plinian eruptive activity. *Journal of Volcanology and Geothermal Research*, 193(1):67 – 81, 2010. ISSN 0377-0273. doi: https://doi.org/10.1016/j.jvolgeores.2010.03.006. URL http://www.sciencedirect.com/science/article/pii/S0377027310000971.

B. G. Ferguson. Minimum variance distortionless response beamforming of acoustic array data. *The Journal of the Acoustical Society of America*, 104(2):947–954, 1998. doi: 10.1121/1.423311. URL https://doi.org/10.1121/1.423311.

P. A. Forsyth, E. L. Vogan, D. R. Hansen, and C. O. Hines. The principles of JANET-A meteor-burst communication system. *Proceedings of the IRE*, 45(12):1642–1657, Dec 1957. ISSN 2162-6634. doi: 10.1109/JRPROC.1957.278296. URL https://ieeexplore.ieee.org/document/4056453.

S. J. Franke, X. Chu, A. Z. Liu, and W. K. Hocking. Comparison of meteor radar and Na doppler lidar measurements of winds in the mesopause region above Maui, Hawaii. *Journal of Geophysical Research: Atmospheres*, 110(D9), 2005. doi: 10.1029/2003JD004486. URL https://agupubs.onlinelibrary.wiley.com/doi/abs/10.1029/2003JD004486.

S. Fukao, T. Sato, T. Tsuda, S. Kato, K. Wakasugi, and T. Makihira. The MU radar with an active phased array system: 1. Antenna and power amplifiers. *Radio Science*, 20(6):

1155–1168, Nov 1985a. doi: 10.1029/RS020i006p01155. URL https://ieeexplore.ieee.org/document/7769002.

S. Fukao, T. Tsuda, T. Sato, S. Kato, K. Wakasugi, and T. Makihira. The MU radar with an active phased array system: 2. In-house equipment. *Radio Science*, 20(6):1169–1176, 1985b. doi: 10.1029/RS020i006p01169. URL https://agupubs.onlinelibrary.wiley.com/doi/abs/10.1029/RS020i006p01169.

S. Fukao, H. Hashiguchi, M. Yamamoto, T. Tsuda, T. Nakamura, M. K. Yamamoto, T. Sato, M. Hagio, and Y. Yabugaki. Equatorial Atmosphere Radar (EAR): System description and first results. *Radio Science*, 38(3), 2003. doi: 10.1029/2002RS002767. URL https://agupubs.onlinelibrary.wiley.com/doi/abs/10.1029/2002RS002767.

T. B. Gabrielson. *Infrasound*, chapter 33, pages 367–372. John Wiley, Ltd, 2007. ISBN 9780470172513. doi: 10.1002/9780470172513.ch33. URL https://onlinelibrary.wiley.com/doi/abs/10.1002/9780470172513.ch33.

K. S. Gage and B. B. Balsley. Doppler radar probing of the clear atmosphere. *Bulletin of the American Meteorological Society*, 59(9):1074–1094, 1978. doi: 10.1175/1520-0477(1978)059. URL https://doi.org/10.1175/1520-0477(1978)059<1074:DRPOTC>2.0.CO;2.

M. Garcés, C. Hetzer, M. Merrifield, M. Willis, and J. Aucan. Observations of surf infrasound in Hawai'i. *Geophysical Research Letters*, 30(24), 2003. doi: 10.1029/2003GL018614. URL https://agupubs.onlinelibrary.wiley.com/doi/abs/10.1029/2003GL018614.

M. Garcés, M. Willis, C. Hetzer, A. Le Pichon, and D. Drob. On using ocean swells for continuous infrasonic measurements of winds and temperature in the lower, middle, and upper atmosphere. *Geophysical Research Letters*, 31(19), 2004. doi: 10.1029/2004GL020696. URL https://agupubs.onlinelibrary.wiley.com/doi/abs/10.1029/2004GL020696.

C. S. Gardner, X. Tao, and G. C. Papen. Simultaneous lidar observations of vertical wind, temperature, and density profiles in the upper mesophere: Evidence for nonseparability of atmospheric perturbation spectra. *Geophysical Research Letters*, 22(20):2877–2880, 1995. doi: 10.1029/95GL02783. URL https://agupubs.onlinelibrary.wiley.com/doi/abs/10.1029/95GL02783.

R. Gelaro, W. McCarty, M. J. Suárez, R. Todling, A. Molod, L. Takacs, C. A. Randles, A. Darmenov, M. G. Bosilovich, R. Reichle, K. Wargan, L. Coy, R. Cullather, C. Draper, S. Akella, V. Buchard, A. Conaty, A. M. da Silva, W. Gu, G.-K. Kim, R. Koster, R. Lucchesi, D. Merkova, J. E. Nielsen, G. Partyka, S. Pawson, W. Putman, M. Rienecker, S. D. Schubert, M. Sienkiewicz, and B. Zhao. The Modern-Era Retrospective analysis for Research and Applications, version 2 (MERRA-2). *Journal of Climate*, 30(14):5419–5454, 2017. doi: 10.1175/JCLI-D-16-0758.1. URL https://doi.org/10.1175/JCLI-D-16-0758.1.

Goddard Earth Sciences Data and Information Services Center (GES DISC). Global Modelling and Assimilation Office (GMAO): M2T3NVASM, 2015. URL https://doi.org/10.5067/SUOQESM06LPK.

V. H. Goerke, J. M. Young, and R. K. Cook. Infrasonic observations of the May 16, 1963, volcanic explosion on the island of Bali. *Journal of Geophysical Research (1896-1977)*, 70(24):6017–6022, 1965. doi: 10.1029/JZ070i024p06017. URL https://agupubs.onlinelibrary.wiley.com/doi/abs/10.1029/JZ070i024p06017.

E. E. Gossard and W. H. Hooke. *Waves in the atmosphere : Atmospheric infrasound and gravity waves, their generation and propagation*, pages 423–440. Elsevier scientific, Amsterdam, 1975. ISBN 0444411968. URL https://lib.ugent.be/catalog/rug01:001379972.

A. Hajduk, E. Pittich, and B. McIntosh. Changes in radar meteor echo rates at sunrise. *Contributions of the Astronomical Observatory Skalnate Pleso*, 9:115, 01 1980. URL https://ui.adsabs.harvard.edu/abs/1980CoSka...9..115H. Provided by the SAO/NASA Astrophysics Data System.

A. E. Hedin, N. W. Spencer, and T. L. Killeen. Empirical global model of upper thermosphere winds based on atmosphere and dynamics explorer satellite data. *Journal of Geophysical Research: Space Physics*, 93(A9):9959–9978, 1988. doi: 10.1029/JA093iA09p09959. URL https://agupubs.onlinelibrary.wiley.com/doi/abs/10.1029/JA093iA09p09959.

A. E. Hedin, M. A. Biondi, R. G. Burnside, G. Hernandez, R. M. Johnson, T. L. Killeen, C. Mazaudier, J. W. Meriwether, J. E. Salah, R. J. Sica, R. W. Smith, N. W. Spencer, V. B. Wickwar, and T. S. Virdi. Revised global model of thermosphere winds using satellite and ground-based observations. *Journal of Geophysical Research: Space Physics*, 96(A5):7657–7688, 1991. doi: 10.1029/91JA00251. URL https://agupubs.onlinelibrary.wiley.com/doi/abs/10.1029/91JA00251.

W. K. Hocking. System design, signal-processing procedures, and preliminary results for the Canadian (London, Ontario) VHF atmospheric radar. *Radio Science*, 32(2):687–706, 1997. doi: 10.1029/96RS03316. URL https://agupubs.onlinelibrary.wiley.com/doi/abs/10.1029/96RS03316.

W. K. Hocking. Temperatures using radar-meteor decay times. *Geophysical Research Letters*, 26(21):3297–3300, 1999. doi: 10.1029/1999GL003618. URL https://ui.adsabs.harvard.edu/abs/1999GeoRL..26.3297H. Provided by the SAO/NASA Astrophysics Data System.

W. K. Hocking. VHF tropospheric scatterer anisotropy at Resolute Bay and its implications for tropospheric radar-derived wind accuracies. *Radio Science*, 36(6):1777–1793, 2001. doi: 10.1029/2000RS001002. URL https://agupubs.onlinelibrary.wiley.com/doi/abs/10.1029/2000RS001002.

W. K. Hocking. Radar meteor decay rate variability and atmospheric consequences. *Annales Geophysicae*, 22, 11 2004a. doi: 10.5194/angeo-22-3805-2004. URL https://www.ann-geophys.net/22/3805/2004/.

W. K. Hocking. Experimental radar studies of anisotropic diffusion of high altitude me-

teor trails. *Earth, Moon, and Planets*, 95(1):671–679, Dec 2004b. ISSN 1573-0794. doi: 10.1007/s11038-005-3446-5. URL https://doi.org/10.1007/s11038-005-3446-5.

W. K. Hocking and T. Thayaparan. Simultaneous and colocated observation of winds and tides by mf and meteor radars over London, Canada (43^o N, 81^o W), during 1994–1996. *Radio Science*, 32(2):833–865, 1997. doi: 10.1029/96RS03467. URL https://agupubs.onlinelibrary.wiley.com/doi/abs/10.1029/96RS03467.

W. K. Hocking, T. Thayaparan, and J. Jones. Meteor decay times and their use in determining a diagnostic mesospheric temperature-pressure parameter: Methodology and one year of data. *Geophysical Research Letters*, 24(23):2977–2980, 1997. doi: 10.1029/97GL03048. URL https://agupubs.onlinelibrary.wiley.com/doi/abs/10.1029/97GL03048.

W. K. Hocking, B. Fuller, and B. Vandepeer. Real-time determination of meteor-related parameters utilizing modern digital technology. *Journal of Atmospheric and Solar-Terrestrial Physics*, 63(2):155 – 169, 2001. ISSN 1364-6826. doi: https://doi.org/10.1016/S1364-6826(00)00138-3. URL http://www.sciencedirect.com/science/article/pii/S1364682600001383. Radar applications for atmosphere and ionosphere research - PIERS 1999.

W. K. Hocking, J. Röttger, R. D. Palmer, T. Sato, and P. B. Chilson. *Atmospheric Radar: Application and Science of MST Radars in the Earth's Mesosphere, Stratosphere, Troposphere, and Weakly Ionized Regions*. Cambridge University Press, 2016. doi: 10.1017/9781316556115.

D. A. Holdsworth, R. J. Morris, D. J. Murphy, I. M. Reid, G. B. Burns, and W. J. R. French. Antarctic mesospheric temperature estimation using the Davis mesosphere-stratosphere-troposphere radar. *Journal of Geophysical Research: Atmospheres*, 111(D5), 2006. doi: 10.1029/2005JD006589. URL https://agupubs.onlinelibrary.wiley.com/doi/abs/10.1029/2005JD006589.

M. Ichihara, M. Takeo, A. Yokoo, J. Oikawa, and T. Ohminato. Monitoring volcanic activity using correlation patterns between infrasound and ground motion. *Geophysical Research Letters*, 39(4), 2012. doi: 10.1029/2011GL050542. URL https://agupubs.onlinelibrary.wiley.com/doi/abs/10.1029/2011GL050542.

International Meteor Organization (IMO). Meteor shower calendar., 2007. URL https://www.imo.net/resources/calendar/. Last accessed February 12, 2016.

C. Jacobi. Meteor heights during the recent solar minimum. *Advances in Radio Science*, 12:161–165, 2014. doi: 10.5194/ars-12-161-2014. URL https://www.adv-radio-sci.net/12/161/2014/.

Japan Meteorological Agency (JMA). Monthly volcanic activity report. Report, Japan Meteorological Agency (JMA), Japan, 2018.

Japan Meteorological Agency (JMA). High-rise meteorological observation database, 2019. URL https://www.data.jma.go.jp/obd/stats/etrn/upper/. Last accessed 8 July, 2019.

P. Jenniskens. Meteor stream activity I. The annual streams. *Astronomy and Astrophysics*, 287:990–1013, Jul 1994. URL https://ui.adsabs.harvard.edu/abs/1994A&A...287..990J. Provided by the SAO/NASA Astrophysics Data System.

F. B. Jensen, W. A. Kuperman, M. B. Porter, and H. Schmidt. *Normal Modes*, pages 337–455. Springer New York, New York, NY, 2011. ISBN 978-1-4419-8678-8. doi: 10.1007/978-1-4419-8678-8_5. URL https://doi.org/10.1007/978-1-4419-8678-8_5.

S. John, K. kishore kumar, K. Subrahmanyam, G. Manju, and Q. Wu. Meteor radar measurements of MLT winds near the equatorial electro jet region over Thumba (8.5^o N, 77^o E): Comparison with TIDI observations. *Annales Geophysicae*, 29:1209–1214, 07 2011. doi: 10.5194/angeo-29-1209-2011. URL https://www.ann-geophys.net/29/1209/2011/.

J. B. Johnson. Generation and propagation of infrasonic airwaves from volcanic explosions. *Journal of Volcanology and Geothermal Research*, 121(1):1 – 14, 2003. ISSN 0377-0273. doi: https://doi.org/10.1016/S0377-0273(02)00408-0. URL http://www.sciencedirect.com/science/article/pii/S0377027302004080.

J. B. Johnson, R. C. Aster, and P. R. Kyle. Volcanic eruptions observed with infrasound. *Geophysical Research Letters*, 31(14), 2004. doi: 10.1029/2004GL020020. URL https://agupubs.onlinelibrary.wiley.com/doi/abs/10.1029/2004GL020020.

J. B. Johnson, J. M. Lees, and H. Yepes. Volcanic eruptions, lightning, and a waterfall: Differentiating the menagerie of infrasound in the ecuadorian jungle. *Geophysical Research Letters*, 33(6), 2006. doi: 10.1029/2005GL025515. URL https://agupubs.onlinelibrary.wiley.com/doi/abs/10.1029/2005GL025515.

G. O. L. Jones, F. T. Berkey, C. S. Fish, W. K. Hocking, and M. J. Taylor. Validation of imaging doppler interferometer winds using meteor radar. *Geophysical Research Letters*, 30(14), 2003. doi: 10.1029/2003GL017645. URL https://agupubs.onlinelibrary.wiley.com/doi/abs/10.1029/2003GL017645.

J. Jones, A. R. Webster, and W. K. Hocking. An improved interferometer design for use with meteor radars. *Radio Science*, 33(1):55–65, 1998. doi: 10.1029/97RS03050. URL https://agupubs.onlinelibrary.wiley.com/doi/abs/10.1029/97RS03050.

J. Kero, C. Szasz, T. Nakamura, D. D. Meisel, M. Ueda, Y. Fujiwara, T. Terasawa, K. Nishimura, and J. Watanabe. The 2009–2010 MU radar head echo observation programme for sporadic and shower meteors: Radiant densities and diurnal rates. *Monthly Notices of the Royal Astronomical Society*, 425(1):135–146, 09 2012. ISSN 0035-8711. doi: 10.1111/j.1365-2966.2012.21407.x. URL https://doi.org/10.1111/j.1365-2966.2012.21407.x.

Kochi University of Technology (KUT). Kochi university of technology infrasound observation data monitoring system, 2015. URL http://infrasound.kochi-tech.ac.jp/infrasound/. Last accessed 20 January, 2019.

A. J. Koscielny, R. J. Doviak, and D. S. Zrnic. An evaluation of the accuracy of some radar wind profiling techniques. *Journal of Atmospheric and Oceanic Technology*, 1(4):309–320, 1984. doi: 10.1175/1520-0426(1984)001<0309:AEOTAO>2.0.CO;2. URL https://doi.org/10.1175/1520-0426(1984)001<0309:AEOTAO>2.0.CO;2.

A. Kozlovsky, R. Lukianova, S. Shalimov, and M. Lester. Mesospheric temperature estimation from meteor decay times during geminids meteor shower. *Journal of Geophysical Research: Space Physics*, 121(2):1669–1679, 2016. doi: 10.1002/2015JA022222. URL https://agupubs.onlinelibrary.wiley.com/doi/abs/10.1002/2015JA022222.

E. Kudeki and G. R. Stitt. Frequency domain interferometry: A high resolution radar technique for studies of atmospheric turbulence. *Geophysical Research Letters*, 14(3):198–201, 1987. doi: 10.1029/GL014i003p00198. URL https://agupubs.onlinelibrary.wiley.com/doi/abs/10.1029/GL014i003p00198.

Kyoto University. Meteor wind and medium frequency radar data over Indonesia, 2015. URL https://database.rish.kyoto-u.ac.jp/arch/iugonet. Last accessed 12 February, 2016.

M. Landès, L. Ceranna, A. Le Pichon, and R. S. Matoza. Localization of microbarom sources using the IMS infrasound network. *Journal of Geophysical Research: Atmospheres*, 117(D6), 2012. doi: 10.1029/2011JD016684. URL https://agupubs.onlinelibrary.wiley.com/doi/abs/10.1029/2011JD016684.

R. Latteck, W. Singer, M. Rapp, B. Vandepeer, T. Renkwitz, M. Zecha, and G. Stober. MAARSY: The new MST radar on Andøya—System description and first results. *Radio Science*, 47(1), 2012. doi: 10.1029/2011RS004775. URL https://agupubs.onlinelibrary.wiley.com/doi/abs/10.1029/2011RS004775.

G. Le Pichon, Alexis and C. Y. Infrasoniv waves from natural sources. In *Proc. 2001 infrasound technology workshop*, Kailua-Kona, Hawaii, 2001.

Lembaga Penerbangan dan Antariksa Nasional (LAPAN). Repository database Sains An-

tariksa, 2015. URL https://bimasakti.sains.lapan.go.id. Last accessed 12 February, 2016.

L. Lima, L. Araújo, E. Alves, P. Batista, and B. Clemesha. Variations in meteor heights at 22.7^o S during solar cycle 23. *Journal of Atmospheric and Solar-Terrestrial Physics*, 133:139 – 144, 2015. ISSN 1364-6826. doi: https://doi.org/10.1016/j.jastp.2015.08.015. URL http://www.sciencedirect.com/science/article/pii/S1364682615300419.

B. A. Lindblad. Solar cycle variations in atmospheric density as deduced from meteor observations. *Meddelanden fran Lunds Astronomiska Observatorium Serie I*, 226:1029–1043, Jan 1967. URL https://ui.adsabs.harvard.edu/abs/1967MeLuF.226.1029L. Provided by the SAO/NASA Astrophysics Data System.

B. A. Lindblad. Solar control of meteor radar rates. In A. Wilson, editor, *Solar Variability as an Input to the Earth's Environment*, volume 535 of *ESA Special Publication*, pages 755–759, Sep 2003. URL https://ui.adsabs.harvard.edu/abs/2003ESASP.535..755L. Provided by the SAO/NASA Astrophysics Data System.

L. Liszka and M. A. Garces. Infrasonic observations of the Hekla eruption of February 26, 2000. *Journal of Low Frequency Noise, Vibration and Active Control*, 21(1):1–8, 2002. doi: 10.1260/02630920260374934. URL https://doi.org/10.1260/02630920260374934.

L. Liu, H. Liu, Y. Chen, H. Le, Y.-Y. Sun, B. Ning, L. Hu, and W. Wan. Variations of the meteor echo heights at Beijing and Mohe, China. *Journal of Geophysical Research: Space Physics*, 122(1):1117–1127, 2017. doi: 10.1002/2016JA023448. URL https://agupubs.onlinelibrary.wiley.com/doi/abs/10.1002/2016JA023448.

T. Lopez, D. Fee, F. Prata, and J. Dehn. Characterization and interpretation of volcanic activity at Karymsky volcano, Kamchatka, Russia, using observations of infrasound, volcanic emissions, and thermal imagery. *Geochemistry, Geophysics, Geosystems*, 14(12):5106–5127,

2013. doi: 10.1002/2013GC004817. URL https://agupubs.onlinelibrary.wiley.com/doi/abs/10.1002/2013GC004817.

K. Maegawa. HRO: A New Forward-Scatter Observation Method Using a Ham-Band Beacon. *WGN, Journal of the International Meteor Organization*, 27(1):64–72, Feb 1999. URL https://ui.adsabs.harvard.edu/abs/1999JIMO...27...64M. Provided by the SAO/NASA Astrophysics Data System.

E. Marchetti, M. Ripepe, G. Ulivieri, S. Caffo, and E. Privitera. Infrasonic evidences for branched conduit dynamics at Mt. Etna volcano, Italy. *Geophysical Research Letters*, 36(19), 2009. doi: 10.1029/2009GL040070. URL https://agupubs.onlinelibrary.wiley.com/doi/abs/10.1029/2009GL040070.

R. S. Matoza and D. Fee. Infrasonic component of volcano-seismic eruption tremor. *Geophysical Research Letters*, 41(6):1964–1970, 2014. doi: 10.1002/2014GL059301. URL https://agupubs.onlinelibrary.wiley.com/doi/abs/10.1002/2014GL059301.

R. S. Matoza, J. Vergoz, A. Le Pichon, L. Ceranna, D. N. Green, L. G. Evers, M. Ripepe, P. Campus, L. Liszka, T. Kvaerna, E. Kjartansson, and Ármann. Long-range acoustic observations of the Eyjafjallajökull eruption, Iceland, April–May 2010. *Geophysical Research Letters*, 38(6), 2011. doi: 10.1029/2011GL047019. URL https://agupubs.onlinelibrary.wiley.com/doi/abs/10.1029/2011GL047019.

B. McIntosh and A. Hajduk. Sunrise Effect on Persistent Radar Echoes from Sporadic Meteors. *Bulletin of the Astronomical Institutes of Czechoslovakia*, 28:280, Jan 1977. URL https://ui.adsabs.harvard.edu/abs/1977BAICz..28..280M. Provided by the SAO/NASA Astrophysics Data System.

D. W. R. McKinley. *Meteor science and engineering.* McGraw-Hill; First Edition edition (1961), 1961. URL https://ui.adsabs.harvard.edu/abs/1961mse..book....M. Provided by the SAO/NASA Astrophysics Data System.

P. M. Millman and D. W. R. McKinley. Meteors. In The Moon Meteorites and Comets, Edited by Gerard P. Kuiper, and Barbarra Middlehurts. Chicago: The University of Chicago Press, 1963, p.674, editor, *Kuiper, Gerard P. and Middlehurst, Barbara M.*, page 674. Univ of Chicago Pr (July 1, 1963), 1963. URL https://ui.adsabs.harvard.edu/abs/1963mmc..book..674M. Provided by the SAO/NASA Astrophysics Data System.

MIROVA. Thermal anomalies, 2018. URL http://www.mirovaweb.it/. Last accessed 13 January, 2018.

S. Mizumoto. Calculation of meteor orbit by multiple-site radio observation and construction of a comprehensive meteor observation system. Master thesis, Kochi University of Technology, Japan, 2015. written in Japanese.

S. Mizumoto, M.-Y. Yamamoto, and M. Batubara. Construction of a meteor orbit calculation system for comprehensive meteor observation at Kochi University of Technology. *Planetary and Space Science*, 173:35 – 41, 2019. ISSN 0032-0633. doi: https://doi.org/10.1016/j.pss.2019.03.004. URL http://www.sciencedirect.com/science/article/pii/S0032063316302756.

National Oceanic and Atmospheric Administration (NOAA). NOAA/ESRL radiosonde database, 2019. URL https://ruc.noaa.gov/raobs/. Last accessed 8 July, 2019.

K. Noguchi and M.-Y. Yamamoto. Development of an automatic echo-counting program for HROFFT spectrograms. In A. in Meteoroid and M. Science, editors, *Trigo-Rodríguez, J. M. and Rietmeijer, F. J. M. and Llorca, J. and Janches, D.*, pages 323–329. Springer New York, New York, NY, 2008. ISBN 978-0-387-78419-9. doi: 10.1007/978-0-387-78419-9_46. URL https://doi.org/10.1007/978-0-387-78419-9_46.

J. V. Olson and C. A. Szuberla. Processing infrasonic array data. In H. of Signal Processing in Acoustics, editor, *Havelock, David and Kuwano, Sonoko and Vorländer, Michael*, pages 1487–1496. Springer New York, New York, NY, 2008. ISBN 978-0-387-30441-0. doi: 10.1007/978-0-387-30441-0_81. URL https://doi.org/10.1007/978-0-387-30441-0_81.

J. V. Olson and C. A. L. Szuberla. Distribution of wave packet sizes in microbarom wave trains observed in Alaska. *The Journal of the Acoustical Society of America*, 117(3):1032–1037, 2005. doi: 10.1121/1.1854651. URL https://doi.org/10.1121/1.1854651.

Y. Omonori. Development of meteor orbit measurement method based on 5ch interferometer and multipoint observation and KUT meteor radio wave - improvement of observation system. Master thesis, Kochi University of Technology, Japan, 2011. written in Japanese.

P. Pecina and M. Simek. Analysis of the Geminid meteor stream, 1958-1997, from radar observations 1997, from radar observations. *Astronomy and Astrophysics*, 344:991–1000, 1999. URL https://ui.adsabs.harvard.edu/abs/1999A&A...344..991P. Provided by the SAO/NASA Astrophysics Data System.

A. Pellinen-Wannberg, E. Murad, N. Brosch, I. Häggström, and T. Khayrov. The solar cycle effect on the atmosphere as a scintillator for meteor observations. *Proceedings of the International Astronomical Union*, 5:249 – 252, 2009. doi: 10.1017/S1743921310001869.

J. M. Picone, A. E. Hedin, D. P. Drob, and A. C. Aikin. NRLMSISE-00 empirical model of the atmosphere: Statistical comparisons and scientific issues. *Journal of Geophysical Research: Space Physics*, 107(A12):SIA 15–1–SIA 15–16, 2002. doi: 10.1029/2002JA009430. URL https://agupubs.onlinelibrary.wiley.com/doi/abs/10.1029/2002JA009430.

D. Ponceau and L. Bosca. Low-noise broadband microbarometers. In Infrasound Monitoring for Atmospheric Studies, editor, *Le Pichon, Alexis and Blanc, Elisabeth and Hauchecorne, Alain*, pages 119–140. Springer Netherlands, Dordrecht, 2009. doi: 10.1007/978-1-4020-9508-5_4. URL https://doi.org/10.1007/978-1-4020-9508-5_4.

L. M. G. Poole. A simplified interferometer design for use with meteor radars. *Radio Science*, 39(2), 2004. doi: 10.1029/2002RS002778. URL https://agupubs.onlinelibrary.wiley.com/doi/abs/10.1029/2002RS002778.

V. Porubcan. Distribution of meteor heights and the solar cycle activity. *Contributions of the Astronomical Observatory Skalnate Pleso*, 22:33–39, 1992. URL https://ui.adsabs.harvard.edu/abs/1992CoSka..22...33P. Provided by the SAO/NASA Astrophysics Data System.

V. Porubcan and G. Cevolani. Distribution of meteor heights and sunrise. *Bulletin of the Astronomical Institutes of Czechoslovakia*, 34:213–219, 06 1983. URL https://ui.adsabs.harvard.edu/abs/1983BAICz..34..213P. Provided by the SAO/NASA Astrophysics Data System.

V. Porubcan, M. Bucek, G. Cevolani, and P. Zigo. Variation of Meteor Heights and Solar-Cycle Activity. *Publications of the Astronomical Society of Japan*, 64(4), 2012. ISSN 0004-6264. doi: 10.1093/pasj/64.4.86. URL https://doi.org/10.1093/pasj/64.4.86.

P. Prikryl. Radar meteor rates and solar activity. *Bulletin of the Astronomical Institutes of Czechoslovakia*, 34:44–50, 1983. URL https://ui.adsabs.harvard.edu/abs/1983BAICz..34...44P. Provided by the SAO/NASA Astrophysics Data System.

L. Qian and S. Solomon. Thermospheric density: An overview of temporal and spatial variations. *Space Science Reviews*, 168:1–27, 2011. doi: 10.1007/s11214-011-9810-z. URL https://link.springer.com/article/10.1007/s11214-011-9810-z.

M. Ripepe, M. Coltelli, E. Privitera, S. Gresta, M. Moretti, and D. Piccinini. Seismic and infrasonic evidences for an impulsive source of the shallow volcanic tremor at Mt. Etna, Italy. *Geophysical Research Letters*, 28(6):1071–1074, 2001. doi: 10.1029/2000GL011391. URL https://agupubs.onlinelibrary.wiley.com/doi/abs/10.1029/2000GL011391.

M. Ripepe, S. De Angelis, G. Lacanna, and B. Voight. Observation of infrasonic and gravity waves at Soufrière Hills volcano, Montserrat. *Geophysical Research Letters*, 37(19), 2010. doi: 10.1029/2010GL042557. URL https://agupubs.onlinelibrary.wiley.com/doi/abs/10.1029/2010GL042557.

Royal Observatory of Belgium (ROB). World data center-sunspot index and long-term solar observations., 2013. URL http://sidc.be/silso/datafiles. Last accessed February 12, 2016.

A. M. Runco. Detection optimization of the progressive multi-channel correlation algorithm used in infrasound nuclear treaty monitoring. master thesis, Air University, 2013. URL https://ntrl.ntis.gov/NTRL/dashboard/searchResults/titleDetail/ADA590009.xhtml.

J. Röttger and H. M. Ierkic. Postset beam steering and interferometer applications of VHF radars to study winds, waves, and turbulence in the lower and middle atmosphere. *Radio Science*, 20(6):1461–1480, 1985. doi: 10.1029/RS020i006p01461. URL https://agupubs.onlinelibrary.wiley.com/doi/abs/10.1029/RS020i006p01461.

E. Salomons. *Computational Atmospheric Acoustics*. Springer Netherlands, 2001. ISBN 9781402003905. URL https://books.google.co.jp/books?id=Lo-tMmH6EqMC.

E. M. Salomons. Caustic diffraction fields in a downward refracting atmosphere. *The Journal of the Acoustical Society of America*, 104(6):3259–3272, 1998. doi: 10.1121/1.423966. URL https://doi.org/10.1121/1.423966.

K. Sato, M. Tsutsumi, T. Sato, T. Nakamura, A. Saito, Y. Tomikawa, K. Nishimura, M. Kohma, H. Yamagishi, and T. Yamanouchi. Program of the Antarctic Syowa MST/IS radar. In *2014 XXXIth URSI General Assembly and Scientific Symposium (URSI GASS)*, pages 1–1, 2014. doi: 10.1109/URSIGASS.2014.6929774. URL https://ieeexplore.ieee.org/document/6929774.

M. Šimek and P. Pecina. Radar sporadic meteor rates and solar activity. *Earth, Moon, and Planets*, 88(2):115–122, 2000. ISSN 1573-0794. doi: 10.1023/A:1015816116844. URL https://doi.org/10.1023/A:1015816116844.

W. Singer, J. Bremer, J. Weiß, W. Hocking, J. Höffner, M. Donner, and P. Espy. Meteor radar observations at middle and arctic latitudes part 1: Mean temperatures. *Journal of Atmospheric and Solar-Terrestrial Physics*, 66(6):607 – 616, 2004. ISSN 1364-6826. doi: https://doi.org/10.1016/j.jastp.2004.01.012. URL http://www.sciencedirect.com/science/article/pii/S1364682604000240. Dynamics and Chemistry of the MLT Region - PSMOS 2002 International Symposium.

A. M. Skellett. The effect of meteors on radio transmission through the Kennelly-Heaviside layer. *Phys. Rev.*, 37:1668–1668, 1931. doi: 10.1103/PhysRev.37.1668. URL https://link.aps.org/doi/10.1103/PhysRev.37.1668.

A. M. Skellett. The ionizing effects of meteors. *Proceedings of the Institute of Radio Engineers*, 23(2):132–149, 1935. ISSN 2162-6626. doi: 10.1109/IRE.1935.6449184. URL https://ieeexplore.ieee.org/document/6449184.

E. Smart and E. A. Flinn. Fast Frequency-Wavenumber Analysis and Fisher Signal Detection in Real-Time Infrasonic Array Data Processing. *Geophysical Journal International*, 26(1-4):279–284, 12 1971. ISSN 0956-540X. doi: 10.1111/j.1365-246X.1971.tb03401.x. URL https://doi.org/10.1111/j.1365-246X.1971.tb03401.x.

S. W. Smith. *The Scientist and Engineer's Guide to Digital Signal Processing*. California Technical Publishing, 1997. URL http://www.dspguide.com. Available at www.dspguide.com.

Space Laboratory of KUT. KUT Infrasound March 2018, 2019. URL https://figshare.com/articles/KUT_Infrasound_March2018/8319824.

G. Stober, C. Jacobi, V. Matthias, P. Hoffmann, and M. Gerding. Neutral air density variations during strong planetary wave activity in the mesopause region derived from meteor radar observations. *Journal of Atmospheric and Solar-Terrestrial Physics*, 74:55 – 63, 2012. ISSN 1364-6826. doi: https://doi.org/10.1016/j.jastp.2011.10.007. URL http://www.sciencedirect.com/science/article/pii/S136468261100280X.

G. Stober, C. Schult, C. Baumann, R. Latteck, and M. Rapp. The geminid meteor shower during the ECOMA sounding rocket campaign: Specular and head echo radar observations. *Annales Geophysicae*, 31:473–487, 2013. doi: 10.5194/angeo-31-473-2013. URL https://www.ann-geophys.net/31/473/2013/.

G. Stober, V. Matthias, P. Brown, and J. L. Chau. Neutral density variation from specular meteor echo observations spanning one solar cycle. *Geophysical Research Letters*, 41(19):6919–6925, 2014. doi: 10.1002/2014GL061273. URL https://agupubs.onlinelibrary.wiley.com/doi/abs/10.1002/2014GL061273.

L. C. Sutherland and H. E. Bass. Atmospheric absorption in the atmosphere up to 160 km. *The Journal of the Acoustical Society of America*, 115(3):1012–1032, 2004. doi: 10.1121/1.1631937. URL https://doi.org/10.1121/1.1631937.

G. J. Symons. The eruption of Krakatoa and subsequent phenomena. *Quarterly Journal of the Royal Meteorological Society*, 14(68):301–307, 1888. doi: 10.1002/qj.4970146809. URL https://rmets.onlinelibrary.wiley.com/doi/abs/10.1002/qj.4970146809.

C. Szasz, J. Kero, A. Pellinen-Wannberg, J. D. Mathews, N. J. Mitchell, and W. Singer. Latitudinal variations of diurnal meteor rates. *Earth, Moon, and Planets*, 95(1):101–107, 2004. ISSN 1573-0794. doi: 10.1007/s11038-005-9007-0. URL https://doi.org/10.1007/s11038-005-9007-0.

H. Takahashi, T. Nakamura, T. Tsuda, R. A. Buriti, and D. Gobbi. First measurement of atmospheric density and pressure by meteor diffusion coefficient and airglow oh temperature in the mesopause region. *Geophysical Research Letters*, 29(8):6–1–6–4, 2002. doi: 10.1029/2001GL014101. URL https://agupubs.onlinelibrary.wiley.com/doi/abs/10.1029/2001GL014101.

The National Aeronautics and Space Administration (NASA). NASA/GSFC's space physics data facility's omniweb data., 2005. URL http://https//omniweb.gsfc.nasa.gov/. Last accessed February 12, 2016.

T. Tsuda, M. Yamamoto, H. Hashiguchi, K. Shiokawa, Y. Ogawa, S. Nozawa, H. Miyaoka, and A. Yoshikawa. A proposal on the study of solar-terrestrial coupling processes with atmospheric radars and ground-based observation network. *Radio Science*, 51(9):1587–1599, 2016. doi: 10.1002/2016RS006035. URL https://agupubs.onlinelibrary.wiley.com/doi/abs/10.1002/2016RS006035.

R. M. Waxler, J. D. Assink, C. Hetzer, and D. Velea. NCPAprop—A software package for infrasound propagation modeling. *The Journal of the Acoustical Society of America*, 141 (5):3627–3627, 2017. doi: 10.1121/1.4987797. URL https://doi.org/10.1121/1.4987797.

C. R. Wilson and J. V. Olson. Mountain associated waves at I53US and I55US in Alaska and Antartica in the frequency passband from 0.015 to 0.10 Hz. *Inframatics*, 3:6–10, 2003.

C. R. Wilson, C. A. L. Szuberla, and J. V. Olson. High-latitude observations of infrasound from Alaska and Antarctica: Mountain associated waves and geomagnetic/auroral infrasonic signals. In Infrasound Monitoring for Atmospheric Studies, editor, *Le Pichon, Alexis and Blanc, Elisabeth and Hauchecorne, Alain*. Springer Netherlands, Dordrecht, 2009. ISBN 978-1-4020-9508-5. doi: 10.1007/978-1-4020-9508-5_13. URL https://doi.org/10.1007/978-1-4020-9508-5_13".

M.-Y. Yamamoto and A. Yokota. Infrasound monitoring for disaster prevention from geophysical destructions. submitted and presented in The 5th Internationnl Symposium on Frontier Technology 2015 (ISFT 2015), Kunming, China (Jul. 2015), 2015.

W. Yi, X. Xue, J. Chen, X. Dou, T. Chen, and N. Li. Estimation of mesopause temperatures at low latitudes using the Kunming meteor radar. *Radio Science*, 51(3):130–141, 2016. doi: 10.1002/2015RS005722. URL https://agupubs.onlinelibrary.wiley.com/doi/abs/10.1002/2015RS005722.

W. Yi, X. Xue, I. M. Reid, J. P. Younger, J. Chen, T. Chen, and N. Li. Estimation of mesospheric densities at low latitudes using the Kunming meteor radar together with SABER temperatures. *Journal of Geophysical Research: Space Physics*, 123(4):3183–3195, 2018. doi:

10.1002/2017JA025059. URL https://agupubs.onlinelibrary.wiley.com/doi/abs/10.1002/2017JA025059.

P. T. Younger, I. Astin, D. J. Sandford, and N. J. Mitchell. The sporadic radiant and distribution of meteors in the atmosphere as observed by VHF radar at Arctic, Antarctic and equatorial latitudes. *Annales Geophysicae*, 27(7):2831–2841, 2009. doi: 10.5194/angeo-27-2831-2009. URL https://www.ann-geophys.net/27/2831/2009/.

P. Zigo, V. Porubčan, G. Cevolani, and G. Pupillo. The activity and mass distribution of the Geminid meteor shower of 1996-2007 from forward scatter radio observations. *Contributions of the Astronomical Observatory Skalnate Pleso*, 39(1):5–17, 2009. URL https://ui.adsabs.harvard.edu/abs/2009CoSka..39....5Z. Provided by the SAO/NASA Astrophysics Data System.

APPENDIX A

Supporting Tables for Chapter 4

Content of this file

Figures A.1 to A.16

Introduction

Additional explanations related to the pictures below are as follows:

- Original infrasound data for event at 15:58 JST on March 9, 2018, at 04:05 JST, 07:46 JST on March 11, 2018, at 12:45 JST on March 12, 2018, at 14:13 JST on March 15, 2018, and at 07:35 JST on March 25, 2018 (Figure A.1 to A.6);

- A set of noise-PDF plots for stations on Shikoku Island during the period of active eruptions (Figure A.7-A.9) and during inactive eruptions (Figure A.10-A.12);

- A set of noise-PDF plots for infrasound stations KUT08 (Figure A.13) and KUT10 (Figure A.14);

- Records of the Mt. Shinmoedake eruptions at 04:05 JST on March 11, 2018 (Figure A.15); and at 12:45 JST on March 12, 2018 (Figure A.16) from the stations on Shikoku Island.

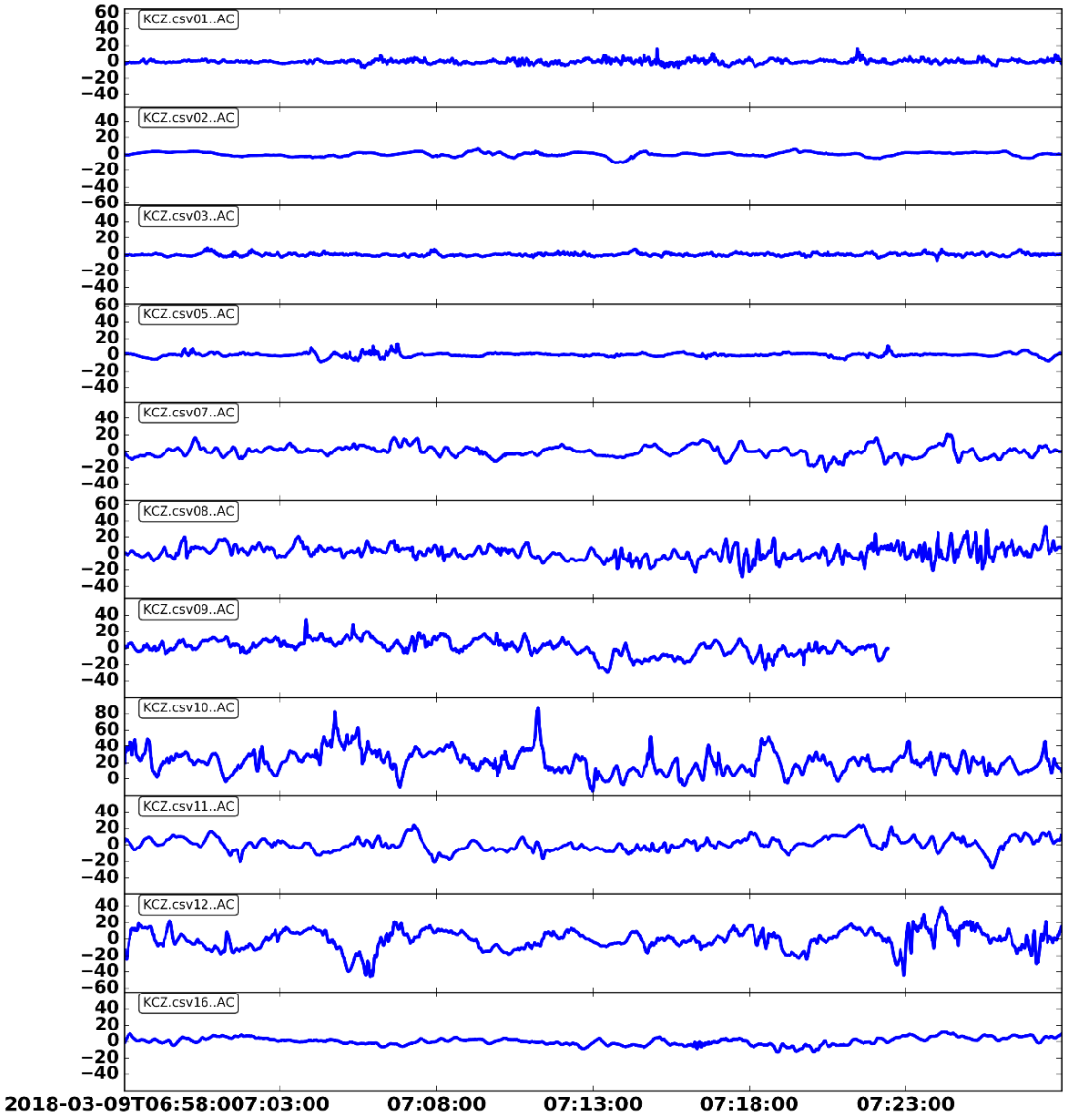

Figure A.1: Infrasonic pressure data for the event at 15:58 JST on March 9, 2018 showing the arrival times of air pressure disturbances for stations on Shikoku Island following the Mt. Shinmoedake eruption. The x-axis is the observation time in UTC, and the y-axis is the infrasonic pressure in Pa.

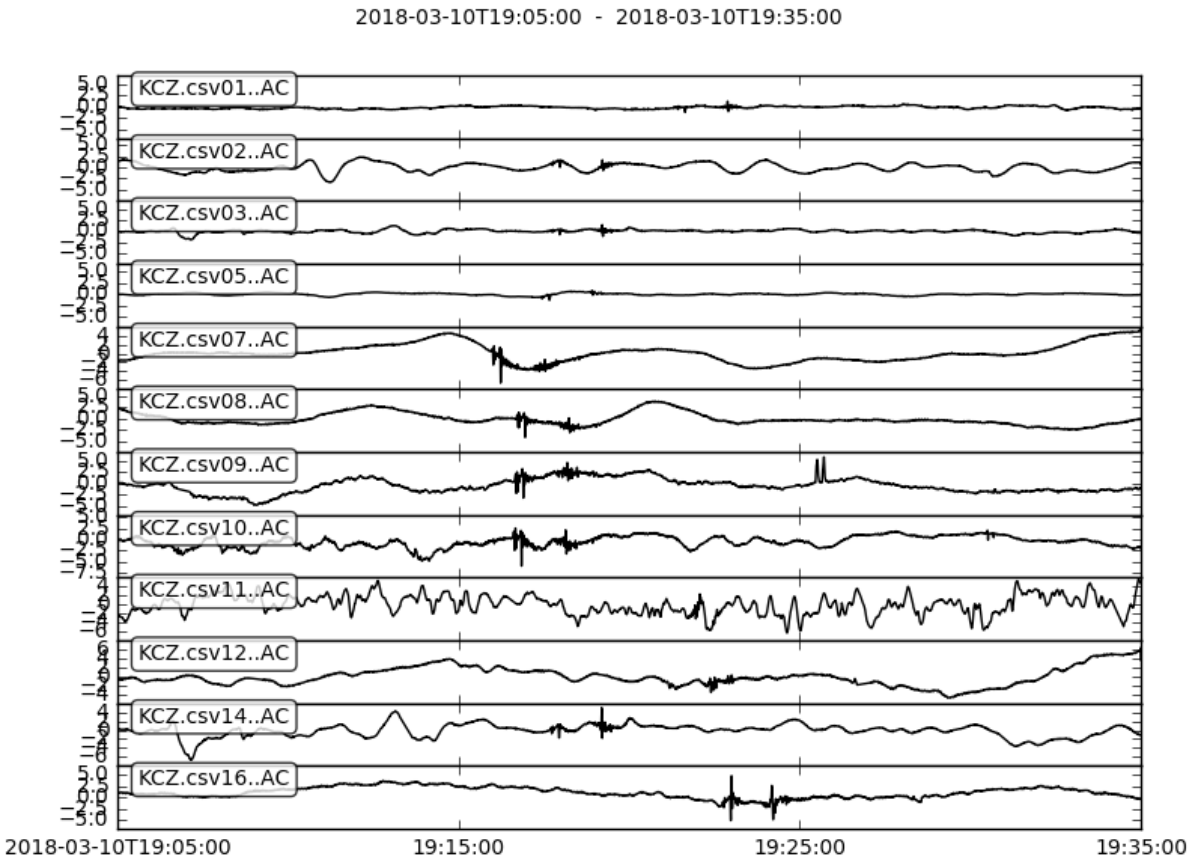

Figure A.2: Infrasonic pressure data for the event at 04:05 JST on March 11, 2018 showing the arrival times of air pressure disturbances for stations on Shikoku Island following the Mt. Shinmoedake eruption. The x-axis is the observation time in UTC, and the y-axis is the infrasonic pressure in Pa.

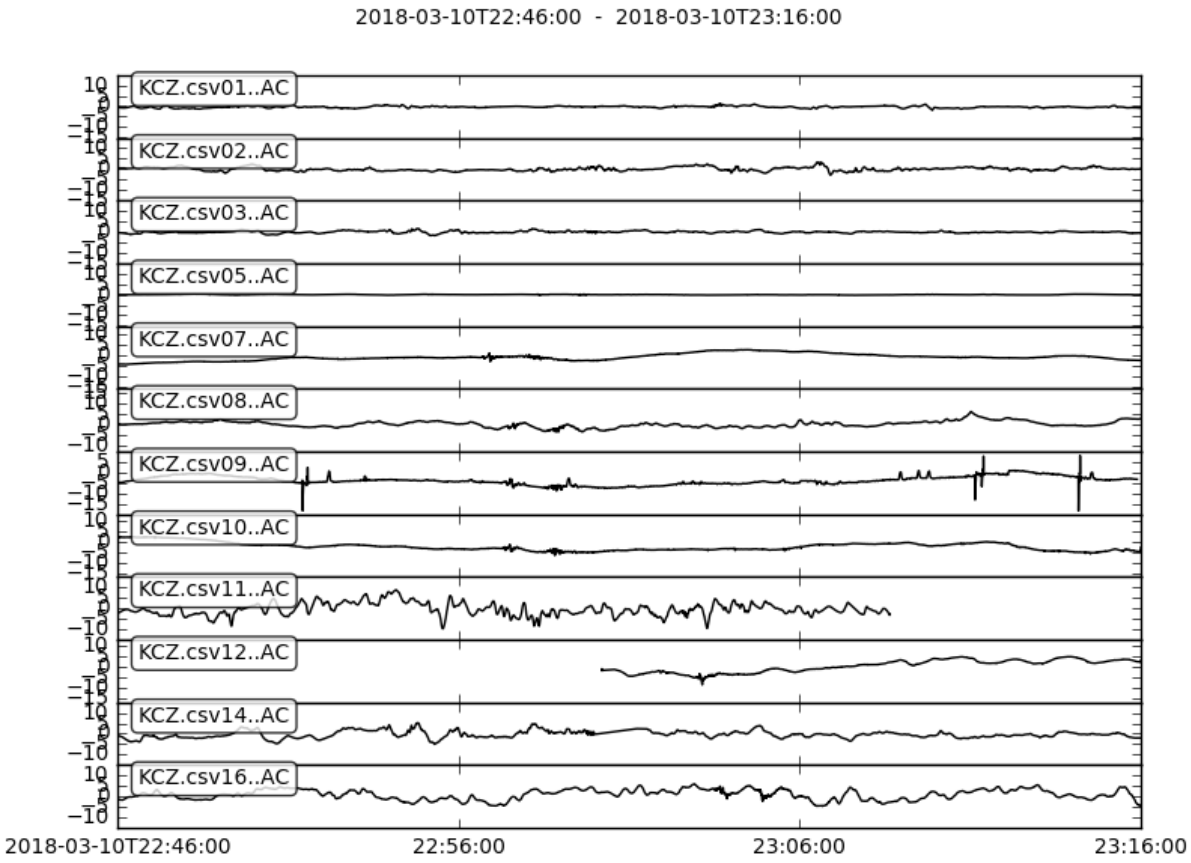

Figure A.3: Infrasonic pressure data for the event at 07:46 JST on March 11, 2018 showing the arrival times of air pressure disturbances for stations on Shikoku Island following the Mt. Shinmoedake eruption. The x-axis is the observation time in UTC, and the y-axis is the infrasonic pressure in Pa.

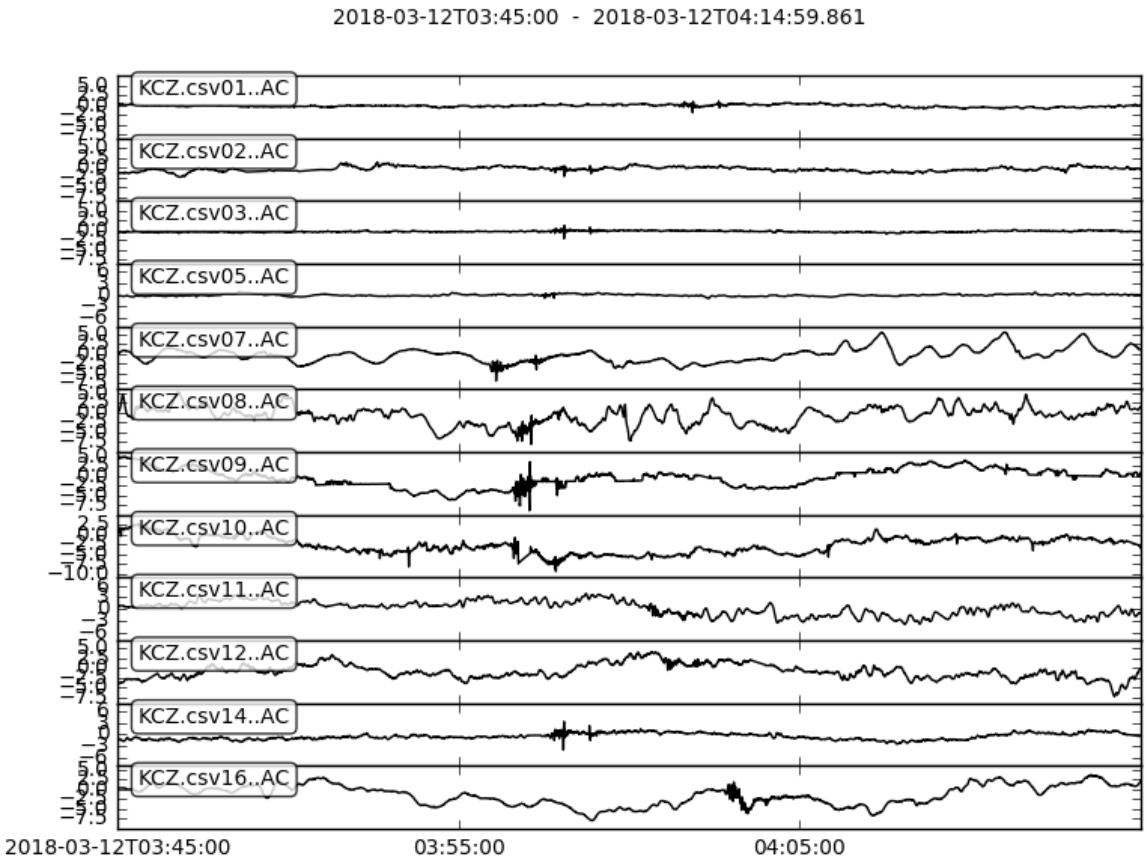

Figure A.4: Infrasonic pressure data for the event at 12:45 JST on March 12, 2018 showing the arrival times of air pressure disturbances for stations on Shikoku Island following the Mt. Shinmoedake eruption. The x-axis is the observation time in UTC, and the y-axis is the infrasonic pressure in Pa.

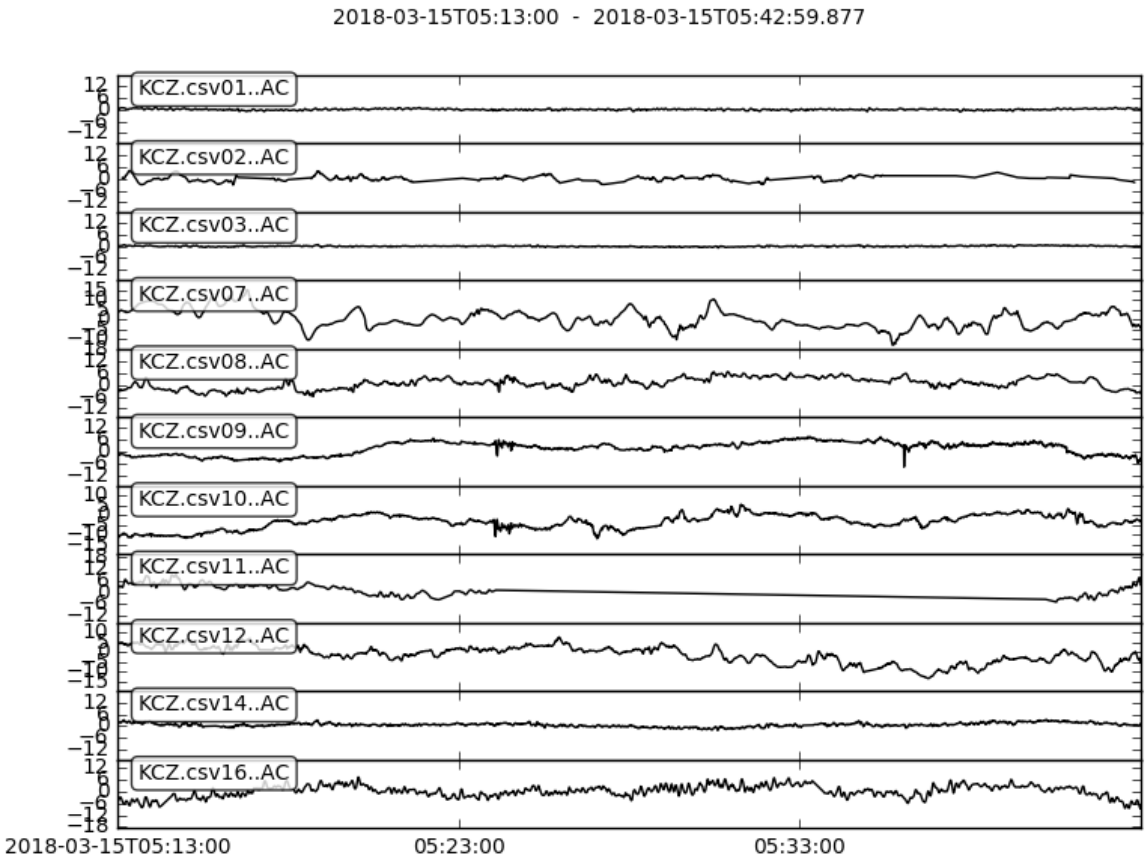

Figure A.5: Infrasonic pressure data for the event at 14:13 JST on March 15, 2018 showing the arrival times of air pressure disturbances for stations on Shikoku Island following the Mt. Shinmoedake eruption. The x-axis is the observation time in UTC, and the y-axis is the infrasonic pressure in Pa.

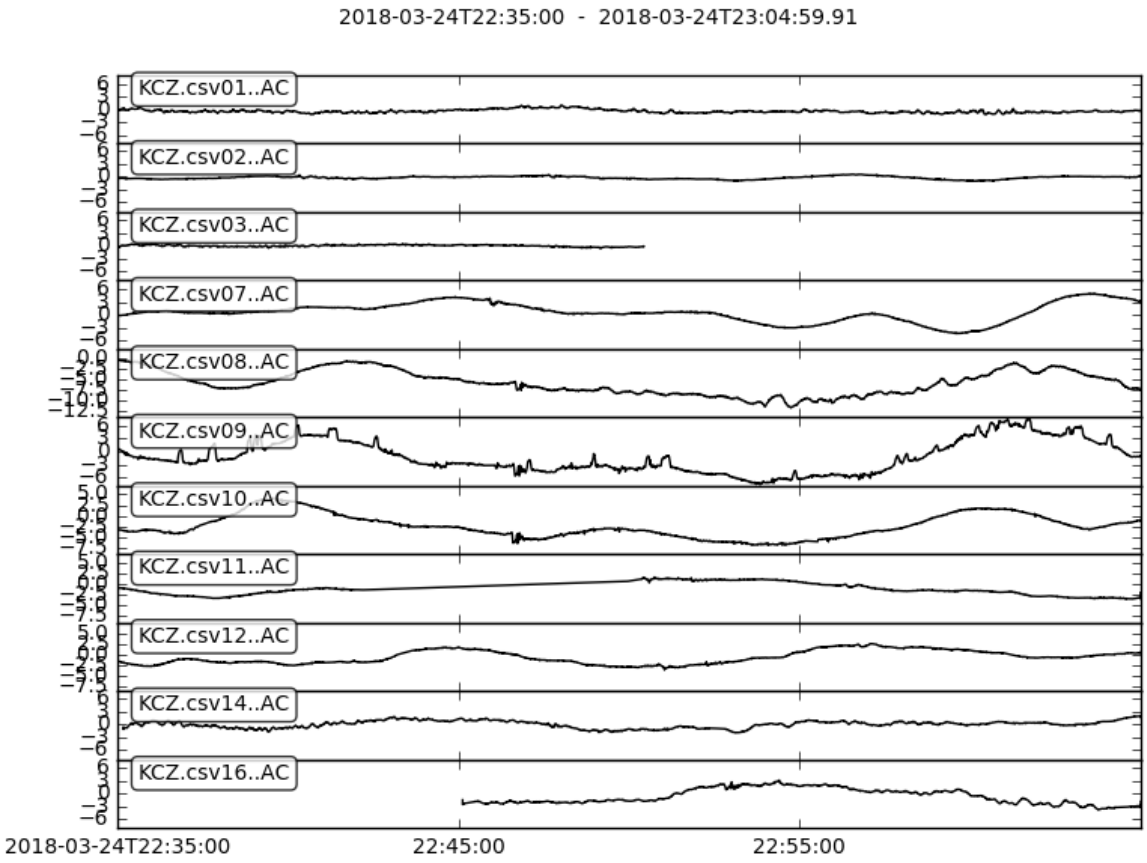

Figure A.6: Infrasonic pressure data for the event at 07:35 JST on March 25, 2018 showing the arrival times of air pressure disturbances for stations on Shikoku Island following the Mt. Shinmoedake eruption. The x-axis is the observation time in UTC, and the y-axis is the infrasonic pressure in Pa.

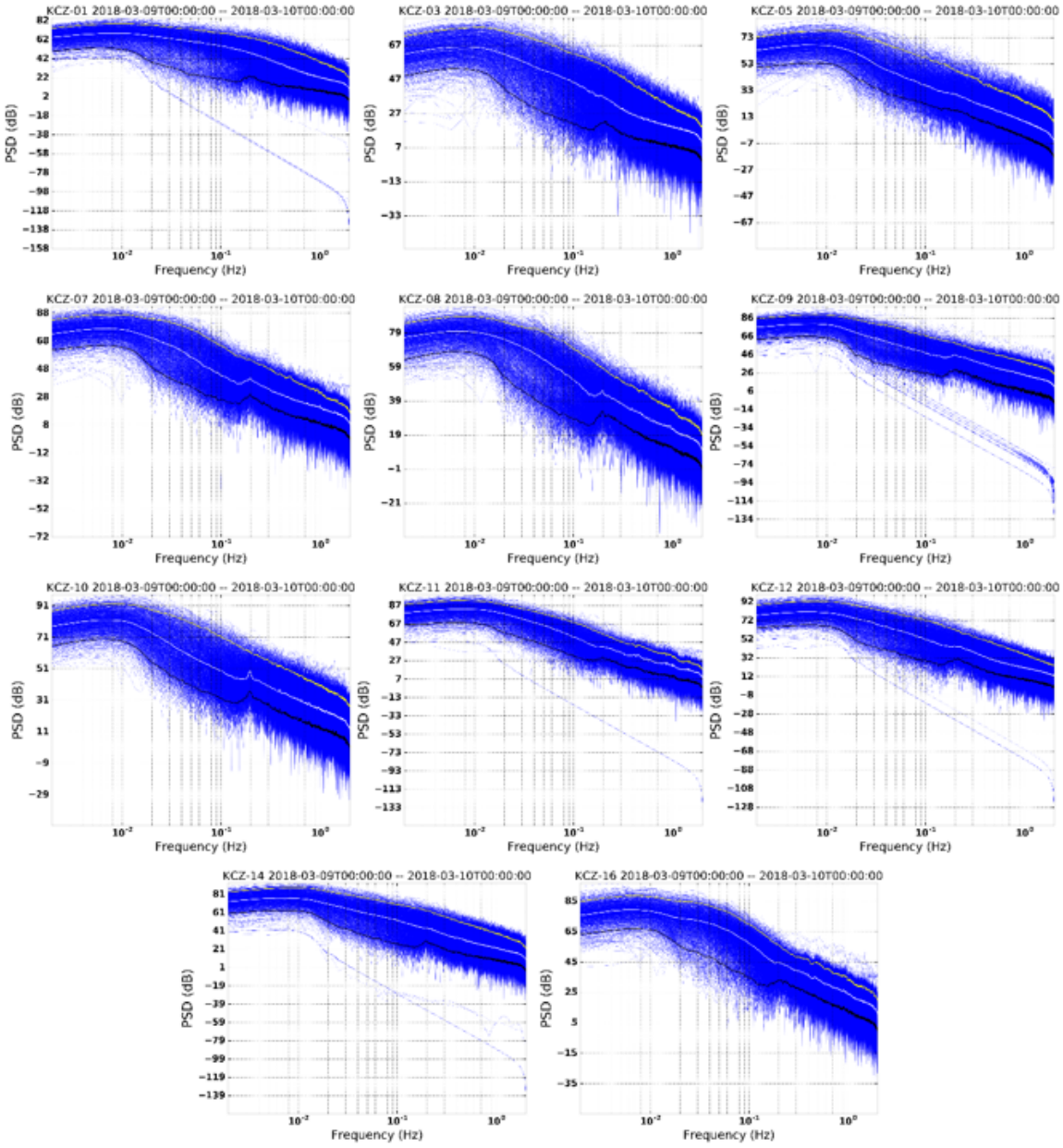

Figure A.7: A set of noise-PSD plots for 11 stations on Shikoku Island during one-day period on March 9, 2018.

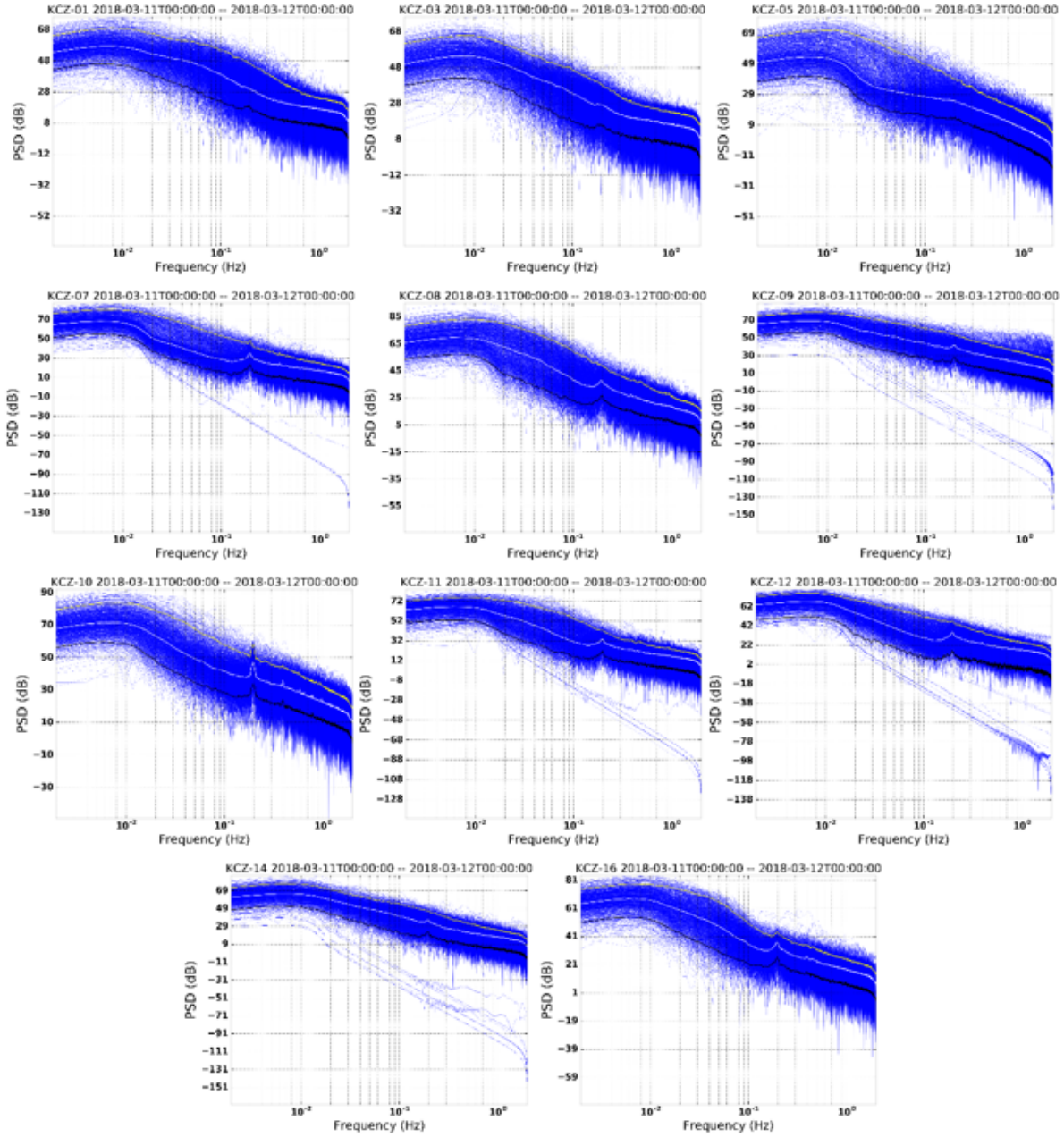

Figure A.8: A set of noise-PSD plots for 11 stations on Shikoku Island during one-day period on March 11, 2018.

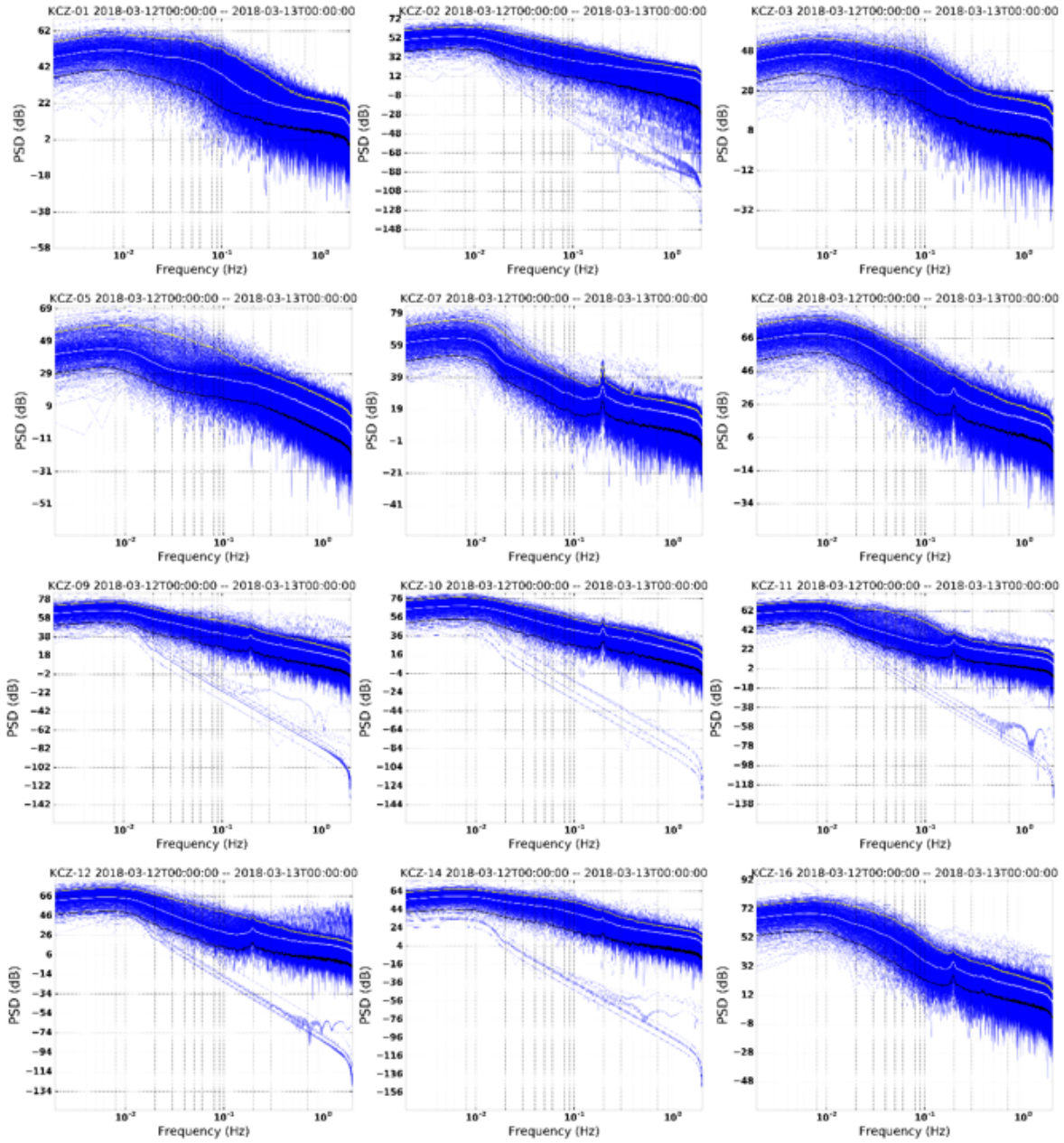

Figure A.9: A set of noise-PSD plots for 12 stations on Shikoku Island during one-day period on March 12, 2018.

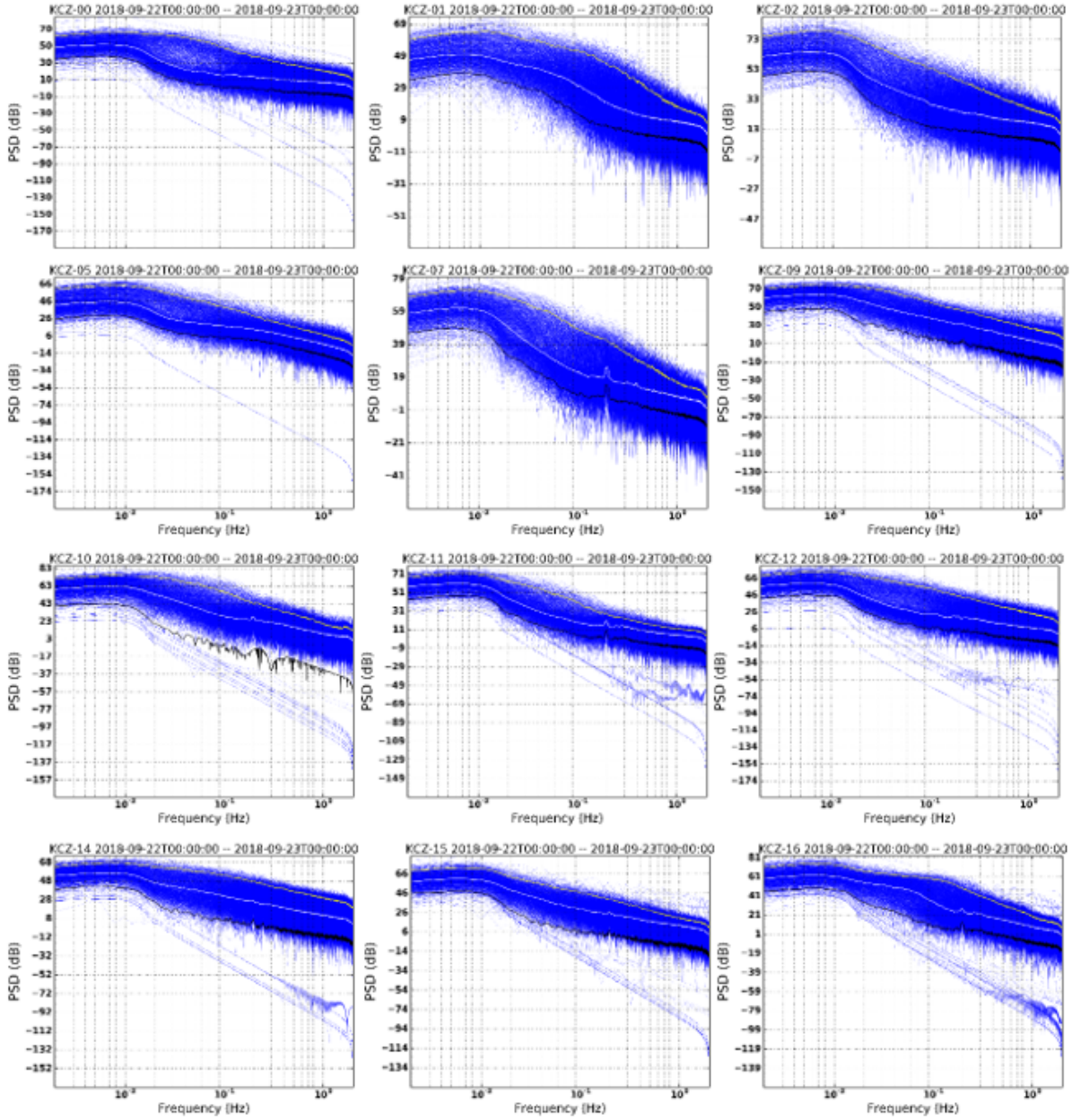

Figure A.10: A set of noise-PSD plots for 12 stations on Shikoku Island during one-day period on September 22, 2018.

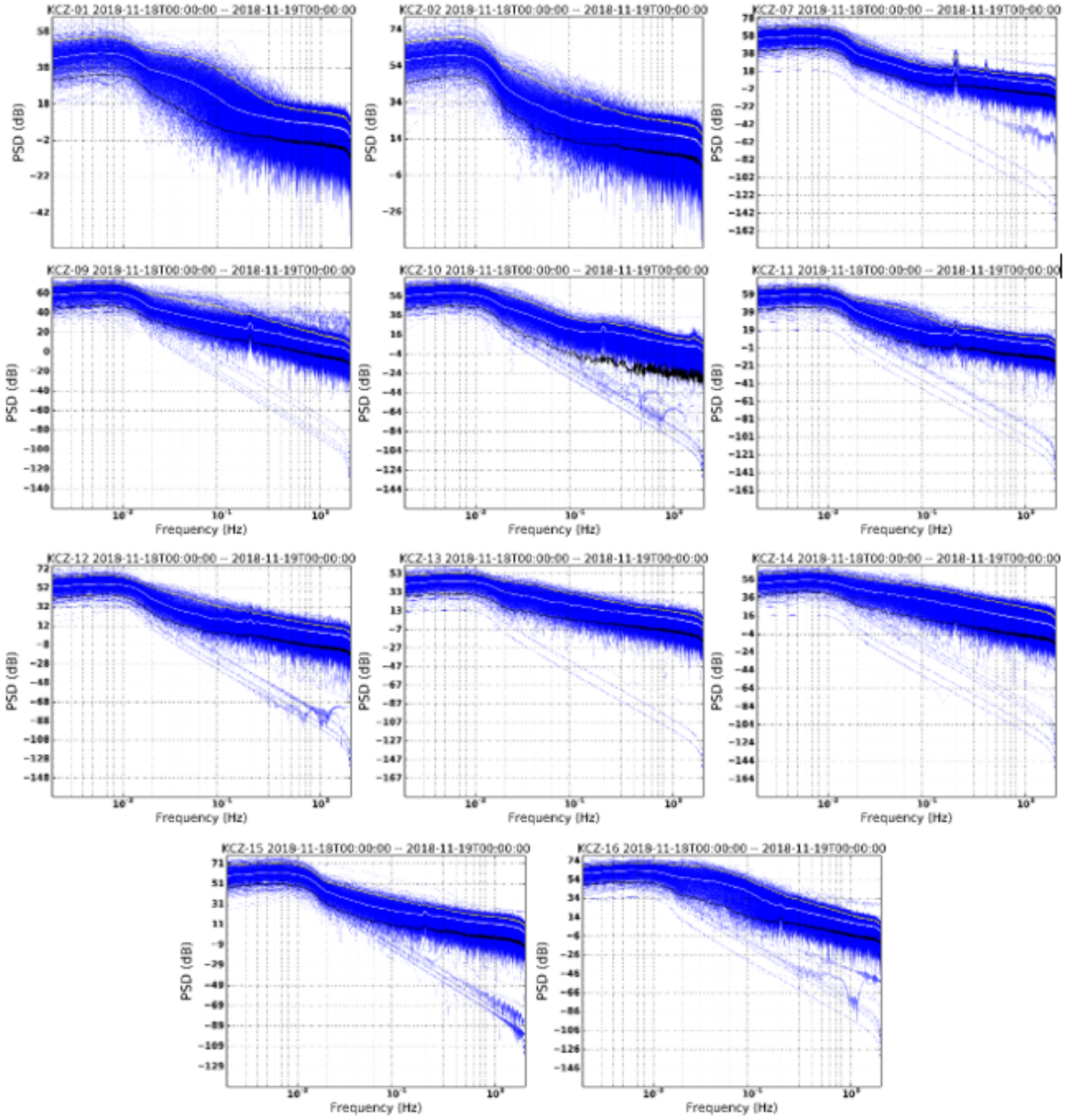

Figure A.11: A set of noise-PSD plots for 11 stations on Shikoku Island during one-day period on November 22, 2018.

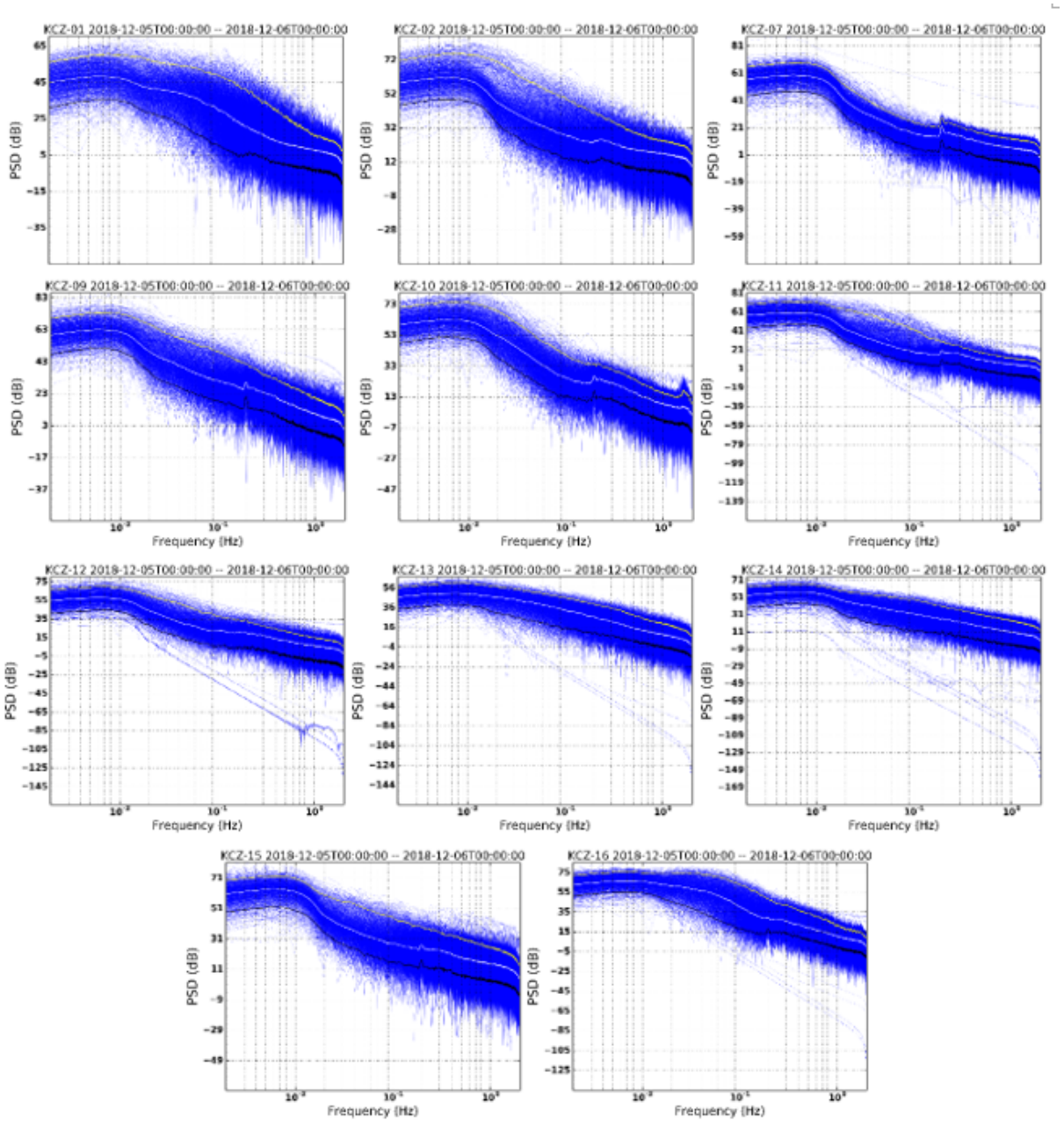

Figure A.12: A set of noise-PSD plots for 11 stations on Shikoku Island during one-day period on December 22, 2018.

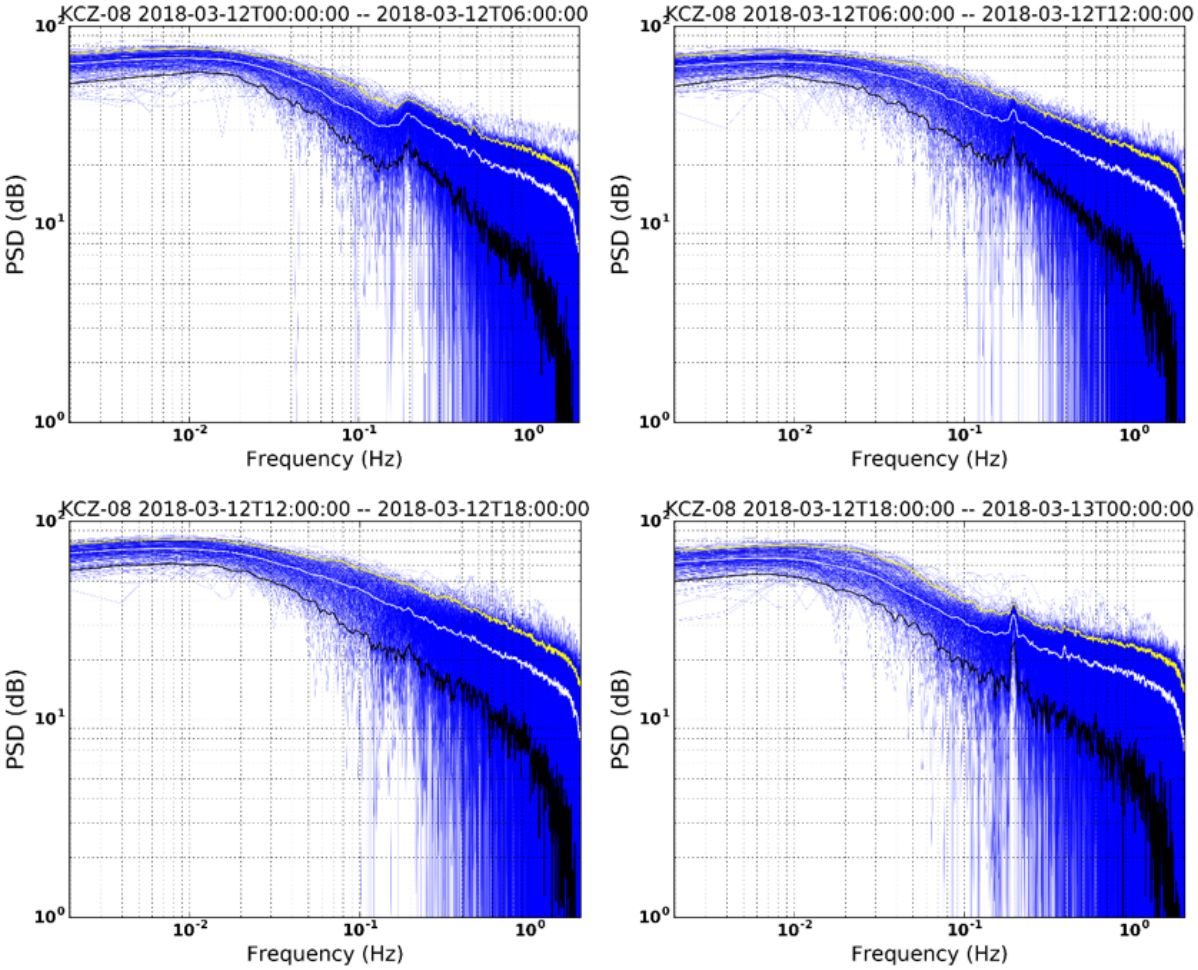

Figure A.13: Power Spectral Density for station KUT08 for all 6-hour time intervals (blue), the 5^{th} and 95^{th} percentiles (yellow and black), the median (white) for each time period.

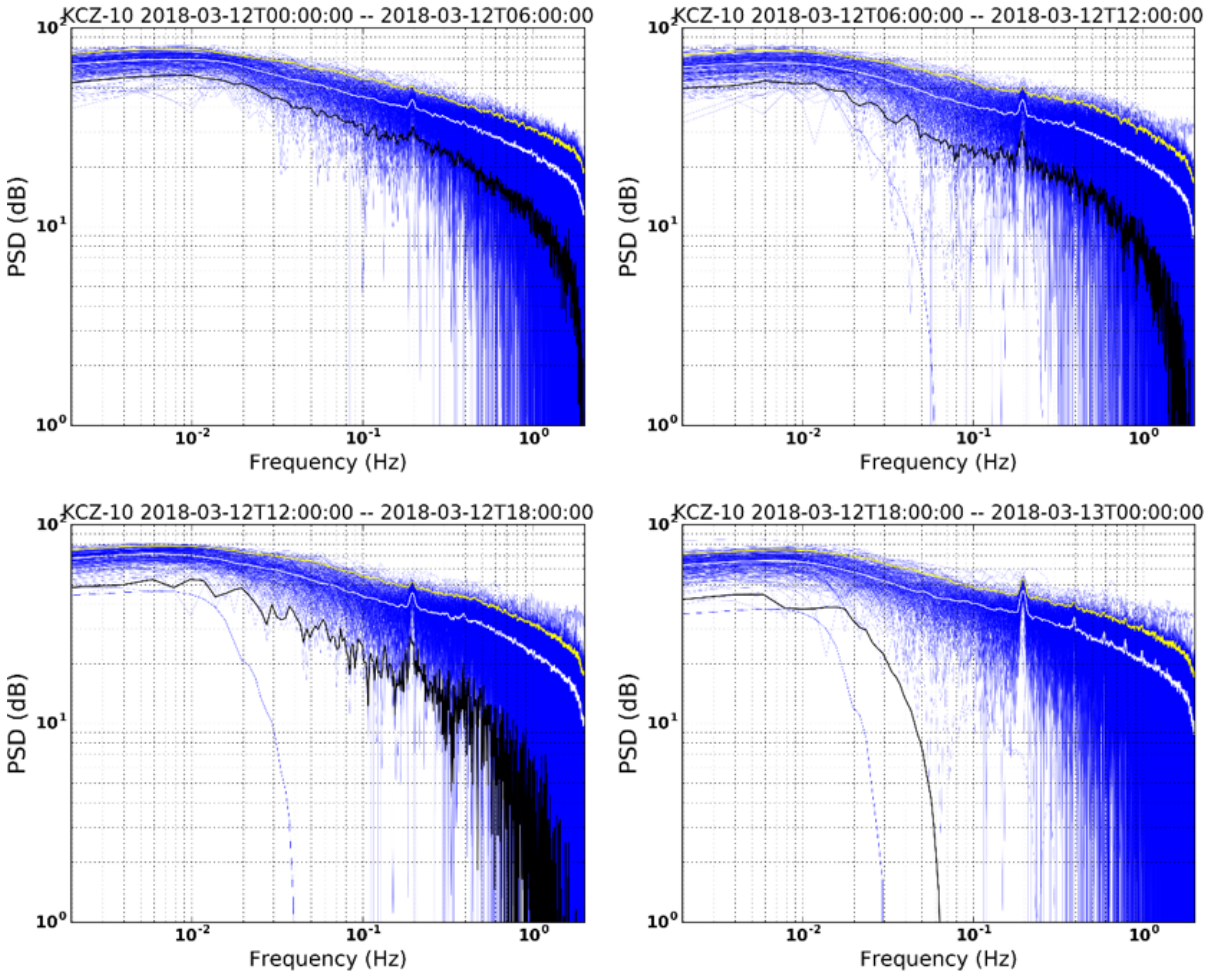

Figure A.14: Power Spectral Density for station KUT10 for all 6-hour time intervals (blue), the 5^{th} and 95^{th} percentiles (yellow and black), the median (white) for each time period.

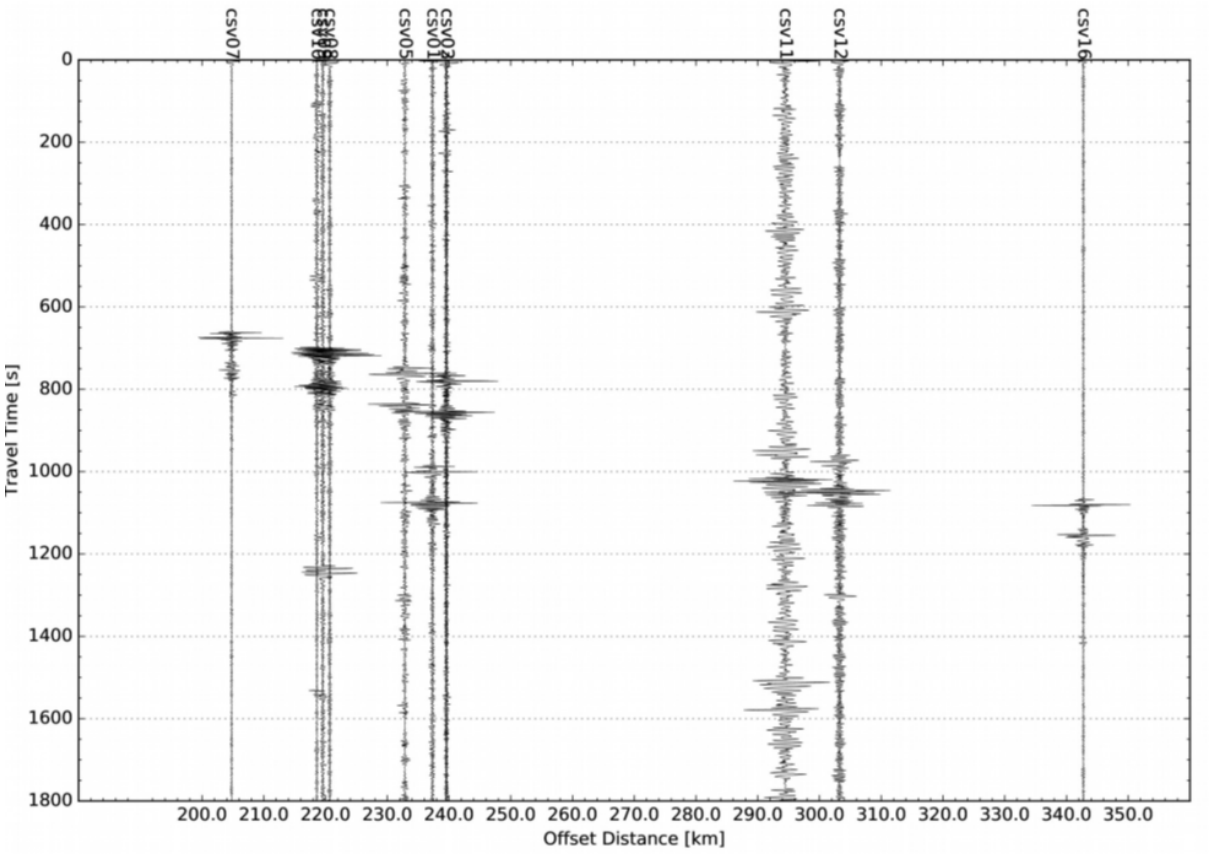

Figure A.15: Records of the Mt. Shinmoedake eruptions at 04:05 JST on March 11, 2018 from the stations on Shikoku Island. The results are filtered in the frequency range 1.0–1.5 Hz based on the PDF plot shown in Figure A.1.

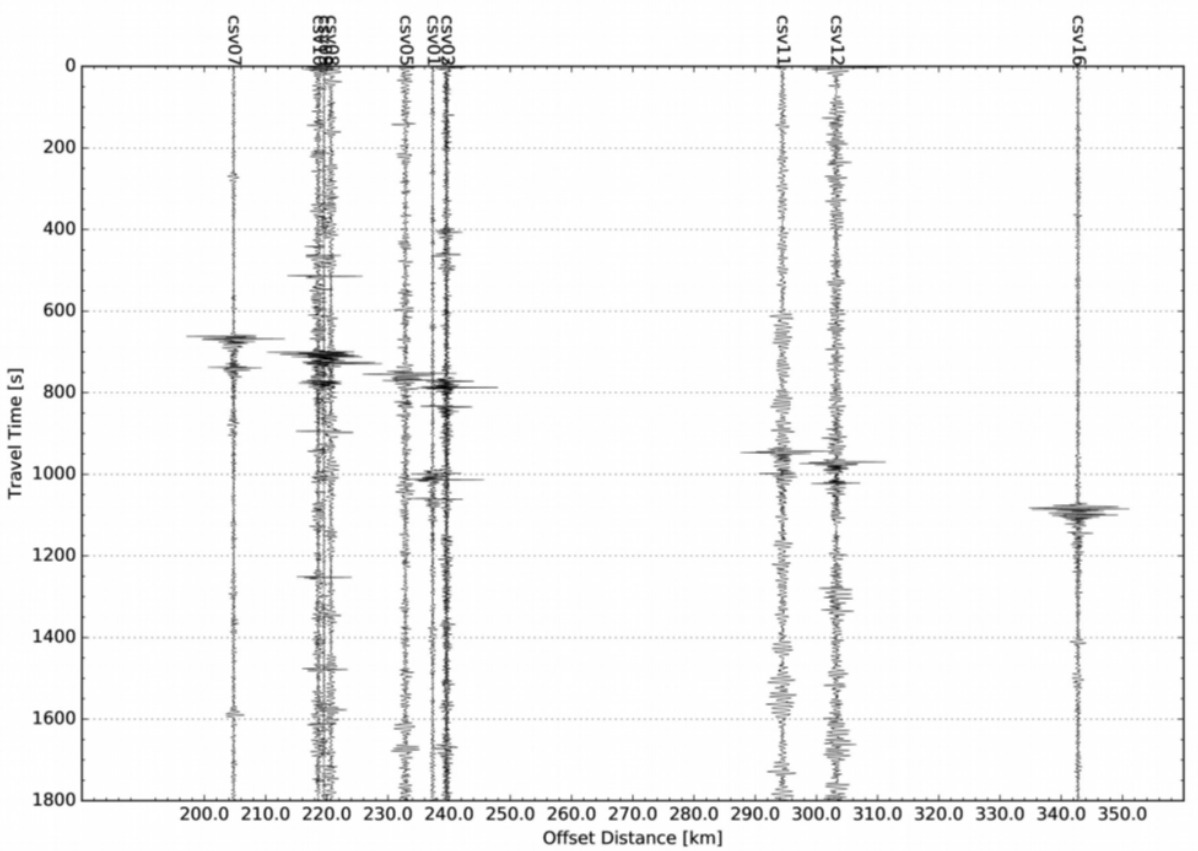

Figure A.16: Records of the Mt. Shinmoedake eruptions at 12:45 JST on March 12, 2018 from the stations on Shikoku Island. The results are filtered in the frequency range 1.0–1.5 Hz based on the PDF plot shown in Figure A.2.

APPENDIX B

Supporting Tables for Chapter 4

Content of this file

Tables B.1 to B.7

Introduction

Additional explanations related to the table below are as follows:

- List of Infrasound Stations operated since 2015 (Table B.1);
- Specifications of the infrasound instrument (ADXII-INF01) (Table B.2).
- A set of result for trace velocity, sound speed and winds speed during the sequence of eruption (Table B.3-B.7).

Table B.1: List of Infrasound Stations operated since 2015.

Station Code	Latitude (^{o}N)	Longitude (^{o}E)	Station Code	Latitude (^{o}N)	Longitude (^{o}E)
KUT00	33.61	133.69	**KUT16**	33.27	134.16
KUT01	33.04	133.03	**KUT17**	33.53	133.76
KUT02	33.05	133.05	**KUT19**	42.60	141.48
KUT03	33.04	133.06	**KUT20**	42.50	143.43
KUT04	32.99	133.00	**KUT21**	41.94	143.24
KUT05	33.04	132.97	**KUT30**	34.97	136.62
KUT06	35.72	139.94	**KUT31**	33.89	136.10
KUT07	32.91	132.72	**KUT32**	34.07	136.19
KUT08	32.73	133.02	**KUT33**	34.49	136.71
KUT09	32.43	133.02	**KUT34**	34.77	137.39
KUT10	32.73	132.99	**KUT35**	34.60	138.22
KUT11	33.45	133.44	**KUT40**	33.57	131.22
KUT12	33.51	133.51	**KUT41**	33.28	131.49
KUT13	33.57	133.67	**KUT51**	35.97	140.64
KUT14	33.50	133.88	**KUT53**	34.98	139.86
KUT15	33.52	134.28	**KUT60**	39.19	141.83

Table B.2: Specifications of the infrasound instrument (ADXII-INF01). (Table is taken from the website of SAYA company.

Integrated Accelerometer	
Measurement range	0-3347 Gal
Frequency characteristics	0.034-1600 Hz (N-S E-W), 0.034-550 Hz
Resolution	16 bit
Audible Noise Sensor	
Measurement range	43-110 dB
Frequency characteristics	10 - 1,000 Hz
Auditory correction	None (= V characteristics)
Time constant	630 ms
Resolution	16 bit
Infrasound Sensor	
Measurement range	$\pm$ 2.422 kPa
Minimum resolution	0.577 mPa
Noise level	$\pm$ 20 mPa (Reduced to 1 mPa after passing through the 64th moving average filter)
D range	143.2 dB
Frequency characteristics	0.001 Hz to 6.25 Hz ($\pm$ 6 dB temperature change low) 0.004 Hz to 6.25 Hz ($\pm$ 6 dB temperature change high)
Pressure Sensor	
Measurement range	15 - 115 kPa
Frequency range	The lower of DC to 1 Hz or Fs/2 (Fs = sampling frequency)
Resolution	16 bit
Temperature Sensor	
Measurement range	0 - 81.92^{o}C
Minimum resolution	0.0000390625^{o}C
D range	128.18 dB

Table B.3: Trace velocity, sound speed and winds speed for the event at 01:54 JST on March 10, 2018.

trace velocity (km/s)	computed reflecting level (km)	speed of sound at reflecting level (km/s)	computed wind at reflecting level (m/s)
0.3350	1.4399	0.325277818	9.722182119
0.3350	1.5166	0.325274685	9.725315545
0.3350	1.5961	0.325195798	9.804202034
0.3350	1.6845	0.325160057	9.839943160
0.3350	1.8324	0.325626272	9.373727642
0.3732	10.8367	0.316632885	56.56711539
0.3732	10.9657	0.315654214	57.54578584
0.3732	37.3657	0.301780930	71.41907002
0.3732	37.5416	0.298794697	74.40530354
0.3732	37.7365	0.297129246	76.07075431
0.3732	37.9515	0.295760593	77.43940752
0.3732	38.1866	0.294541827	78.65817264
0.3732	38.4431	0.293433228	79.76677169
0.3732	38.7222	0.292411739	80.78826056
0.3732	39.0255	0.291471553	81.72844670
0.3732	39.3568	0.290626862	82.57313816
0.3732	39.7272	0.289967581	83.23241873
0.3732	40.1652	0.289709429	83.49057104
0.3732	40.7612	0.290648088	82.55191233
0.3732	42.1918	0.297878168	75.32183238
0.3732	43.5031	0.296536556	76.66344415
0.3732	44.3570	0.294886571	78.31342954
0.3732	45.1104	0.293690615	79.50938464
0.3732	45.9062	0.293385329	79.81467132
0.3732	46.9604	0.295442497	77.75750315

Table B.4: Trace velocity, sound speed and wind speed estimated from two groups station for the eruption event at 04:27 JST on March 10, 2018.

trace velocity (km/s)	computed reflecting level (km)	speed of sound at reflecting level (km/s)	computed wind at reflecting level (m/s)
0.3348	1.42946	0.325598916	9.201084137
0.3348	1.49758	0.325690738	9.109262193
0.3348	1.56360	0.325576043	9.223957085
0.3348	1.62898	0.325484421	9.315579014
0.3348	1.71553	0.325607258	9.192741898
0.3796	38.03560	0.304693914	74.90608578
0.3796	38.19180	0.302572334	77.02766643
0.3796	38.35990	0.300978453	78.62154739
0.3796	38.54110	0.299556019	80.04398150
0.3796	38.7380	0.298241732	81.35826769
0.3796	38.95470	0.297028054	82.57194622
0.3796	39.19860	0.295935128	83.66487235
0.3796	39.4800	0.294998002	84.60199795
0.3796	39.8100	0.294245979	85.35402063
0.3796	40.20370	0.293754432	85.84556846
0.3796	40.69630	0.293704736	85.89526412
0.3796	41.34800	0.294328155	85.27184474
0.3796	42.08730	0.294463136	85.13686400
0.3796	42.71670	0.293427926	86.17207369
0.3796	43.25450	0.292187302	87.41269842
0.3796	43.77040	0.291113614	88.48638648
0.3796	44.30470	0.290312404	89.28759629
0.3796	44.89420	0.289979343	89.62065746
0.3796	45.64590	0.290964984	88.63501621
0.3796	65.11220	0.314644180	64.95581989

Table B.5: Trace velocity, sound speed and wind speed estimated from two groups station for the eruption event at 10:15 JST on March 10, 2018.

trace velocity (km/s)	computed reflecting level (km)	speed of sound at reflecting level (km/s)	computed wind at reflecting level (m/s)
0.3594	39.9089	0.290542614	68.85738557
0.3594	40.1616	0.289447290	69.95270985
0.3594	40.4331	0.288431978	70.96802162
0.3594	40.7267	0.287491410	71.90858995
0.3594	41.0440	0.286626235	72.77376492
0.3594	41.3926	0.285874717	73.52528343
0.3594	41.7801	0.285279684	74.12031628
0.3594	42.2209	0.284937343	74.46265693
0.3594	42.7487	0.285056852	74.34314806
0.3594	43.4134	0.285884170	73.51583016
0.3594	44.2833	0.287671768	71.72823158
0.3594	45.5280	0.291667995	67.73200548
0.3594	62.2862	0.315529086	43.87091370

Table B.6: Trace velocity, sound speed and wind speed estimated from two groups station for the eruption event at 12:45 JST on March 12 2018.

trace velocity (km/s)	computed reflecting level (km)	speed of sound at reflecting level (km/s)	computed wind at reflecting level (m/s)
0.3679	10.7776	0.328495285	39.40471505
0.3679	10.8273	0.327257281	40.64271950
0.3679	10.8826	0.326234093	41.66590702
0.3679	10.9440	0.325224690	42.67530961
0.3679	11.0124	0.324216955	43.68304501
0.3679	11.0891	0.323211611	44.68838862
0.3679	11.1755	0.322242417	45.65758303
0.3679	11.2750	0.321332908	46.56709184
0.3679	11.3911	0.320531090	47.36890986
0.3679	11.5293	0.319916338	47.98366224
0.3679	11.7023	0.319664811	48.23518875
0.3679	11.9410	0.320333731	47.56626937
0.3679	46.2706	0.309988674	57.91132581

Table B.7: Trace velocity, sound speed and wind speed estimated from two groups station for the eruption event at 14:13 JST on March 15 2018.

trace velocity (km/s)	computed reflecting level (km)	speed of sound at reflecting level (km/s)	computed wind at reflecting level (m/s)
0.3785	1.5892	0.342010153	36.48984751
0.3785	10.3707	0.335842021	42.65797922
0.3785	10.4181	0.334839063	43.66093753
0.3785	10.4699	0.333887805	44.61219511
0.3785	10.5263	0.332931442	45.56855832
0.3785	10.5871	0.331952358	46.54764164
0.3785	10.6526	0.330949705	47.55029519
0.3785	10.7234	0.329921699	48.57830113
0.3785	10.7998	0.328884430	49.61556989
0.3785	10.8833	0.327843452	50.65654769
0.3785	10.9753	0.326828553	51.67144663
0.3785	11.0790	0.325880891	52.61910928
0.3785	11.2001	0.325090270	53.40972982
0.3785	11.3528	0.324711471	53.78852881
0.3785	11.5795	0.325504806	52.99519392

PUBLICATION I

***

Batubara, M., Yamamoto, M.-Y., Madkour, W., & Manik, T. (2018). *Long-term distribution of meteors in a solar cycle period observed by VHF meteor radars at near-equatorial latitudes*. Journal of Geophysical Research: Space Physics, 123, 10,403– 10,415. https://doi.org/10.1029/2018JA025906.

Journal of Geophysical Research: Space Physics

TECHNICAL REPORTS: DATA
10.1029/2018JA025906

Key Points:
- The 13-year observation of the meteor echo distribution has been conducted at Kototabang and Biak, Indonesia
- The atmospheric temperature of CIRA and total density of NRLMSISE-00 in the equator show a clear relationship with the solar radio index
- The variation of meteor heights on the equator is possibly due to changes in atmospheric mass density

Correspondence to:
M. Batubara,
mario.batubara@lapan.go.id

Citation:
Batubara, M., Yamamoto, M.-Y., Madkour, W., & Manik, T. (2018). Long-term distribution of meteors in a solar cycle period observed by VHF meteor radars at near-equatorial latitudes. *Journal of Geophysical Research: Space Physics*, *123*, 10,403–10,415. https://doi.org/10.1029/2018JA025906

Received 23 JUL 2018
Accepted 22 SEP 2018
Accepted article online 22 OCT 2018
Published online 15 DEC 2018

Long-Term Distribution of Meteors in a Solar Cycle Period Observed by VHF Meteor Radars at Near-Equatorial Latitudes

M. Batubara[1,2], M.-Y. Yamamoto[1], W. Madkour[1], and T. Manik[2]

[1]School of System Engineering, Kochi University of Technology, Kochi, Japan, [2]Space Science Center, Indonesian Institute of Aeronautics and Space, Bandung, Indonesia

Abstract We investigated meteor height and number of meteor echoes over a 13-year observation period, with the data recorded by the meteor wind radar systems in Kototabang (0.20°S, 100.32°E) and Biak (1.17°S, 136.10°E), Indonesia. We aimed to investigate the changes in meteor peak height according to solar activity, represented by the solar radio index F10.7, and the number of solar sunspots, R, compared with the empirical results of the Mass Spectrometer Incoherent Scatter Extending (MSISE) and Committee on Space Research International Reference Atmosphere models. We found that (i) the daily meteor count rates at both sites in the period from 2003 to 2016 could be used to determine the dynamics in the upper atmosphere, where peak conditions occurred in the middle of the year; (ii) through a statistical approach using the normal distribution function, the variation in meteor peak height showed a positive correlation with the trend in solar activity; and (iii) comparison between the two empirical models and our observations showed two points where annual air density seemed to have a clear relationship with peak meteor height. In addition, the annual neutral density pattern of the model was related to the daily meteor count every year, although it showed a pattern opposite to the solar activity trends.

Plain Language Summary Meteor wind radar systems at Indonesia are designed to study upper atmospheric dynamics around the equator region from the meteoroid interactions with Earth's atmosphere that results in a series of ionization processes. In this study, we investigate whether such solar radiation can affect the change of meteor height around the equatorial region. To do this, we use two equatorial meteor radars located in Kototabang and Biak, Indonesia. We have used global atmosphere models and solar observation data to evaluate how well solar activity affects meteor heights variation on the equatorial region. This study provides the science-interested public, especially atmospheric researchers with the distribution of meteor occurrence as well as their heights that cross through the equatorial atmosphere. Perhaps the general goal of the study is to provide insight into meteor activity across the unique equatorial region and to complement global distribution of meteor activity in the world.

1. Introduction

The meteor is a natural phenomenon, in which a meteoroid enters the Earth's atmosphere at supersonic speeds between 11 and 71 km/s and produces a streak of light and ionized trail due to friction with the Earth's atmosphere. Because meteors can be observed by radar in various weather conditions, observers utilize radar to obtain detailed information about meteors. The information from radio wave signals reflected by the ionized trails of meteors allows studies of the dynamics in the upper and lower mesosphere (Brown et al., 2008; Ceplecha et al., 1998; Hocking et al., 2001; Younger et al., 2009).

The development of radar systems, with their various advantages and target types, has progressed rapidly. One of these systems, the very high frequency radar with the "all-sky" radar technique, has been used widely to determine the position, movement, and total flux of meteors in the Northern Hemisphere (Brown et al., 2008; Hocking et al., 1997, 2001; Jacobi, 2014; Stober et al., 2014; Stober & Chau, 2015; Szasz et al., 2005; Yi et al., 2016; Younger et al., 2009), Southern Hemisphere (Clemesha & Batista, 2006; Lima et al., 2015), and at the equator (Batubara et al., 2011; Matsumoto et al., 2016; Szasz et al., 2005; Younger et al., 2009). These radar parameters can provide information about meteor characteristics (mass, entry velocity, density, and angle of arrival) and the condition of the atmosphere at locations through which meteoroids travel and ablate (Kaiser, 1954; Lindblad, 1967; Pifko et al., 2013; Stober et al., 2011, 2012, 2014; Takahashi et al., 2002; Yi et al., 2018).

There is considerable complexity in the Earth's atmospheric conditions, especially pertaining to neutral atmospheric density and temperatures in the mesosphere and lower thermosphere (MLT) region. Temporally and spatially, the trends of these two parameters are affected by the external energy of the MLT system, its internal dynamics, and coupling of the thermosphere and ionosphere (Qian & Solomon, 2012). To date, information on the meteor backscatter signal has allowed us to determine variations in atmospheric neutral density (Clemesha & Batista, 2006; Lima et al., 2015; Stober et al., 2014; Takahashi et al., 2002; Yi et al., 2018) and atmospheric neutral temperature in the region of meteoroid ablation (Hocking et al., 1997; Holdsworth et al., 2006; Kozlovsky et al., 2016; Yi et al., 2018). However, neutral atmospheric conditions in the MLT region are generally determined via empirical models. Recently, the atmosphere model NRLMSISE-00 explicitly added the "oxygen anomaly" component to describe the contribution of nonthermospheric species at high altitudes and allow the user to calculate the total neutral mass density of the thermosphere, thus revealing the thermospheric mass density and anomalous oxygen contribution in the thermosphere (Picone et al., 2002). The model database contains relevant observation data (e.g., satellite and ground-based data) and produces a temperature and density structures similar to an equatorial mesosphere layer. Qian and Solomon (2012) comprehensively reviewed variation in neutral atmospheric conditions at thermosphere altitudes using the model. Meanwhile, Stober et al. (2012) used the NRLMSISE-00 prediction model to analyze neutral atmospheric variation in terms of solar activity effects in the middle region. The neutral density variations seem dependent on the solar cycle effects over spanning one solar cycle.

The Committee on Space Research (COSPAR) devised an empirical atmosphere model, called the COSPAR International Reference Atmosphere (CIRA), of atmospheric temperatures and densities. The model accurately reproduces most of the characteristic features of the atmosphere and the general structure of the tropopause, stratopause, and mesopause with almost global coverage (80°N–80°S). For example, Clemesha and Batista (2006) evaluated atmospheric temperature trends in the MLT region with a simulation tool of the CIRA86 model for analysis of meteor height variation.

The role of solar activity in meteor height and meteor rate has been reported and discussed. Several researchers (Hajduk et al., 1980; Lindblad, 1967, 2003; Liu et al., 2017; McIntosh & Hajduk, 1977; Prikryl, 1983; Simek & Pecina, 2000; Szasz et al., 2005; Yi et al., 2018; Younger et al., 2009; Zigo et al., 2009) have observed variation in the intensity of meteor echoes and meteor rates due to the influence of solar activity. Additionally, other researchers have been used from radar at low latitude on southern hemisphere (Lima et al., 2015) and on northern hemisphere (Jacobi, 2014; Pecina & Simek, 1999; Pellinen-Wannberg et al., 2009; Porubčan & Cevolani, 1983) to investigate the effects of solar activity, described by solar radio flux, F10.7, and the number of solar sunspot (R), on meteor height distribution.

It is well known that the effects of the condition of the upper atmosphere and solar activity on meteor altitude have been relatively underreported for the equatorial region. Investigating the phenomenon of meteoroid entry into the Earth's atmosphere could be important because of effects of solar activity, the influence of Earth's atmosphere as the penetration medium, and other aspects. In this study, we investigated the phenomenon of meteoroid penetration into the Earth's atmosphere in the context of the variation in meteor heights observed by meteor radar around the equator. Specifically, we addressed three aspects. First, we checked that the period of data collection was appropriate for further processing. Second, we compared our findings with the results of empirical atmosphere models. Third, we evaluated the results in terms of the insights gained. The characteristics of our radar system and the radar data format are described herein.

This paper is organized as follows. In section 2, we present the specifications and configurations of various radar systems and the format of the meteor radar data. In section 3, the data used in this activity, the initial processing of the raw meteor radar data, and the method used to obtain the maximum meteor heights are described in detail. The results regarding the annual and diurnal distributions of meteors around the equator, trends in solar activity (as represented by R), solar radio fluxes over the complete solar activity cycle period, and a comprehensive discussion are presented in section 4. Finally, a brief summary of our findings is provided in section 5.

2. Indonesian Meteor Observation Systems

There are two meteor radar systems installed in the Indonesian Archipelago. These radar systems are located in the western part of Indonesia, at Kototabang (0.20°S, 100.32°E), and in the eastern part, at Biak (1.17°S,

Table 1
Specifications of Meteor Radar Systems in Kototabang and Biak

Parameter	MWR Kototabang	MWR Biak
Frequency (MHz)	37.7	33.32
Bandwidth (kHz)	200	200
Pulse width (uS)	13.3	13.3
Output power (kW)	12	12
Duty cycle (%)	5 (max)	5 (max)
Pulse repetition frequency (Hz)	2144	2144
TX antenna	Single circular polarized three-element cross Yagi	Single circular polarized three-element cross Yagi
RX antenna	Five circular polarized two-element cross Yagi	Five circular polarized two-element cross Yagi

Note. MWR = meteor wind radar.

136.10°E; Fukao et al., 2003). The two instruments are both allSKy interferometric METeor (SKiYMET) radar systems, which are optimized for upper atmospheric measurements.

The meteor radar in Kototabang has been operating since 15 November 2002, 1 year after the establishment of the Equatorial Atmosphere Radar system (Fukao et al., 2003). A decade later, a meteor radar system was installed in eastern Indonesia, on the island of Biak, which has been operational since 31 May 2011. The two radar systems are separated by approximately 4,000 km. The specifications of both meteor radar systems are listed in Table 1.

Recently, a state-of-the-art SKiYMET radar was installed at the above locations for continuous monitoring of the atmospheric dynamics within the MLT region. Detailed descriptions of this radar and the meteor detection algorithms can be found in Hocking et al. (2001). The receiving antenna uses the configuration initiated by Jones et al. (1998), named the Jones Webster Hocking (JWH) configuration, and is arranged into two perpendicular arms with spacings of 2 and 2.5 λ to yield unambiguous angles of meteor arrival. These radars utilize the interferometric technique to determine the position of meteor trails in the sky without ambiguity in the angle of arrival.

The radar data acquisition system (RDAS) represents another type of radar system, operated by a single PC using a UNIX system to control and analyze selected observation parameters; the RDAS also has multitasking capabilities. The data obtained from RDAS are written to a new type of file, called a *confirmed event* file. The contents of this confirmed event file are used to determine the locations of meteors in the sky and other physical parameters of meteors. The parameters are then written into an ASCII text file, the meteor position data, for further study. The fields of the meteor position data file are described in Table 2.

3. Data

Data from both meteor radars can be accessed via the Repository Data Sains Antariksa database server in Indonesia and the Research Institute for Sustainable Humanosphere (RISH) databases, Kyoto University (2015), Japan (Lembaga Penerbangan dan Antariksa Nasional, 2015). We used data from both meteor radars to cover the total solar cycle (January 2003 to December 2016).

Table 2
Description of the Meteor Position Data File

Data field	Description
Date	Detection data relative to UTC
Time	Time of detection in UTC
File	File name extension used to store the raw data for a given detection
Rge	Range of the detection in kilometers
Ht	Corrected height above ground of the detection in kilometers
Vrad	Radial drift velocity of the trail in meters per second
DelVr	Standard deviation of the radial velocity measurement obtained from the five antenna pairs in the interferometer
Theta	Zenith angle of the detection in degrees
Phi0	Azimuth angle of the detection in degrees measured anticlockwise from East
Ambig	Number of locations of detected ambiguous meteors
Delphase	Greater phase error between antennae
Ant-pair	Antenna pair with the greatest phase error
IREX	Receiver channel used in the analysis
Amax	Peak value of the amplitude of the meteor echo
Tau	Decay time of the meteor in seconds
Vmet	Entrance speed of the meteor in kilometers per second
Snrdb	Signal-to-noise ratio for the meteor

Note. UTC = Universal Time Coordinated.

The possibility of detecting a meteor in the upper atmosphere depends on its speed, range, zenith angle, height, and position. We began by checking the signal-to-noise ratio (SNR) and the amplitude of the radio signals emanating from the meteor trails. The zenith angle is very important because it is used to calculate the heights for the corresponding positions of each meteor detection. Thus, the zenith was chosen as the main metric for selecting the desired radio signals. In this study, we limited the zenith angle to less than 50° to allow selection of strong meteor echoes and avoid the range uncertainty associated with detections closer to the horizon, when evaluating the trends in meteor rate and height.

The all-sky radar can detect large populations of meteor echoes, which are normally distributed within the altitude range of 70–100 km with a peak value of around 90 km (Hocking et al., 1997). Each detected meteor echo is also likely to include the effects of instrument errors, such as bias errors, that could cause more diversity in the measured heights. Thus, the authors cited the above proposed method to perform bias correction by inverting the equation of measured meteor height (h_m), to extract the corrected meteor height. A Gaussian distribution function was used for our data fitting to obtain statistical information on the meteors. Then we applied the meteor height correction equation proposed by Hocking et al., (1997):

$$h_T = \frac{\sigma_T^2 + \sigma_P^2}{\sigma_P^2} h_m - \frac{\sigma_T^2}{\sigma_P^2} h_P \quad (1)$$

where h_T is the height of a meteor echo, h_m is the measured height of the echo, σ_p is the standard deviation of h_m, σ_T is the uncertainty in meteor height, and h_P is the height at the peak meteor count rate.

Currently, the meteor observation data in Indonesia already cover almost the entire 11-year solar cycle, represented by F10.7 and R. The number of solar sunspots has long been known to vary with a period of repetition of about 11 years, that is, the solar cycle. The peak sunspot population is known as the solar maximum, which is separated from the next maximum by a gap known as the solar minimum. We attempted to evaluate the trends in these parameters over the complete period of the solar cycle and compared them to our meteor radar data results. The monthly R values, provided by the World Data Center Sunspot Index and the Long-term Solar Observations, Royal Observatory of Belgium (2013), were applied to evaluate the variation in solar cycle activity. Because there is a close connection between shortwave solar radiation and radio microwaves, F10.7 was taken as an indicator of the shortwave radiation from the Sun. Daily values of F10.7, as recorded at the NASA OMNIWeb Data Facility (The National Aeronautics and Space Administration, 2005), were used in the present analysis.

Finally, we investigated the atmospheric conditions in the MLT region, especially the variations in neutral atmospheric density and temperature and compared these with our analysis results. All of these parameters were obtained from the NRLMSISE-00 Atmosphere Model (Community Coordinated Modeling Center-NASA, 2002) and the CIRA86 of the Community Coordination Model Center (CIRA, 1990).

4. Results and Discussion

At the beginning of our investigation, we evaluated the Kototabang and Biak meteor radar data within the range of SNR values considered appropriate for further processing. The zenith angle was selected to limit the range of the desired SNR values to the criterion values above the median value, which is more concentrated in the zenith angle less than 1 radiant, or equal to 57°. Figure 1b shows the trend in height distribution and the total number of meteor echoes detected by the Kototabang meteor radar on 14 December 2005, based on the previously selected zenith angle. The left panel shows the meteor height distribution plot calculated based on the total detection rate (1-km height resolution; horizontal pink bars) and the scatter plot of the meteor height distribution based on continuous detection (blue dots, center). The bottom panel shows the daily trend in the total number of meteor echoes detected per hour. In general, in 1 day, the peak number of meteor echoes can reach about 600 counts at a height of about 90 km, at the time of sunrise (red arrow). This clearly shows that the largest meteor counts appear globally between midnight and dawn, and usually, the peak counts occur near sunrise, as explained by several studies on daily cycles (Hajduk et al., 1980; Lindblad, 2003; McIntosh & Hajduk, 1977); continuous changes in the intensity of solar radiation could cause changes in the level of ionization in the atmosphere at the height of meteor passage and thus affect the total quantization of meteor echo detection. In addition, the Earth's orbit motion and the direction of Earth's rotation affect the number of meteoroids that hit the Earth's atmosphere. The results that we obtained were similar to the meteor distribution patterns measured at other equatorial latitudes, for example, on the island of Ascension at 8°S latitude (Szasz et al., 2005). Meanwhile, changes in altitude could not be detected in the daily data, so there was a need to investigate data with a longer period, that is, annual data.

The annual variation in meteor rate detected by the Kototabang and Biak meteor radars since their establishments are shown in Figure 2. The meteor radars at Kototabang and Biak typically had about 4,000–18,000 and 8,000–32,000 underdense-type meteor echo detections per day, respectively. The detection algorithm for both radar systems, explained by Hocking et al. (2001), has proved very effective at removing nonmeteor signals such as aircraft and lightning signals, as well as sporadic E-region reflections such as ionospheric echoes. In the case of radio waves reflected by meteor trails, how a radio frequency wave reacts with such ionized trails depends on their ionization level due to changes in total electron density within the trail line, as the reflected energy of the incident signals depends on the plasma frequency of the trails. As shown in Figure 2, the peak amount of meteor echo received daily by the Biak system is larger than that of Kototabang due to the chosen operating frequency of the system (Table 1). The meteor detections in this study were restricted to meteors detected at the zenith angle range mentioned above, and these ranged in number from 2,000–14,000 to 5,000–30,000 underdense-type meteor echo detections per day,

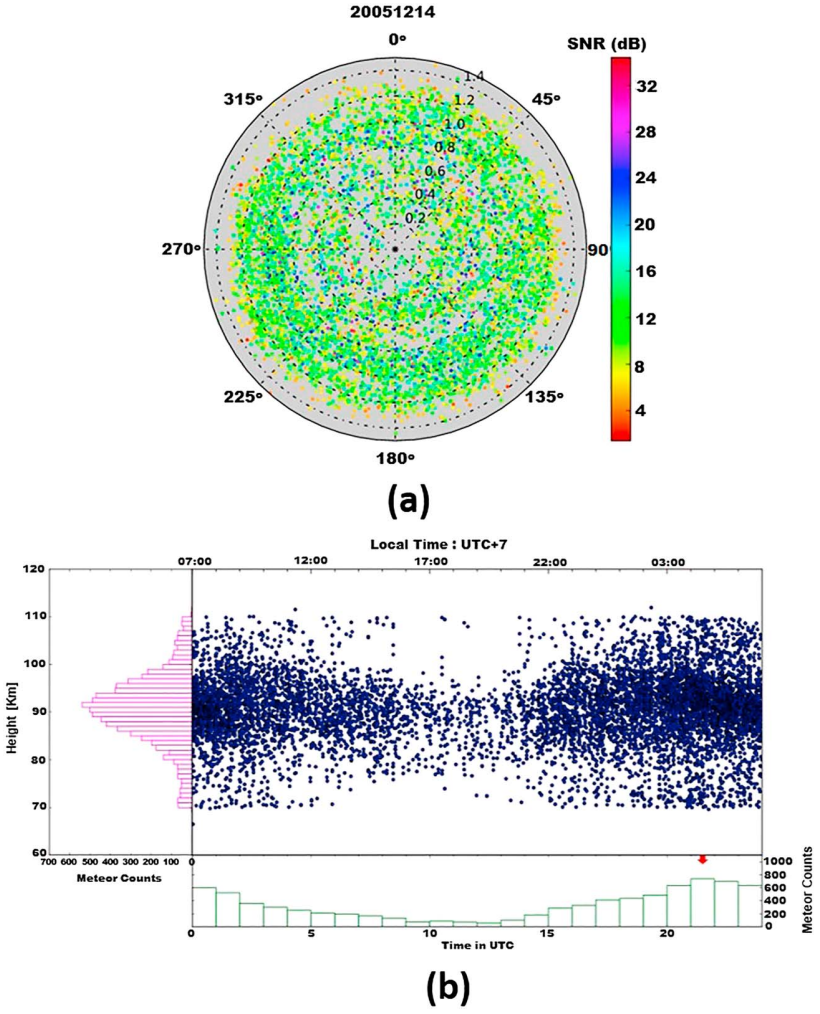

Figure 1. The observation data for 14 December 2005, obtained at Kototabang. (a) The contour of angular distribution of the detected echo signal-to-noise ratio value. (b) Meteor count as a function of meteor height (horizontal pink bars; left), a scatterplot of detected meteors as a function of meteor height (shown as blue dots; center), and diurnal meteor counts (vertical green bars; bottom).

respectively. In general, both detection profiles show oscillating patterns, with a peak around midyear. The data for Biak continuously show more than 4,000 detections per day during 2011–2016. However, the detection data for Kototabang were continuous only during the first 9 years of operation. Therefore, we used 9 years' worth of Kototabang meteor radar data (2003–2011) and 6 years of Biak radar meteor data (2011–2016) to investigate variation in meteor height. To clarify the variation in annual meteor rate, data were plotted as shown in Figures 2c and 2d. The annual variation in meteor rate showed a clear periodicity, with two peaks appearing in December–January and June–July, and two valleys occurring around March–April and October–November. The total number of detected meteor echoes depends on the number of radar signal reflected back by ionized particles. In accordance with (McKinley, 1961), the meteor count depends on the Earth's orbital position with respect to the Sun, and the direction of the radar beam with respect to the meteor trail zone, possible additional factors include the seasonal variation in meteor echoes, as well as a background ionospheric ionization in the atmosphere formed separately from interactions with meteors. However, interestingly, we observed a trend toward a change in the seasonal meteor rate. It can also be observed that the detection rates increased from the beginning of 2003 to 2006 and showed a decreasing trend thereafter. Therefore, a more in-depth discussion of these results is necessary. We found that the diurnal variation in meteor rates was affected by periodic solar radiation as given by Hajduk et al. (1980), Lindblad (2003), and McIntosh and Hajduk (1977); the variation

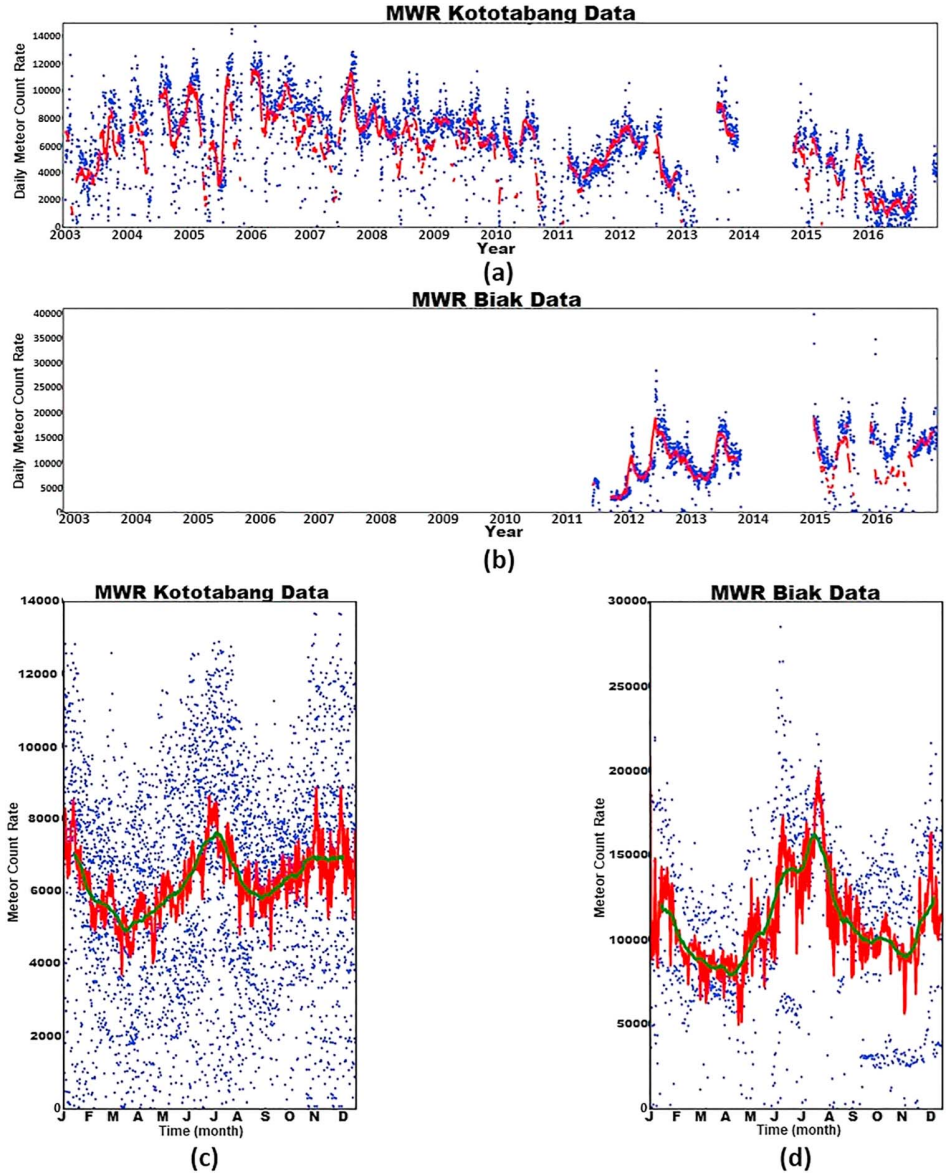

Figure 2. Daily meteor count rate (blue dots) at Biak for the period of 2011–2016 (first row) and at Kototabang for the period of 2003–2016 (second row), together with the 30-day running averages (red lines). Annual variation in meteor count rates at Biak (bottom-left) and Kototabang (bottom-right). The red line is the daily mean count rate and the green line is the 30-day running average. MWR = meteor wind radar.

in meteor count rate reach their peaks once per year (Liu et al., 2017; Szasz et al., 2005; Yi et al., 2018; Younger et al., 2009; and the annual variation in meteor rates appears to have an inverse relationship with the 11-year solar cycle (Lindblad, 1967; Prikryl, 1983). This will be considered separately in this section.

Range aliasing often occurs in radar implementations that depend on separation between transmitted pulses at a specific pulse repetition frequency. Dealiasing in the echo range is performed by producing various range ensembles for each candidate r_i. The height of a meteor radar candidate, at range r_i and angle theta from the zenith, is then determined using the formula

$$h_i = \sqrt{r_e^2 + r_i^2 + 2r_e r_i \cos\theta} - r_e, \tag{2}$$

where θ is the zenith angle, r_e is the Earth's radius, and $r_i = r + ir_{amb}; i = 0, 1, 2, \ldots, N; N = \frac{r_{max}}{r_{amb}}; r_{amb} = \frac{c}{2PRF}$. For our radars, the maximum echo range r_{max} is assumed to be about 520 km based on the maximum

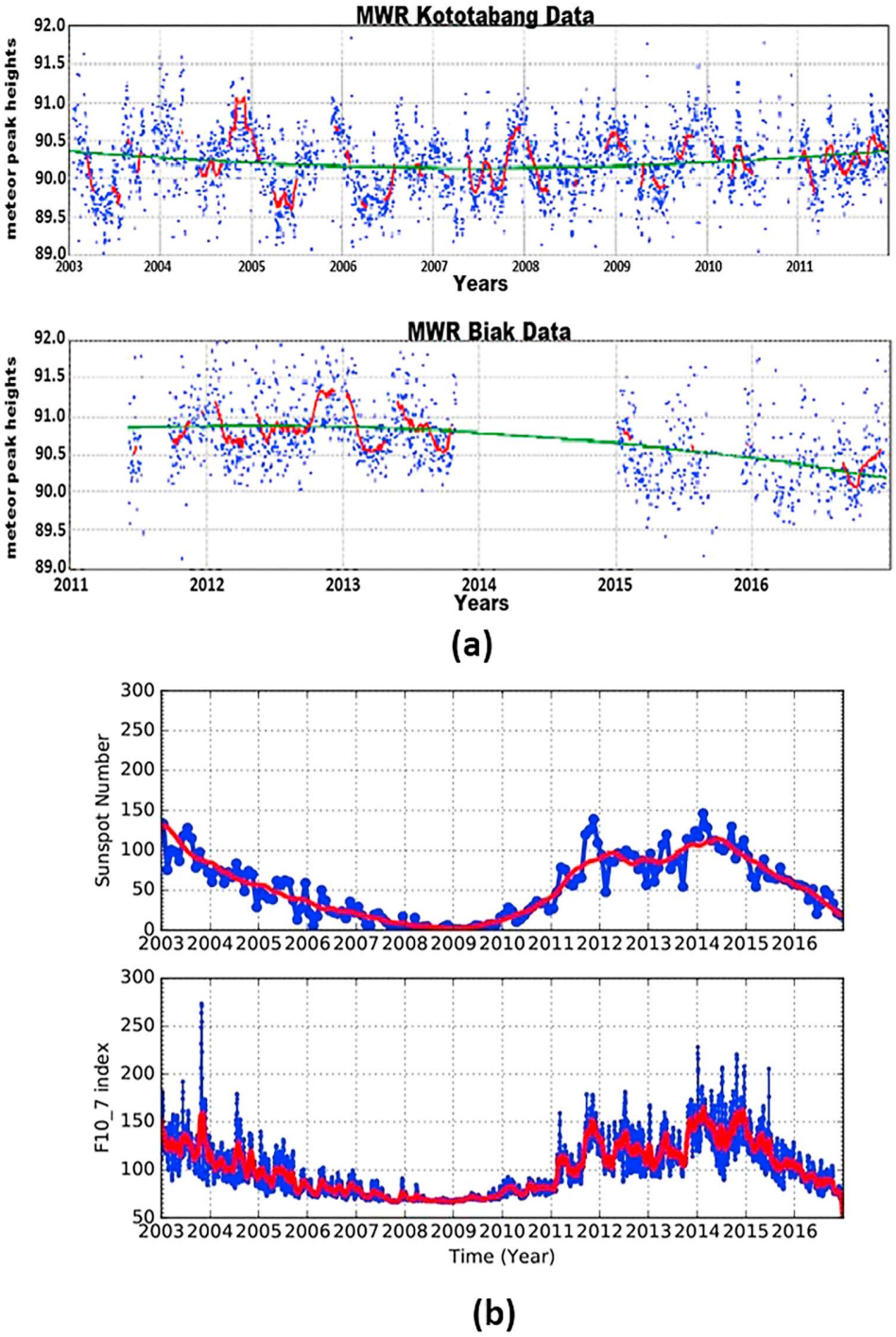

Figure 3. (a) Scatterplots of meteor peak heights at Kototabang for the period 2003–2011 (top) and Biak for the period 2011–2016 (bottom). The red curves show the 31-day running average and the green line is the fitting curve of the data. (b) Time series of the daily solar sunspot number, R (Royal Observatory of Belgium, 2013), and the solar radio flux, F10.7 index (OMNI web, 2005). MWR = meteor wind radar.

expected zenith angle of 80° and a height of 110 km. As shown in Figure 1b, the rates of meteor echoes are counted at each altitude and the Gaussian distribution function was used to obtain the meteor heights at the maximum detection rate. The distributions of the meteor peak heights obtained from the Kototabang and Biak meteor radars are shown in Figure 3a. The meteor heights show annual and semiannual components

that reach a peak at the end of the year, at altitudes of approximately 91.0 km, with minimums occurring mid-year at a height of approximately 89.5 km. Additionally, overall, the meteor height profile shows a parabolic-like curve over the 11-year solar cycle. Therefore, quadratic functions were used to ascertain the change in the meteor count rate trend. The green line shows the parabolic curve, in which the minimum and maximum peaks occur during 2007–2008 and 2012–2013, respectively. On the other hand, there seems to be a connection between the variation in meteor count rate (Figure 2) and that in meteor peak (Figure 3a). Many factors can influence the meteor count rate (e.g., the background population of ionized particles in the atmosphere and accumulated traces of meteor trails). The connection between solar activity and meteor count rate has been studied and discussed in temporal and spatial terms, by several researchers (Hajduk et al., 1980; Lindblad, 2003; McIntosh & Hajduk, 1977; Prikryl, 1983; Simek & Pecina, 2000). These studies provided a possible explanation of the changes observed in meteor rate according to variations in solar activity. On a timescale of many years, variations in shortwave solar radiation during the solar cycle may influence the meteor rates observed by a radar system.

Figure 3b shows the R (top panel) and F10.7 (bottom panel) values for the period 2003–2016; the changes in both have been the main targets of study to date, especially in terms of their effects on the atmospheric environment. The correlation between peak meteor height and solar activity is explained by F10.7 and R, as shown previously by many researchers (Buček et al., 2012; Porubčan et al., 2012; Porubčan & Cevolani, 1983; Porubčan & Getman, 1992). Other researchers (Jacobi, 2014; Lima et al., 2015; Lindblad, 1967) have conducted similar investigations using a meteor radar operating at a nonequatorial latitude and found good concordance between meteor height and solar activity parameters. Some parameters have provided long-term information about the variation in atmospheric conditions in the MLT region and their relation to solar activity. As mentioned previously, the meteor phenomenon depends on the incoming velocity and mass of the meteoroid. Air density also plays an important role in meteor ablation, wherein the height of the meteor echo peak becomes lower as density decreases (Clemesha & Batista, 2006; Stober et al., 2012). Therefore, the height of the meteor echo peak observed during the solar cycle can be interpreted as a consequence of the change in air density in the upper atmosphere caused by solar activity. In the following, an investigation of the relationship between solar activity and meteor peak height in the equatorial latitudes of Indonesia is discussed.

Our observation data include almost a full 11-year solar cycle, which is represented by the daily F10.7 and monthly R values and also by their 30-day running averages (red lines in Figure 3b). As shown in Figures 3a and 3b, there is a similar trend between the fitting curve of meteor peak height and the two solar activity parameters, although there are slight differences in time between them and an absence of data in 2014 due to system improvements being carried out at that time. To evaluate the correlations between average F10.7 and R values on an annual basis, the average meteor peak heights were used. Figure 4 shows three panels. The top-left and top-right panels present mean annual meteor peak height as a function of F10.7 and R values, respectively. The bottom panel shows the annual mean values of meteor peak height (blue line), and F10.7 (green line) and R values (red line). As shown in the figures, the annual mean meteor peak height, from the meteor radar observations at the Indonesian equator for 14 years (2003–2016), shows an adequate correlation (in the scale of ~0.8) with solar radio flux index F10.7 (Figure 4a) and solar sunspots R (Figure 4b). In addition, Figure 4c shows the annual plot of mean meteor peak height as a function of both solar parameters above, in which the trends show its uniformity in phase.

Despite the slight changes in the fitting curves seen in the top and bottom panels of Figure 3a, it is estimated that the minimum value occurred in 2007–2008, and the peak was in 2012–2013. This indicates a change in the average meteor height of ~0.1 km over a long period of solar activity, and the residual value is well represented statistically. From this perspective, the correlation between F10.7 and R seems attractive for investigating neutral temperature and density in the region of meteor ablation around the equator based on global empirical model calculations.

The annual height profiles over the altitude range of 88 to 94 km were also derived. These profiles are shown for both Kototabang and Biak in Figure 5. In Figure 5a (data from Kototabang), a clear cycle is apparent in the data. During the interval from December to February, the peak meteor count rate occurred at heights of ~90.5 km. However, between June and July, the peak meteor count rate was observed at lower heights (~90 km). Annual variation in the height of the peak meteor count rate was also observed at Biak (Figure 5b). During the period December to February, peak count rates occurred at heights of ~91 km, but during December to April, the peak count rates were observed at heights of ~90.5 km. Both profiles

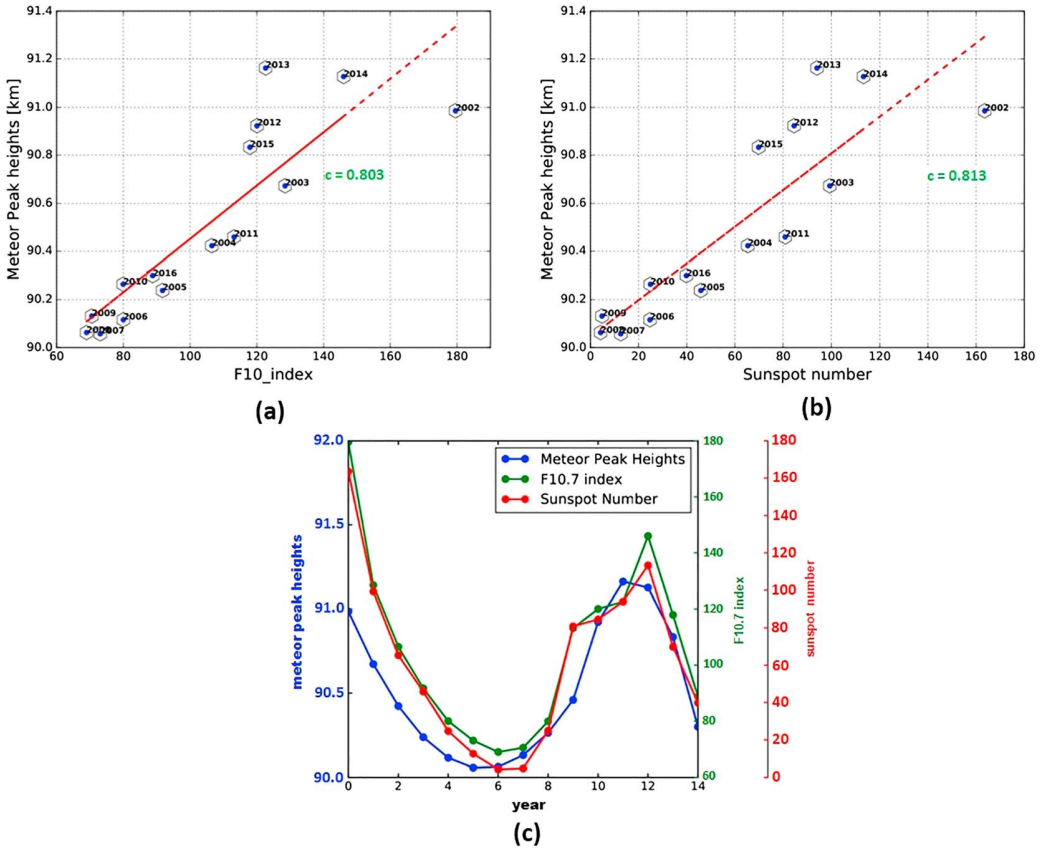

Figure 4. Annual mean meteor peak height as a function of annual F10.7 index a and R b, and c annual plot of mean meteor peak height (blue), mean R (red), and mean F10.7 (green).

showed anomalous meteor peak heights around April, July, October, and December (DoY 120, 220, 290, and 345). These anomalies are thought to have occurred simultaneously with the peak meteor shower period. The peaks of the Lyrid, Perseids, Orionid, and Geminid meteor showers occurred in the four periods (DoY 112, 225, 294, and 348; International Meteor Organization, 2007).

The temperature profile over the equatorial region calculated by NRLMSISE-00 could not seem to explain the variation of meteor peak height, while the temperature profile of the CIRA calculation shows its representation. To compare the annual trends in meteor peak height and mass density, as predicted by the empirical

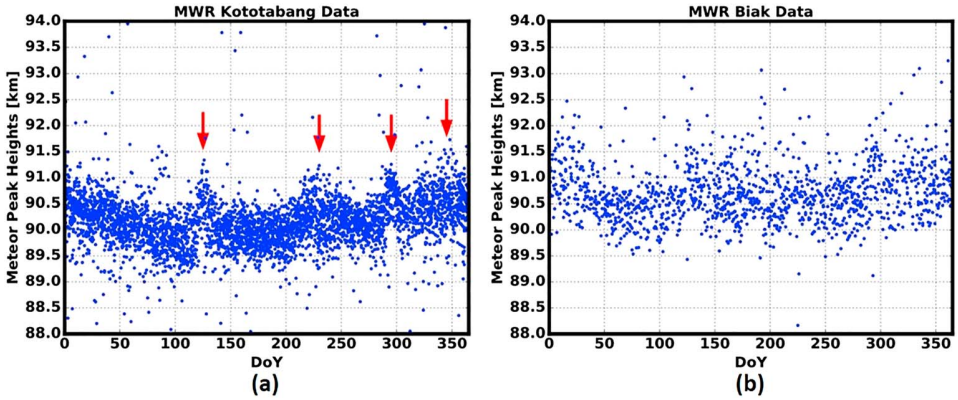

Figure 5. Annual cycle of meteor peak height based on 13 and 5 years' worth of data collected at Kototabang (left) and Biak (right), respectively. MWR = meteor wind radar.

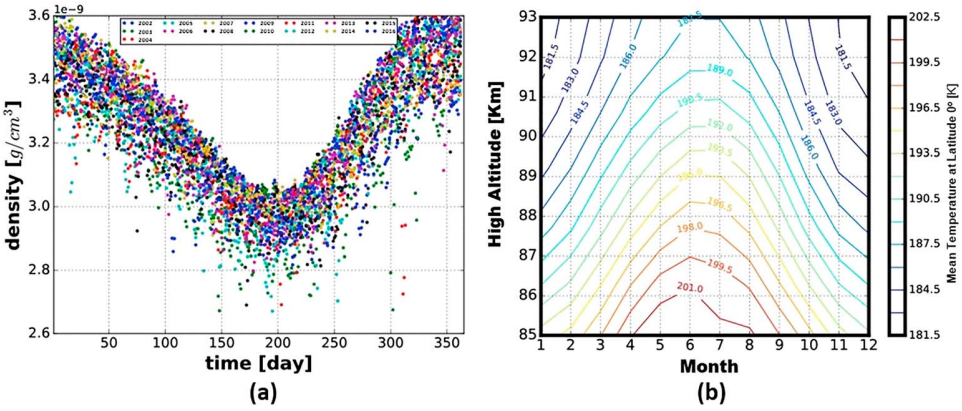

Figure 6. Annual pattern in predicted meteor density based on the NRLMSISE-00 model, as a function of day of the year for a 15-year period (left), and contour plot of mean temperature at equatorial latitudes predicted by the COSPAR International Reference Atmosphere model (right). The density profile is calculated at 90 km altitude.

models, we used the NRLMSISE-00 model to calculate the predicted density, and the CIRA model to predict the temperature at around 90 km height. As mentioned earlier, the NRLMSISE-00 with solar cycle effects and oxygen anomaly contributions can provide information about the conditions at high atmospheric altitudes. According to (Picone et al., 2002), below 73 km, this model uses coefficients from the MSISE90 model, but at the height of the MLT region, the coefficients are constrained to maintain consistency of the total mass density at the ground. According to (Stober et al., 2014), in high-altitude cases, the NRLMSISE-00 indicates no agreement between the mass density at MLT altitude and the effects of solar activity shown by the F10.7 and Ap indexes. An illustration of the annual variation in air density at meteor peak heights, during the period of 2002–2016 for the equatorial region derived from the NRLMSISE-00 model, is shown in Figure 6a. Similarly, information from the CIRA model on atmospheric temperatures in the MLT region over equatorial latitudes is shown in Figure 6b. Overall, Figure 6 shows that the minimum density, followed by the maximum temperature at the meteor peak height, occurs midyear (around June–July). On the other hand, the density value per day in 2002–2016 (Figure 7a) shows a different phase pattern to that of the solar activity cycle given by F10.7 and R (Figure 3b). Underscoring this relationship, the average yearly trend in mass density is shown in Figure 7b. These results accord with Stober's study in 2014 regarding the relationship of variations in solar activity with atmospheric density, where the NRLMSISE-00 model shows no obvious effect of the solar cycle at the MLT region according to the F10.7. In fact, they expected that there is no agreement between NRLMSIS and the air density, because NRLMSIS does not account for greenhouse gas effects in the lower and middle atmosphere.

We observed a variety of techniques to determine meteor peak heights in the literature. For example, the techniques of Liu et al. (2017) and Stober et al. (2014) use harmonic functions with a periodicity reflecting that

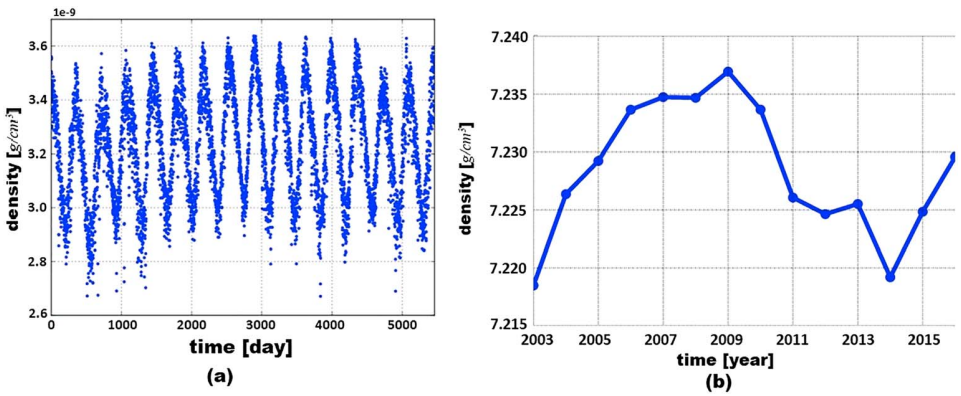

Figure 7. Scatterplot of atmospheric density as a funtion of time [day 01 = 1 Jan 2003], as predicted by the NRLMSISE-00 model at 90 km altitude (left), and annual mean atmospheric density at 90 km altitude as function of time (right).

of the solar activity cycle. Three other techniques, that is, those of Jacobi (2014), Lima et al. (2015), and Porubčan and Cevolani (1983), used a linear regression approach to obtain the meteor peak heights. These techniques are all assumed to rely on a combination of the annual mean heights at high latitudes and other periodic components. As described in (Hocking et al., 1997), a normal distribution function can be fitted into meteor radar data to obtain meteor peak heights. Note that the present results on meteor height are calculated based on the technique proposed by Hocking, but for the equatorial case, the peak value was taken from the maximum value of height distribution, assumed to be normally distributed. As shown in Figures 5 and 6, the relationship between density and meteor height seems clear, whereby the air density in the atmosphere each year affects the meteor height. This is in contrast to the results in Figures 7 and 3a, in which these parameters do not show a clear relationship. As shown in Figure 2, in particular for the meteor rate measured at Kototabang, the annual change in the number of detected meteor echoes generally shows an association with the change in atmospheric air density shown in Figure 7. The illustration above shows that the effect of solar activity on atmospheric density in the MLT region involves multiple processes, including atmospheric heating, particle drifting, and coupling processes, and remains among the issues that need to be further explored using large data sets at different locations.

5. Conclusions

In summary, we herein presented 13 years' worth of meteor observation data from the all-sky meteor very high frequency radar systems in Kototabang (0.20°S, 100.32°E) and Biak (1.17°S, 136.10°E), Indonesia. The observational data were used to map the distribution of the detected meteor echoes.

We compared our observations with the solar activity represented by F10.7 and R. Based on the normal distribution function (Hocking et al., 1997), the meteor peak heights showed a positive correlation with solar activity.

As solar activity initially impacts the Earth's equatorial atmosphere, especially affecting the atmospheric temperature and air density in the upper atmosphere, variation in the numbers of meteor echoes, neutral atmospheric parameters, and solar activity were examined. The results of the CIRA and NRLMSISE-00 empirical model calculations were used to obtain information on neutral atmospheric parameters in the MLT region at equatorial latitudes. We noted the following:

1. Annually, variations in meteor height peaks in the equatorial region showed a uniform double peak pattern and varied by neutral atmospheric density in the MLT region at equatorial latitudes.
2. In contrast, the average trend in annual neutral density did not vary by solar activity, which reinforces Stober's suggestion regarding the relationship between solar activity and atmospheric density based on MSISE model calculations.
3. The variation in atmospheric density predicted by the MSISE model at 90-km altitude followed the meteor count rate trend observed at the equatorial region for the period of 2003–2016.

Considering these results, the annual change in meteor peak height involves complex mechanistic processes independent of the major influence of solar activity, such as widening and narrowing at the intersection area between trajectories of the circular meteoric belt, according to the thickness of the Earth's atmosphere, which can in turn shift the region of meteoroid interaction with the Earth's atmosphere in a vertical direction parallel to altitude. Whether there is a causal relationship between the above parameters and meteor interactions with the Earth's atmosphere remains an open question. Nevertheless, the results over the equatorial region obtained in this study may serve as a reference for future studies of global atmospheric dynamics.

Acknowledgments
The present work was supported by SSP program of Kochi University of Technology. We are grateful to the Indonesian National Institute of Aeronautics and Space and RISH, Kyoto University, Japan, for providing the meteor radar data. We acknowledge use of NASA/GSFC's Space Physics Data Facility's OMNIWeb (or CDAWeb or ftp) service and OMNI data. The meteor radar data were obtained from the IUGONET-RISH Kyoto University database center (http://database.rish.kyoto-u.ac.jp/arch/iugonet/) and accessible repository (https://figshare.com/articles/mpd_KTB_2002_2016/7091933 and https://figshare.com/articles/mpd_BIK_2011_2016/7091729). The solar sunspot and solar radiation index F10.7 were obtained from the World Data Center Sunspot Index (http://sidc.be/silso/datafiles) and the NASA OMNIWeb Space Physics data facility (http://https//omniweb.gsfc.nasa.gov/). The atmospheric model-derived data were obtained from the Community Coordinated Modeling Center (https://ccmc.gsfc.nasa.gov/pub/modelweb/atmospheric/cira/) and (https://ccmc.gsfc.nasa.gov/modelweb/models/nrlmsise00.php). We thank the two reviewers for their constructive comments and helpful suggestions on an earlier version of the manuscript.

References

Batubara, M., Suryana, R., Manik, T., & Sitompul, P. (2011). Kototabang-West Sumatera meteor radar: System design and initial results of a large scale meteor echo. In *2011 6th International Conference on Telecommunication Systems, Services, and Applications (TSSA)* (pp. 17–21). IEEE. https://doi.org/10.1109/TSSA.2011.6095399

Brown, P., Weryk, R. J., Wong, D. K., & Jones, J. (2008). A meteoroid stream survey using the Canadian Meteor Orbit Radar. *Icarus*, *195*(1), 317–339. https://doi.org/10.1016/j.icarus.2007.12.002

Buček, M., Porubčan, V., & Zigo, P. (2012). Solar activity and Perseid meteor heights. *Contributions of the Astronomical Observatory Skalnate Pleso*, *42*(1), 22–32.

Ceplecha, Z., Borovicka, J., Graham, E. W., Revelle, O. D., Hawkes, R. L., Porubcan, V., et al. (1998). Meteor phenomena and bodies. *Space Science Reviews*, *84*, 327–471. https://doi.org/10.1023/A:1005069928850

Clemesha, B., & Batista, P. (2006). The quantification of long-term atmospheric change via meteor ablation height measurements. *Journal of Atmospheric and Solar-Terrestrial Physics*, *68*(17), 1934–1939. https://doi.org/10.1016/j.jastp.2005.12.008

Community Coordinated Modeling Center-NASA (2002). NRLMSISE-00 atmosphere model. Retrieved February 12, 2016, from http://https//ccmc.gsfc.nasa.gov/modelweb/models/nrlmsise00.php

COSPAR International Reference Atmosphere (1990). Empirical models of atmospheric. Retrieved February 12, 2016, from https://ccmc.gsfc.nasa.gov/

Fukao, S., Hashiguchi, H., Yamamoto, M., Tsuda, T., Nakamura, T., Yamamoto, M. K., et al. (2003). Equatorial atmosphere radar (EAR): System description and first results. *Radio Science*, *38*(3), 1053. https://doi.org/10.1029/2002RS002767

Hajduk, A., Pittich, E. M., & McIntosh, B. A. (1980). Changes in radar meteor echo rates at sunrise. *Contrib. Astron. Obs. Skalnaté Pleso*, *9*, 115. Retrieved from http://articles.adsabs.harvard.edu/cgi-bin/nph-iarticle_query?db_key=PRE&bibcode=1980CoSka...9..115H&letter=.&classic=YES&defaultprint=YES&whole_paper=YES&page=115&epage=115&send=Send+PDF&filetype=.pdf

Hocking, W. K., Fuller, B., & Vandepeer, B. (2001). Real-time determination of meteor-related parameters utilizing modern digital technology. *Journal of Atmospheric and Solar-Terrestrial Physics*, *63*(2–3), 155–169. https://doi.org/10.1016/S1364-6826(00)00138-3

Hocking, W. K., Thayaparan, T., & Jones, J. (1997). Meteor decay times and their use in determining a diagnostic mesospheric temperature-pressure parameter: Methodology and one year of data. *Geophysical Research Letters*, *24*(23), 2977–2980. https://doi.org/10.1029/97GL03048

Holdsworth, D. A., Morris, R. J., Murphy, D. J., Reid, I. M., Burns, G. B., & French, W. J. R. (2006). Antarctic mesospheric temperature estimation using the Davis mesosphere-stratosphere-troposphere radar. *Journal of Geophysical Research*, *111*, D05108. https://doi.org/10.1029/2005JD006589

International Meteor Organization (2007). Meteor Shower Calendar. Retrieved February 12, 2016, from https://www.imo.net/resources/calendar/

Jacobi, C. (2014). Meteor heights during the recent solar minimum. *Advances in Radio Science*, *12*, 161–165. https://doi.org/10.5194/ars-12-161-2014

Jones, J., Webster, A. R., & Hocking, W. K. (1998). An improved interferometer design for use with meteor radars. *Radio Science*, *33*(1), 55–65. https://doi.org/10.1029/97RS03050

Kaiser, T. R. (1954). Theory of the meteor height distribution obtained from radio-echo observations I. Shower meteors. *Monthly Notices of the Royal Astronomical Society*, *114*(1), 39–51. https://doi.org/10.1093/mnras/114.1.39

Kozlovsky, A., Lukianova, R., Shalimov, S., & Lester, M. (2016). Mesospheric temperature estimation from meteor decay times during Geminids meteor shower. *Journal of Geophysical Research: Space Physics*, *121*, 1669–1679. https://doi.org/10.1002/2015JA022222

Kyoto University (2015). Meteor wind and medium frequency radar data over Indonesia. Retrieved February 12, 2016, from http://database.rish.kyoto-u.ac.jp/arch/iugonet/

Lembaga Penerbangan dan Antariksa Nasional (2015). Repository database Sains Antariksa. Retrieved February 12, 2016, From https://bimasakti.sains.lapan.go.id

Lima, L. M., Araújo, L. R., Alves, E. O., Batista, P. P., & Clemesha, B. R. (2015). Variations in meteor heights at 22.7°S during solar cycle 23. *Journal of Atmospheric and Solar-Terrestrial Physics*, *133*, 139–144. https://doi.org/10.1016/j.jastp.2015.08.015

Lindblad, B. A. (1967). Solar cycle variation in atmospheric density as deduced from meteor observations. *Meddelanden Fran Lunds Astronomiska Observatorium Series I*, *226*, 1029–1043. Retrieved from http://articles.adsabs.harvard.edu/cgi-bin/nph-iarticle_query?db_key=AST&bibcode=1967MeLuF.226.1029L&letter=.&classic=YES&defaultprint=YES&whole_paper=YES&page=1029&epage=1029&send=Send+PDF&filetype=.pdf

Lindblad, B. A. (2003). *Solar control of meteor radar rates. Solar variability as an input to the Earth's environment. International Solar Cycle Studies (ISCS) Symposium, 23-28 June 2003, Tatranska Lomnica, Slovak Republic* (ESA SP-535, pp. 755–759). http://lup.lub.lu.se/record/528078

Liu, L., Liu, H., Chen, Y., Le, H., Sun, Y. Y., Ning, B., et al. (2017). Variations of the meteor echo heights at Beijing and Mohe, China. *Journal of Geophysical Research: Space Physics*, *122*, 1117–1127. https://doi.org/10.1002/2016JA023448

Matsumoto, N., Shinbori, A., Riggin, D. M., & Tsuda, T. (2016). Measurement of momentum flux using two meteor radars in Indonesia. *Annales Geophysicae*, *34*(3), 369–377. https://doi.org/10.5194/angeo-34-369-2016

McIntosh, B. A., & Hajduk, A. (1977). Sunrise effect on persistent radar echoes from sporadic meteors. *Bulletin of the Astronomical Institutes Czechoslovak*, *28*(5), 280–285. Retrieved from http://articles.adsabs.harvard.edu/cgi-bin/nph-iarticle_query?db_key=AST&bibcode=1977BAICz..28..280M&letter=.&classic=YES&defaultprint=YES&whole_paper=YES&page=280&epage=280&send=Send+PDF&filetype=.pdf

McKinley, D. W. R. (1961). *Meteor science and engineering*. United States of America: McGraw-Hill.

Pecina, P., & Simek, M. (1999). Analysis of the Geminid meteor stream, 1958 – 1997, from radar observations. *Astronomy and Astrophysics*, *1000*, 991–1000. Retrieved from http://articles.adsabs.harvard.edu/cgi-bin/nph-iarticle_query?db_key=AST&bibcode=1999A%26A...344..991P&letter=.&classic=YES&defaultprint=YES&whole_paper=YES&page=991&epage=991&send=Send+PDF&filetype=.pdf

Pellinen-Wannberg, A., Murad, E., Brosch, N., Häggström, I., & Khayrov, T. (2009). The solar cycle effect on the atmosphere as a scintillator for meteor observations. *Proceedings of the International Astronomical Union*, *5*(S263), 249–252. https://doi.org/10.1017/S1743921310001869

Picone, J. M., Hedin, A. E., Drob, D. P., & Aikin, A. C. (2002). NRLMSISE-00 empirical model of the atmosphere: Statistical comparisons and scientific issues. *Journal of Geophysical Research*, *107*(A12), 1468. https://doi.org/10.1029/2002JA009430

Pifko, S., Janches, D., Close, S., Sparks, J., Nakamura, T., & Nesvorny, D. (2013). The meteoroid input function and predictions of mid-latitude meteor observations by the MU radar. *Icarus*, *223*(1), 444–459. https://doi.org/10.1016/j.icarus.2012.12.014

Porubčan, V., Bucek, M., Cevolani, G., & Zigo, P. (2012). Variation of meteor heights and solar-cycle activity. *Publications of the Astronomical Society of Japan*, *64*, 1–5.

Porubčan, V., & Cevolani, G. (1983). Distribution of meteor heights and sunrise. *Astronomical Institutes of Czechoslovakia, Bulletin (ISSN 0004–6248)*, *34*, 213–219. Retrieved from http://adsbit.harvard.edu/cgi-bin/nph-iarticle_query?1983BAICz..34..213P&defaultprint=YES&filetype=.pdf

Porubčan, V., & Getman, V. S. (1992). Distribution of meteor heights and the solar cycle activity. *Contributions of the Astronomical Observatory Skalnate Pleso*, *22*, 33–39. Retrieved from http://adsabs.harvard.edu/full/1992CoSka..22...33P

Prikryl, P. (1983). Radar meteor rates and solar activity. *Astronomical Institutes of Czechoslovakia, Bulletin (ISSN 0004–6248)*, *34*, 44–50. https://doi.org/10.1023/A:1015816116844

Qian, L., & Solomon, S. C. (2012). Thermospheric density: An overview of temporal and spatial variations. *Space Science Reviews*, *168*(1–4), 147–173. https://doi.org/10.1007/s11214-011-9810-z

Royal Observatory of Belgium (2013). World Data Center-Sunspot Index and Long-term Solar Observations. Retrieved February 12, 2016, From http://sidc.be/silso/datafiles

Simek, M., & Pecina, P. (2000). Radar sporadic meteor rates and solar activity. *Earth, Moon and Planets*, *88*(2), 115–122. https://doi.org/10.1023/A:1015816116844

Stober, G., & Chau, J. L. (2015). A multistatic and multifrequency novel approach for specular meteor radars to improve wind measurements in the MLT region. *Radio Science*, *50*, 431–442. https://doi.org/10.1002/2014RS005591

Stober, G., Jacobi, C., Matthias, V., Hoffmann, P., & Gerding, M. (2012). Neutral air density variations during strong planetary wave activity in the mesopause region derived from meteor radar observations. *Journal of Atmospheric and Solar-Terrestrial Physics*, *74*, 55–63. https://doi.org/10.1016/j.jastp.2011.10.007

Stober, G., Jacobi, C., & Singer, W. (2011). Meteoroid mass determination from underdense trails. *Journal of Atmospheric and Solar-Terrestrial Physics*, *73*(9), 895–900. https://doi.org/10.1016/j.jastp.2010.06.009

Stober, G., Matthias, V., Chau, J. L., & Brown, P. (2014). Neutral air density variations derived from specular meteor echo observation spanning one solar cycle. *Geophysical Research Letters*, *41*, 6919–6925. https://doi.org/10.1002/2014GL061273.Specular

Szasz, C., Kero, J., Pellinen-Wannberg, A., Mathews, J. D., Mitchell, N. J., & Singer, W. (2005). Latitudinal variations of diurnal meteor rates. *Earth, Moon and Planets*, *95*(1–4), 101–107. https://doi.org/10.1007/s11038-005-9007-0

Takahashi, H., Nakamura, T., Tsuda, T., Buriti, R. A., & Gobbi, D. (2002). First measurement of atmospheric density and pressure by meteor diffusion coefficient and airglow OH temperature in the mesopause region. *Grl*, *29*(8), 6-1–6-4. https://doi.org/10.1029/2001gl014101

The National Aeronautics and Space Administration (2005). NASA/GSFC's Space Physics Data Facility's OMNIWeb Data. Retrieved February 12, 2016, from http://https//omniweb.gsfc.nasa.gov/

Yi, W., Xue, X., Chen, J., Dou, X., Chen, T., & Li, N. (2016). Estimation of mesopause temperatures at low latitudes using the Kunming meteor radar. *Radio Science*, *51*, 130–141. https://doi.org/10.1002/2015RS005722

Yi, W., Xue, X., Reid, I. M., Younger, J. P., Chen, J., Chen, T., et al. (2018). Estimation of mesospheric densities at low latitudes using the Kunming meteor radar together with SABER temperatures. *Journal of Geophysical Research: Space Physics*, *123*, 3183–3195. https://doi.org/10.1002/2017JA025059

Younger, P. T., Astin, I., Sandford, D. J., & Mitchell, N. J. (2009). The sporadic radiant and distribution of meteors in the atmosphere as observed by VHF radar at Arctic, Antarctic and equatorial latitudes. *Annales Geophysicae*, *27*(7), 2831–2841. https://doi.org/10.5194/angeo-27-2831-2009

Zigo, P., Porubčan, V., Cevolani, G., & Pupillo, G. (2009). The activity and mass distribution of the Geminid meteor shower of 1996-2007 from forward scatter radio observations. *Contributions of the Astronomical Observatory Skalnate Pleso*, *39*(1), 5–17. Retrieved from http://articles.adsabs.harvard.edu/cgi-bin/nph-iarticle_query?db_key=AST&bibcode=2009CoSka..39....5Z&letter=.&classic=YES&defaultprint=YES&whole_paper=YES&page=5&epage=5&send=Send+PDF&filetype=.pdf

PUBLICATION II

***

Mizumoto, S., Yamamoto, M.-Y., & Batubara, M. (2019). *Construction of a meteor orbit calculation system for comprehensive meteor observation at Kochi University of Technology*. Planetary and Space Science, 173,35-41. https://doi.org/10.1016/j.pss.2019.03.004.

Planetary and Space Science 173 (2019) 35–41

Contents lists available at ScienceDirect

Planetary and Space Science

journal homepage: www.elsevier.com/locate/pss

Construction of a meteor orbit calculation system for comprehensive meteor observation at Kochi University of Technology

Satoshi Mizumoto [a,*], Masa-yuki Yamamoto [a], Mario Batubara [a,b]

[a] Kochi University of Technology, Japan
[b] Space Science Center, Indonesian National Institute of Aeronautics and Space (LAPAN), Indonesia

A B S T R A C T

The development of a Ham-band Radio meteor Observation (HRO) Interferometer (IF) at Kochi University of Technology began in 2003. Meteor orbit calculation system uses multi-site radio observation with global positioning system (GPS) timing combined with 5 channel (5 ch) interferometer. The HRO-IF utilizes forward-scattering of 53.750 MHz continuous radio waves transmitted from the Sabae station, realized in 2012. Since the last development, the observation data has been used to study the upper atmosphere from the meteor phenomenon. Here, we introduce the results of the 2015 Geminid meteor shower recorded by forward-scatter multi-site observations as a low-cost and low-power 24/7 continuous meteor observation system, as well as the concept of a comprehensive radio meteor orbit calculation system. As a result, 20 examples of Geminid meteor shower events with 3 levels of noise signal classification recorded in our observations. The predicted Geminid meteor shower speed is about 34 ± 8.86 km/s based on the average value of 12 meteor shower data group in the minimum noise signal category (class A).

1. Introduction

When comets approach the Sun, they release dust particles ranging in diameter from about several micrometres to several centimetres. These dust particles gradually deviate from the original cometary dust trail due to the perturbation effects of the gravitational forces of planets, such as Jupiter or Saturn, and begin to be distributed across the Solar System. When the Earth approaches the cometary dust trail, some of the dust particles enter the atmosphere, collide with atmospheric particles, and ablate at high temperatures. Upon interaction, upper atmospheric species and the vaporised dust components emit light and heat, and are thus observed as meteors. The emission of light is associated with a narrow high-density plasma column formed for a short time along the meteor trajectory at heights between 80 km and 120 km, close to the ionospheric E layer that exists in the lower thermosphere of the Earth's atmosphere (Fig. 1). Meteors can be observed with 24/7 continuous operation using the scattering of radio waves from ionised plasma.

There are a few groups constantly observing the activities of meteors in other Japanese research organizations. The Research Institute for Sustainable Humanosphere (RISH), Kyoto University, has a large-scale middle and upper atmospheric radar (MU radar) that can detect meteor shower activity in detail by a high-power backscattering method, using the same location as a transmitting and receiving station (Kero et al., 2012). However, its observation period has limitations, *i.e.*, the MU radar cannot always perform its observation of the meteors because the observation time is occupied by the observation of other atmospheric phenomena. A forward scattering meteor radar using 53.750 MHz Very High Frequency (VHF) continuous radio waves (CW) without any pulse codes for observation of meteor shower activities has been operated at Kochi University of Technology (KUT) since 2003.

A huge meteor event, a so-called bolide, may produce a sound signal at the time of its atmospheric entry. The meteor seen as a large fireball flying in the atmosphere at supersonic speed can sometimes cause a bass shock wave sound for a few minutes afterwards. Infrasound (*i.e.,* sound below the limit of human hearing at around a frequency of 20 Hz) is generated in the sky at the same time as the strong shock wave. It arrives at the Earth's surface at the speed of sound and can be observed using high-sensitivity infrasound sensors (Le Pichon et al., 2013). Infrasound can be generated by many types of explosive events, such as rocket launches (Kaschak et al., 1970), nuclear bomb tests and huge chemical explosions (Christie and Campus, 2009), re-entry of satellites or large space debris (Yamamoto et al., 2011), volcanic eruptions (Johnson, 2004), tsunamis (Arai et al., 2011), landslides and thunder (Lin and Langston, 2007). The data (arrival time, direction, shock pressure change) of the wave taken during artificial re-entry is very important for estimation of the mass of a meteor, which cannot be accurately

* Corresponding author.
E-mail addresses: s.mizumoto0918@gmail.com (S. Mizumoto), yamamoto.masa-yuki@kochi-tech.ac.jp (M.-y. Yamamoto), mario.batubara@lapan.go.id (M. Batubara).

https://doi.org/10.1016/j.pss.2019.03.004
Received 14 September 2016; Received in revised form 18 January 2019; Accepted 11 March 2019
Available online 18 March 2019
0032-0633/

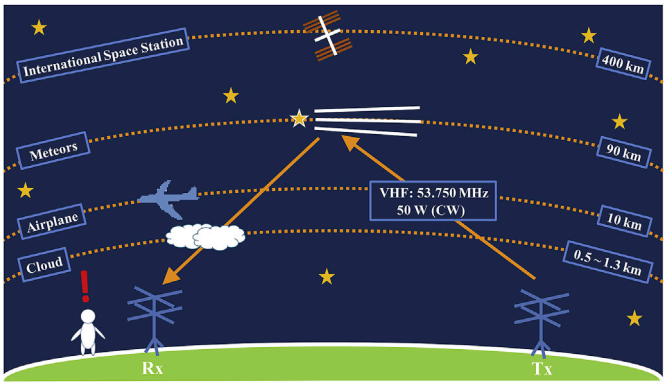

Fig. 1. Schematic view of meteor in atmosphere.

determined for tiny particles by electromagnetic observation (Brown et al., 2013).

Huge datasets of meteors and fireballs have been archived from naked-eye visual observations in history (Ceplecha et al., 1998). In addition to optical observations, high-sensitivity cameras are used for precise observation (SonotaCo, 2009). The data provided by radio observations and infrasound sensors must be compared to optical observations as calibration datasets to improve their reliability, because the distinction of each meteor phenomenon under the influence of environmental radio/sound noise at each observation site is difficult. We can confirm the optic imaging meteor data by checking with naked-eye or automatic image processing; this represents an important element in verifying that the data detected by radio and infrasound observations were real signals of meteors and fireballs at precisely the same time as each phenomenon. On the other hand, observation of electromagnetic waves and infrasound has a statistical advantage of continuous operation under rainy weather conditions and even in the daytime. Here, we introduce the results for the Geminid meteor shower obtained by multiple-site forward scattering radio meteor observation, design of a comprehensive meteor observation system using multiple-site forward scattering radio observation and represent the speed of the Geminid meteor shower classified by the multi-site HRO-IF system.

2. Meteor radio observation

A streak of light glow on the clear-dark sky due to the entry of meteoroids into the Earth's atmosphere may produce effects such as ionization of atmospheric molecules. During the entry of meteoroids or dust particles into the upper atmosphere, atoms vaporized via meteoroid collisions with air molecules created the ionized trail and plasma column. At this time, the high-density plasma column whose diameter is small compared to the length of the trail is formed due to the diffusion effect in a short period along the trajectory of the meteor. The ionised pillar scatters radio waves of a frequency less than a certain value depending on the plasma density (plasma frequency). The radio observation of meteors uses the meteor trail plasma as a scattering medium in the sky. The density characteristics of meteor plasma are used in the observation method of Ham-band Radio meteor Observation (HRO). Radio meteor observation using ham-band radio waves was established in Japan during the peak period of the Leonid meteor shower activity from 1998 to 2002. Amateur meteor observers and ham operators spread all over Japan focused on meteor astronomy mainly since a guidebook (RMG editing committee, 2002) introduced the details of HRO observation. The HRO method is based on receiving the VHF beacon wave of 50 W, 53.750 MHz in the amateur radio band, transmitted from the National Institute of Technology, Fukui College at Sabae, Fukui prefecture, with 24/7 continuous operation. Thereby, meteors can be observed without being blocked by poor weather or daylight (Maegawa, 1999). The VHF wave can propagate only in a certain range, like FM radio broadcasting waves (76–90 MHz in Japan). It cannot be received at the observation point far from the transmission station due to the attenuation by distance as well as obstacles of mountains and/or buildings. However, the transmitted waves can be detected at the receiving station once scattered from an ionised meteor plasma pillar. We have been operating the HRO radio observation at KUT using the characteristics of the forward scattering method.

There are few groups engaged in meteor radio observation at Japanese research institutes. Observation of meteor radio waves with backscattering methods such as MU radar, it is possible to obtain very accurate meteor parameters in a short time due to its 1-MW high-power transmission with a composed radar system from many antenna groups (Kero et al., 2012). However, available operation time of the MU radar is limited only for campaign periods, and thus the detection of meteor echoes for occasional sporadic meteor bursts is almost impossible. The University of Western Ontario developed the Canadian Meteor Orbit Radar (CMOR), which has produced many statistical studies. The CMOR team established two receiver stations in the neighbourhood (6.2 and 8.1 km) of CMOR backscatter transmitting receiving sites (Jones et al., 2005). In addition, the CMOR systems have added three more receiving sites since 2009 (Blaauw et al., 2011). Observations have been carried out to receive meteor-scattered radio waves by five antennas, like the KUT system with multiple remote sites. The Southern Argentina Agile MEteor Radar (SAAMER) Orbital System (OS) installed an arrayed transmitting station and two remote receiving stations (8 km and 13 km) similar to the CMOR observation system (Janches et al., 2015). In Japan, similar observations have been carried out to receive meteor-scattered radio waves by five-channel interferometry. Therefore, KUT is currently the only research group continuously observing meteor activity by five-channel interferometry (5ch HRO-IF) with application of the forward scattering method.

3. Principle of multiple-site observation

The basic development of the HRO meteor radio observation began in 2003 at KUT, and we developed the 3 channel (3ch) HRO-IF system, which was improved to the current 5ch HRO-IF system in 2005, to begin continuous meteor observation (Horiuchi, 2005; Okamoto, 2005). The previous 3ch HRO-IF had a large measurement error in the arrival angle calculated from phase differences, especially in the case of lower elevation angles. Thus, the accuracy of the observation was limited only at elevation angles $> 45°$. To resolve this problem, we developed the 5ch HRO-IF using the Jones concept (Fig. 2) (Jones and Webster, 1991; Jones et al., 1998). Due to the limited space at the KUT campus, we applied the concept using 1 λ and 1.5 λ (Fig. 3) (Noguchi, 2009).

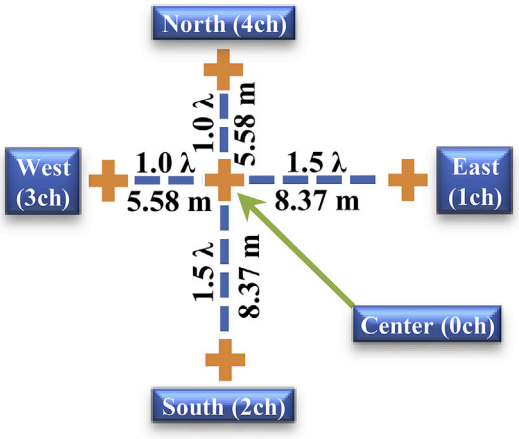

Fig. 2. Antenna configuration of 5-ch HRO-IF.

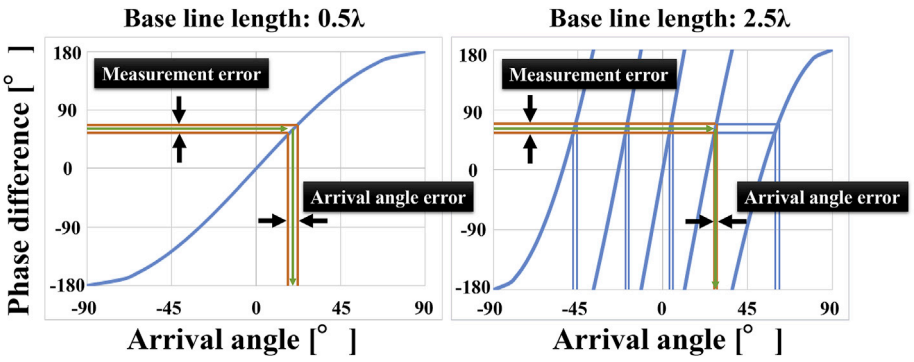

Fig. 3. Relation between phase difference and arrival angle by 5-ch HRO-IF.

After realising stable automatic observations with the 5ch HRO-IF operating for approximately 2 years (Noguchi and Yamamoto, 2008), the measurement accuracy of the arrival angle improved (Madkour et al., 2016). Furthermore, we can plot the meteor appearance position projected on a map assuming 90 km as the average altitude of the meteors, and show their locations on a web page in quasi-real-time (Noguchi, 2009). In 2014, we restarted the radio observation, and successfully observed two irregular meteor showers, *i.e.*, the Camelopardalis and Phoenicids; and the major meteor shower, Daytime Arietids; as well as major annual swarms, Leonids, Geminids and Quadrantids. In 2014, we started the 5ch HRO-IF system with continuous operation of two remote sites as a multi-site observation system (Mizumoto, 2015).

Two observation sites were added to the 5ch HRO-IF, therefore meteor echo data can be obtained at almost the same time at three independent sites. We can calculate the meteor trajectory angle and velocity using slight time differences between these sites. Therefore, we can judge whether each echo is originating from a seasonal meteor shower or from the sporadic background, as well as compare the datasets with radio observations.

Each of the two newly added sites has the same antenna as an element of the 5ch HRO-IF. We use wave extraction software for meteor observation with precise timing (Yamasaki, 2012). This software generates receiving intensity trends with 100-ms accuracy with the usually operated waveform analysis results of receiving signal at 100-ms resolution for each 10-min observation bin. Here, we have to obtain high-accuracy time differences for the calculation of meteor trajectory angle and velocity from multi-site observation. The meteor velocity in the Earth's atmosphere is about 11 km/s to 72 km/s depending on its Kepler orbit around the Sun (Ceplecha et al., 1998).

Thus, there must be a distance at least 10 km between the 5ch HRO-IF and the other two remote sites (Otoyo and Geisei). The 5ch-interferometer software analyses the receiving signal with a 100-ms time frame, and calculates the meteor appearance time, azimuth, and elevation parameters. When we successfully observe a meteor simultaneously by multi-site observation at all three sites, it is necessary to maintain the accuracy of time by a global positioning system (GPS) signal and launch the wave extraction software. The received signal is analysed with 1-ms time resolution for all observation stations. Then, we can calculate the meteor trajectory angle and velocity by each time difference if a meteor shower radiant is assumed. Meteor trajectory angle and velocity calculation procedures are as follows (Fig. 4):

$$A_z = \tan^{-1}\left(\frac{v_2 \cos\theta_2 - v_1 \cos\theta_1}{v_1 \sin\theta_1 - v_2 \sin\theta_2}\right) \quad (1)$$

$$v_1 = \frac{d_1}{t_1} \quad (2)$$

$$v_2 = \frac{d_2}{t_2} \quad (3)$$

where A_z is the meteor trajectory azimuth angle (°, North = 0°), θ_1 is the positional relation between KUT and Otoyo (°), θ_2 is the positional relation between KUT and Geisei (°), d_1 is the distance from KUT to Otoyo (km), d_2 is the distance from KUT to Geisei (km), t_1 is the time difference between KUT and Otoyo (s), and t_2 is the time difference between KUT and Geisei (s). Determination of the three-dimensional velocity of the observed meteor is performed using the radiant point of the meteor shower. The shower-originating meteors come in parallel from a known radiant point to the Earth. The radiant point can be shown as a point on the celestial sphere (Fig. 5). The meteor can be seen as moving from the radiant point if it originated from a certain meteor shower. Although, meteors may be seen spreading away from one spot of the radiant for all directions in the celestial sphere, the meteor shower's entry to the Earth occurs in parallel with the same entry angle from space at the same time period. In this case, the categorization between meteor shower and sporadic is determined based on their initial velocity and direction of motion (Valsecchi et al., 1999). In addition, using the equations described above with the actual data, we can distinguish the origin of

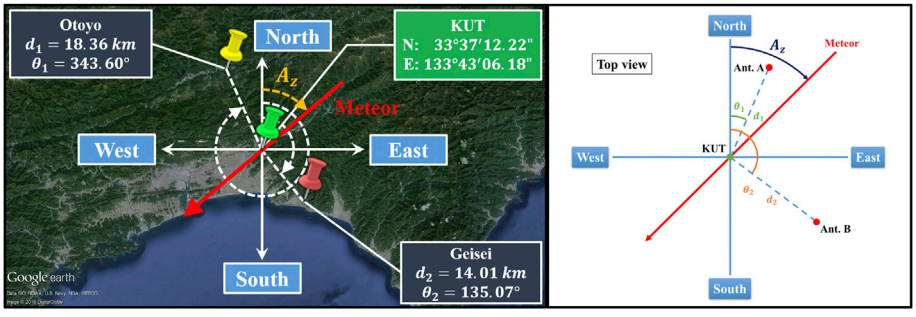

Fig. 4. Locational relation of observatories for multiple-site observation.

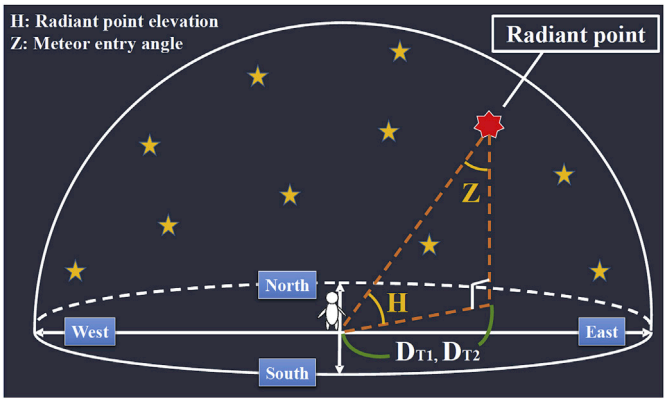

Fig. 5. Relation of radiant point elevation and meteor entry angle.

each meteor, *e.g.*, whether a meteor is a Geminid or is sporadic. Referring to Figs. 4 and 5, the three-dimensional meteor speed using the radiant point is calculated as follows:

$$V = \frac{V_H}{\cos H} \tag{4}$$

$$V_H = \frac{\left(\frac{D_{T1}}{t_1}\right) + \left(\frac{D_{T2}}{t_2}\right)}{2} \tag{5}$$

$$D_{T1} = d_1 cos(\theta_1 - A_z) \tag{6}$$

$$D_{T2} = d_2 cos(\theta_2 - A_z) \tag{7}$$

where V is the meteor velocity entrance on the celestial sphere (km/s), D_{T1} and D_{T2} are the horizontal distance in the meridional and zonal directions (km), Z is the meteor entry zenith angle (°), and V_H is the meteor velocity on the horizontal plane (km/s). The entry zenith angle Z of the meteor to the Earth is calculated after creating a right-angled triangle on a vertical plane as its oblique line is from the observation point to the radiant point. It is possible to estimate the speed of the meteor shower from the formula described above (Fig. 5).

4. Observation results

We observed Geminid meteor shower for one week (Dec. 11–17, 2015) by a multiple-site radio observation. This results in 20 events of Geminid meteor showers with various noise classification level. At the same time, we performed optical observation at KUT. The field of view of the camera used was aimed toward the East. We obtained velocity information by adding the two new observation sites at Otoyo and Geisei on the 5ch HRO-IF at KUT. We obtained 56 simultaneous meteor echo data at all three receiving stations. Example waveform data are shown in Fig. 6. Using the time differences from the results of waveform data, we calculated the meteor velocity, trajectory angle data for 20 meteor echo datasets, and calculated the meteor positioning data by 5ch HRO-IF for 20 datasets. The remaining 36 meteor echo datasets could not be used for calculation of actual meteor velocities because these meteor echo datasets were disturbed by noise due to the low receiving power. The observation results of the 2015 Geminid meteor shower shown in Table 1 indicate a number of parameters as follows from the left: 1) Date; 2) Meteor appearance time in LT (JST = UT + 9); 3) Time difference between KUT and Otoyo; 4) Time difference between KUT and Geisei; 5 and 6) Appearance latitude and longitude of the meteor for which the appearance altitude (90 km) of the meteor is supposed; 7) Meteor trajectory (MT) angle (°, North = 0°); 8) Radiant point (RP) azimuth angle of the Geminids; 9) Radiant point elevation angle of the Geminids; 10)

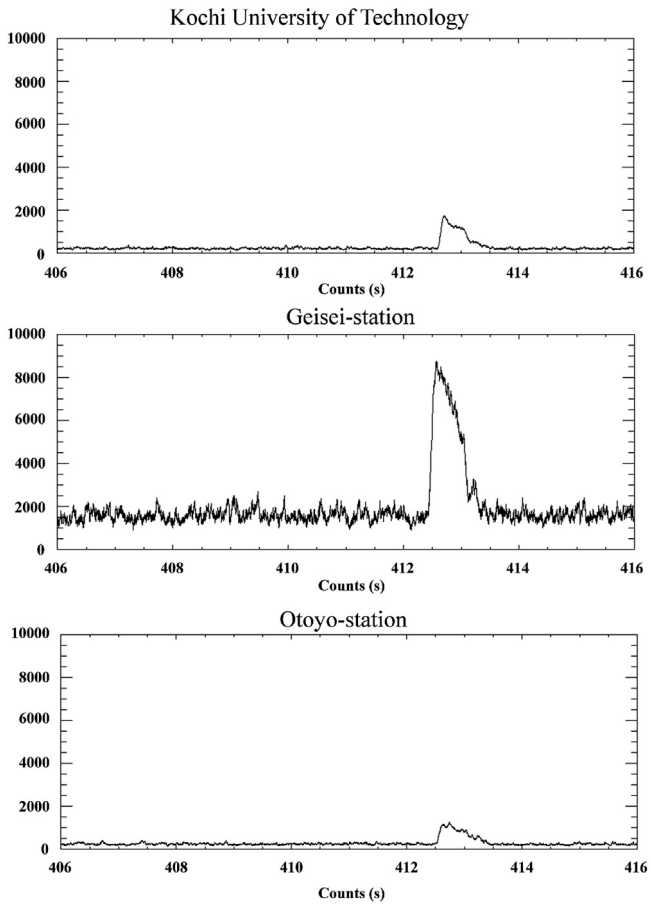

Fig. 6. Simultaneous observation example at each observation site (X axis: Time on Dec. 13, 2015, between 19:26:46 and 19:26:56, Y axis: Relative intensity of receiving power).

Threshold parameter for classification; 11) Meteor entry zenith angle Z; 12) Horizontal component of meteor velocity; 13) Actual meteor velocity in 3-D space; 14) Classification as Geminid or sporadic meteor (here, Geminids were defined as having a difference between the RP angle and MT angle $< 25°$, while sporadic meteors had an angle $> 25°$, and meteors with velocities > 50 km/s were removed from the Geminids as described below); and 15) Classification of the noise level (A: Clear; B: Normal; and C: Noisy).

We calculated that the Geminid meteor shower had an average velocity of 34.02 ± 8.86 km/s based on 12 recorded data of meteors with the A classification of clear noise level. As the Geminid meteor shower has been reported to have average speeds of around 35 km/s (Ceplecha et al., 1998; Jenniskens, 1994; Stober et al., 2013), this result corresponded well with the expected velocity (Table 1). We removed meteors with velocities > 50 km/s from the Geminids group as another peak of sporadic meteors was reported at the same time period of Geminid in previous radio meteor observations (Stober et al., 2013). Thus, a distribution with two peaks of velocity was seen with one peak at around 35 km/s corresponding to the Geminids and another at 50–70 km/s corresponding to sporadic meteors. Fast meteors around 60 km/s may have originated from the north apex source (Kero et al., 2012). Therefore, we removed the fast meteors from our data. An example is shown in Fig. 7, in which the meteor appeared travelling south-south-west at about 104 km far from KUT, and the meteor trajectory was directed west-south-west. The radiant point of the Geminids was located at east-north-east. The difference in angle between the meteor trajectory (MT) angle and the radiant point (RP) angle was 168.27°, which was

Table 1
Observation results of the Geminids meteor shower.

Appearance time		Time differences		Appearance location		MT angle	RP direction		Threshold	Meteor entry angle	Horizontal component			Velocity	Distinction	Classified
Date	Time [JST]	t1 [s]	t2 [s]	Latitude	Longitude	Az [°]	RP azimuth [°]	H [°]	Th [°] =< ±25°	Z [°]	VH1 [km/s]	VH2 [km/s]	VH [km/s]	V [km/s]	Gem./Spo.	Class
Dec. 11, 2015	16:31:59	−0.090	0.436	–	–	78.59	29.87	−17.00	48.72	107.00	17.78	17.75	17.77	–	Spo.	B
	20:40:29	0.034	0.140	–	–	69.25	65.28	21.92	3.97	68.09	40.88	41.00	40.94	44.13	Gem.	B
Dec. 12, 2015	1:11:57	0.370	0.230	–	–	57.85	92.98	76.89	−35.13	13.11	13.46	13.48	13.47	–	Spo.	A
	5:43:22	0.908	0.417	–	–	55.72	282.98	46.30	−227.26	43.70	6.21	6.21	6.21	–	Spo.	A
	7:11:26	0.292	−1.212	–	–	259.58	291.14	28.75	−31.56	61.26	6.54	6.55	6.55	–	Spo.	C
	7:24:53	1.596	1.336	–	–	60.00	292.47	26.14	−232.46	63.86	2.71	2.70	2.71	–	Spo.	C
	9:24:45	0.310	−0.270	–	–	314.77	306.02	4.44	8.76	85.56	51.87	51.89	51.88	–	Spo.	A
	19:18:55	−0.020	0.210	–	–	75.72	56.53	7.28	19.20	82.72	34.00	34.00	34.00	34.28	Gem.	A
	22:11:47	−0.104	0.278	–	–	83.92	74.46	40.55	9.46	49.45	31.63	31.62	31.63	41.63	Gem.	C
Dec. 13, 2015	6:59:03	0.180	−0.049	–	–	31.13	290.32	30.39	−259.19	59.61	68.89	68.78	68.84	–	Spo.	A
	6:59:15	0.877	−0.173	–	–	35.99	290.34	30.35	−254.35	59.65	12.77	12.77	12.77	–	Spo.	A
	7:37:06	−0.700	0.515	34°20′20.4″N	132°47′42.0″E	153.42	294.10	23.05	−140.68	66.95	25.81	25.83	25.82	–	Spo.	A
	8:44:57	0.152	−0.102	–	–	343.50	301.57	10.57	41.93	79.43	120.79	120.78	120.79	–	Spo.	A
	18:32:05	−0.050	0.185	–	–	80.46	50.94	0.88	29.52	89.12	43.80	43.84	43.82	–	Spo.	A
	18:48:07	0.155	0.088	–	–	57.20	53.10	3.34	4.10	86.66	33.42	33.41	33.42	33.48	Gem.	A
	18:49:58	0.244	0.001	–	–	45.22	53.34	3.64	−8.13	86.36	35.78	40.00	37.89	37.97	Gem.	A
	19:26:52	0.070	0.180	–	–	67.19	57.97	9.89	9.22	80.12	29.29	29.28	29.29	29.73	Gem.	A
	19:44:20	−2.821	0.043	–	–	224.51	60.02	12.99	164.50	77.01	3.17	3.26	3.22	–	Spo.	A
	19:54:29	−0.148	0.262	–	–	91.93	61.17	14.83	30.76	75.17	38.99	39.01	39.00	–	Spo.	A
	19:54:34	0.113	0.233	–	–	66.00	61.18	14.84	4.82	75.16	21.50	21.50	21.50	22.24	Gem.	A
	20:25:32	0.040	0.262	–	–	70.71	64.54	20.58	6.17	69.42	23.25	23.13	23.19	24.77	Gem.	A
	20:39:34	0.525	0.412	–	–	59.54	66.00	23.23	−6.46	66.77	8.50	8.50	8.50	9.25	Gem.	C
	20:50:46	−0.205	0.240	–	–	109.67	67.13	25.38	42.53	64.63	52.73	52.75	52.74	–	Spo.	A
	20:50:55	−0.114	0.246	–	–	87.37	67.15	25.40	20.22	64.60	38.33	38.33	38.33	42.43	Gem.	A
	21:14:37	0.104	0.247	–	–	66.78	69.48	30.00	−2.71	60.01	20.96	20.97	20.97	24.21	Gem.	A
	21:19:52	−2.452	0.232	–	–	221.27	69.99	31.02	151.28	58.98	4.00	4.01	4.01	–	Spo.	A
	21:36:29	−0.011	0.283	–	–	74.43	71.56	34.29	2.87	55.71	24.55	24.28	24.42	29.56	Gem.	C
	21:41:24	−0.100	0.239	–	–	85.57	72.02	35.27	13.54	54.73	38.10	38.08	38.09	46.65	Gem.	A
	21:44:01	0.163	0.209	–	–	63.03	72.27	35.79	−9.24	54.21	20.67	20.67	20.67	25.48	Gem.	A
	22:00:03	−0.060	0.255	–	–	79.41	73.74	38.99	5.67	51.02	31.00	30.98	30.99	39.87	Gem.	A
	22:08:43	0.030	0.120	–	–	69.14	74.54	40.72	−5.40	49.28	47.67	47.58	47.63	–	Spo.	A
	22:36:32	−0.004	0.218	–	–	73.99	77.04	46.35	−3.06	43.65	30.00	31.06	30.53	44.23	Gem.	B
	22:36:56	0.089	0.144	–	–	64.55	77.08	46.43	−12.53	43.57	32.47	32.43	32.45	47.08	Gem.	A
	22:57:48	−0.019	0.200	–	–	75.72	78.95	50.69	−3.24	39.31	35.79	35.70	35.75	–	Spo.	C
	23:13:09	0.200	0.700	32°41′24.7″N	133°34′44.4″E	68.61	80.34	53.84	−11.73	36.16	8.00	7.99	8.00	13.56	Gem.	B
	23:27:58	0.010	4.190	–	–	73.55	81.70	56.89	−8.15	33.11	2.00	1.59	1.80	3.30	Gem.	C
Dec. 14, 2015	0:11:14	−1.510	0.250	–	–	217.77	85.93	65.87	131.84	24.13	7.12	7.12	7.12	–	Spo.	C
	1:35:01	−0.112	0.515	–	–	78.90	102.14	83.29	−23.24	6.71	15.18	15.15	15.17	–	Spo.	B
	5:55:20	0.650	0.440	–	–	58.46	284.77	42.28	−226.30	47.72	7.37	7.39	7.38	–	Spo.	B
	7:48:47	−0.100	0.380	–	–	80.24	295.73	20.10	−215.48	69.90	21.20	21.24	21.22	–	Spo.	C
	9:42:46	0.290	−0.260	–	–	311.77	309.49	0.45	2.29	89.56	53.79	53.81	53.80	–	Spo.	A
Dec. 15, 2015	0:27:49	0.274	0.329	33°50′53.9″N	133°32′24.0″E	62.58	88.24	70.14	−25.66	19.86	12.81	12.80	12.81	–	Spo.	B
	0:33:26	0.025	0.490	–	–	72.57	88.94	71.31	−16.37	18.69	13.20	13.20	13.20	41.20	Gem.	C
	5:38:45	1.455	0.595	34°13′40.4″N	133°26′16.8″E	54.94	283.62	44.84	−228.68	45.16	4.03	4.03	4.03	–	Spo.	C
	6:20:09	0.003	0.170	33°34′10.2″N	133°29′06.0″E	73.24	287.39	36.52	−214.16	53.48	40.00	38.88	39.44	–	Spo.	C
	6:34:56	0.730	1.010	33°59′33.0″N	133°18′00.0″E	63.54	288.78	33.59	−225.24	56.41	4.40	4.40	4.40	–	Spo.	C
	7:05:55	−0.330	0.400	33°43′08.4″N	134°02′09.6″E	107.54	291.76	27.53	−184.22	62.47	31.06	31.05	31.06	–	Spo.	A
	8:43:54	0.250	0.140	34°26′40.6″N	133°04′58.8″E	57.10	302.38	9.37	−245.28	80.63	20.84	20.86	20.85	–	Spo.	A
	10:57:28	−0.455	0.505	34°02′47.4″N	133°15′21.6″E	113.26	321.67	−11.60	−208.40	101.60	25.76	25.76	25.76	–	Spo.	A
Dec. 16, 2015	0:05:32	0.124	0.080	–	–	58.12	86.16	66.32	−28.05	23.68	39.52	39.50	39.51	–	Spo.	A
	8:20:54	−0.200	0.181	34°01′08.4″N	133°27′25.2″E	130.83	300.14	12.75	−169.31	77.25	77.20	77.18	77.19	–	Spo.	B
	11:07:47	0.346	0.271	–	–	59.52	324.17	−13.38	−264.64	103.38	12.92	12.92	12.92	–	Spo.	B

(*continued on next page*)

Table 1 (*continued*)

Appearance time		Time differences		Appearance location		MT angle	RP direction		Threshold	Meteor entry angle	Horizontal component			Velocity	Distinction	Classified
Date	Time [JST]	t1 [s]	t2 [s]	Latitude	Longitude	Az [°]	RP azimuth [°]	H [°]	Th [°] =< ±25°	Z [°]	VH1 [km/s]	VH2 [km/s]	VH [km/s]	V [km/s]	Gem./Spo.	Class
Dec. 17, 2015	17:53:56	−0.425	0.387	–	–	130.21	47.18	−3.32	83.03	93.32	36.07	36.07	36.07	–	Spo.	C
	1:05:06	−0.115	0.151	–	–	103.16	95.73	79.55	7.43	10.45	78.78	78.74	78.76	–	Spo.	A
	2:27:20	−0.049	0.168	33°57′45.0″N	133°18′18.0″E	81.13	259.00	82.81	−177.88	7.19	49.18	49.11	49.15	–	Spo.	C
	2:46:00	−0.245	0.104	–	–	197.61	264.98	78.95	−67.37	11.05	62.12	62.12	62.12	–	Spo.	B

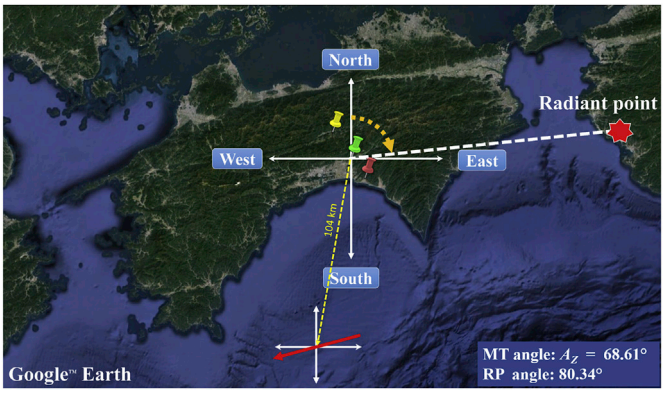

Fig. 7. Relationship between meteor trajectory angle and radiant point angle (At 23:13:09 JST on Dec. 13, 2015).

almost a straight line (*i.e.*, 180°). Accordingly, this meteor was identified as a Geminid. There were several possible explanations for the slight discrepancy between 168.27° and 180°. First, the meteor's trajectory angle may have been changed by the effect of the Earth's gravity. Second, there may have been an error in observation accuracy in the forward scattering meteor radio observation method. Previously, we attempted to perform calibration to increase the accuracy (Noguchi, 2009) and obtained a measurement error of ±10° with strong meteor echo intensity, long duration, and meteor echo elevation angle > 25°. Therefore, the observation results indicated that the meteor trajectory angle and meteor shower radiant point had a discrepancy < 25°. During the observation period of the Geminids 2015, we could not obtain simultaneously observed data for radio and optical observation due to bad weather. We obtained no infrasonic signal during the 2015 Geminids observation.

5. Conclusion

We successfully obtained simultaneously observed meteor echo datasets by multiple-site forward scattering meteor radio observation at three observation sites. The observation systems in these three locations only receive continuous radio waves at the 53.750 MHz frequency emitted from Sabae station, Fukui, Japan. Based on multiple-site radio observations with a 5ch HRO-IF, we calculated the meteor trajectory parameters by time differentiation of each meteor echo detection at the three sites of KUT, Otoyo, and Geisei. Here, we calculated an average velocity of 34 ± 8.86 km/s for the Geminids from 12 selected observation data based on the lowest noise signal classification. This predicted velocity has a close difference with the previously reported average velocity for the Geminids. During the Geminid observation period, clear double velocity peak characteristics were reported. Not many simultaneously observed meteor echo datasets were obtained by multiple sites. Therefore, we will continue observation of many meteor showers. We will attempt multiple-site observation continuously, to determine the characteristics of other meteor showers using the KUT multiple-site radio observation system. Furthermore, we will develop and use the 5ch HRO-IF at other locations. After such trials, we will obtain meteor height data, to consider the appearance height for precise calculation of meteor velocity. There have been many previous comparative studies of radio and optic meteor observations (Edwards et al., 2008; Noguchi, 2009; Rendtel, 2004), and at the time of re-entry of the "Hayabusa" capsule, the artificial meteor event was used as a useful example for infrasound signal calibration (Yamamoto et al., 2011). The infrasound observations are expected to detect total power of meteors in the energy estimation of fireball-class meteors (Edwards et al., 2008). In future studies, we would like to collect meteorites after obtaining various significant meteor parameters by the three observation techniques.

Acknowledgements

The authors are greatly indebted to Kimio Maegawa, Geisei astronomical observatory, Midori-no Tokeidai and anonymous referees for their valuable supports and suggestions.

Appendix A. Supplementary data

Supplementary data to this article can be found online at https://doi.org/10.1016/j.pss.2019.03.004.

References

Arai, N., Iwakuni, M., Watada, S., Imanishi, Y., Murayama, T., Nogami, M., 2011. Atmospheric boundary waves excited by the tsunami generation related to the 2011 great Tohoku-Oki earthquake. Geophys. Res. Lett. 38 (21). https://doi.org/10.1029/2011GL049146.

Blaauw, R.C., Campbell-Brown, M.D., Weryk, R.J., 2011. A meteoroid stream survey using the Canadian Meteor Orbit Radar - III. Mass distribution indices of six major meteor showers. Mon. Not. Roy. Astron. Soc. 414 (4), 3322–3329. https://doi.org/10.1111/j.1365-2966.2011.18633.x.

Brown, P.G., Assink, J.D., Astiz, L., Blaauw, R., Boslough, M.B., Borovička, J., Brachet, N., Brown, D., Campbell-Brown, M., Ceranna, L., Cooke, W., De Groot-Hedlin, C., Drob, D., Edwards, W., Evers, L., Garces, M., Gill, J., Hedlin, M., Kingery, A., Laske, G., Le Pichon, A., Mialle, P., Moser, D., Saffer, A., Silber, E., Smets, P., Spalding, R., Spurny, P., Tagliaferri, E., Uren, D., Weryk, R., Whitaker, R., Krzeminski, Z., 2013. A 500-kiloton airburst over Chelyabinsk and an enhanced hazard from small impactors. Nature 503 (7475), 238–241. https://doi.org/10.1038/nature12741.

Ceplecha, Z., Borovicka, J., Graham, E.W., Revelle, O.D., Hawkes, R.L., Porubcan, V., Simek, M., 1998. Meteor Phenomena and Bodies, pp. 327–471. https://doi.org/10.1023/A:1005069928850.

Christie, D.R., Campus, P., 2009. The IMS infrasound network: design and establishment of infrasound stations. In: Infrasound Monitoring for Atmospheric Studies, pp. 29–75. https://doi.org/10.1007/978-1-4020-9508-5_2.

RMG Editing Committee, 2002. In: Takuji, Nakamura (Ed.), Radio meteor observation guidebook. CQ Publishing Co., Ltd. in Japanese .

Edwards, W.N., Brown, P.G., Weryk, R.J., ReVelle, D.O., 2008. Infrasonic observations of meteoroids: preliminary results from a coordinated optical-radar-infrasound observing campaign. In: Advances in Meteoroid and Meteor Science, pp. 221–229. https://doi.org/10.1007/978-0-387-78419-9_31.

Horiuchi, J., 2005. Basic Development of Interferometer System in Radio Meteor Observation 1. Kochi University of Technology.

Janches, D., Close, S., Hormaechea, J.L., Swarnalingam, N., Murphy, A., O'Connor, D., Vandepeer, B., Fuller, B., Fritts, D., Brunini, C., 2015. The Southern Argentina Agile MEteor Radar Orbital System (SAAMER-OS): an initial sporadic meteoroid orbital survey in the southern sky. Astrophys. J. 809 (1). https://doi.org/10.1088/0004-637X/809/1/36.

Jenniskens, P., 1994. Meteor stream activity. Astron. Astrophys. 287, 990–1013.

Johnson, J.B., 2004. Volcanic eruptions observed with infrasound. Geophys. Res. Lett. 31 (14), L14604. https://doi.org/10.1029/2004GL020020.

Jones, J., Webster, A.R., 1991. Forward-scatter Radiant Mapping (Asteroids, Comets, Meteors).

Jones, J., Webster, A.R., Hocking, W.K., 1998. An improved interferometer design for use with meteor radars. Radio Sci. 33 (1), 55–65. https://doi.org/10.1029/97RS03050.

Jones, J., Brown, P., Ellis, K.J., Webster, A.R., Campbell-Brown, M., Krzemenski, Z., Weryk, R.J., 2005. The Canadian meteor orbit radar: system overview and preliminary results. Planet. Space Sci. 53 (4), 413–421. https://doi.org/10.1016/j.pss.2004.11.002.

Kaschak, G., Donn, W.L., Fehr, U., 1970. Long-range infrasound from rockets. J. Acoust. Soc. Am. 48 (1A), 12–20. https://doi.org/10.1121/1.1912102.

Kero, J., Szasz, C., Nakamura, T., Meisel, D.D., Ueda, M., Fujiwara, Y., Terasawa, T., Nishimura, K., Watanabe, J., 2012. The 2009-2010 MU radar head echo observation programme for sporadic and shower meteors: radiant densities and diurnal rates. Mon. Not. Roy. Astron. Soc. 425 (1), 135–146. https://doi.org/10.1111/j.1365-2966.2012.21407.x.

Le Pichon, A., Ceranna, L., Pilger, C., Mialle, P., Brown, D., Herry, P., Brachet, N., 2013. The 2013 Russian fireball largest ever detected by CTBTO infrasound sensors. Geophys. Res. Lett. 40 (14), 3732–3737. https://doi.org/10.1002/grl.50619.

Lin, T.-L., Langston, C.A., 2007. Infrasound from thunder: a natural seismic source. Geophys. Res. Lett. 34, L14304. https://doi.org/:10.1029/2007GL030404.

Madkour, W., Yamamoto, M.-Y., Kakinami, Y., Mizumoto, S., 2016. A low cost meteor observation system using radio forward scattering and the interferometry technique. Exp. Astron. 41 (1–2), 243–257. https://doi.org/10.1007/s10686-015-9488-4.

Maegawa, K., 1999. HRO: a new forward-scatter observation method using a ham-band beacon. *Wgn.* J. Int. Meteor.Org 27 (1), 64–72.

Mizumoto, S., 2015. Calculation of Meteor Orbit by Multiple-Site Radio Observation and Construction of a Comprehensive Meteor Observation System. Kochi University of Technology.

Noguchi, K., 2009. High-accuracy Direction Findings of Meteors and Developmment of an Automatic Meteor Observation System by 5-channel Radio Interferometer. Kochi University of Technology.

Noguchi, K., Yamamoto, M.-Y., 2008. Development of an automatic echo-counting program for HROFFT spectrograms. In: Advances in Meteoroid and Meteor Science, vol. 102, pp. 323–329. https://doi.org/10.1007/978-0-387-78419-9_46.

Okamoto, G., 2005. Basic Development of Interferometer System in Radio Meteor Observation 2. Kochi Universtiy of Technology.

Rendtel, J., 2004. Almost 50 years of visual Geminid observations. WGN, J. Int. Meteor Org. 32 (2), 57–59.

SonotaCo, 2009. A meteor shower catalog based on video observations in 2007–2008. *WGN*. J. Int. Meteor.Org 37 (2), 55–62.

Stober, G., Schult, C., Baumann, C., Latteck, R., Rapp, M., 2013. The Geminid meteor shower during the ECOMA sounding rocket campaign: specular and head echo radar observations. Ann. Geophys. 31 (3), 473–487. https://doi.org/10.5194/angeo-31-473-2013.

Valsecchi, G.B., Jopek, T.J., Froeschlé, C., 1999. Meteoroid stream identification: a new approach - I. Theory. Mon. Not. Roy. Astron. Soc. 304 (4), 743–750. https://doi.org/10.1046/j.1365-8711.1999.02264.x.

Yamamoto, M.-Y., Ishihara, Y., Hiramatsu, Y., Kitamura, K., Ueda, M., Shiba, Y., Furumoto, M., Fujita, K., 2011. Detection of acoustic/infrasonic/seismic waves generated by hypersonic re-entry of the HAYABUSA capsule and fragmented parts of the spacecraft. Publ. Astron. Soc. Jpn. 63 (5), 971–978. https://doi.org/10.1093/pasj/63.5.971.

Yamasaki, T., 2012. Improvement of the KUT Radio Meteor Observation System and Development of Meteor Trajectory Measurement Method Based on 5-channels Interferometer and Multi-Site Observation. Kochi University of Technology.

PUBLICATION III

***

Batubara, M., and Yamamoto, M.-Y. (2020). *Infrasound Observations of Atmospheric Disturbances Due to a Sequence of Explosive Eruptions at Mt. Shinmoedake in Japan on March 2018*. Journal of MDPI: Remote Sens. 2020, 12(4), 728; https://doi.org/10.3390/rs12040728.

remote sensing

MDPI

Technical Note

Infrasound Observations of Atmospheric Disturbances Due to a Sequence of Explosive Eruptions at Mt. Shinmoedake in Japan on March 2018

Mario Batubara [1,2,*] and Masa-yuki Yamamoto [1]

[1] School of System Engineering, Kochi University of Technology, Kochi 782-8502, Japan; yamamoto.masa-yuki@kochi-tech.ac.jp

[2] Space Science Center, Indonesian National Institute of Aeronautics and Space, Bandung, West Java 40173, Indonesia

* Correspondence: mario.batubara@lapan.go.id or batubaramario@gmail.com

Received: 27 November 2019; Accepted: 18 February 2020; Published: 22 February 2020

Abstract: Thirty infrasound sensors have been operated over Japan since 2015. We developed the irregular array data processing in order to detect and estimate the parameters of the arrival source waves by using infrasound data related to the sequence of the volcanic eruption at Mt. Shinmoedake in March 2018. We found that the apparent velocity at the ground was equal to the acoustic velocity at particular reflection levels. The results were confirmed through a comparison of the findings of the apparent velocity with a wave propagation simulation on the basis of the azimuth, infrasound time arrivals, and the state of the atmospheric background using global atmospheric models. In addition, simple ideas for estimating horizontal wind speeds at certain atmospheric altitudes based on infrasound observation data and their validation and comparison were presented. The calculated upper wind speed and wind observed by radiosonde measurements were found to have a qualitative agreement. Propagation modeling for these events estimated celerities in the propagation direction to the sensors that were consistent with the tropospheric and stratospheric ducting. This study could inspire writers, in particular, and readers, in general, to take advantage of the benefits of infrasound wave remote-sensing for the study of the Earth's atmospheric dynamics.

Keywords: infrasound; propagation speed; infrasound sensor; atmospheric disturbance

1. Introduction

Infrasound is classified as sound waves with frequencies below the 'normal' limit of human hearing and is often cited as the frequency range 0.02–10 Hz [1]. These waves are generated from various human-made and natural sources and can propagate efficiently over regional and global scales of thousands of kilometers, with low intrinsic attenuation [2,3]. For instance, very large sources (e.g., massive volcanic eruptions) can produce inaudible waves dominated by very low frequencies, particularly in the near-infrasonic range of 1–20 Hz [4], and were found to be well-correlated across a local network, suggesting a contribution from point source infrasound [5].

The advantages of infrasound waves have been exploited by researchers studying the characteristics of sound sources across the globe. Since 2015, in a collaboration between national industries and the Earth Space and Exploration System Laboratory (ESESL) of Kochi University of Technology (KUT) in Japan, new instrument designs have been developed to increase land-use efficiency and integrate surface meteorological measurements with seismology components. In addition, the system has been deployed for operation in various locations in Japan, especially in

the Shikoku Island region. Since the observation network was established, our sensors have successfully detected and recorded several natural phenomena that produced infrasound waves (e.g., explosive volcanic eruptions and an intense earthquake that occurred in Japan). Three explosive volcanic eruptions were detected by the sensor, at Mt. Aso in 2016, Mt. Sakurajima in 2017, and Mt. Shinmoedake in 2018.

The majority of high-amplitude volcanic infrasound is attributable to the eruptive acceleration of compressed volatiles from vents [5,6]. Such infrasound may result from either a long period of acceleration of erupted gas from a compact vent or from an impulsive source distributed over a large region. In both cases, it is possible to detect infrasound from the eruption. There have been several previous reports of infrasonic observations likely caused by volcanic eruptions. One of these reports was based on the examination of air pressure data from one station, combined with a verification method implemented at another station (i.e., cross-correlation) [7,8]. Other reports were based on the evaluation of air pressure measurements from small-array sensors at locations close to the mountain cauldron (i.e., <10 km) [4,9–11] and analyses of the International Monitoring System (IMS) infrasound network [12–20] using the progressive multi-channel correlation (PMCC) technique [21,22]. Similar way in Russia [23], Italy [24,25], and Ecuador [10] also detected lower frequency waves associated with volcanic eruptions, in which air pressure disturbances traveled radially and uniformly away from source points. In general, the sensor array system used is relatively close to the observed source point (d $<$ 10km) with a fairly homogeneous distance between sensors (close and equal distances). These investigations found some clear changes in air pressure originating from volcanic eruptions, with amplitudes of >20 Pa. However, the propagation speeds inferred from the infrasonic detection (0.02–0.05 Hz) reported in above previous studies varied considerably, with apparent velocities ranging from ∼338 to ∼420 m/s.

A common objective in infrasound data processing is the estimation of the arrival direction (azimuth) of the incoming signals. Several methods for determining the azimuth of a source have been implemented. Frequency-wavenumber (f-k) analysis in combination with delay and sum beamforming in the time domain of the incoming signals [26], using the PMCC algorithm [21,27], computes time delays and uses the sum of the delays between unique sensor pairs to establish relationships for estimation of the arrival direction of the source for each window of the data. These methods are conducted using regular arrays of closely spaced sensors. Recently, our lab carried out three-dimensional ray-tracing using the vertical of atmospheric profiles, e.g., horizontal wind and temperature, to figure out the sound propagation profiles.

This work primarily focused on the development new methods and their applications by using remote sensing with infrasound waves through the utilization of infrasound data analysis for studying the upper atmosphere. We focused on powerful transient signals that travel through the atmosphere, which provided us with a quantitative basis to estimate infrasound specifications through a Radar Beam Swinging method implementation into our infrasound data processing. Here, we present our findings on far field infrasound returns from Mnt. Shinmoedake in Japan (31.9098°N, 130.8863°E), which was observed during sequences of explosive activity in March 2018. These explosions have estimated results in a strong explosive range. The identified source was then used to estimate the horizontal atmospheric wind velocity at certain altitude from recorded signal properties. Depending on the background atmospheric condition at low-mid altitude, the arrival signals are observed during sequence of explosive volcanic activities. It was also found that the comparison of the atmospheric wind speed between the infrasound observation and the radiosonde observation are relatively in good agreement. It was also found that the comparison of the atmospheric wind speed between the infrasound observation and the radiosonde observation are relatively in good agreement. Additionally, the implementation of the Radar Beam Swinging into our infrasound sensor array system gives a possible way to detect the source waves for further atmospheric wind estimation, even though it still meets several limitation during the processing. However, our results suggest the utilities of infrasound techniques could be used for atmospheric study.

This manuscript is structured as follows. An overview of the infrasound network used in this study is described in Section 2. Section 3 provides a description of the instrument specifications, which is followed by a description of the data set in Section 4. The selection of the data is described in Section 5. Details of the evaluation tools used in the methodology are given in Section 6. The results and discussion focus on the potential use of the infrasound network for geophysical variability analyses of our findings regarding atmospheric disturbances.

2. Infrasound Station Sites

The first operation of an infrasound sensor in Kuroshio city in Kochi prefecture occurred in 2016, following careful evaluation of the individual sensor performance. Currently, a total of 30 infrasound sensors are distributed uniformly over the Japanese islands and are in continuous operation. Providing an information about natural disaster such especially as earthquake and tsunami over the Shikoku region, the network likewise uses two different types compact sensors to ensure the detection of infrasound waves generated by both natural and man-made activities. The Japanese infrasound station network is shown in Figure 1, with their geographic coordinates listed in Table S1 in the supporting information. The network is denser on Shikoku Island, where it is used for the detection of natural disasters, such as tsunamis and volcanic eruptions.

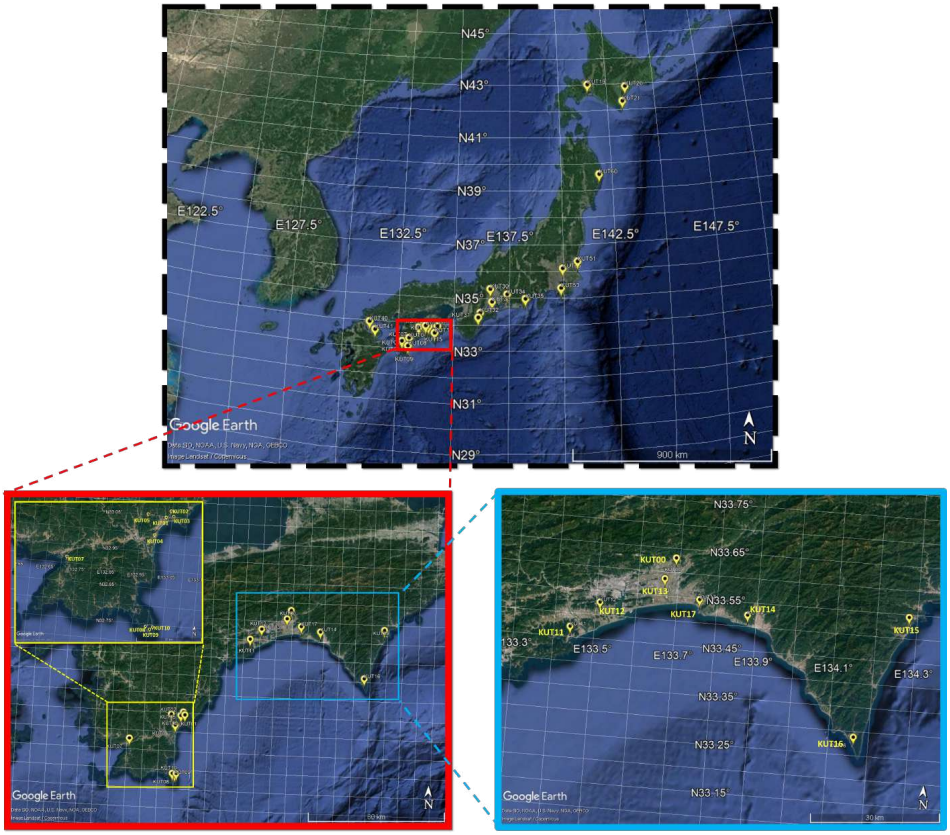

Figure 1. The locations of infrasound sensors (type: ADXII-INF01) in Japan. (**top**) Distribution of sensor location over Japan; (**bottom**) infrasound sensor location over Shikoku island, Japan.

3. Overall Description of the Instrument

Since 2005, KUT has collaborated with several local institutions in an initiative to build an infrasound sensor that is integrated with several micro-electro-mechanic system (MEMS) sensors to measure 3-axis acceleration in seismic waves, atmospheric temperature, atmospheric pressure, and the level of audible noise. The sensor system is also equipped with a signal processing unit for continuous real-time processing and network-connecting ports for data acquisition [28].

A full description of the specifications of the infrasound instrument is given in Table S2 in the supporting information and can be found in the company's website [29]. The infrasound system, consisting of four types of high sensitivity sensors with additional of a dynamic data logger and a high speed digitizer, which is able to monitor the ambient condition of the environment (e.g., ground acceleration, local temperature, audible noise level, atmospheric pressure, and sound pressure level) and is therefore flexible to control through the internet connection. In 2016, we announced a total of five infrasound sensors were installed as a model area, and in 2017 we expanded the network to a total of 15 locations along the coastal area in Kochi Prefecture, and built a network to detect the arrival of tsunami-induced infrasound from the land surface.

At almost all stations, the four parameters are continuously digitized at 4 Hz by each individual sensor. The instrument was specially designed to be windproof and easy to install.

The sensor can be used to monitor infrasound sources from geophysical activities, such as volcanic eruptions, snow slides, landslides, thunderstorms, and tornadoes, as well as human-made activity (e.g., explosions, spaceship re-entry, etc.).

4. Overall Description of the Infrasound Data Set

The collection of observational data from our infrasound sensor network can be monitored through the KISONS-Kochi University of Technology Infrasound Observation Data Network System [30]. This data set includes the 3-D acceleration of earthquakes (Gal), audible sound (dB), atmospheric pressure (kPa), infrasound pressure (mPa), and sensor temperature (°C). They are provided for each time period of data needed by the user in the form of a comma separated value (CSV) file format, with file naming formats, such as SS_Y1Y1Y1Y1M1M1D1D1h1h1m1m1s1s1_Y2Y2Y2Y2M2M2D2D2h2 h2m2 m2s2 s2s2.csv, and the information in Table 1:

Table 1. List of information on filename code.

Filename Code	Information
SS	Station code
$Y_nY_nY_nY_n$	Year
M_nM_n	Month
D_nD_n	Day
h_nh_n	Hour
m_nm_n	Minnute
s_ns_n	Second

Index "n" describes the beginning (numbered 1) and end (numbered 2) of the time period over which data were selected. For the purposes of infrasound analysis, we recommend using the infrasound AC signal parameter (column 10 in the CSV file). It should be noted that the data displayed on the web page could change at any time due to maintenance and internal investigations of the system. Therefore, the availability and demand for data can vary and should be determined before use of the system. The observation data set used in this study can also be accessed in repository stores, such as Figshare [31].

5. Activity at Mt. Shinmoedake in March, 2018

Mount Shinmoedake (elevation ∼1421 m), is a stratovolcano located in southwest Kyushu Island (31°34′46.33″N, 130°39′29.67″E) and is part of a cluster of volcanoes around Mt. Kirishima (red triangle in Figure 2).

Figure 2. Topographic map of Mt. Shinmoedake and the Mt. Kirishima volcano cluster. Image is taken from Japan Meteorological Agency (JMA) website.

Mount Shinmoedake is one of the currently active volcanoes in Japan. According to a report from the Japan Meteorological Agency (JMA), [32], volcanic activity suddenly recommenced at the beginning of March 2018, and persisted through to April 2018. Violent eruptions ejected ballistic projectiles and the resulting ash plume was blown away from the crater. Figure 3 shows an automated analysis of Moderate Resolution Imaging Spectroradiometer (MODIS) data distributed by the LANCE-MODIS data system and published on the Middle InfraRed Observation of Volcanic Activity (MIROVA) website [33]. The figure showing the thermal anomalies as the volcanic radiative power (VRP) in logarithmic scale, recorded at Mt. Shinmoedake volcano in 2018, clearly shows the sudden intense activity from early March to early April with the category of power intensity in range between moderate and very high, followed by isolated events in May and June 2018. The highest peak appeared and occurred on the 9th and 10th, where the eruption particularly produced the most significant air vibration. We also evaluated infrasound data recorded by the JMA during the major eruptions of the volcano at the start time shown in Table 2.

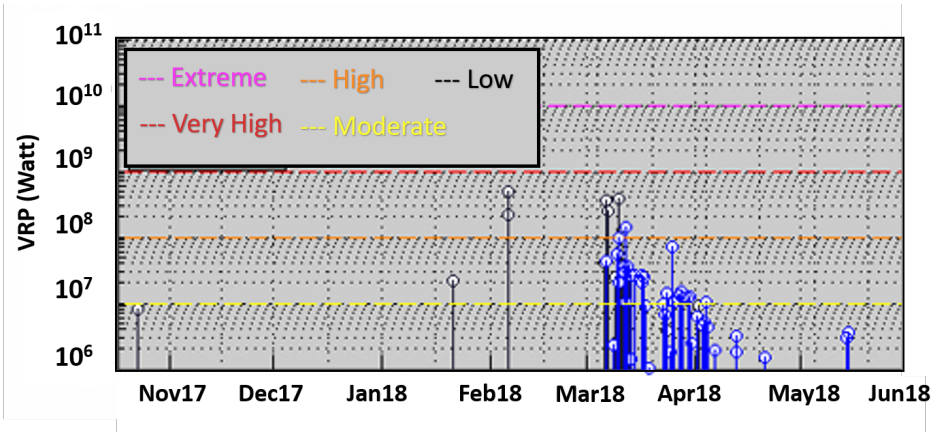

Figure 3. Log of the radiative power of Mt. Shinmoedake, Japan, during 2018 (table is taken from the Middle InfraRed Observation of Volcanic Activity (MIROVA) website, [33]. The color lines, respectively, describe for extreme level (pink); very high level (red); high level (orange); moderate level (yellow); and low level (black).

Table 2. Recorded major eruptions of Mt. Shinmoedake in the period 10–25 March 2018. JST = Japan standard time.

Date of Eruption	Time (JST = UTC + 9)	Date of Eruption	Time (JST = UTC + 9)
9 March 2018	15:58	11 March 2018	04:05
10 March 2018	01:54		07:46
	04:27	12 March 2018	12:45
	10:15	15 March 2018	14:13
	13:32	25 March 2018	07:35
	18:11		

Original infrasound data on 10 March 2018, at 01:54, 04:27, 10:15, and 18:11 Japan standard time [JST]), are shown in Figure 4. Strong signals and dense vibrations from the individual eruptions were recorded at stations KUT07, KUT08, KUT09, and KUT10. At the closest station to the crater (distance = 204.29 km), KUT07, a pressure change was first observed about 625 s after the eruption, with delays of another few seconds at other stations. Signals at the farthest station, KUT16 (342.90 km), showed relatively long arrival times (∼18 min) and similarly dense vibrations to those at stations KUT07, KUT08, KUT09, and KUT10. We also observed other signatures at stations KUT01-KUT05, with small volumes/amplitudes. Figures S1–S6 in the supporting information shows similar profiles for other time periods than those in Table 2. We found that twelve stations with different locations had their own signatures that were likely to have originated from several sources, such as waves from the seashore, referred to as microbaroms [34] and mountain-associated waves [35]. In this study, an attempt was made to minimize these to obtain infrasound data sourced from volcanic eruptions.

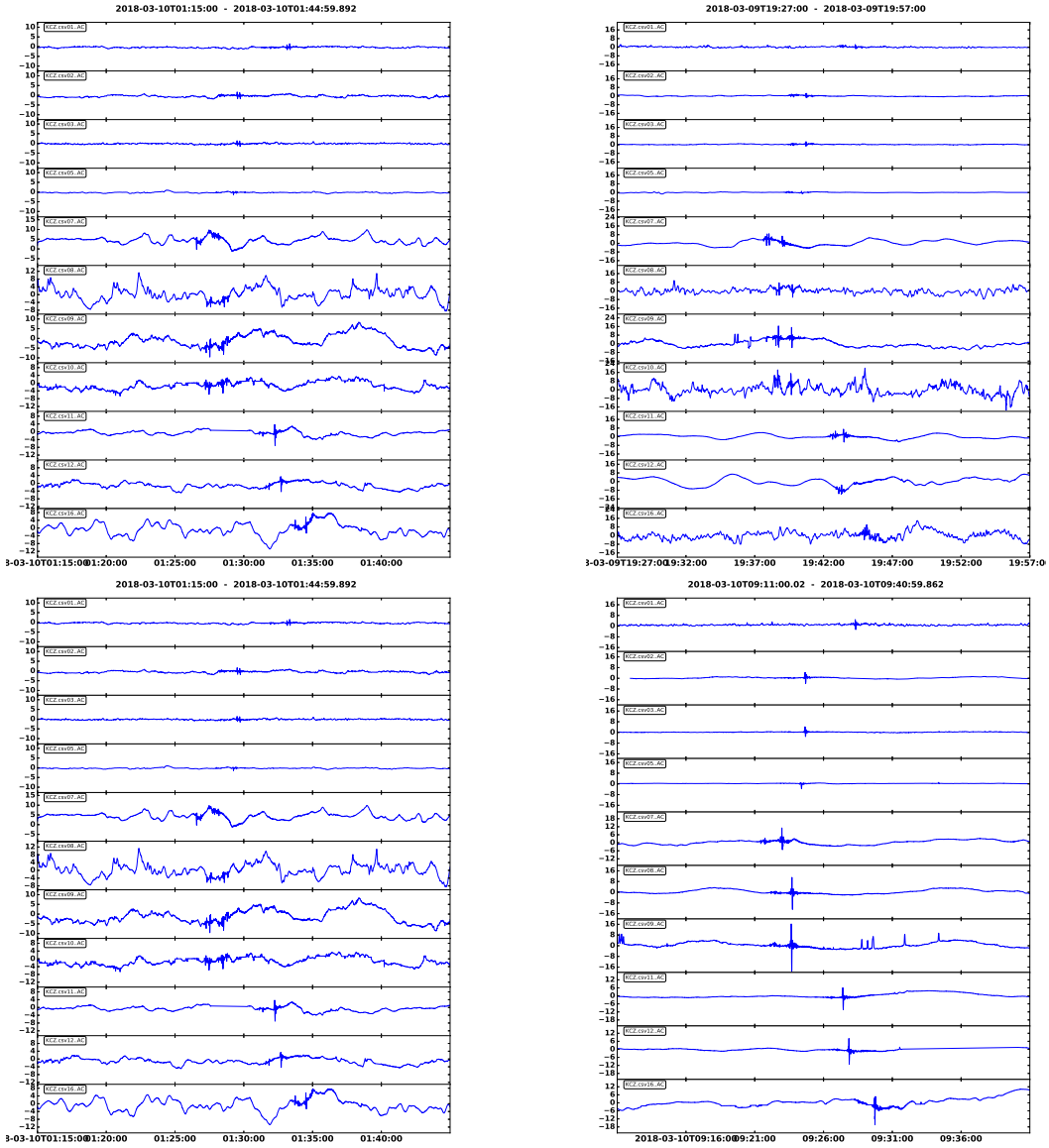

Figure 4. Records of infrasonic pressure data for 10 March 2018, at 01:54 Japan standard time (JST) (top-left), 04:27 JST (top-right), 10:15 JST (bottom-left), and 18:11 JST (bottom-right), showing the arrival times of air pressure disturbances for stations on Shikoku Island following the Mt. Shinmoedake eruption on 10 March 2018. The *x*-axis is the observation time in UTC, and the *y*-axis is the infrasonic pressure in Pa.

6. Basic Methodology

The basic idea of our approach was to use the set of delays between signals to detect the suspected source waves by steering the array beam to different directions or points in a horizontal scanning region (see Figure 5a).

For our analysis, there were two main data processing steps. Firstly, we evaluated the ambient noise at each individual station to estimate the occurrence probability for each frequency bin of the recorded signals. In this step, we parsed the continuous time series for each station into segments (1-h time series) that overlapped by 50% and distributed them continuously throughout the day. This overlapping reduced the variance in power spectral density (PSD) estimates. The PSD processing computed repeating fast-Fourier transforms (FFT) for each of the separate overlapping time bins of the 1-h time series. The final PSD estimates for the 1-h data were then calculated as the 5th and 95th

percentiles of the distribution of individual PSD curves. Plots of the PSDs for our entire period of interest were generated from all individual stations and used for analysis and data quality control.

Secondly, we determined output parameters from irregular array signal processing, such as angle of arrival (azimuth), signal power, the apparent speed, and correlation index. Figure 5b shows schematics that illustrate the processes undertaken in this step. In more detail, at the beginning, several constants and parameters are initialized beside the recorded files. Then, it comes into the main process that split in three sub-processes as follows: (1) The 1st sub-process is called "xyzgeomWINs", where four actions are executed firstly; (2) the process moves to the 2nd part, named "xyzSTEERs", which generates a steering array based on the delays between observed signals; and (3) the level of signal coherency between sensors was evaluated for all windowed data at every time shift increment. During this process, rotation scanning to a specific point, based on the calculated time lag between the multiple sensors and a cosine-tapered window function of a certain period length, with the time overlap as a data discontinuity reducer, was applied in the source detection scheme. The window length was chosen to be proportional to the envelope width of the recorded signals. This process continued until the end of the observation data time was reached, and parameters, such as the azimuth angle, signal strength, apparent velocity, and correlation index, were obtained.

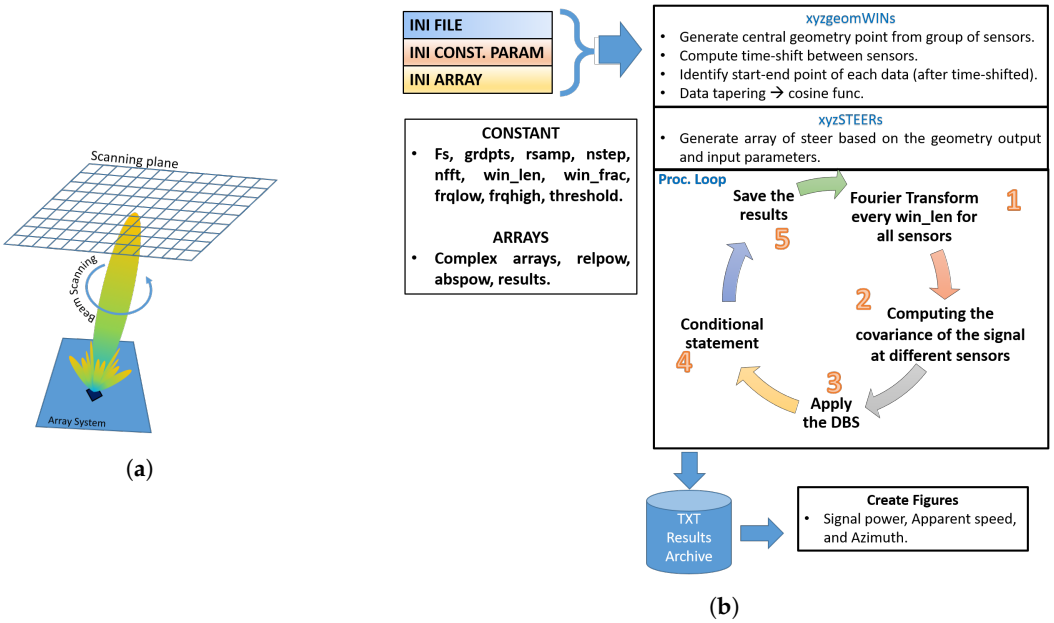

Figure 5. The illustration of the approach used in this study. (**a**) The idea behind Radar Beam Swinging in steering the beam of the array on a scanning plane to detect a suspected source waves. (**b**) Schematic illustrating the steps in our approach to determine the arrival direction and propagation speed of the incoming signal's source.

To estimate the atmospheric layer where the signal was deflected or refracted down toward the sensor on the Earth, infrasound wave propagation modeling was applied. The propagation modeling used in this study was an approximation of the planar parabolic equation (PE) method [36], with a nonlinear ray tracing model as an addition of the method to draw propagation paths and estimate the arrival time in a three-dimensional inhomogeneous moving medium and the atmospheric background [37]. This method is used to estimate the power loss of a wave transmission as a function of range and altitude. The simulation was run to examine a frequency of 1.25 Hz out to 500 km for the sequence of eruptions listed in Table 2. The frequency range is chosen in order to eliminate the frequency of the interference signals, such as microbarom signals, at around 0.2 Hz and the other mountain wave signals at around 0.7 Hz. The frequency of 1.25 Hz is the center of our band pass filter (1.0–1.5 Hz). This 1.25 Hz frequency is chosen to avoid the remaining harmonic of those interference signals. For the atmospheric absorption of sound, the method used the parameters from Reference [38],

which works well even in the upper atmosphere up to 160 km. The simulation also assumed a ground boundary condition as a perfect reflector (rigid plane and no topography).

For a typical source, as listed in Table 2, the sound level at the receiver position depends on the ground conditions, barriers, and meteorological conditions between the source and receiver. In this study, we concentrated on wind effects for sound propagation and ray tracing simulations, assuming the ground surface is perfect reflector without any topography. Therefore, the deviations between the different calculations were caused by parameter variations in the atmospheric profiles. The most important atmospheric effect considered in the study was the refraction caused by wind and vertical atmospheric parameters obtained by the Modern-Era Retrospective analysis for Research and Applications, Version 2 (MERRA-2) and Naval Research Laboratory Mass Spectrometer and Incoherent Scatter Radar, Exosphere (NRLMSISE-00) global atmospheric models. For this study, the 3-h time-averaged horizontal wind, pressure, and temperature fields were accessed via the GMAO web service (Goddard Earth Sciences Data and Information Services Center) [39]. The neutral atmospheric density is retrieved from the model provided by the Community Coordinated Modeling Center [40] in order to complement the atmospheric background conditions in the simulation.

As illustrated in Figure 6, assuming a planar of m-th sensors at locations $\vec{x}_m$ in the xy-plane of our coordinates. The idea of our beam-scanning calculations is quite simple: if a propagating signal is present in an array's aperture, the sensor outputs are individually weighted and delayed, and then all signals are added together, reinforcing the signal with respect to noise or waves propagating in different directions. The delays that reinforce the signal are directly related to the length of time it takes for the signal to propagate between sensors. In Figure 6, the signal denoted by s(t), traveling from the source at the point $\vec{x}_0$ and an array of all m-th sensors located at $\{\vec{x}_m, m = 0, \cdots, M-1\}$. The array's phase center can be defined as the vector quantity $\sum \vec{x}_m$. For simplicity, we choose the origin of our coordinate system to coincide with the phase center, $\sum_{m=0}^{M-1} \vec{x}_m = 0$. The possible absence of a sensor at the array's phase center does not preclude using it as the origin and defining all the sensor positions relative to it. The waveform measured by the m-th sensor is $y_m(t) = f(\vec{x}_m, t)$. The output of our beam-scanning is $z(t) \equiv \sum_{m=0}^{M-1} w_m y_m(t - \Delta_m)$, where w_m and Δ_m are the amplitude weight and the sensor delay, applying to the output of each sensor. We use the cosine taper function as the amplitude weight to reduce discontinuity between signals. The delays are adjusted to focus the array's beam on signals propagating in a particular direction $\vec{\xi}_0 = -\vec{x}_0/|\vec{x}_0|$. Similarly, at the m-th sensor, the direction of propagation vector $\vec{\xi}_0$ equals $\vec{\xi}_{0,m} = (\vec{x}_m - \vec{x}_0)/r_{0,m}$, where $r_{0,m}$ is the distance between m-th sensor location and $\vec{x}_0$. In the applications, the origin of the source is undetermined whether the source is located in the near or far field. Thus, for far-field (plane wave) propagation, the vector $\vec{\xi}_0$ does not vary with sensor location, however, for near-field sources, the apparent direction of propagation varies across the array and is thus defined relative to the m-th sensor, $\vec{\xi}_{0,m}$ (see Figure 6). Our case assumes that a far-field source radiates a plane wave having signal s(t) propagates across our array of all m-th sensors in the direction $\vec{\xi}_0$. The waveform within the array's aperture is given by $f(\vec{x}, t) = s(t - \vec{\alpha}_0 \cdot \vec{x})$, where $\vec{\alpha}_0 = \vec{\xi}_0/c$ is the slowness vector. At a particular sensor, the waveform is expressed by $y_m(t) = s(t - \vec{\alpha}_0 \cdot \vec{x}_m)$; the signal output of our beam-scanning becomes $z(t) = \sum_{m=0}^{M-1} w_m s(t - \Delta_m - \vec{\alpha}_0 \cdot \vec{x}_m)$. The set of sensor delay is given by $\Delta_m = -\vec{\alpha} \cdot \vec{x}_m = \frac{-\vec{\xi} \cdot \vec{x}_m}{c}$, thus the output of beam-scanning signal z(t) becomes $z(t) = \sum_{m=0}^{M-1} w_m s(t + (\vec{\alpha} - \vec{\alpha}_0) \cdot \vec{x}_m)$. The output of the velocity vector can be used to calculate the arrival angle of the target, defined by $tan^{-1}\left(\frac{\alpha_{0,Y}}{\alpha_{0,X}}\right)$, as well as the apparent speed proportional to $\frac{1}{\vec{\alpha}_0}$, where $\alpha_{0,X}$ and $\alpha_{0,Y}$ are the slowness in the x and y axes, respectively.

For the purposes of computation, we first consider the input to a single sensor at the location $\vec{x}_m$ in terms of a phase shift rather than time delay as $y_m(t - \Delta_m) = y_m(t) \cdot e^{-i\omega\Delta_m}$, where $y_m(t) = e^{-i(\omega t - \vec{k} \cdot \vec{x}_m)}$ and the term of $e^{-i\omega\Delta_m}$ represents the phase delay associated with the signal at the m-th sensor, called steering vector $\boldsymbol{e}$. The beam-scanning output may again be expressed as $z(t) = \sum_{m=0}^{M-1} w_m \cdot y_m(t) \cdot e^{-i\omega\Delta_m}$. Then, if the phase delay is included in the received signal

vector $\vec{Y} = y_m(t) \cdot e^{-i\omega\Delta_m}$, the term $z(t)$ in vector notation becomes $\vec{z} = \vec{w}^H\vec{Y}$, where $\vec{w}^H$ is the weighting vector, and H denotes the complex conjugate transpose. Assuming that the array has already steered to a particular direction, the power of the output signal could be estimated by $P(\vec{z}) = \sigma^2 = \mathbb{E}\left\{|\vec{z}|^2\right\} = \vec{w}^H\mathbb{R}\vec{w}$, where $\mathbb{R} = \mathbb{E}\left\{\vec{Y}\vec{Y}^H\right\}$ is the correlation matrix of the incoming signal. Using the term of steering vector $\boldsymbol{e}$, the power spectral density of the array output may then be given by using the correlation matrix $\mathbb{R}$ and the steering vector $\vec{e}$ as $P(\vec{e}) = \vec{e}^H\mathbb{R}\vec{e}$. In order to have the beam of our array been unity gain in the output, the power of variance $P(z)$ of the output signal $z(t)$ should be minimized. The solution for optimum weight with respect to this can be given by $\vec{w} = \dfrac{\mathbb{R}^{-1}\vec{e}}{\vec{e}\mathbb{R}^{-1}\vec{e}}$, and the power becomes $\dfrac{1}{\vec{e}^H\mathbb{R}^{-1}\vec{e}}$.

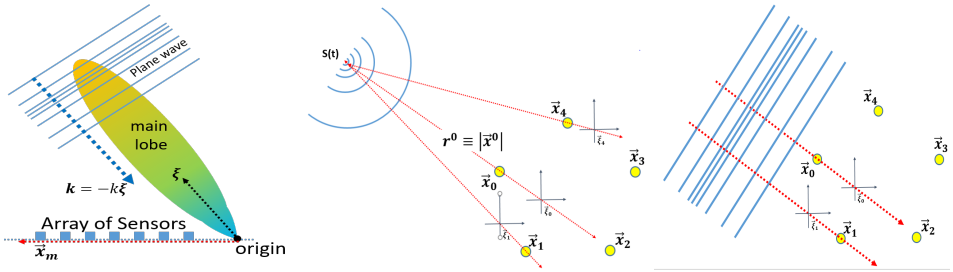

Figure 6. The phase center of the array is the origin of a coordinate system. $\vec{x}^0$ denote as a source location emits a signal s(t) that propagates to the array in a particular direction $\vec{\xi}^0$. The distance between the origin and the source is $\mathbf{r} \equiv |\vec{x}^0|$. (**Left**) Illustration of sensor array, the direction represented by a main lobe and a plane wave incident from direction of the main lobe. (**Right**) The illustration for far-field propagation, the apparent direction of propagation does not vary with sensor location.

Finally, we determined the upper wind speed, and then, the direction of the properties of the signal can be recorded. We consider the sound velocity and wind velocity are the function of z and the heterogeneous of the multi-layered Earth's atmosphere, where each sound ray segment undergoes refraction in such an altitude, which makes the ray becomes more curved and horizontal at its ape; therefore, the trace velocity on the surface is approximately equal to the effective sound speed along its propagating path at the altitude there. This relation may then given by by $c'_{tr} = \nu c_{tr}$, where c'_{tr}, c_{tr}, and ν are referred to as the effective sound speed at an altitude of the reflection, the trace velocity, and the constant factor, i.e., the initial launch angle and atmospheric properties. Trace velocity is constant, along with the ray path, as long as range-independent. In the case of wind case, the trace velocity, using the dispersion relation $\omega = ck$, is given by

$$c_{tr} = \frac{c(z)}{sin\theta} + w(z),$$

where $w(z)$ is the wind velocity at the altitude of z, and θ is the zenith angle. At the turning z_{tr}, the zenith angle is $\theta = \pi/2$; hence, we obtain

$$c'_{tr} = c(z_{tr}) + w(z_{tr}).$$

7. Results and Discussion

7.1. Coherent Ambient Infrasonic Noise across Stations on Shikoku Island, Japan

Before proceeding to the next analysis steps, which involved filtering signals to reduce noise and the contributions from signals originating from sources that were not of interest, we first applied our method to evaluate the amount of coherent ambient noise for an infrasonic source, using 6–12 h of data at the same times as the eruption events described in Section 5.

It should be noted that all installed sensors are surrounded by mountainous areas, and some of them are close to the ocean. Previous studies investigated mountain-associated infrasound waves by using small arrays of infrasound sensors [41,42]. It was found that the orographically generated infrasonic waves were continuous, with frequencies in the range 0.007–0.1 Hz, and their amplitudes were usually fairly small but occasionally exceeded 1 Pa. The airflow over mountain ranges can generate low-frequency infrasonic waves that can propagate over distances of up to 10–20 km. There is strong evidence that a significant proportion of the events observed in this study were related to wave oscillations at the surface of the ocean (e.g., microbaroms and surf). These ubiquitous waves have frequencies in the range 0.12–0.35 Hz for microbarom sources [34], and 1–20 Hz for sea surf [9]. The microbaroms are also usually characterized by an energy peak between 0.2 and 0.3 Hz in the background infrasound noise and are known to interfere with the detection of explosive events [13] and long-range volcanic eruption signals [43]. As shown in Figure 7, as well as Figures S7–S9 in the supplementary file, the observations at all locations were dominated by these typical airflow signals. More comprehensively, Figure 7 shows an example set of PSD-noise plots for 12 stations on Shikoku Island during a one-day period on 10 March 2018, from consecutive 3-min data segments. PSD for selected stations draw in blue, the 5th and 95th percentiles are plotted in red and black, and the median is in white. Three-min windows and cosine-tapper are used to minimize smoothing of the amplitude distribution in the outer of each data window. All plots of PSD were generated for all stations and used for data quality control and interpretation. Figures S10–S12 in the supplementary file show a set of PSD plots for stations on Shikoku Island for three time periods (e.g., September, November, and December) when the volcano was not in the active phase. Based on all PSDs, the interpretations were as follows. (1) A bit slope spectrum appeared in the data during the time period of the volcanic eruption. These patterns are thought due to the existence of time gaps in the data (Figure 7b,c,e,g,i–k). (2) At stations located on the mountain slope, such as stations KUT05 (Figure 7d), KUT 01 (Figure 7a), and KUT02 (Figure 7b), mountain winds mostly affected the characteristics of the recorded data as infrasonic pressure anomalies. This resulted in the spectral distribution, in the frequency range between 0.01 and 0.1 Hz, undergoing a wide expansion, which depressed the microbarom signals. We noted that the mountain-associated waves were predominantly recorded at the stations in mountainous regions. (3) Signals with a high intensity in the frequency of about 0.2 Hz, commonly called microbaroms, appeared to dominate the recorded data from the stations located close to the ocean (e.g., KUT07 (Figure 7e), KUT08 (Figure 7f), KUT09 (Figure 7g), KUT10 (Figure 7h), KUT14 (Figure 7k), and KUT16 (Figure 7l)). (4) There were monthly seasonal changes in the cumulative signals recorded by each sensor. The total signal recorded during the winter period was more intense than in the opposite season [44,45]. Through global atmosphere circulation, especially in the mid-latitude region, jet stream flows stronger during winter period than the opposite one. (5) Finally, as an addition to the PSD results described above, a comparison was made of the daily background noise among all individual stations. Their variations at infrasound stations were highly variable by season, time of day, and station. Station KUT07 was selected as a sample for the examination of daily PSD variations because it was more responsive to the changes in spectral variations of the received signals. As a result, similar to Bowman's study, our findings found no significant peak anomalies in the infrasonic noise spectra during noontime (Figure 8). Other similar profiles for other stations during the same time period are shown in Figures S13–S14 in the supplementary file. The dominant frequency found in the PSD profile was then used as the basis for selecting filtered frequencies in our array processing scheme, described in Section 6.

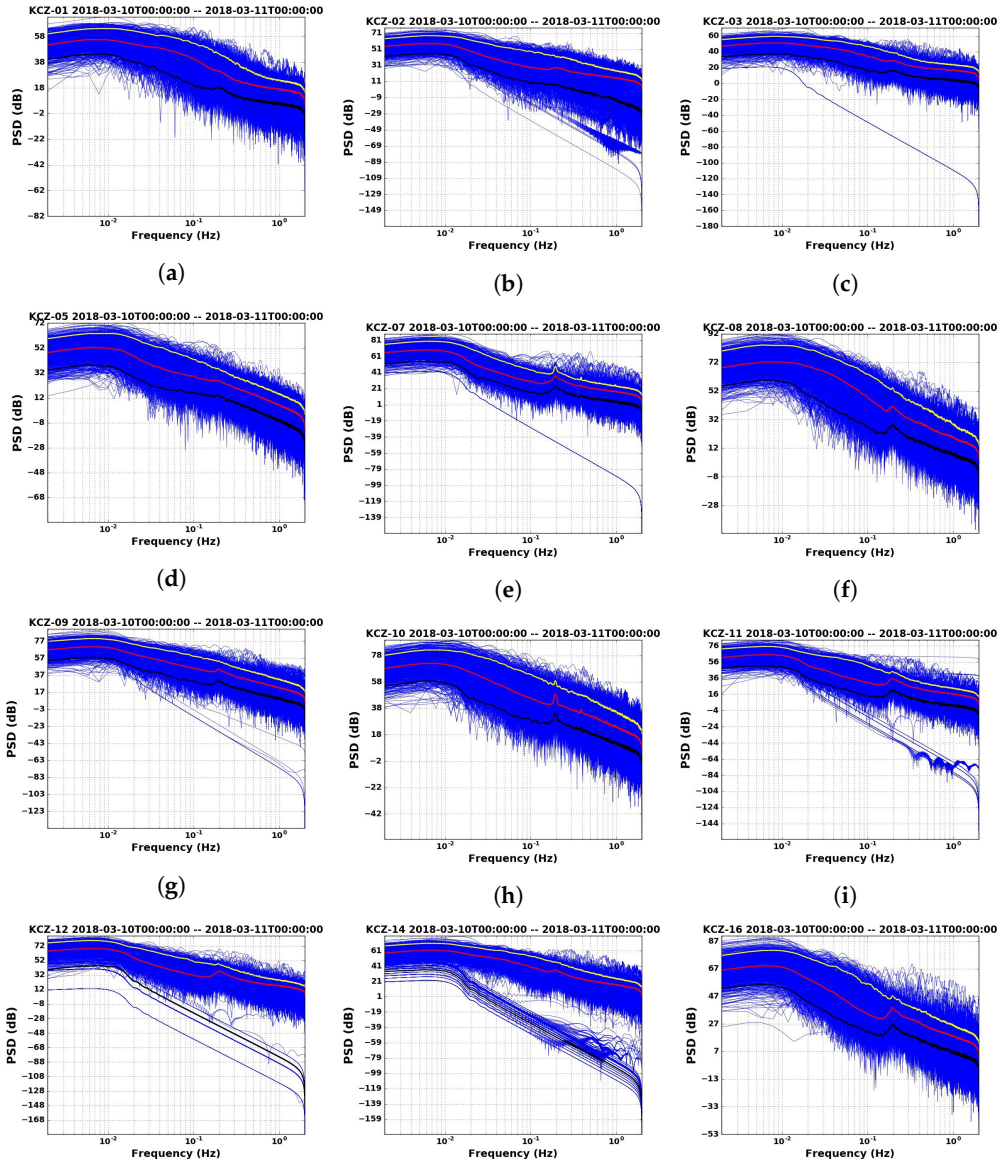

Figure 7. A set of power spectral density (PSD) plots for stationson Shikoku Island during a one-day period on 10 March 2018 (blue). The 5th and 95th percentiles (black and red) and the median (white) for each plot. Figure (**a**–**l**) show the PSD results of the one-day signals recorded by sensor KUT01, KUT02, KUT03, KUT05, KUT07, KUT08, KUT09, KUT10, KUT11, KUT12, KUT14, and KUT16, respectively.

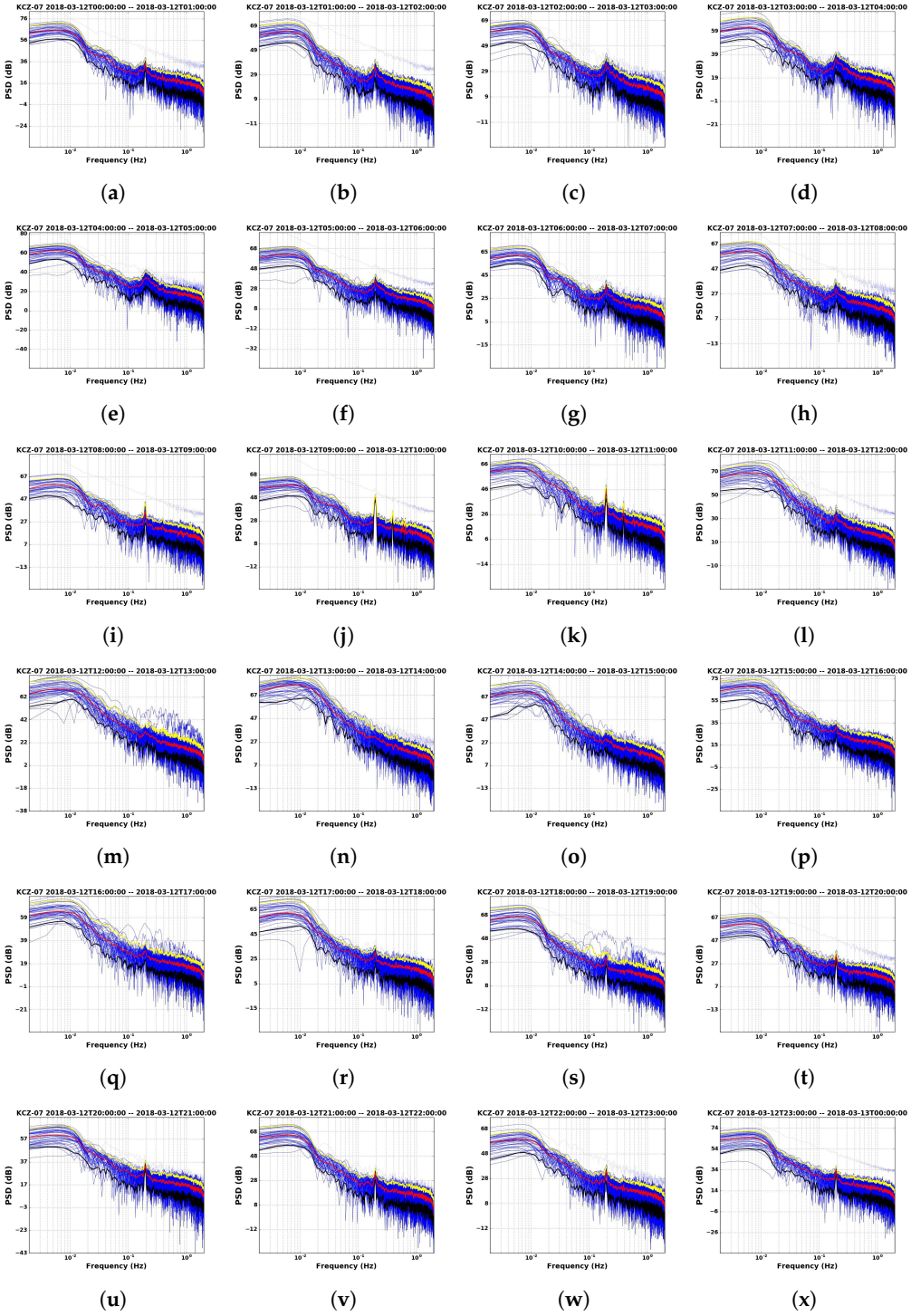

Figure 8. Power spectral density (PSD) for station KUT07 on 12 March 2018 for all time intervals (blue), the 5th and 95th percentiles (yellow and black), and the median (white) value for each time interval. The rows group plots by 1-h time intervals for 4 h. Figure (**a**–**x**) respectively show the PSD results of the one-hour signals recorded by sensor KUT07.

7.2. Infrasound Propagation During the March 2018 Eruptions at Mt. Shinmoedake in Japan

Infrasound generated by explosive eruptions of the volcano was recorded by typical microphones at various distances from the crater. In general, the observed signals traveled across the infrasound stations at near-acoustic wave speeds, indicating that the infrasonic wave fronts propagated a great distance across the Earth's surface.

In combination with automated processing, the infrasound data provides a basis for more detailed propagation studies assessing wave characteristics. When the location of the source can be associated with a known infrasound source, confidence in estimations of the source localization and propagation speed from the events is high. To illustrate these properties, we focused on data from events described in Section 5, where the origin time determined for each event is shown in Table 2. Each event generates multiple arrival times at different stations, where the times increase as a function of propagation distance (Figure 9). These figures show typical records for the Mt. Shinmoedake eruptions during March, 2018, from stations across Shikoku Island, after bandpass filtering between 1.0 and 1.5 Hz, avoiding the interference signals from the sources described in Section 7.1 (based on Figure 4). Similar plots for the events on 11 and 12 March 2018, are shown in Figures S15 and S16 in the supplementary file. Each figure clearly shows the propagation of the disturbance signature at ∼625 s after the explosion. To estimate the propagation speed of the incoming waves, an envelope of source waves was calculated based on the absolute amplitude of the infrasonic waves recorded at the infrasound stations. In general, four terms could be used to characterize such signals: the beginning, transition, middle, and end periods of the sound wave. To estimate the starting point of each suspected detection, the gradient of the slope at the beginning of the wave envelope was calculated by the elevation angle larger than 45°. Each estimated point corresponds to the position and time of a suspected detection. The gradient of the data for six samples, obtained using numerical linear regression, was used to estimate the propagation speed (see Table 3). The propagation speed of the detected signals from the sequence explosive eruption of Mt. Shinmoedake on March 2018 was estimated to be 336.6 ± 6.3 m/s.

Notably, this propagation speed (∼336 m/s) is the speed that the wave travel on the surface from the closest station, sensor number KUT07 to the farthest one, sensor number KUT16. In this case, the sound velocity is about 333 m/s. In a report of Campus in 2006, they estimated a similarly low propagation speed (∼324 m/s) for the 2005 eruption of Lascar volcano in northern Chile, which was recorded by an IMS station about 800 km from the crater [18]. For another event, the 2002 eruption of the Hekla Volcano in the Iceland, Liszka and Garces, in 2002 [14] found that the infrasound propagation speed varied between 315 and 324 m/s. Meanwhile, a higher speed was also detected by an IMS station. The 2005 eruption of Mt. St. Helens generated low-frequency waves traveling at about 352 m/s [18]. The discrepancy between the two eruptions is understandable since the two types of disturbance occurred at different locations.

However, in general, infrasound in the atmosphere propagates at the sound speed of around 340 m/s near the surface/or ground. It is also generally accepted that infrasound propagates at a velocity that typically varies with temperature and the fundamental properties of the propagation medium, as well as the wind velocity [46]. From the above, the speed inferred from our analysis (∼336 m/s) is in the range of typical propagation speeds of infrasonic pressure disturbances from both natural and artificial explosion sources (e.g., chemical and nuclear explosions) [47,48].

Table 3. Overall summary of the calculated propagation speeds of the detected signals.

No.	Event Time (JST)	$t_{detection}$ (after Event Time, s)	Δt (s)	Estimated Speed (m/s)
1	0154 on 10 March 2018	657	413	334.18
2	0427 on 10 March 2018	637	398	346.78
3	1015 on 10 March 2018	683	419	329.40
4	1118 on 10 March 2018	625	409	337.45
5	0405 on 11 March 2018	659	406	339.95
6	1245 on 10 March 2018	652	416	331.77

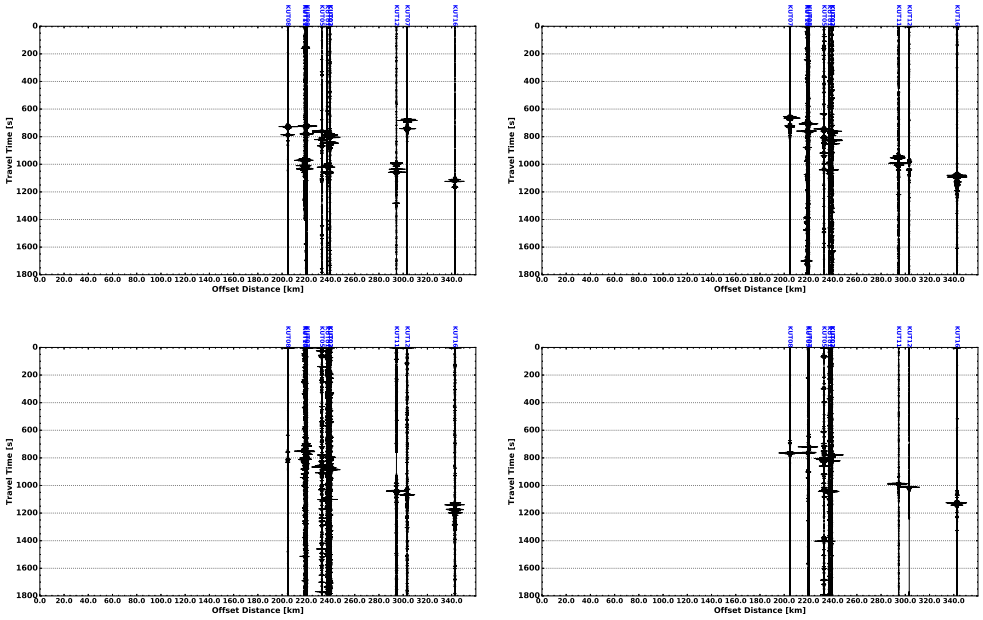

Figure 9. Records of the Mt. Shinmoedake eruptions on 10 March 2018, at 01:54 JST (**top-left**), 04:27 JST (**top-right**), 10:15 JST (**bottom-left**), and 18:11 JST (**bottom-right**), from the stations on Shikoku Island. The results are filtered in the frequency range 1.0–1.5 Hz based on the PDF plot shown in Figure 4.

7.3. Infrasound Source Detection

After applying the spectral analysis technique to all infrasound data recorded several hours after the event, it was found that the dataset indicated a peak high spectral density value of around 0.2 Hz, which was the microbarom signal. To avoid this dominant microbarom signal, the frequency range was band-pass filtered with range of 1.0–1.5 Hz. This frequency range was then applied to the filtered data to detect signals in the second process described in Section 6. Figure 10 shows the typical results of the detection process from our calculation, applied to selected station data in the period following the first Mt. Shinmoedake eruption on 9 March 2018, at 06:58 UTC. The figure shows data from four stations located close to the volcano (top panel in Figure 10) and three stations located around 290 km from the source point (bottom panel in Figure 10). From top to bottom, the figure shows the stacked signals received after bandpass filtering, the maximum power at every processing step, the arrival direction as the azimuth angle, and the velocity along the waveform. The color scale indicates the correlation coefficient for the corresponding time window and is a measure of the statistical significance of the source detection. In the recorded data for 9 March 2018, at 06:58 UTC, all of the infrasound data detected by the sensors were propagated at constant speeds, but the estimated azimuths of the incoming signals differed slightly from the actual location of the volcano, which was likely due to the presence of winds and the surface height (i.e., hills), which can cause a signal's path to stray from the arc of a circle that connects the source to the sensors. A second example is shown in the bottom panel of Figure 10, where the recorded signals were taken from sensors located around 290 km from the infrasound source. In this figure, the signal amplitude is clearly lower amplitude than the result of the upper panel due to many factors, such as topographic absorption and atmospheric conditions. In addition, there was an indication of signals originating from the lower stratosphere within the stable velocity area seen in the velocity panel. A signal phase higher than the sound speed at the ground will be refracted back to the ground along a path where their effective sound speed is approximately equal to the apparent velocity. The apparent speed is calculated based on the sequence signals that is recorded by the sensor at station located close to the source (top panel in Figure 10), indicating the arrival signal as a refraction from the layer at about the troposphere. Meanwhile, the apparent speed in the bottom of Figure 10, showing higher speed than the speed shown in the top panel in Figure 10.

Therefore, in the bottom panel in Figure 10, the arrival wave is deducted as a result of refraction at the altitude higher than the troposphere (e.g., stratosphere) due to the flow strength of jet stream on both layers. Generally, jet stream on the stratosphere has a speed higher than on the troposphere. In identifying signal phases and their propagation paths, the celerities, apparent velocities, and back azimuths can be used as a consistency check.

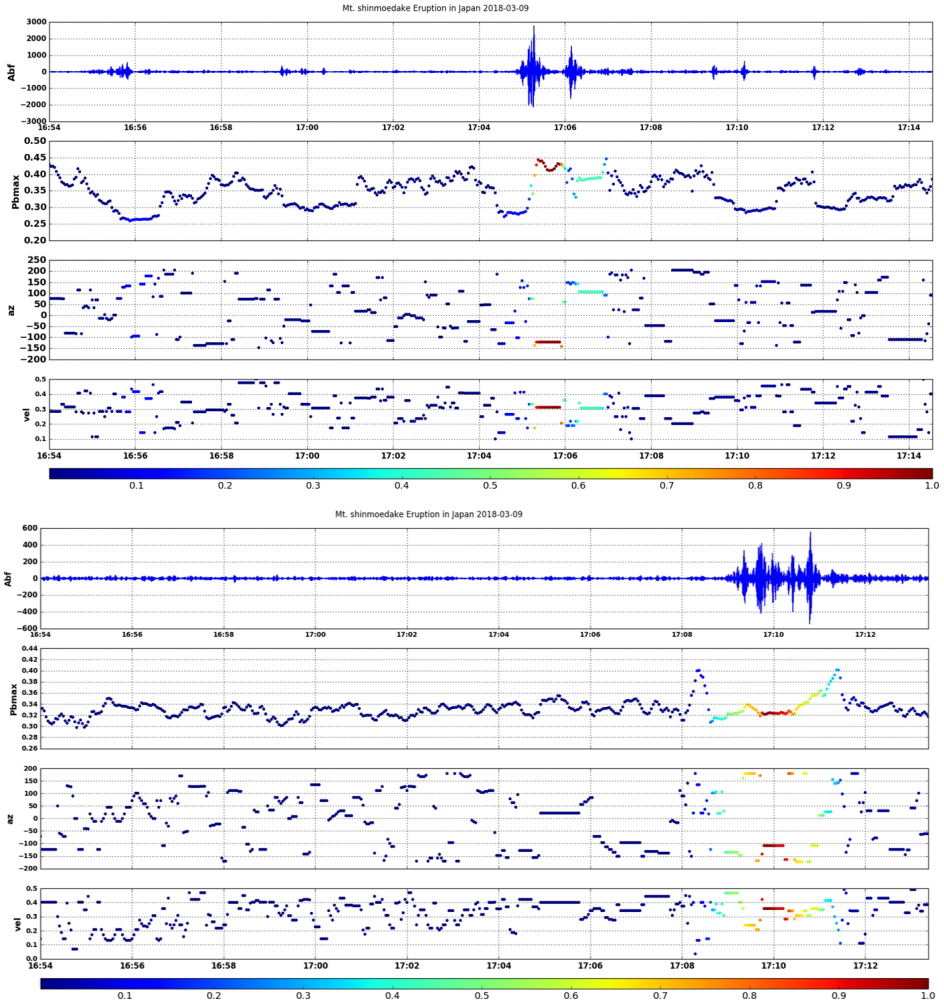

Figure 10. (**Top panel**) Array processing results for the 9 March 2018 at 06:58 UTC based on the data of the closest station to the source point. Clear arrival with both arrival direction and apparent velocity are presented in stable value. The detection is colored by the coherent coefficient. (**Bottom panel**) Similar processing on the same period based on the second group of station data.

7.4. Infrasound Ray-Propagation

To explain the asymmetry of the location results and to make an infrasound source map, a wave propagation simulation was performed for a broad source area using the planar approximation parabolic equation (PE) method as described in Section 6, and empirical atmospheric data from MERRA-2 and NRLMSISE-00 models were used to predict the power of wave transmission depending on elevation and distance. The resulting MERRA-2 atmospheric specifications provided global estimates of the winds, temperature, and pressure up to 75 km altitude at 3 h intervals and were used in the wave propagation calculations. To account for atmospheric density, available lower and middle atmospheric data were typically provided by the NRLMSISE-00 empirical model.

Figure 11 shows the atmospheric background state above Mt. Shinmoedake on 9 March 2018, at 04:30 UTC. The left panel depicts the eastward and northward winds, denoted by blue and red lines,

respectively. Fundamental atmospheric components are shown in the right panel. Long-range sound propagation is primarily determined by horizontal wind components and temperature gradients in terms of altitude, time, and geographic location. Sound is refracted downwards by positive temperature gradients ($\frac{dT}{dz} > 0$), and the sound speed at the refraction layer is larger and equal to the sound speed at the ground, $c(z_{tr}) \geq c(0)$ in the windless condition. In the wind case, horizontal wind components, such as positive wind shear, may give play important role in the refraction process. As shown in Figure 11, in the troposphere, temperature decreased up to altitudes below 20 km but, interestingly, a positive temperature gradient occurred twice around altitudes of 5 and 10 km. The layer above this, the stratosphere, was characterized by a strong positive temperature gradient that was predominantly due to the absorption of solar energy in the ozone layer. A smaller layer above it, the stratopause, had a local maximum vertical temperature at an altitude of around 40 to 50 km. In the mesosphere, the temperature decreased dramatically to the minimum state. Obviously, the zonal wind speed was higher than its meridional counterpart in two regions, the altitudes above 10 to 20 km and 30 to 60 km. The maximum value of these jet streams at altitudes near the stratopause and tropopause may have contributed to a ducting layer that refracted sound propagation in a downward direction. Furthermore, during the event, the winds were characterized by a moderately strong eastward zonal wind jet, peaking at ∼40, ∼44, and ∼57 m/s at altitudes of 10, 55, and 68 km, respectively. The meridional winds were greatest at an altitude of 40–60 km. Both the zonal and meridional components of the tropospheric winds had a positive direction, triggering a tropospheric jet to the northeast. For propagation to the north, the sound was predicted to be ducted in the stratosphere, beginning at an altitude of ∼60 km. The main features of the wind specification in the period of 9 March 2018, at 04:30 UTC were a dominance of strong eastward and northward jet streams, peaking at ∼60 and ∼10 km for the stratospheric and tropospheric jets, respectively.

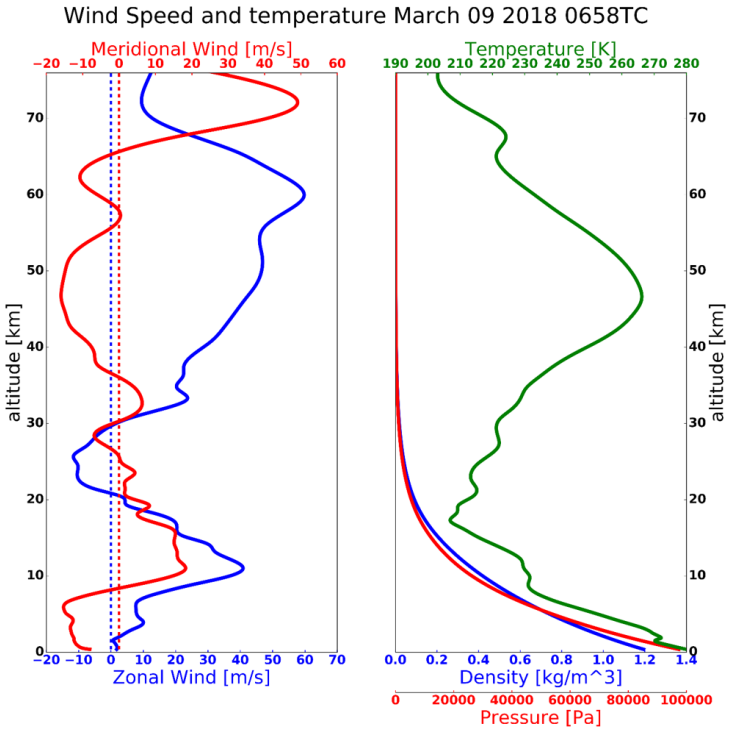

Figure 11. Modern-Era Retrospective analysis for Research and Applications, Version 2 (MERRA-2) and Naval Research Laboratory Mass Spectrometer and Incoherent Scatter Radar, Exosphere (NRLMSISE-00) atmospheric profiles above the source for use in the wave propagation calculation. (left panel) Winds, with the eastward winds as a blue solid line and northward winds as a blue dotted line. (right panel) Fundamental atmospheric parameters, vertical temperature, density, and pressure shown in green, blue, and red lines.

The effective sound speed profiles for propagation to the east predominantly reflected these two wind jets, with great tropospheric and stratospheric ducting predicted for the selected event beginning at altitude ∼10 and ∼60 km. In Figure 12, the along-path wind speed is represented by the difference between the adiabatic (blue line) and effective sound speed (red line) in all directions of wave propagation. It is clearly shown that the westerly wind has a significant impact by completing the formation of the tropo-stratopause sound duct. There was no sound ducting predicted for the west and south propagation, but there was significant tropo-stratospheric ducting for the north and east propagation. Additionally, in this case, the jet stream was large enough to have a qualitative impact on the effective sound speed profiles.

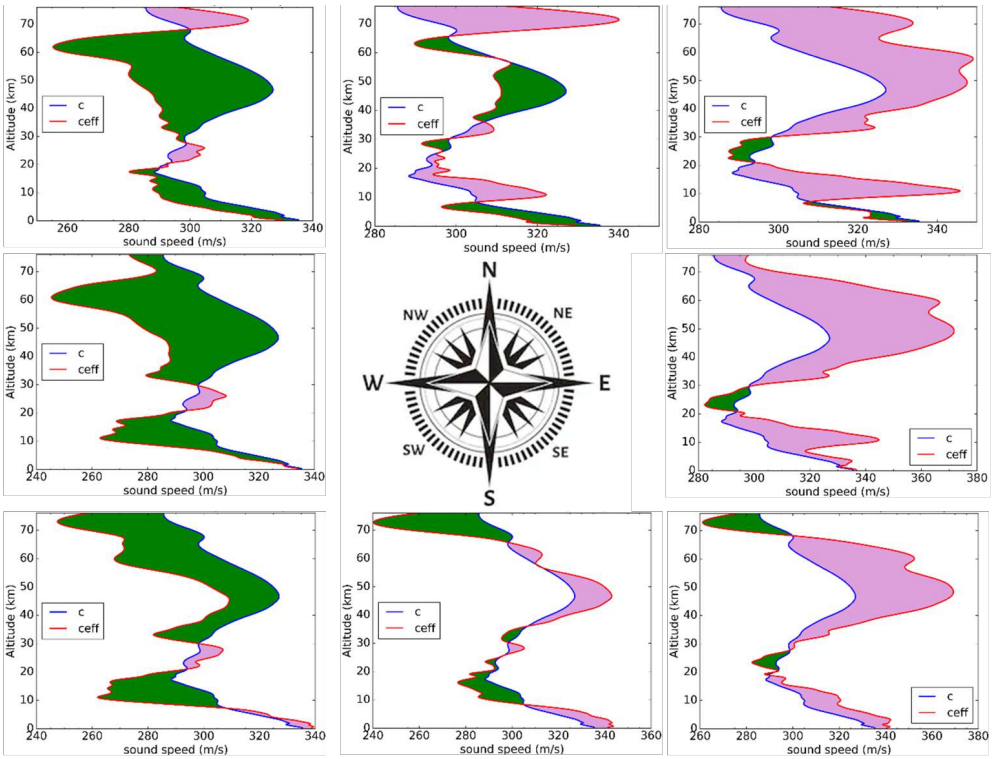

Figure 12. Effective sound speed comparisons for Modern-Era Retrospective analysis for Research and Applications, Version 2 (MERRA-2) and Naval Research Laboratory Mass Spectrometer and Incoherent Scatter Radar, Exosphere (NRLMSISE-00) model specifications above Mt. Shinmoedake on 9 March 2018, at 04:30 UTC. Purple shading represents the condition when $c_{eff} \geq$ c.

By incorporating the calculated horizontal wind components and vertical atmospheric parameters from the models (see Figure 11), upper altitude reflections of infrasound sources from the north to the east were obtained, as shown in Figure 12. According to the classical ray theory, strong arrivals (totally ducted) were refracted from altitudes for which the effective sound speed was larger than the adiabatic sound speed at the source level (purple shaded color). Figure 12 shows that, for northern propagation, the ducting layer was formed at altitudes above 60 km, although the effective speed of sound at the height of 10 km (see Figure 12) appeared to be greater than the adiabatic sound speed and was a possible candidate for the ducting process; however, the index of the sound speed ratio was not sufficient to form a ducting layer due to the weak meridional component at this height. In the east and northeast propagation, shown in Figure 12, infrasound waves were refracted back to the ground by two different layers, at 40 and 10 km (for eastward propagation) and above 45 and 10 km (for northeast propagation). The eastward and northeastward propagations had three dominant sound speed ratios, which occurred at altitudes around 10 and 40 km. Both profiles had the same index ratio

at an altitude of 10 km, but at altitudes above 40 km, they began to show different behaviors in each direction of propagation. For the eastward direction in Figure 13, in addition to being deflected at an altitude of 10 km, the infrasound wave was guided back to the ground at an altitude of 40 km and less of the wave energy propagated to the higher altitude. This was presumably because the index of the two sound speed ratios at an altitude of 40 km in the profile of eastward propagation was significant enough to produce a ducting layer that could guide the wave back to the ground. Infrasound wave energy could possibly have a bias for the upper layer when the index of the two sound speed ratios at a lower altitude was not sufficient to trigger the ducting process, as seen in the east and northeastward propagation profile and clearly in the relationship shown in Figure 12 for similar propagation directions.

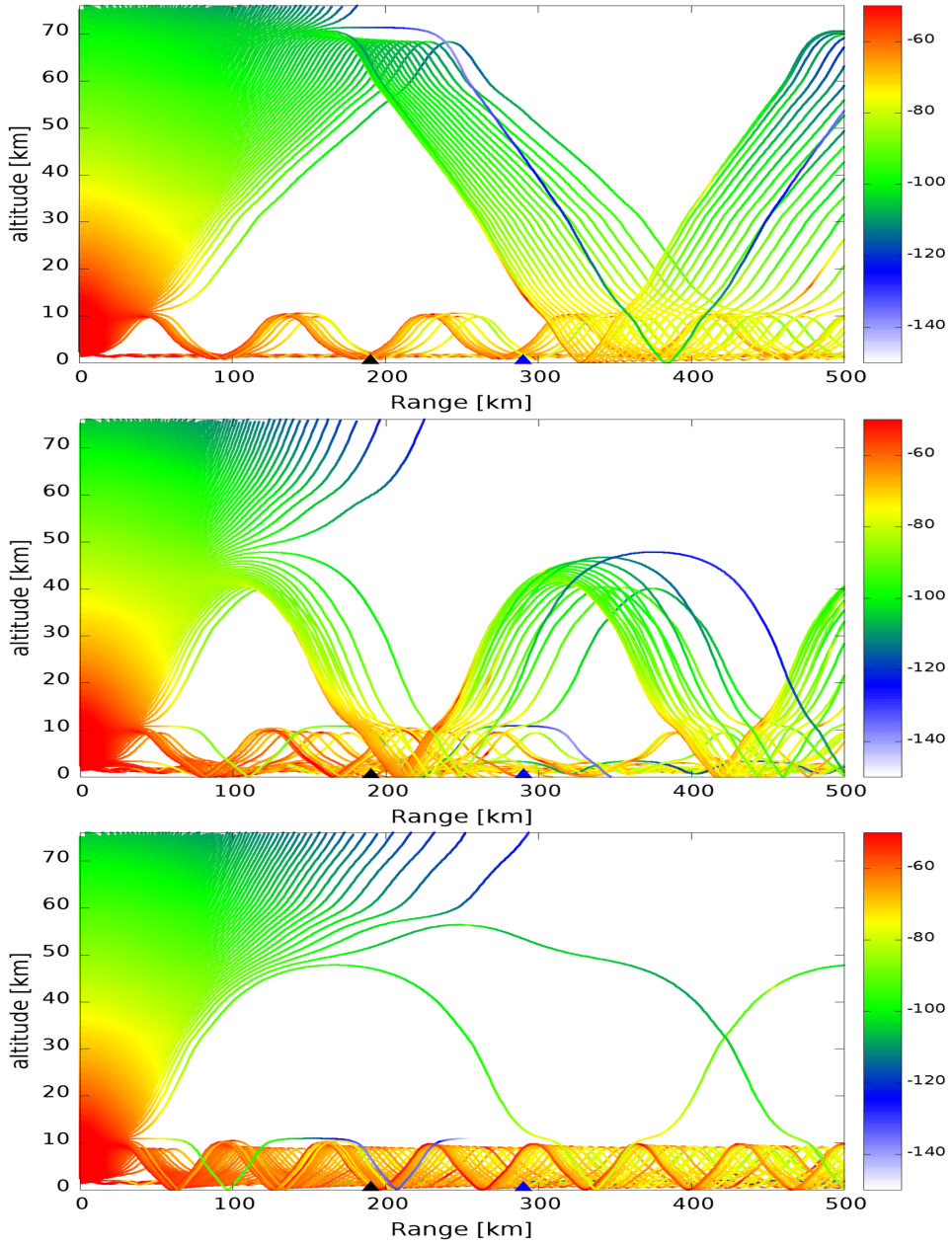

Figure 13. Ray tracing plot for the power transmission from Mt. Shinmoedake at 0 km at the left edge of the plot out to 500 km. The plot was constructed using atmospheric data for 9 March 2018, at 04:30 UTC. The top, middle, and bottom figures show the results for the northward, eastward, and northeastward propagation directions, respectively. The color plot represents the sound wave power transmission in dB per km of propagation of the infrasonic wave at a frequency of 1.25 Hz.

The wind jet streams that flowed eastward during the event were significantly larger than those that flowed in the opposite direction. The jet stream produced large tropospheric channels to the east and northeast at an altitude of about 10 km, and in the stratosphere at an altitude of ∼40 to 60 km. At the stations used in this study, which were located northeast of the source location, some tropospheric and stratospheric arrivals were recorded. Based on Figure 9, as well as Figures S12 and S13 in the supplementary file, two examples of station groups were selected, with the results shown in Figure 10. The first and second groups of stations were each about 190 and 290 km from the source location (marked by the black and blue triangles in Figure 13). In addition, at our selected stations, which were located at a distance of about 190 km northeast from the source, only the arrival of the tropospheric north-east propagation was estimated throughout the day, mainly due to the strong wind jet flow around the troposphere and a negative inversion in the boundary layer, with a positive temperature gradient. For the second station group (marked by blue triangles), the two northeast propagation arrivals from the troposphere and stratosphere were estimated throughout the day, because of the presence of the two jet streams in those layers.

In the case of the Mt. Shinmoedake explosion on 9 March 2018, the rays intersecting an area of radius ∼500 km, centered on the source point (marked by the red triangle), were selected to construct a power transmission map (Figure 14). The color code shows the intensity of the power strength at the arrival of the infrasound for each area of the grid. This figure shows the effect of the wind jet corresponding to the background condition of the vertical atmosphere above the source, with the blue colors indicating higher observed amplitudes. As expected, waves propagated over a large area to the northeast of the volcanic region as a potential infrasound source, thus defining a large possible source area. At the time of the eruption, the strong zonal wind blowing toward the northeast would limit the detection of sources west of the volcano. The intensity of the partial strength (blue) repeated itself in concentric bands, resulting from some dominant deflection to the ground. Fortunately, several infrasonic stations detected signature signals from volcanic eruptions, with two phases arriving from the stratosphere and troposphere. The arrival of tropospheric infrasonic waves dominated the signal reception in the first station group, while the stratospheric arrivals were received at the second station group. In addition, the attenuation was very high, with a high absorption power estimated to the south and west after ∼300 km from the source point. In other situations, although the northeast propagation generally dominated, a small number of our sensors in the eastern part of Shikoku Island detected the event.

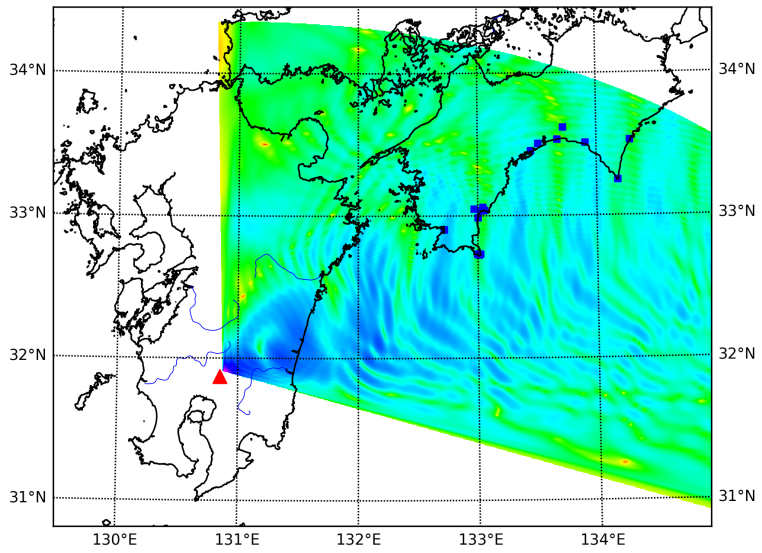

Figure 14. Sound wave power maps in dB for 9 March 2018, at 04:30 UTC from the 1.25 Hz propagation modeling. The red triangle is the Mt. Shinmoedake volcano. The color plot represents the sound wave power loss in dB, where the blue is a larger loss than the green.

The various phases of an infrasonic arrival observed by sensors on the ground are determined by the type of propagation path. The paths are predominantly through the tropospheric, stratospheric, and thermospheric waveguides, and depend on their travel times. A wave quantity called celerity can be used to infer the properties of the signal phase. The celerity is defined as the ratio of the range to travel time for one or several multipath bounces and is a measure of the horizontal propagation speed and the path length. Consequently, the closer the propagation path to the horizontal, the closer the speed is to the speed of sound on the ground. Signals that travel along the troposphere obviously arrive first, with celerities close to the speed of sound at the ground. Above the troposphere, stratospheric arrivals have smaller celerities, usually ranging from 0.28 and 0.31 km/s [49]. Finally, the predicted turning height as a function of range and celerity was determined to infer the signal phase properties and propagation paths. We presented a typical example of the analysis of data from the Mt. Shinmoedake eruption period on 9 March 2018, at 06:58 UTC, which enabled a detailed study of sound propagation over time. From classical ray theory, we inferred that the waveguide would be fully channeled if the effective sound velocity at a certain height was relatively large against the sound speed at the ground. The results were shown as the turning height, with the function of celerity and range shown in Figure 15. Typically, three types of arrival were estimated. The first type of arrivals, were called boundary arrivals and were turned back at a height around ∼5 km, with a celerity range of between 0.33 and 0.34 km/s. The second type turned back at altitudes around ∼10–20 km, with an estimated celerity around 0.31 km/s. Along the stratospheric path, there was a double turning height at the same range of celerity of about 0.28 to 0.30 km/s. It was clearly shown that the presence of a strong horizontal wind flow at altitude could alter the length of time required to travel through their path. This effect is shown as a slope pattern in each turning height.

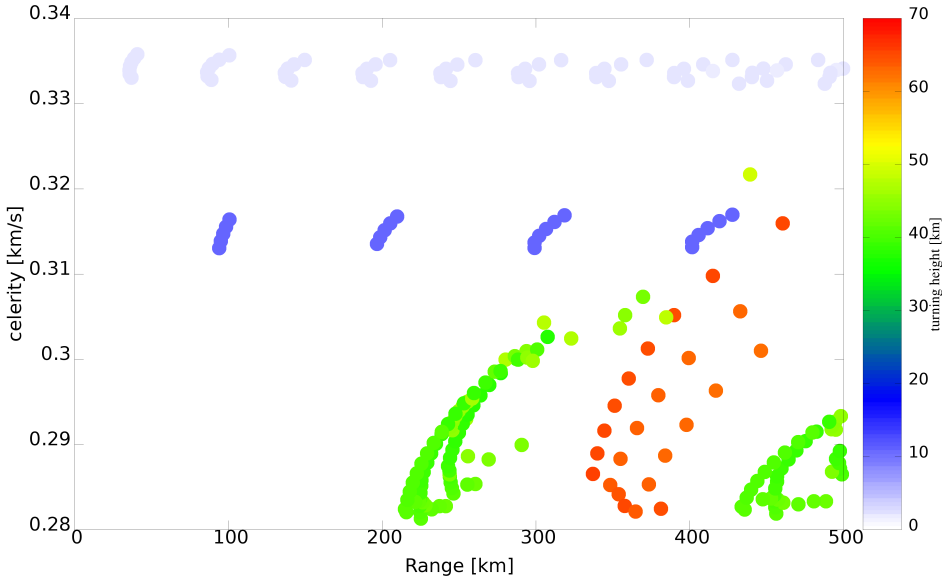

Figure 15. Celerity-range diagram. The colored dots represent troposphere and stratosphere ducting according to the turning height.

7.5. Comparison of Wind Speed

Two dubiety were found in the approach of atmospheric wind estimation, and one was the exact turning altitude to be estimated and the temperature at this altitude to also be obtained. The altitude level of reflection was estimated by the procedure described in Reference [44] and implemented in the acoustic ray tracing model [36], including the possibility of atmospheric wind, and three fundamental atmospheric profiles, retrieved from MERRA-2 and NRLMSISE-00 models for corresponding time periods above the source location. By applying the initial winds and temperature during the events into the acoustic ray tracing model, the level of infrasonic reflection in a real azimuth propagation from

the source are obtained as given in the ray plot (Figure 16, bottom). Rays are plotted at 1° intervals of incidence angles. The stratospheric reflection at about 46 km as a result of the stratospheric jet stream at that time. The rays with lower angles of incidence were not reflected back to the ground which is probably due to the dissipation effects that attenuate the signal.

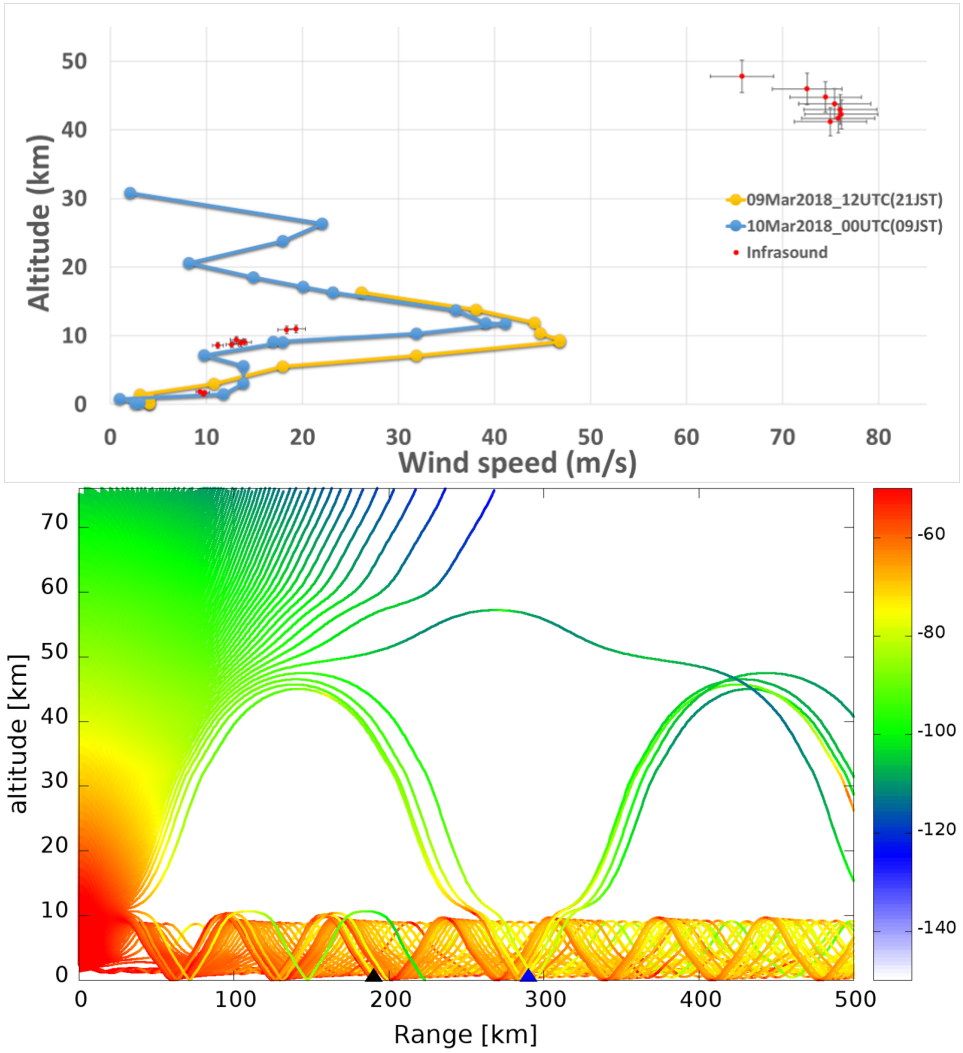

Figure 16. Typical results on 9 March 2018, at 06:58 UTC. (**top**) Wind velocity obtained by calculation (red dot) and radiosonde observations (blue and yellow circles). (**bottom**) Typical ray-tracing results for a real azimuth propagation from the source to the array sensor. The colored dots represent troposphere and stratosphere ducting according to the turning height. The colored plot represents sound wave power transmission in dB per kilometer of propagation of the infrasonic wave at a frequency of 1.25 Hz.

Figure 17 shows a typical result of radiosonde observation on 9 March 2018 at 00:00 UTC and 12:00 UTC above Shinomisaki station, Japan (33.45°N, 135.77°E). The observation data can be accessed from the JMA database [50] and NOAA (National Oceanic and Atmospheric Administration) [51]. The jet stream in the troposphere, around 10 km of altitude flows strongly in the northeast direction as similar as the MERRA-2 model shown in Figure 11.

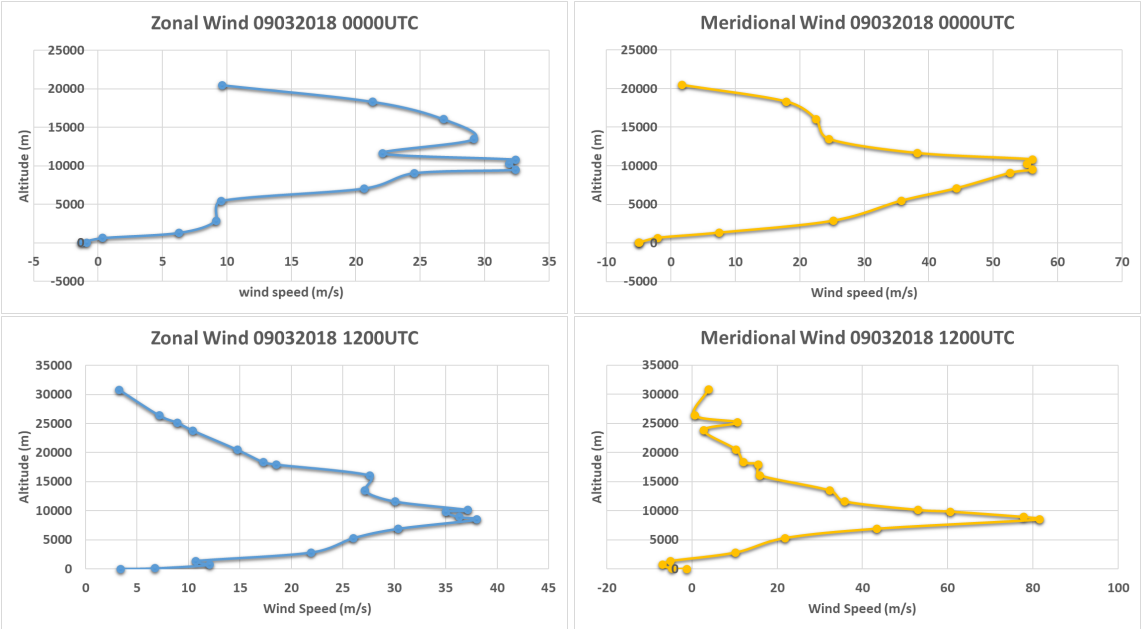

Figure 17. A typical result from radiosonde observation above Shinomisaki station, Japan (33.45°N, 135.77°E), on 9 March 2018 at 00 UTC (the first line panel) and 12 UTC (the second line panel). The zonal and the meridional winds are, respectively, drawn in blue and yellow lines.

Using the result on 9 March 2018 at 06:58 UTC as an example, the sound speed at an altitude of about 40 km was rather low (299 m/s at 41 km, Table 4), indicating the propagation velocity in this layer. Array processing estimated a trace velocity in the propagation direction toward the sensors, with a particular azimuth and speed. As the estimation of trace velocity, based on the recorded signals in this period, was about 375 m/s, the wind over our station at about 41 km was about 76 m/s. In the troposphere, the east wind speeds above our stations at altitudes of 9 and 10 km were about 51 and 53 m/s, respectively. Wind velocity results for this period are shown in the right column of Table 4. The strong wind jets controlled the observed arrivals and further illustrated the importance of the zonal wind jet on propagation simulation. The atmospheric specifications up to the lower stratosphere were sufficient for qualitative propagation simulations. The ray tracing and parabolic modeling of the array are shown in the bottom of Figure 16. Ray tracing predicted the arrival phase of the troposphere at the closest station to the source, labeled as a black triangle, and the arrival phase of the stratosphere at the other station, labeled as a blue triangle, with the sound speed and reflection level given in Table 4.

Typical velocity results for the recorded signals on 9 March 2018 at 06:58 UTC and a comparison with the radiosonde data from local observation at height up to 30 km are presented in Figure 16. A comparison of the calculated wind velocities and radiosonde observation up to the altitude of the radiosonde indicated a qualitative agreement. However, there is still a need to obtain calculated wind velocities above the radiosonde altitude for a comparison with direct measurements (e.g., a stratospheric balloon experiment). The other calculated wind velocities and their comparisons for the the eruption times listed in Table 2 are shown in Tables S3–S7 of the supplementary file.

Table 4. Trace velocity, sound speed, and wind speed.

Trace Velocity (km/s)	Computed Reflection Level (km)	Speed of Sound at Reflecting Level (km/s)	Computed wind at Reflecting Level (m/s)
0.3350	1.4399	0.3253	9.7222
0.3350	1.5166	0.3253	9.7253
0.3350	1.5961	0.3252	9.8042
0.3350	1.6845	0.3252	9.8399
0.3350	1.8324	0.3256	9.3737
0.3350	9.5787	0.3238	11.2130
0.3350	9.7079	0.3223	12.6592
0.3350	9.8632	0.3214	13.5737
0.3350	10.0666	0.3210	13.9832
0.3350	10.3885	0.3219	13.1369
0.3350	10.8367	0.3166	18.3671
0.3350	10.9657	0.3157	19.3458
0.3732	41.1735	0.2982	74.9928
0.3732	41.6614	0.2974	75.8096
0.3732	42.2479	0.2971	76.1437
0.3732	42.9495	0.2972	76.0207
0.3732	43.7830	0.2978	75.4465
0.3732	44.7582	0.2987	74.4873
0.3732	45.9465	0.3006	72.5645
0.3732	47.7888	0.3074	65.7910

8. Conclusions

We conducted an analysis of infrasonic data regarding the suspected signatures of an infrasonic pressure disturbance, which was likely to have been caused by an explosive eruption of Mt. Shinmoedake in Japan during the time period listed in Table 2. Specifically, we evaluated individual infrasound data from various stations to identify the characteristics of a particular wave, mostly in terms of its strength, arrival angle, and propagation speed.

Using data from an infrasonic sensor located on Shikoku Island, we then concluded that the propagation speed of the infrasound disturbance associated with the eruption was 336.6 ± 6.3 m/s. The propagation speed was calculated based on the distance between the sensor and the crater, and the delay time between each eruption event and the time of the first detection of the disturbance observed at each infrasonic station. The calculated propagation velocities of around 336 m/s were within the typical range of propagation speeds for similar eruptions [18], which have been observed and analyzed previously. They were also in general agreement with the effective speed of propagation of sound waves [1].

The implementation of the RBS concept into an irregular infrasound array system gives a possible way to detect the source waves, in which the parameter output of the detected source waves are then used for further atmospheric wind velocity estimation. The comparison of the atmospheric wind speed between the infrasound observation and the regional radiosonde observation are relatively in good agreement, although the wind at above the radiosonde altitude still remains works for validations and comparisons through a further improvement of approaches. A knowledge of the trace velocity at these reflection levels would, therefore, be sufficient to calculate the wind speed at the reflection altitudes, giving results that were consistent with direct observations.

The simulation of wave propagation for the Mt. Shinmoedake eruption on 9 March 2018 predicted a map of the distribution of high amplitude arrivals in the northeast direction from the source point. The atmospheric profile in the upper stratosphere was sufficient for qualitative simulations. The strong wind jets further indicated the importance of horizontal wind in the detection and propagation of source waves. Unobserved upper atmospheric arrivals to the sensor arrays were likely in the locations that were still in the range of the shadow zone. However, the arrays did record valuable infrasound arrivals where the western and central array clearly recorded signatures that corresponded to well-estimated tropospheric and stratospheric arrivals.

In summary, we developed a relatively low-cost infrasound sensor array with an irregular shape configuration, our data processing technique for the source detection, and the horizontal wind speed estimation. The sensors were capable of detecting a series of anomalous infrasonic pressure disturbances associated with eruptions of Mt. Shinmoedake during March 2018. We develop a novel irregular array processing for the detection of the infrasound source waves using the common radar scanning scheme. We also introduced a novel idea for the horizontal wind speed estimation using the infrasound observation. The wind speed estimated from infrasound observation showed a profile which is close to the profile obtained by radiosonde. However, it still needs some validations for the estimated wind at above the radiosonde altitude. In addition, as the methods and approaches described in this paper are still based on the general assumptions for simplifying the analysis, we recommend the same procedure be tested for other types of infrasound sources, with some additional adaptive parameters in the procedure.

Supplementary Materials: A set of supplementary figures and tables are available at http://www.mdpi.com/2072-4292/12/4/728/s1.

Author Contributions: Conceptualization, M.B. and M.-y.Y.; methodology, M.B.; software, M.B.; validation, M.B. and M.-y.Y.; formal analysis, M.B.; investigation, M.B.; resources, M.B.; data curation, M.B.; writing—original draft preparation, M.B.; writing—review and editing, M.B. and M.-y.Y.; visualization, M.B.; supervision, M.-y.Y.; project administration, M.-y.Y.; funding acquisition, M.-y.Y. All authors have read and agreed to the published version of the manuscript.

Funding: This research was funded by the Special Scholarship Program of Kochi University of Technology, Japan.

Acknowledgments: This work was funded by Kochi University of Technology (KUT), Japan, under a Special Scholarship Program (SSP), KUT-IONS (Kochi University of Technology Infrasonic Observation Network System), which supplied the system for data acquisition and infrasound sensors, as well as the networking system information. The team of sensor development comprises a large number of people. Y. Ishihara, Y. Nishiyama, T. Yamada, Y. Manabe, K. Ikehara, and A. Yokota played a critical role in organizing the entire experiment from inception through development. The authors are grateful for their partial contributions in every part of sensor development, mechanical ideas, manufacturing, testing, and calibration work since 2005. We are grateful to the Japan Meteorological Agency (JMA), Japan, and the National Oceanic and Atmospheric Administration (NOAA) for providing the radiosonde data. The radiosonde data can be downloaded from https://ruc.noaa.gov/raobs/ and https://www.data.jma.go.jp/obd/stats/etrn/upper/. We acknowledge use of the Global Modeling and Assimilation Office (GMAO) web service and the NASA Goddard Earth Sciences (GES) Data and Information Services Center (DISC) for accessible the MERRA2 data in https://doi.org/10.5067/SUOQESM06LPK. The infrasound data were obtained from the Kochi University of Technology Infrasound database center (http://infrasound.kochi-tech.ac.jp/infrasound) and accessible repository (https://doi.org/10.6084/m9.figshare.8319824.v2). The atmospheric model-derived data were obtained from the Community Coordinated Modeling Center (https://ccmc.gsfc.nasa.gov/modelweb/models/nrlmsise00.php). We thank the MIROVA for the thermal anomalies data from http://mirovaweb.it/. We thank the reviewers and the editors for their constructive comments and helpful suggestions on an earlier version of the manuscript.

Conflicts of Interest: The authors declare no conflict of interest.

References

1. Drob, D.P.; Picone, J.M.; Garcés, M. Global morphology of infrasound propagation. *J. Geophys. Res. Atmos.* **2003**, *108*. [CrossRef]
2. Evers, L.; Haak, H. Tracing a meteoric trajectory with infrasound. *Geophys. Res. Lett.* **2003**, *30*, 2246. [CrossRef]
3. Garces, M.; Caron, P.; Hetzer, C.; Le Pichon, A.; Bass, H.; Drob, D.; Bhattacharyya, J. Deep infrasound radiated by the Sumatra earthquake and tsunami. *Eos Trans. Am. Geophys. Union* **2005**, *86*. [CrossRef]
4. Johnson, J.B.; Aster, R.C.; Kyle, P.R. Volcanic eruptions observed with infrasound. *Geophys. Res. Lett.* **2004**, *31*. [CrossRef]
5. Johnson, J. Generation and propagation of infrasonic airwaves from volcanic explosions. *J. Volcanol. Geotherm. Res.* **2003**, *121*, 1–14. [CrossRef]
6. Gabrielson, T.B. Infrasound. In *Encyclopedia of Acoustics*; John Wiley, Ltd.: Chichester, UK, 2007; Chapter 33, pp. 367–372. [CrossRef]
7. Ichihara, M.; Takeo, M.; Yokoo, A.; Oikawa, J.; Ohminato, T. Monitoring volcanic activity using correlation patterns between infrasound and ground motion. *Geophys. Res. Lett.* **2012**, *39*. [CrossRef]

8. Matoza, R.S.; Fee, D. Infrasonic component of volcano-seismic eruption tremor. *Geophys. Res. Lett.* **2014**, *41*, 1964–1970. [CrossRef]
9. Garcés, M.; Hetzer, C.; Merrifield, M.; Willis, M.; Aucan, J. Observations of surf infrasound in Hawaii. *Geophys. Res. Lett.* **2003**, *30*. [CrossRef]
10. Johnson, J.B.; Lees, J.M.; Yepes, H. Volcanic eruptions, lightning, and a waterfall: Differentiating the menagerie of infrasound in the Ecuadorian jungle. *Geophys. Res. Lett.* **2006**, *33*. [CrossRef]
11. Ripepe, M.; Coltelli, M.; Privitera, E.; Gresta, S.; Moretti, M.; Piccinini, D. Seismic and infrasonic evidences for an impulsive source of the shallow volcanic tremor at Mt. Etna, Italy. *Geophys. Res. Lett.* **2001**, *28*, 1071–1074. [CrossRef]
12. Goerke, V.H.; Young, J.M.; Cook, R.K. Infrasonic observations of the May 16, 1963, volcanic explosion on the island of Bali. *J. Geophys. Res.* **1965**, *70*, 6017–6022. [CrossRef]
13. Evers, L.G.; Haak, H.W. Listening to sounds from an exploding meteor and oceanic waves. *Geophys. Res. Lett.* **2001**, *28*, 41–44. [CrossRef]
14. Liszka, L.; Garces, M.A. Infrasonic Observations of the Hekla Eruption of February 26, 2000. *J. Low Freq. Noise Vib. Act. Control* **2002**, *21*, 1–8. [CrossRef]
15. Christie, D.; Kennett, B.; Tarlowski, C. Detection of Regional and Distant Atmospheric Explosions at IMS Infrasound Stations. In Proceedings of the Infrasound Technology Workshop, Kailua-Kona, Hawaii, 12–15 November 2001.
16. Campus, P.; Christie, DR.; Brown, D. Detection of infrasound from the eruption of Manam volcano on January 27, 2005. In Proceedings of the Infrasound Technology Workshop, Tahiti, French Polynesia, 28 November–2 December 2005.
17. Evers, L.; Haak, H. The detectability of infrasound in The Netherlands from the Italian volcano Mt. Etna. *J. Atmos. Solar-Terr. Phys.* **2005**, *67*, 259–268. [CrossRef]
18. Campus, P. Monitoring volcanic eruptions with the IMS infrasound network. *Inframatics* **2006**, *15*, 6–12.
19. Campus, P. The IMS infrasound network: Detection of a large variety of events including volcanic eruptions. In Proceedings of the 8th International Conference on Theoretical and Computational Acoustics, Crete, Greece, 2–5 July 2007.
20. Caudron, C.; Taisne, B.; Garcés, M.; Alexis, L.P.; Mialle, P. On the use of remote infrasound and seismic stations to constrain the eruptive sequence and intensity for the 2014 Kelud eruption. *Geophys. Res. Lett.* **2015**, *42*, 6614–6621. [CrossRef]
21. Cansi, Y. An automatic seismic event processing for detection and location: The PMCC Method. *Geophys. Res. Lett.* **1995**, *22*, 1021–1024. [CrossRef]
22. Cansi, Y.; Le Pichon, A. Infrasound Event Detection Using the Progressive Multi-Channel Correlation Algorithm. In *Handbook of Signal Processing in Acoustics*; Springer: New York, NY, USA, 2009; pp. 1425–1435._77. [CrossRef]
23. Lopez, T.; Fee, D.; Prata, F.; Dehn, J. Characterization and interpretation of volcanic activity at Karymsky Volcano, Kamchatka, Russia, using observations of infrasound, volcanic emissions, and thermal imagery. *Geochem. Geophys. Geosyst.* **2013**, *14*, 5106–5127. [CrossRef]
24. Marchetti, E.; Ripepe, M.; Ulivieri, G.; Caffo, S.; Privitera, E. Infrasonic evidences for branched conduit dynamics at Mt. Etna volcano, Italy. *Geophys. Res. Lett.* **2009**, *36*. [CrossRef]
25. Ripepe, M.; De Angelis, S.; Lacanna, G.; Voight, B. Observation of infrasonic and gravity waves at Soufrière Hills Volcano, Montserrat. *Geophys. Res. Lett.* **2010**, *37*. [CrossRef]
26. Olson, J.V.; Szuberla, C.A. Processing Infrasonic Array Data. In *Handbook of Signal Processing in Acoustics*; Havelock, D., Kuwano, S., Vorländer, M., Eds.; Springer: New York, NY, USA, 2008; pp. 1487–1496._81. [CrossRef]
27. Cansi, Y.; Klinger, Y. An automated data processing method for mini-arrays. *News Lett* **1997**, *11*, 2–4.
28. Yamamoto, M.Y.; Yokota, A. Infrasound Monitoring for Disaster Prevention from Geophysical Destructions. In Proceedings of the 5th Internationnl Symposium on Frontier Technology 2015 (ISFT 2015), Kunming, China, 24–28 July 2015.
29. SAYA Inc. Infrasound Sensor ADX3I-INF01LE. Multifunction-I/O XIII. Available online: https://www.saya-net.com/products/INF01.html (accessed on 22 February 2020).

30. Kochi University of Technology (KUT). Kochi University of Technology InfraSound Observation Data Monitoring System. Real Time Infrasound Data - KUT. Available online: http://infrasound.kochi-tech.ac.jp/infrasound/graph.php (accessed on 20 January 2019).
31. Space Laboratory of KUT. KUT Infrasound March 2018. Available online: https://figshare.com/articles/KUT_Infrasound_March2018/8319824/1 (accessed on 26 November 2019).
32. Japan Meteorological Agency (JMA). *Monthly Volcanic Activity Report*; Tokyo, Japan, 2018. Available online: https://www.data.jma.go.jp/svd/vois/data/tokyo/eng/volcano_activity/monthly.htm. (accessed on 26 November 2019).
33. MIROVA. Middle InfraRed Observation of Volcanic Activity - Thermal Anomalies. Available online: http://www.mirovaweb.it/?action=about (accessed on 13 January 2018).
34. Garcés, M.; Willis, M.; Hetzer, C.; Le Pichon, A.; Drob, D. On using ocean swells for continuous infrasonic measurements of winds and temperature in the lower, middle, and upper atmosphere. *Geophys. Res. Lett.* **2004**, *31*. [CrossRef]
35. Landès, M.; Ceranna, L.; Le Pichon, A.; Matoza, R.S. Localization of microbarom sources using the IMS infrasound network. *J. Geophys. Res. Atmos.* **2012**, *117*. [CrossRef]
36. Waxler, R.M.; Assink, J.D.; Hetzer, C.; Velea, D. NCPAprop—A software package for infrasound propagation modeling. *J. Acoust. Soc. Am.* **2017**, *141*, 3627–3627. [CrossRef]
37. Gossard, E.E.; Hooke, W.H. Waves in the atmosphere: Atmospheric infrasound and gravity waves: Their generation and propagation. In *Developments in Atmospheric Science 2*; Elsevier Scientific: Amsterdam, The Netherlands, 1975; pp. 423–440.
38. Sutherland, L.C.; Bass, H.E. Atmospheric absorption in the atmosphere up to 160 km. *J. Acoust. Soc. Am.* **2004**, *115*, 1012–1032. [CrossRef]
39. Goddard Earth Sciences Data and Information Services Center (GES DISC). Global Modelling and Assimilation Office (GMAO) (2015). Available online: https://disc.gsfc.nasa.gov/datasets/M2T3NVASM_V5.12.4. (accessed on 12 February 2018).
40. Community Coordinated Modeling Center-NASA. NRLMSISE-00 Atmosphere Model 2001. Available online: https://ccmc.gsfc.nasa.gov/modelweb/models/nrlmsise00.php (accessed on 12 February 2018).
41. Wilson, C.R.; Olson, J.V. Mountain associated waves at I53US and I55US in Alaska and Antartica in the frequency passband from 0.015 to 0.10 Hz. *Inframatics* **2003**, *3*, 6–10.
42. Wilson, C.R.; Szuberla, C.A.L.; Olson, J.V. High-latitude Observations of Infrasound from Alaska and Antarctica: Mountain Associated Waves and Geomagnetic/Auroral Infrasonic Signals. In *Infrasound Monitoring for Atmospheric Studies*; Le Pichon, A., Blanc, E., Hauchecorne, A., Eds.; Springer: Dordrecht, The Netherlands, 2009; pp. 415–454._13. [CrossRef]
43. Matoza, R.S.; Vergoz, J.; Le Pichon, A.; Ceranna, L.; Green, D.N.; Evers, L.G.; Ripepe, M.; Campus, P.; Liszka, L.; Kvaerna, T.; et al. Long-range acoustic observations of the Eyjafjallajökull eruption, Iceland, April–May 2010. *Geophys. Res. Lett.* **2011**, *38*. [CrossRef]
44. Donn, W.L.; Rind, D. Natural Infrasound as an Atmospheric Probe. *Geophys. J. Int.* **1971**, *26*, 111–133. [CrossRef]
45. Donn, W.L.; Rind, D. Microbaroms and the Temperature and Wind of the Upper Atmosphere. *J. Atmos. Sci.* **1972**, *29*, 156–172. [CrossRef]
46. Evers, L.G.; Haak, H.W. The Characteristics of Infrasound, its Propagation and Some Early History. In *Infrasound Monitoring for Atmospheric Studies*; Le Pichon, A., Blanc, E., Hauchecorne, A., Eds.; Springer: Dordrecht, The Netherlands, 2009; pp. 3–27._1. [CrossRef]
47. Assink, J.; Averbuch, G.; Shani-Kadmiel, S.; Smets, P.; Evers, L. A Seismo-Acoustic Analysis of the 2017 North Korean Nuclear Test. *Seismol. Res. Lett.* **2018**, *89*, 2025–2033. [CrossRef]
48. Ceranna, L.; Le Pichon, A.; Green, D.N.; Mialle, P. The Buncefield explosion: A benchmark for infrasound analysis across Central Europe. *Geophys. J. Int.* **2009**, *177*, 491–508. [CrossRef]
49. Brown, D.J.; Katz, C.N.; Le Bras, R.; Flanagan, M.P.; Wang, J.; Gault, A.K. Infrasonic Signal Detection and Source Location at the Prototype International Data Centre. *Pure Appl. Geophys.* **2002**, *159*, 1081–1125. [CrossRef]

50. Japan Meteorological Agency (JMA). High-rise Meteorological Observation Database. Available online: https://www.data.jma.go.jp/obd/stats/etrn/upper/ (accessed on 8 July 2019).
51. NOAA/ESRL Radiosonde Database. National Oceanic and Atmospheric Administration (NOAA). Available online: https://ruc.noaa.gov/raobs/ (accessed on 8 July 2019).

PUBLICATION IV

***

Batubara, M., Yamamoto, M.-Y., & Saito, H. (2020). *Results from infrasound monitoring using integrated sensors data by means of a network along multisite point over Japan*. Proceedings of the 14th International Conference on Vibration Problems (ICOVP 2019).

Results from infrasound monitoring using integrated sensors data by means of a network along multisite point over Japan.

Mario Batubara[1,2], Masa-yuki Yamamoto[1], Saito Hiroaki [1]
[1]School of System Engineering, Kochi University of Technology, Kochi, Japan
[2]Space Science Center, National Institute of Aeronautics and Space (LAPAN), Indonesia

Abstract

A spread of infrasound sensor has recently been installed over Japan through a research program of Kochi University of Technology (KUT), primarily for natural disaster mitigation over this region (e.g. tsunami disaster). Sensors installed at over 20 points over Japan continuously recorded multi-parameter signals (e.g. ground acceleration, local temperature, audible noise level, atmospheric pressure and sound pressure level) integrated in a compact instrument. Scientifically, the program aims to contribute both to understanding of infrasound sources over Japan and an expansion of the spatial coverage of the Japanese infrasound network. The monitoring results were transferred continuously to the main database server in Chiba under File Transfer Protocol (FTP) line communication. Through this session, we present (1) the detail of our infrasound network recently done as an irregular array systems; (2) the system description of our sensor in detail;(3) the implementation of irregular array signal processing for our infrasound cases; (4) Several confirmed of detected infrasound signals from natural activity phenomena are presented. The features calculated for the signals detected are used to associate signals with event and observe individually instrument performance. The results show the potential of the sensors and its network for making continuous infrasound monitoring under effective and efficient installation.

1. Introduction

Infrasound is classified as sound waves with frequencies below the 'normal' limit of human hearing, and is often cited as the frequency range 0.02–10 Hz [1]. These waves are generated from various man-made and natural sources and can propagate efficiently over regional and global scales of thousands of kilometers, with low intrinsic attenuation [2,3]. For instance, very large sources (e.g., massive volcanic eruptions) can produce buoyancy waves dominated by very low frequencies, particularly in the near-infrasonic range of 1–20 Hz [4], and were found to be well-correlated across a local network, suggesting a contribution from point source infrasound [5]. The advantages of infrasound waves have been exploited by researchers studying the characteristics of sound sources across the globe.

Since 2015, in a collaboration between national industries and the Earth Space and Exploration System Laboratory (ESESL) of Kochi University of Technology (KUT), Japan, new instrument designs have been developed to increase land-use efficiency and integrate surface meteorological measurements with seismology components. In addition, the system has been deployed for operation in various locations in Japan, especially in the Shikoku Island region. Since the observation network was established, our sensors have successfully detected and recorded several natural phenomena that produced infrasound waves (e.g., explosive volcanic eruptions and an intense earthquake that occurred in Japan). Three explosive volcanic eruptions were detected by the sensor, at Mt. Aso in 2016, Mt. Sakurajima in 2017, and Mt. Shinmoedake in 2018 as well as the medium to high magnitude scale of the earthquake occurred in Japan were also recorded.

Besides early mitigation of tsunami monitoring, this network of observations is also contributes in understand the dynamical process and structure of the atmosphere. With regard to the variability of their dynamics in spatial and temporal, the observation focuses on the air pressure recording at the individual infrasound sensor. The infrasound measurement itself have shown their potentiality measurements and the detection of atmospheric dynamics [6]. The infrasound measurements had been used for investigating variations in the middle and upper atmosphere [7–9]. Here a self-construction of our sensor with their location and a basic methodology are described for systematically analyzing temporal and spatial variability of infrasonic waves structures based on our infrasonic network. A modified approach of source wave characteristics is also introduced. We consider up to long period observation of infrasonic data and focus on the most phenomenal geophysical event occurred in Japan.

The infrasound network located over the Shikoku island, Japan is described in more detail in section 2. The description of sensor is drawn briefly in section 3. Section 4 deals with the information on the analysis tools applied in this study. Several examples of the characteristic of the ambient noise environment of the selected infrasound stations and the verified infrasonic wave generated by the earthquake and volcanic eruption in Japan are presented in section 5 and 6. The discussion presented is focused on the capability of infrasonic network in Shikoku island, Japan for atmospheric studies in the context of our findings.

2. Infrasound Station Sites at Shikoku island, Japan

The first operation of an infrasound sensor in Kuroshio city in Kochi prefecture occurred in 2016, following careful evaluation of the individual sensor performance. Currently, a total of 20 infrasound sensors are distributed uniformly over the Japanese islands and are in continuous operation. The Japanese infrasound station network is shown in Figure 1 with their geographic coordinates listed in table 1, where the network is denser on Shikoku Island for the detection of natural disasters, such as tsunamis and volcanic eruptions.

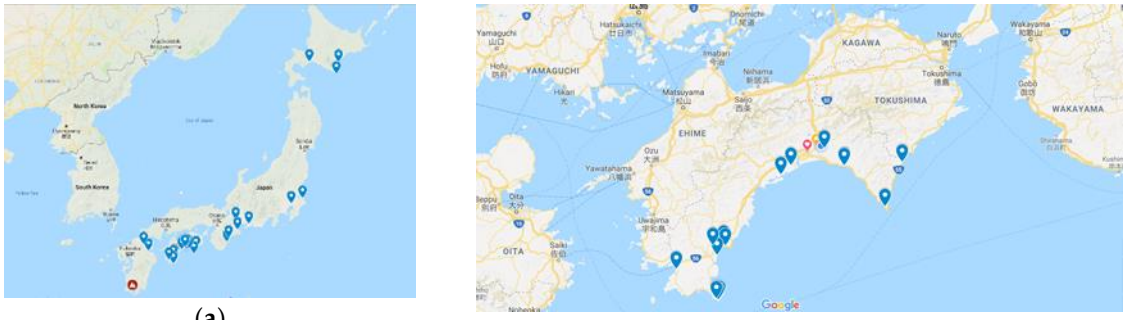

(**a**) (**b**)

Figure 1. The locations of infrasound sensors (type: ADXII-INF01) in Japan. (a) Distribution of sensor location over Japan; (b) Infrasound sensor location over Shikoku island, Japan.

All data recorded by the sensors are sent via the File Transfer Protocol (FTP) to the database server where they are archived, and are also displayed online at http://infrasound.mydns.jp/. Routine analysis of the combined data from several stations/sensors provides an advantage in determining the sources of infrasonic waves.

Table 1. List of Stations Used for Infrasound Studies

Station Code	Latitude (ºN)	Longitude (ºE)	Station Code	Latitude (ºN)	Longitude (ºE)
CSV01	33.03638889	133.03111111	**CSV14**	33.50333333	133.87944444
CSV02	33.05472222	133.04611111	**CSV15**	33.524319	134.280939
CSV03	33.04055556	133.05638889	**CSV16**	33.268	134.164161
CSV04	32.98527778	132.99888889	**CSV19**	42.60222222	141.47972222
CSV05	33.04138889	132.97138889	**CSV20**	42.49888889	143.43250000
CSV06	35.71583333	139.94416667	**CSV21**	41.93611111	143.24083333
CSV07	32.90555556	132.71805556	**CSV30**	34.96500000	136.62444444
CSV08	32.73194444	133.01861111	**CSV31**	33.88833333	136.10000000
CSV09	32.4315235	133.01861111	**CSV32**	34.07055556	136.19083333
CSV10	32.73222222	132.99444444	**CSV33**	34.48750000	136.70916667
CSV11	33.451039	133.441789	**CSV34**	34.76916667	137.39138889
CSV12	33.50611111	133.51111111			

3. Description of the Instrument

Since 2005, KUT collaborated with several local institutions to take the initiative to build an infrasound sensor that is integrated with several MEMS (Micro-Electro-Mechanic System) sensors in order to measure 3-axis acceleration in seismic waves, atmosphere temperature, atmospheric pressure and the level of audible noise sound. Apart from that, the sensor system is also equipped with a signal processing unit for continuous processing in real time and network connecting ports for data acquisition [10].

A full description of the specifications of the infrasound instrument is given in Table 2. At almost all stations, the four parameters in Table 2 are continuously digitized at 4 Hz by each individual sensor. The instrument was specially design to be windproof and easy to install.

With its performance, the sensor can be applied to monitor infrasound sources from geophysical activities such as volcanic eruptions, snow slides, land-slides, thunderstorms, tornadoes, etc., as well as human-made activity (e.q. explosions, spaceship re-entry, etc.).

Table 2. Specifications of the infrasound instrument (ADXII-INF01).

Integrated Accelerometer	
Measurement range	0–3347 Gal
Frequency characteristics	0.034–1600 Hz (N-S E-W), 0.034–550 Hz (V)
Resolution	16 bit
Audible Noise Sensor	
Measurement range	43–110 dB
Frequency characteristics	10–1,000 Hz
Auditory correction	None (= V characteristics)
Time constant	630 ms
Resolution	16 bit
Infrasound Sensor	
Measurement range	± 2.422 kPa
Minimum resolution	0.577 mPa
Noise level	± 20 mPa (Reduced to ± 1 mPa after passing through the 64th moving average filter)
D range	143.2 dB
Frequency characteristics	0.001 Hz to 6.25 Hz (± 6 dB temperature change low) 0.004 Hz to 6.25 Hz (± 6 dB temperature change high)
Pressure Sensor	
Measurement range	15–115 kPa
Frequency range	The lower of DC to 1 Hz or $F_s/2$ (F_s = sampling frequency)
Resolution	16 bit
Temperature Sensor	
Measurement range	0–81.92°C
Minimum resolution	0.0000390625°C

4. Analysis tools

4.1. Spectral analysis tools

For our analysis, there were two main data processing steps. First, we evaluated the ambient noise at each individual station to estimate the occurrence probability for each frequency bin of the recorded signals. In this step, we parsed continuous time series for each station into segments (30-min time series) that overlapped by 25%, and distributed them continuously throughout the period of interest. This overlapping reduced the variance in power spectral density (PSD) estimates. The PSD processing computed repeat fast-Fourier transforms (FFT) for each of the separate overlapping time bins of the 30-m time series. The final PSD estimates for the 30-min data were then calculated as the 5^{th} and 95^{th} percentiles of the distribution of individual PSD curves. Plots of PSD for all of our interest period were generated from all individual stations and used for analysis and data quality.

4.2. Irregular Array Sensor Processing

Second, we determined the azimuth and signal propagation speed detected by a group of infrasonic sensors. The basic idea of our approach was to use the set of delays between signals to steer the array to different areas or points in a scanning region. When the steering direction coincides with a source, the maximum output power will be observed. Figure 2 shows a schematic that illustrates the processes undertaken in this step. In more detail, each signal was filtered individually using different frequency bands based on the results of the previously estimated PSD. Then, as shown in Figure 2, further processing of each group of signals was performed via several operations. First, to examine signal coherency and further minimize the effects of discontinuity between the end and the starting point of the time series, a set of time shifts between sensors and a cosine taper were applied. Second, we directed the rotation scanning to a specific point by using a set of time shifts. Finally, the peak coherence was calculated to identify the signal source. In this step, we applied cosine-tapered windows of 120 s duration with 90% overlap in the spectral processing of each sensor, and determined the covariance of the signals at different stations. The window length was chosen to be proportional to the envelope width of the signals.

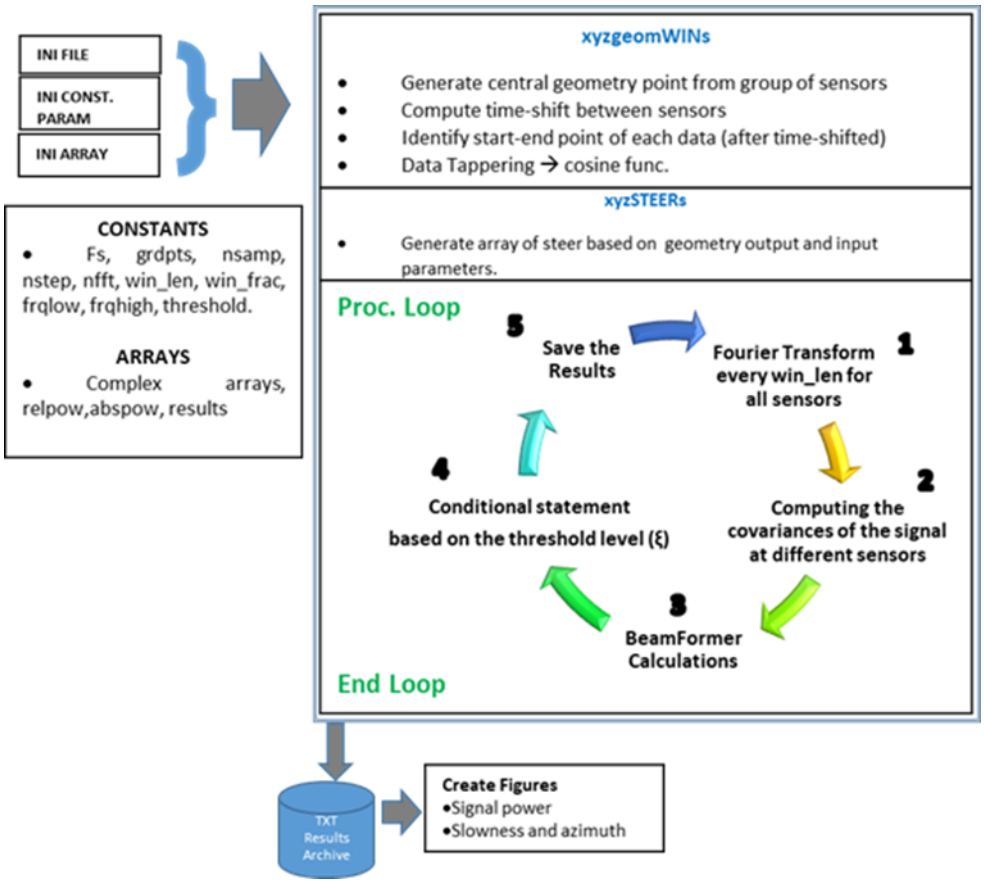

Figure 2. Schematic illustrating the steps in our approach to determine the arrival direction and propagation speed of the incoming signal's source.

5. Ambient noise level in the Shikoku Island

The ambient infrasound noise environment is captured by almost 25 single sensors distributed over Shikoku island. The captured noise was measured using Power Spectral Density as described in section 4.1. Figure 3 shows samples PSD plot for selected station in Shikoku island. All spectra in blue lines calculated for 30-m observation time, while red and green lines are the low and high-noise level, respectively. The maximum at each frequency of the 95th percentiles of all 25 PSD distributions from individual stations. Similarly, the low-noise level is calculated for one week observation time (±3 days of March 10th, 2018). Clearly seen that the microbarom peak appear in the low-noise and the median level, but is swept out by the wind in the high-noise level.

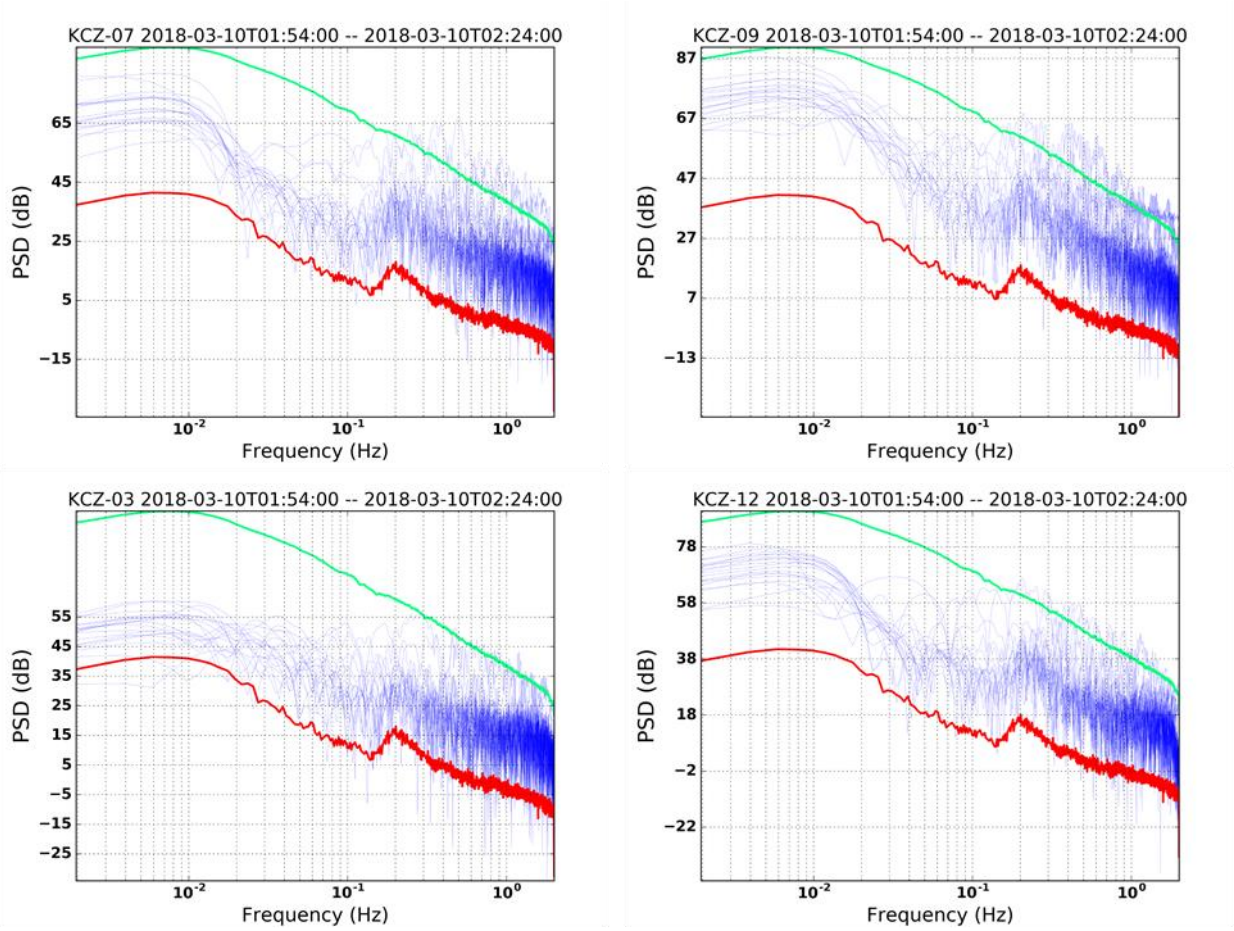

Figure 3. Power Spectral Density for selected station in Shikoku island. The low and high noise levels are shown in red and green.

6. Examples of observation and discussion

The infrasonic sensor network of KUT is designed to support the mitigation of geophysical destructive as well as the need for understanding the atmospheric characteristics from source wave propagation. As described in the section of instrument specification, its component is quite sensitive to detect small changes of infrasonic pressure. The stations in this network mostly located near the coastal line which dominant variety of microbarom sources. A number of infrasonic signals are recorded continuously at all stations in the infrasonic station network over Shikoku island. Some of these signals is found difficulties to identify the source. However, currently, several interesting infrasound sources have been identified using observation data from our infrasound network since the establishment.

We note that there are probably many other sources that have not yet been identified or classified. Many of these signals, such as signals from volcanic eruptions represent an excellent calibration sources for the infrasound network as well as has advantage to be used to assess the detection capability of the infrasound network. Infrasonic signals generated by earthquakes are observed at our infrasound stations. The following sections provide a sample of typical observations at the infrasound station network over Japan.

6.1. Volcano explosions

Volcanic eruptions are very important source of infrasonic sources [11–15]. Infrasound from volcanic activity originate primarily in the atmospheric perturbation caused by the explosive ejection of volcanic materials from the vents and crater of the volcano. The KUT infrasound network has shown the potential to provide a contribution to the monitoring of volcanic eruptions around the Japan. A number of volcanic eruption have been recorded since the establishment at infrasound stations. Some examples are shown in Figure 4.

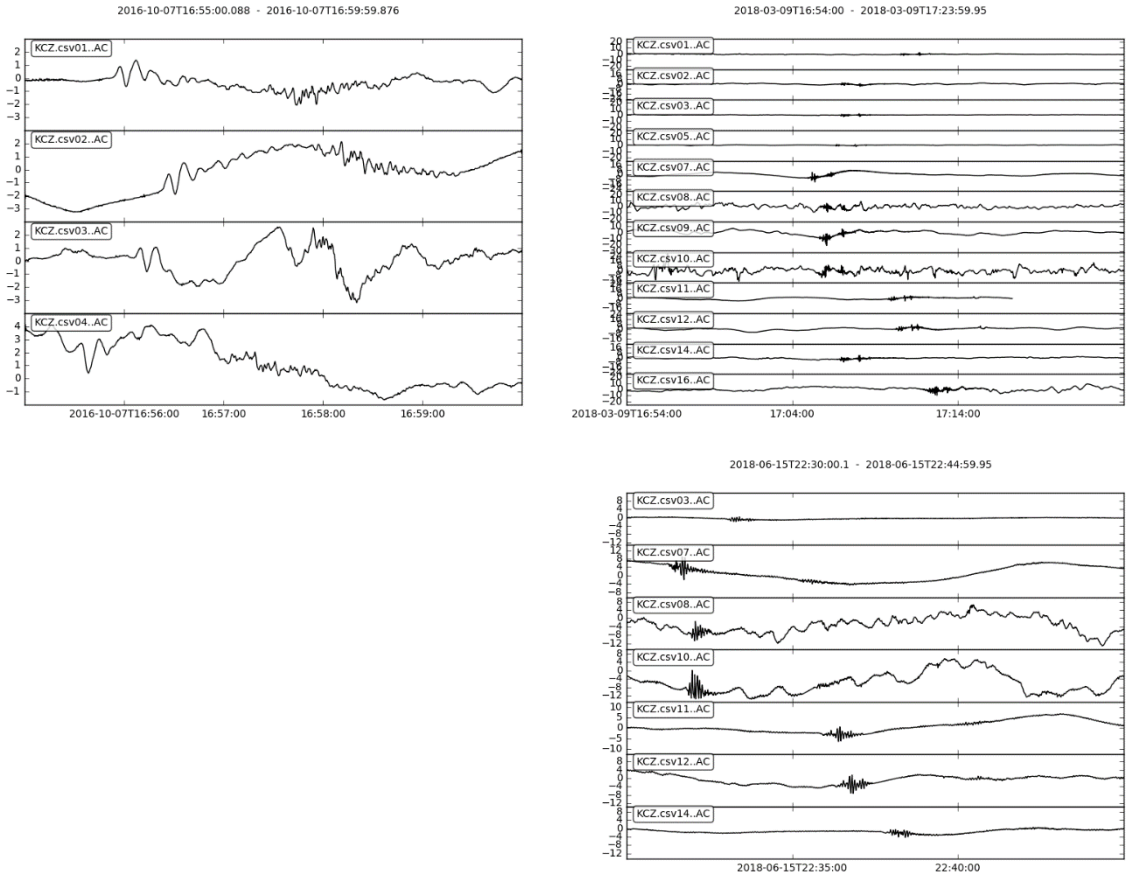

Figure 4. Real sampled signals from sensors. [top-left] Four stations records a first successful detection of Mt. Aso eruptions on October 8th, 2016 at 01:46 JST, first large explosive of Mt. Shinmoedake on March 10th, 2018 at 01:54 JST [top-right], and last volcanic eruption from Sakurajima volcano on June 16th, 2018 at 07:30 JST [bottom-right]. All data was sampled at 4 Hz of sampling rate.

The first records of volcanic activity from mount Aso, Japan observed one month after the first station establishment in September 2016 at four pioneer stations (CSV01; CSV02; CSV03; CSV04), in Shikoku island, Japan are shown in top-left figure 4. Mount Aso (32.8844^{o}N, 131.1039^{o}E) is the largest active volcano in Japan. Its last largest eruption start began at 01:46 am (JST) on October 8th, 2016 with an explosive eruption of volcanic ash clouds to ~11.9 km above sea level (ASL) along ~3.5 minutes [16]. This information was announced by the Japan Meteorological Agency (JMA) at 01:55 on the same day. A change in the Infrasound pressure from explosion at the summit of Aso was detected about 8.5 minutes after the explosive eruption (around 01:55:30) at the shortest stations of CSV04 at a distance of approximately 179.28 km and then after 8 minutes 55

seconds (around 01:55:55). A similar change in the pattern was also observed at sensor number 2(CSV02) around after 9 minutes 5 seconds (about 01:56:05).

Shinmoedake volcano is a 1431 m of elevation in Kagoshima prefecture, South-Eastern part of Japan (31.9117°N, 130.8833ºE) and a part of the Mount Kirishima cluster of volcanoes. The explosion shows significant eruption, which produces ash plume reaching heights of up to 7500 feet and generate strong air vibrations in the surrounding area. The recording of the Mt. Shinmoedake eruptions firstly explode on March 10th, 2018, at 01:54 JST within a period of ~1.5 minutes are presented in right corner of figure 4. Infrasound from explosions at the summit of Shinmoedake volcano was first detected by sensor number 7 (CSV07) as the shortest distance from the source point, approximately 205.74 km. The activity of volcano at Shinmoedake was dominant signal recorded clearly at station CSV07, CSV08, CSV09 and CSV10.

The detection of the eruption of Mt. Shinmoedake on June 16th, 2018, at 07:30 JST is shown in bottom right figure 4. All records show significant and clear signature of the explosive eruption, which creates a tall ash plume and pyroclastic flow that rose about 4700 meter above the crater and then drifted to the west. Similar to the second sample eruption above, sensor number 7 (CSV07) get the first detection earlier than others. All each group waves of the event depict a nice propagation through the location of the sensor. The sensor number 07 (CSV07) is therefore very well located for monitoring volcanic activity at the Kyushu island, South-western part of Japan.

The first analysis was performed for band-passed signals in the frequency range of 0.1-0.5 Hz, which cover the main frequency of the eruptions at each individual stations. Figure 5 shows an example of a wave propagating in this frequency band with each arrival time at the various station. These type of data were used to calculate wave propagation speed in the horizontal direction.

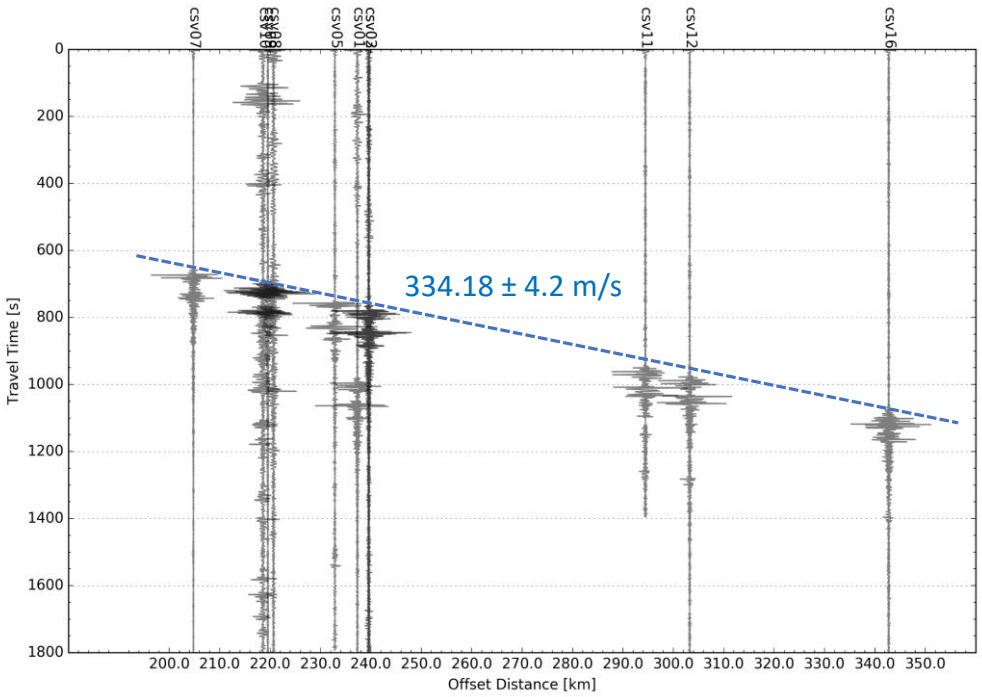

Figure 5. Band-pass filtered signals at frequencies of 0.1-0.5 Hz recorded at 12 stations in the Shikoku network. The name of station and the distance from the source point are labeled on the top and the bottom of the plot. The left label express the travel time in seconds after the event. The original waves of this plot is similar to the waves presented in the top-right figure 4.

The first arrival time of a wave at individual station was defined by the difference peak of the explosion pressure after band pass filtering. Then, all collected first arrival coordinates was used to calculate the approximate propagation speed by using a common linear regression method as shown in figure 6 draw as a dash-blue line with an approximate speed and its deviation. Repeating this procedure to the data shown in top-left and bottom-right figure 4, the approximate of propagation speeds was 341 ± 3.6 m/s and 339 ± 5.2 m/s respectively. The inferred propagation speed of around 336 m/s falls in the range of typical propagation speeds for similar eruptions [17], as well as artificial sources of large explosions (e.g., chemical and nuclear explosions) [18,19] that have been observed and analyzed previously. The speed is also in general agreement with the effective speed of sound wave propagation [1].

To identify infrasound signals from the volcanic eruptions, array data analyzed through the process described in section 4.2. Figure 6 displays an example of the detection process applied to selected station data in the period following the Mt. Shinmoedake eruption on March 10th, 2018. From top to bottom, the figure shows the stacked received signals after band pass filtering, maximum power at every time step processing, arrival direction as azimuth angle and velocity along the waveform. All of the infrasound data detected by the sensors had propagation speeds consistent with previous results of the present work, but the estimated azimuths of the suspected incoming signals differed slightly from the actual location of the volcano, likely due to the presence of winds and the higher contour of the Earth's surface (i.e., hills), which can cause a signal's path to stray from that of the arc of a circle that connects the source to the sensors.

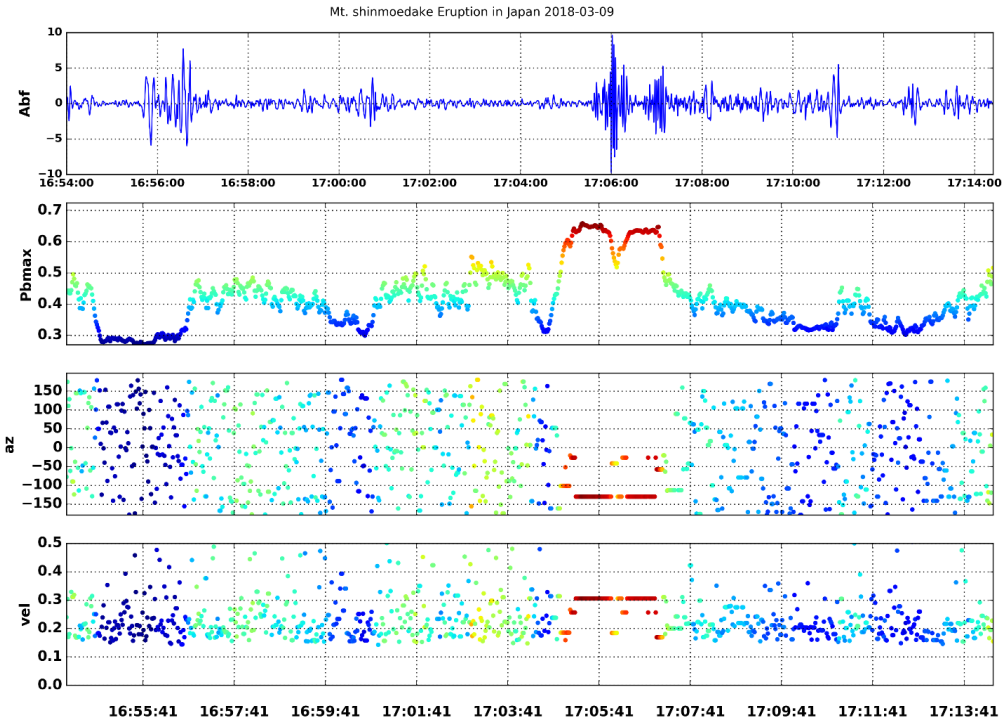

Figure 6. Array processing results for the March 10th, 2018 at 01:54 JST. Clear arrival with both arrival direction and apparent velocity are presented in stable value. The detection are colored by the coherent coefficient.

6.2. The earthquakes

Earthquake-generated infrasound signatures have been recorded from recent worldwide modern infrasound arrays such as the global infrasound network of the International Monitoring System of the Comprehensive Nuclear Test-Ban Treaty [20]. These characteristics of signatures have been analyzed to predict earthquake source points and ground-air coupling studies [21]. Infrasound signals associated with a large earthquake are classified according to the source location relative to the epicenter and receiver locations as local infrasound. It requires an infrasound sources with a significant ground motion to disturb the air pressure. In the present study, two samples of recorded earthquake occurred in Japan are presented. The distribution of seismic intensity aftershocks and the epicenter source reported by the Japan Meteorological Agency (JMA) shows that the distribution scope of the seismic intensity correspond to the earthquake magnitude (figure 7). The earthquake epicenter in the left figure 7 was near Tomakomai and shaking was felt strongly in Hokkaido and Aomori prefecture, Japan. Meanwhile, the earthquake in the right figure 7 was near Tanabe city and the shake spread out to several prefecture in Shikoku and Kansai regions.

Examples of infrasonic signals associated with an earthquake in Japan several times after the establishment of sensor network are shown in figure 8. The signals associated with an earthquake in Tomakomai, Hokkaido, Japan that occurred on September 6th, 2018, with a moment magnitude M = 6.6 at the center point (42.6861N, 141.9294E, http://earthquake.usgs.gov), are shown in left figure 8. Signals from this earthquake were detected at stations in the southern of Hokkaido, Japan. The original signals shows dense air pressure variation up to 8-10 Pa and

period of about 150 s (~2.5 min) at the shortest station (top panel of left figure 8). Nevertheless, we also find quite similar signatures to the other station west side from the epicenter (bottom panel of left figure 8). The amplitude is smaller than the previous ~5-7 Pa and for a period of about 150 s (~2.5 min).

On November 2nd, 2018, a medium scale earthquake occurred on the East side of Shikoku island, with a moment magnitude of M = 5.4 earthquake, which was in a depth of 44 km (33º41.4'N,135º11.7'E, https://www.data.jma.go.jp). Despite its deep center, infrasound signals associated with this earthquake were recorded at three stations at Muroto of Kochi prefecture, Japan. Right panel of figure 8 shows the original signals at three stations over Kochi prefecture, Japan (CSV14, CSV15 and CSV16). The infrasound wave follows the local infrasound by ~20 seconds for the main shock (07:53:54 UTC) with small amplitude fluctuation of about ~1 Pa and for a period of about 70 s (~1 min).

Figure 9 shows the infrasound signals from the earthquake that were recorded by infrasound stations at Hokkaido, Japan. Infrasound channels are band-pass filtered in the frequency range of 0.5-1.0 Hz. The initial signal was followed by ~1 minute duration infrasound signals lasting around ~120-400 seconds after the earthquake; such long wave pattern were apparently generated by ground shaking around the epicenter and in the surrounding regions.

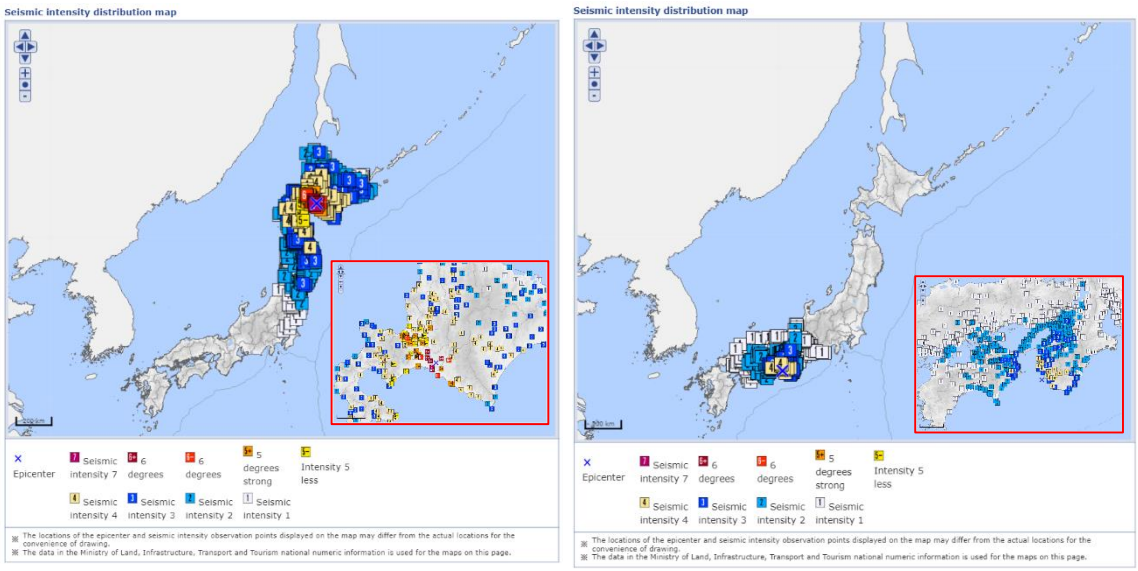

Figure 7. Geographical map of the distribution seismic intensity. (left) The Tomakomai-earthquake on September 5th, 2018, at 18:07:59 UTC. (right) The Tanabe-earthquake on November 2nd, 2018, at 07:53:54 UTC. The location of epicenter and seismic intensity observation point are labeled with blue cross sign and colored square with scaled intensity number, respectively (https:/www.data.jma.go.jp/).

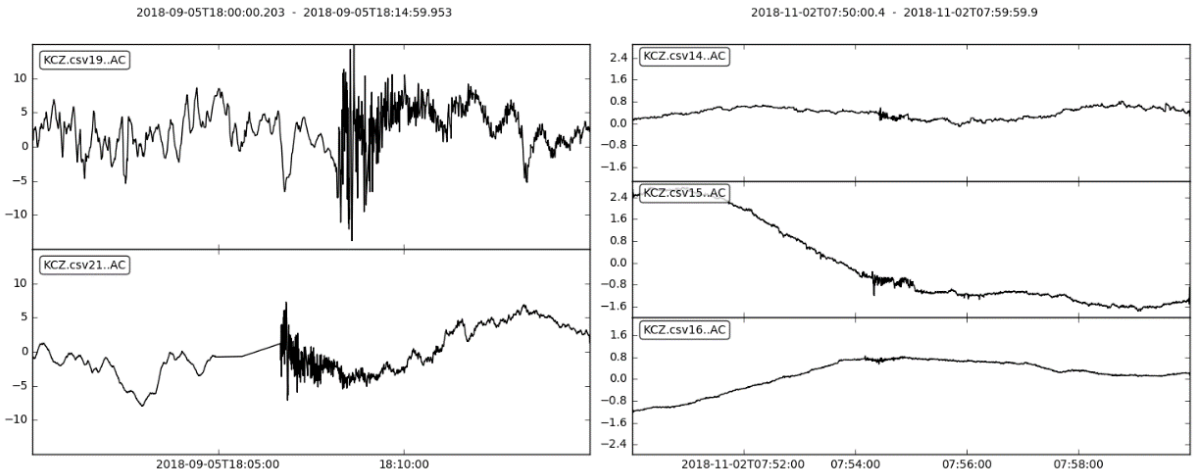

Figure 8. Example of signals recorded at KUT sensor network in Japan. The original signals associated with the earthquake in Tomakomai, Hokkaido on September 5th, 2018, at 18:07 UTC (left) and in Tanabe, Wakayama on November 2nd, 2018, at 07:53 UTC (right).

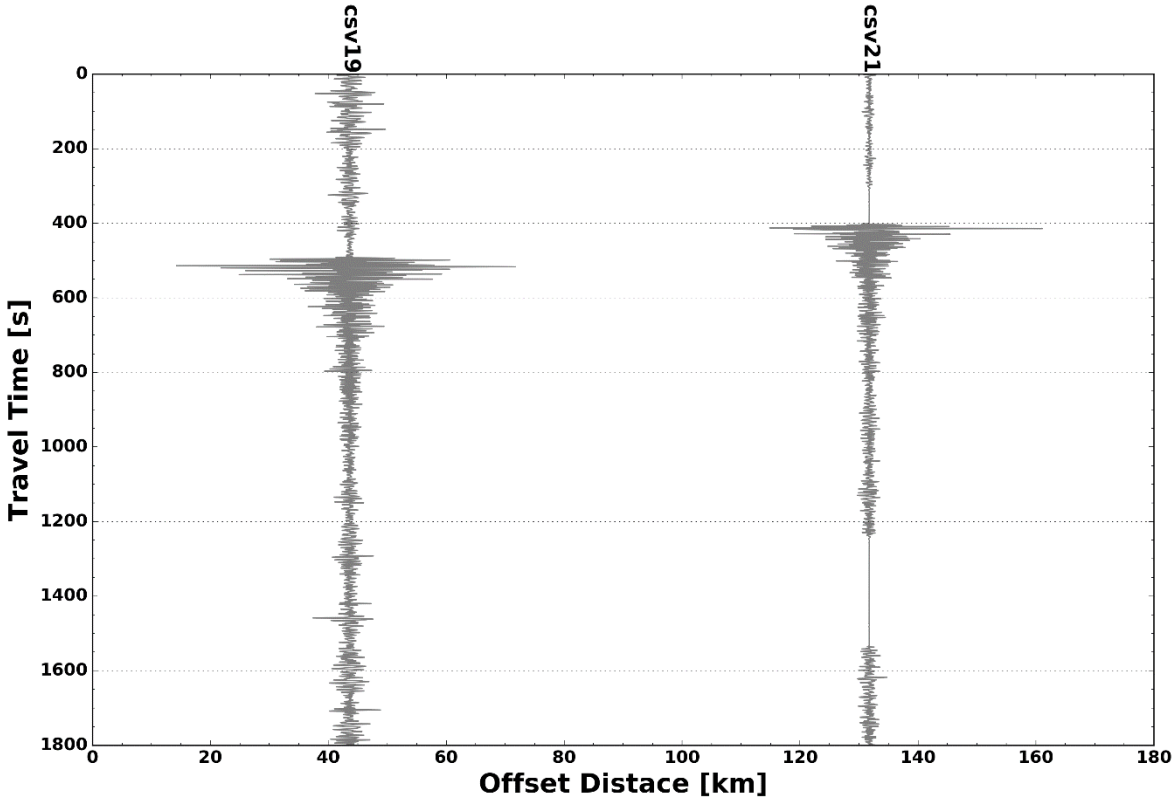

Figure 9. Band-pass filtered signals at frequencies of 0.5-1.0 Hz recorded at 2 stations near the earthquake epicenter on September 5th, 2018, at 18:07 UTC. The name of station and the distance from the source point are labeled on the top and the bottom of the plot. The left label express the travel time in seconds after the event. The original waves of this plot is similar to the waves presented in the left panel figure 8.

7. Conclusions and future work

In this report, the data cover a fairly wide range of both geo-potential event on the ground magnitudes. Within this events, a distribution of infrasound sensor over Japan has been clearly detected their signatures. The strong explosion at mt. Aso, mt. Sakurajima and mt. Shinmoedake, Japan, on October 8th,2016, at 01:46 JST, March 10th, 2018, at 01:54 JST and June 16th, 2018, at 07:30 JST respectively were clearly detected by the sensors. As an example, the calculated apparent velocity and arrival direction of the source range from several kilometer per second and close to the source point. The mid-high earthquake of September 5th, 2018, at 18:07 UTC and November 2nd, 2018, at 07:53 UTC that occurred near Hokkaido and Shikoku island, Japan generated infrasonic waves were also recorded by the sensors.

An interesting possibility for the future that there is a wide potential opportunities for research in this field. The use of ground source parameterizations through magnitude may be able to improve the understanding source wave characteristics such as frequency, amplitude and duration for each events. Comparing with the wave propagation modeling by a comprehensive fluid-dynamic computations should be pursued. In particular, the use of realistic surface and atmospheric background characteristic data in the extension distance range of the propagation wave from strong source wave would be advantage and could help to explain duration characteristics. A growing infrasound sensor network in Japan offers the possibility of detection of infrasound from the earthquake and volcano eruptions. In the future, the network would widely expand observation point in order to enlarge the database of source detections for analysis and studies.

References

1. Drob, D.P.; Picone, J.M.; Garcés, M. Global morphology of infrasound propagation. *J. Geophys. Res. Atmos.* **2003**, *108*, 1–12.
2. Evers, L.G.; Haak, H.W. Tracing a meteoric trajectory with infrasound. *Geophys. Res. Lett.* **2003**, *30*, 1–4.
3. Garcés, M.; Caron, P.; Hetzer, C.; Le Pichon, A.; Bass, H.; Drob, D.; Bhattacharyya, J. Deep infrasound radiated by the Sumatra earthquake and tsunami. *Eos, Trans. Am. Geophys. Union* **2005**, *86*, 317–320.
4. Jhonson, J.B.; Aster, R.C.; Kyle, P.R. Volcanic eruptions observed with infrasound. *Geophys. Res. Lett.* **2004**, *31*, L14604.
5. Johnson, J.B. Generation and propagation of infrasonic airwaves from volcanic explosions. *J. Volcanol. Geotherm. Res.* **2003**, *121*, 1–14.
6. Blanc, E.; Le Pichon, A.; Ceranna, L.; Farges, T.; Marty, J.; Herry, P. Global Scale Monitoring of Acoustic and Gravity Waves for the Study of the Atmospheric Dynamics. In *Infrasound Monitoring for Atmospheric Studies*; Le Pichon, A., Blanc, E., Hauchecorne, A., Eds.; Springer Netherlands: Dordrecht, 2009; pp. 647–664 ISBN 978-1-4020-9508-5.
7. Smets, P.S.M.; Evers, L.G. The life cycle of a sudden stratospheric warming from infrasonic ambient noise observations. *J. Geophys. Res.* **2014**.
8. Assink, J.D.; Waxler, R.; Drob, D. On the sensitivity of infrasonic traveltimes in the equatorial region to the atmospheric tides. *J. Geophys. Res. Atmos.* **2012**.
9. Le Pichon, A.; Blanc, E.; Drob, D.; Lambotte, S.; Dessa, J.X.; Lardy, M.; Bani, P.; Vergniolle, S. Infrasound monitoring of volcanoes to probe high-altitude winds. *J. Geophys. Res. Atmos.* **2005**, *110*.
10. Yamamoto, M.-Y.; Yokota, A. *Infrasound Monitoring for Disaster Prevention from Geophysical Destructions*;
11. Evers, L.G.; Haak, H.W. Recent observations at the Deelen Infrasound array. In Proceedings of the Infrasound Technology Workshop; Kailua-Kona, Hawaii, 2001.
12. Le Pichon, A.; Guilbert, J.; Cansi, Y. Infrasonic waves from natural sources. In Proceedings of the Infrasound Technology Workshop; Kailua-Kona, Hawaii, 2001.
13. Christie, D.; Kennett, B.; Tarlowski, C. DETECTION OF REGIONAL AND DISTANT ATMOSPHERIC EXPLOSIONS AT IMS INFRASOUND STATIONS. In Proceedings of the 27th Seismic Research; 2005.
14. Campus, P. Monitoring volcanoes at the CTBT IMS network. In Proceedings of the The 2006 infrasound technology workshop; Alaska, USA, 2006.
15. Campus, P. The IMS infrasound network: detection of a large variety of events including volcanic eruptions. In Proceedings of the The 2007 infrasound technology workshop; Tokyo, Japan, 2007.
16. Sato, E.; Fukui, K.; Shimbori, T. Aso volcano eruption on October 8, 2016, observed by weather radars. *Earth, Planets Sp.* **2018**, *70*, 105.
17. Campus, P. Monitoring volcanic eruptions with the IMS infrasound network. *Inframatics* **2006**, *15*, 6–12.
18. Assink, J.; Averbuch, G.; Shani-Kadmiel, S.; Smets, P.; Evers, L. A Seismo-Acoustic Analysis of the 2017 North Korean Nuclear Test. *Seismol. Res. Lett.* **2018**, *89*.
19. Ceranna, L.; Le Pichon, A.; Green, D.N.; Mialle, P. The Buncefield explosion: a benchmark for infrasound analysis across Central Europe. *Geophys. J. Int.* **2009**, *177*, 491–508.
20. Christie, D.R.; Campus, P. The IMS infrasound network: Design and establishment of infrasound stations. In *Infrasound Monitoring for Atmospheric Studies*; 2009; pp. 29–75 ISBN 9781402095078.

21. Le Pichon, A.; Guilbert, J.; Vega, A.; Garcés, M.; Brachet, N. Ground-coupled air waves and diffracted infrasound from the Arequipa earthquake of June 23, 2001. *Geophys. Res. Lett.* **2002**, *29*, 33–34.

Table 1. List of Stations Used for Infrasound Studies

Station Code	Latitude (ºN)	Longitude (ºE)	Station Code	Latitude (ºN)	Longitude (ºE)
KCZ00	33.6097	133.6916	KCZ **15**	33.5243	134.2809
KCZ01	33.0363	133.0311	KCZ **16**	33.2680	134.1641
KCZ02	33.0547	133.0461	KCZ **17**	33.5277	133.7575
KCZ 03	33.0405	133.0563	KCZ **19**	42.6022	141.4797
KCZ 04	32.9852	132.9988	KCZ **20**	42.4988	143.4325
KCZ 05	33.0413	132.9713	KCZ **21**	41.9361	143.2408
KCZ 06	35.7158	139.9441	KCZ **30**	34.9650	136.6244
KCZ 07	32.9055	132.7180	KCZ **31**	33.8883	136.1000
KCZ 08	32.7319	133.0186	KCZ **32**	34.0705	136.1908
KCZ 09	32.4315	133.0186	KCZ **33**	34.4875	136.7091
KCZ 10	32.7322	132.9944	KCZ **34**	34.7691	137.3913
KCZ 11	33.4510	133.4417	KCZ **35**	34.6000	138.2241
KCZ 12	33.5061	133.5111	KCZ **40**	33.5708	131.2191
KCZ 13	33.5652	133.6672	KCZ **41**	33.2844	131.4872
KCZ 14	33.5033	133.8794	KCZ **51**	33.9655	140.6447